

---

# Ab initio calculations of nuclei using chiral interactions with realistic saturation properties

---

**Ab initio Rechnungen von Atomkernen basierend auf chiralen Wechselwirkungen mit realistischen Saturierungseigenschaften**

Zur Erlangung des Grades eines Doktors der Naturwissenschaften (Dr. rer. nat.)

genehmigte Dissertation von M.Sc. Johannes Simonis, geb. in Dernbach/Westerwaldkreis

Tag der Einreichung: 4. Juli 2017, Tag der Prüfung: 19. Juli 2017

Darmstadt 2017 – D 17

1. Gutachten: Prof. Achim Schwenk, Ph.D.

2. Gutachten: Prof. Dr. Hans-Werner Hammer



TECHNISCHE  
UNIVERSITÄT  
DARMSTADT

Fachbereich Physik  
Institut für Kernphysik  
Theoriezentrum

Ab initio calculations of nuclei using chiral interactions with realistic saturation properties  
Ab initio Rechnungen von Atomkernen basierend auf chiralen Wechselwirkungen mit realistischen  
Saturierungseigenschaften

Genehmigte Dissertation von M.Sc. Johannes Simonis, geb. in Dernbach/Westerwaldkreis

1. Gutachten: Prof. Achim Schwenk, Ph.D.
2. Gutachten: Prof. Dr. Hans-Werner Hammer

Tag der Einreichung: 4. Juli 2017

Tag der Prüfung: 19. Juli 2017

Darmstadt 2017 – D 17

Bitte zitieren Sie dieses Dokument als:

URN: urn:nbn:de:tuda-tuprints-70314

URL: <http://tuprints.ulb.tu-darmstadt.de/7031>

Dieses Dokument wird bereitgestellt von tuprints,

E-Publishing-Service der TU Darmstadt

<http://tuprints.ulb.tu-darmstadt.de>

[tuprints@ulb.tu-darmstadt.de](mailto:tuprints@ulb.tu-darmstadt.de)

---

## Abstract

---

Ab initio calculations of nuclei from the valley of stability to the drip lines are a prime challenge in low-energy nuclear theory. The interactions in atomic nuclei, being composed of protons and neutrons, are governed by strong interactions. The fundamental theory of strong interactions is quantum chromodynamics (QCD). Due to the non-perturbative nature of QCD at low energies a direct calculation of nuclear forces from the underlying theory is presently not possible. However, chiral effective field theory (EFT) connects the symmetries of QCD to nuclear forces, enabling a systematic derivation of nuclear interactions, naturally including many-nucleon forces and uncertainty estimates. Chiral EFT interactions are generally softer than phenomenological interactions, but their low- and high-momentum components can still be coupled strongly. Using renormalization group (RG) methods, e.g., the similarity renormalization group, this coupling can be removed by a unitary transformation, resulting in even softer interactions. In addition to advances on nuclear forces and RG methods, several ab initio approaches have been developed in recent years to calculate medium-mass nuclei in a systematically improvable way.

We employ some of these advanced many-body approaches in our calculation of nuclei, starting from a set of chiral two- and three-nucleon interactions that, when used in perturbative calculations of symmetric nuclear matter, reproduce empirical saturation properties within theoretical uncertainties. We study ground- and excited-state energies of doubly open-shell nuclei from oxygen to calcium using valence-space interactions derived using many-body perturbation theory. Given the prominent role of the calcium isotopic chain, we perform coupled-cluster calculations to investigate stable and short-lived neutron-rich calcium isotopes. The ab initio calculations reveal that the size of the neutron skin of  $^{48}\text{Ca}$  is much smaller than results from density functional theory. In addition, the very steep increase in charge radii up to  $^{52}\text{Ca}$  measured recently questions the neutron shell closure at  $N = 32$  and provides an intriguing benchmark for our coupled-cluster calculations. We extend our study to ground states of closed-shell nuclei from  $^4\text{He}$  to  $^{78}\text{Ni}$  using the in-medium similarity renormalization group (IM-SRG). The experimental binding-energy and charge-radius systematics is well described, encouraging the decoupling of valence-space interactions with the IM-SRG to study also open-shell nuclei. The results for ground- and excited-state energies as well as for charge radii of open-shell nuclei achieve a similar level of agreement found in the closed-shell calculations, enabling broad predictions for future experiments up to mass number  $\sim 80$ .



---

## Zusammenfassung

---

Ab initio Berechnungen von Atomkernen vom Tal der Stabilität bis zu den Grenzen der Neutronen- und Protonenstabilität sind eine fundamentale Herausforderung der theoretischen Kernphysik. Die Wechselwirkungen in Atomkernen, welche aus Protonen und Neutronen bestehen, werden durch starke Wechselwirkungen bestimmt. Die fundamentale Theorie der starken Wechselwirkung ist die Quantenchromodynamik (QCD). Durch die nicht perturbative Beschaffenheit der QCD im Niederenergiebereich ist es zur Zeit nicht möglich Kernkräfte direkt aus der zugrunde liegenden Theorie zu berechnen. Die chirale effektive Feldtheorie (EFT) verbindet jedoch die Symmetrien der QCD mit Kernkräften und ermöglicht eine systematische Berechnung von nuklearen Wechselwirkungen einschließlich Vielteilchenkräften und Unsicherheitsabschätzungen. Wechselwirkungen basierend auf der chiralen EFT sind im Allgemeinen weicher als phänomenologische, dennoch kann eine starke Kopplung von Komponenten bei niedrigen und hohen Impulsen bestehen. Unter Verwendung von Methoden der Renormierungsgruppe (RG), z.B. der Similarity Renormalization Group, kann diese Kopplung durch eine unitäre Transformation entfernt und damit die Wechselwirkung weicher gemacht werden. Zusätzlich zum Fortschritt bei Kernkräften und RG Methoden wurden in den vergangenen Jahren mehrere ab initio Zugänge entwickelt, um mittelschwere Atomkerne in einer systematisch verbesserungsfähigen Art zu berechnen.

Wir verwenden einige dieser modernen Vielteilchenmethoden in unseren Berechnungen von Atomkernen, ausgehend von einem Satz von Zwei- und Dreiteilchenkräften, welche unter Verwendung einer störungstheoretischen Rechnung für symmetrische Kernmaterie den empirischen Saturierungspunkt innerhalb theoretischer Unsicherheiten reproduzieren. Wir untersuchen Atomkerne mit nicht abgeschlossenen Schalen von Sauerstoff bis Calcium ausgehend von Valenzschalenwechselwirkungen, welche aus Vielteilchenstörungstheorie berechnet wurden. Durch die bedeutende Rolle der Calciumisotopenkette führen wir Coupled-Cluster Rechnungen für stabile und kurzlebige, neutronenreiche Calciumisotope durch. Unsere ab initio Rechnungen zeigen, dass die Dicke der Neutronenhaut von  $^{48}\text{Ca}$  viel kleiner ist als Resultate aus Dichtefunktionaltheorie. Außerdem stellt der starke Anstieg in den kürzlich gemessenen Ladungsradien bis  $^{52}\text{Ca}$  den Neutronenschalenabschluss  $N = 32$  in Frage und bietet einen Benchmark für unsere Coupled-Cluster Rechnungen. Wir erweitern unsere Untersuchung der Grundzustände auf Atomkerne mit abgeschlossenen Schalen zwischen  $^4\text{He}$  und  $^{78}\text{Ni}$  mit Hilfe der In-Medium Similarity Renormalization Group (IM-SRG). Die experimentelle Systematik von Bindungsenergien und Ladungsradien wird gut beschrieben und ermutigt das Entkoppeln von Valenzschalenwechselwirkungen mit der IM-SRG, um Atomkerne mit offenen Schalen zu untersuchen. Die Ergebnisse für Grundzustands- und Anregungsenergien sowie Ladungsradien für Atomkerne mit offenen Schalen erreichen eine ähnliche Übereinstimmung wie im Fall von Rechnungen für Atomkerne mit abgeschlossenen Schalen, und ermöglichen damit umfassende Vorhersagen für zukünftige Experimente bis zur Massenzahl  $\sim 80$ .



---

---

## Contents

---

<b>1</b>	<b>Introduction</b>	<b>7</b>
<b>2</b>	<b>Chiral effective field theory for nuclear forces</b>	<b>11</b>
2.1	Quantum chromodynamics	11
2.2	Chiral effective field theory for low-energy QCD	14
2.2.1	Basic principles	14
2.2.2	Chiral effective field theory	14
2.3	Old and new regularization schemes	17
2.4	Novel fitting strategies for the determination of the low-energy couplings	19
<b>3</b>	<b>Similarity renormalization group</b>	<b>21</b>
<b>4</b>	<b>Chiral NN+3N Hamiltonians used in this work</b>	<b>25</b>
<b>5</b>	<b>Jacobi-momentum and single-particle harmonic-oscillator bases</b>	<b>27</b>
5.1	Two-body bases	27
5.2	Three-body bases	30
5.2.1	Partial-wave decomposition and transformation to relative harmonic oscillator states	31
5.2.2	Basis representation of the antisymmetrizer	32
5.2.3	Three-body Talmi Moshinsky transformation	35
<b>6</b>	<b>Many-body approaches</b>	<b>41</b>
6.1	Normal ordering	43
6.2	Many-body perturbation theory for valence-space interactions	48
6.2.1	Basics	48
6.2.2	Time-dependent Rayleigh-Schrödinger perturbation theory	51
6.3	Hartree-Fock method	60
6.4	In-medium similarity renormalization group	63
6.4.1	Basics and flow equations	64
6.4.2	Generators	66
6.4.3	General observables and Magnus formulation	69
6.5	Coupled-cluster method	71
6.5.1	Coupled-cluster theory for closed-shell nuclei	72
6.5.2	Equation-of-motion techniques	76
6.5.3	General observables	79
<b>7</b>	<b>Exploring <i>sd</i>-shell nuclei</b>	<b>81</b>
<b>8</b>	<b>Calcium isotopic chain</b>	<b>87</b>
8.1	Coupled-cluster calculations of energies, radii and charge densities	87
8.2	Neutron and weak-charge distributions of the $^{48}\text{Ca}$ nucleus	88
8.3	Unexpectedly large charge radii of neutron-rich calcium isotopes	92
<b>9</b>	<b>In-medium similarity renormalization group calculations of nuclei</b>	<b>95</b>
9.1	Closed-shell nuclei from $^4\text{He}$ to $^{78}\text{Ni}$	95
9.2	Closed-shell nuclei in the vicinity of $A \sim 100$	100
9.3	Open-shell isotopic chains	100
9.3.1	Ground-state energies and radii	101
9.3.2	Excited states	104
<b>10</b>	<b>Summary and outlook</b>	<b>107</b>
<b>A</b>	<b>Isobaric multiplet mass equation applied in the <i>sd</i>-shell</b>	<b>109</b>





## 1 Introduction

The discovery of the neutron by Chadwick in 1932 [1] provided the basis for the understanding of atomic nuclei as compound, self-bound objects composed of protons and neutrons. While first theoretical descriptions of atomic nuclei were performed semi-empirically within the liquid-drop model, e.g., the Bethe-Weizsäcker mass formula developed in 1935 [2], more sophisticated microscopic models emerged, assuming nucleons to strongly interact through meson exchanges as proposed in the seminal work by Yukawa [3].

The development of quantum chromodynamics (QCD), describing the interaction of color-charged quarks via gluon exchanges, put the field on a new level with interactions in atomic nuclei to be governed by residual strong interactions between the color-charge neutral nucleons. Although the fundamental aspects of QCD had been established in the beginning of the 1970s, meson-exchange or phenomenological nucleon-nucleon (NN) potentials were still widely used in the 1990s and are even used nowadays. The reason for that is the non-perturbative nature of QCD at low energies complicating a direct analytical derivation of nuclear forces from the underlying theory. However, in the beginning of the 1990s Weinberg [4] opened a new era in nuclear physics by laying the foundations of chiral effective field theory (EFT), see Refs. [5, 6] for recent reviews. This approach connects the symmetries of QCD to nuclear forces, allowing a systematic derivation of nuclear forces including consistent many-body forces, consistent electroweak currents, and uncertainty estimates.

In addition to nuclear forces, systematic approaches are needed to solve the non-relativistic many-body Schrödinger equation without uncontrolled truncations. A pioneer of these so called *ab initio* many-body methods is the nuclear Green's Function Monte Carlo (GFMC) method [7–9]. Here, the many-body Schrödinger equation is solved by performing the integration over the particle coordinates stochastically, while summations in spin-isospin space are performed explicitly. Consequently, the method provides very accurate results, but is computationally very expensive and allows only calculations of nuclei with mass number  $A \leq 12$ . In addition, approaches based on large-scale diagonalizations, e.g., the no-core shell model (NCSM) [10], are able to perform quasi-exact calculations of up to  $p$ - and even lower  $sd$ -shell nuclei by employing importance truncation (IT) [11] techniques. Moreover, in recent years several *ab initio* approaches have been established to solve the nuclear many-body problem beyond mass number  $A > 20$ , as shown in Fig. 1.1, in a truncated but controlled and systematically improvable way. These

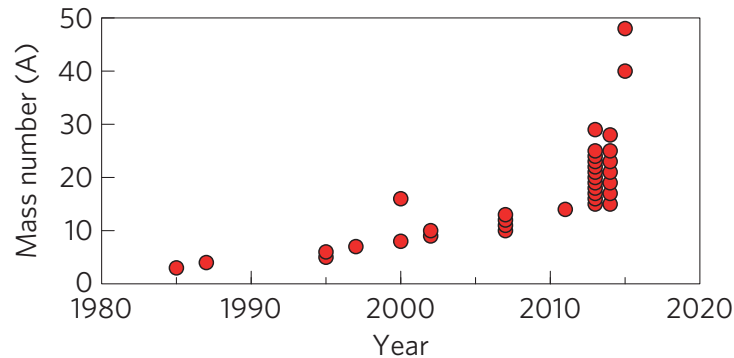


**Figure 1.1:** Progress in the *ab initio* calculation for the nuclear  $A$ -body problem. The progress in the mass number  $A$  was only linear until 2010 because the exponentially increasing computer power was used for exponentially expensive many-body methods. New methods with a polynomial scaling in  $A$  have greatly increased the reach in recent years. Taken from Ref. [12].

methods are coupled-cluster (CC) theory [13], the In-Medium Similarity Renormalization Group (IM-SRG) [14] and self-consistent Green's function (SCGF) theory [15] as well as nuclear lattice EFT [16]. While some of these methods are limited to closed-shell or singly open-shell systems, others have been generalized to doubly open-shell systems as well as the calculation of excited-state properties.

Although the coupling of low and high momenta is weaker for non-local interactions based on chiral EFT compared to phenomenological potentials, all of the many-body methods mentioned above that rely on a matrix representation of the Hamiltonian have benefited from methods to decouple low and high momentum degrees of freedom. Different renormalization group methods, such as the similarity renormalization group (SRG) [17], have been developed, enabling many-body calculations with an accelerated convergence with respect to the model-space size. However, the evolution of, e.g., a two-body interaction will induce many-body forces, in general, up to the  $A$ -body level, making a careful analysis of the induced contributions necessary [18, 19].

While for some ab initio methods mentioned above the formal inclusion of three-nucleon (3N) forces, either induced or from the starting Hamiltonian, is straightforward, e.g., GFMC, lattice EFT, or NCSM calculations, others require a generalization to the three-body level, as successfully performed for CC theory [20–22]. Moreover, the computational cost of NCSM or CC calculations usually increases by orders of magnitude when including 3N forces explicitly. Thus, the development of the normal-ordering approximation allows to include up to two-body contributions of 3N forces, enabling calculations based on a two-body formalism. Nevertheless the calculation of a reference state, e.g., in a Hartree-Fock calculation, to perform the normal ordering is done at the full three-body level. This poses an enormous challenge for the transformation of 3N matrix elements into the single-particle basis when aiming at the calculation of heavy nuclei.

Instead of directly aiming at the calculation of finite nuclei, nuclear matter is often considered as an intermediate benchmark. Nuclear matter is a system of infinite size with a given ratio of protons and neutrons, determined by the proton fraction  $x = n_p/(n_p + n_n)$  with the finite proton and neutron density  $n_p$  and  $n_n$ . While nuclear interactions are taken into account, the Coulomb interaction among protons is omitted. The extreme case of no protons, i.e.,  $x = 0$ , is called neutron matter. The system with an equal amount of protons and neutrons, i.e.,  $x = 0.5$ , corresponds to symmetric nuclear matter, while systems with an arbitrary fraction of protons and neutrons are denoted by asymmetric nuclear matter.

A long standing issue in low-energy nuclear physics was the reproduction of nuclear matter saturation. While the important role of 3N forces for saturation was suggested long ago [23, 24], progress has been hindered by difficulties to formulate consistent 3N forces for meson-exchange or phenomenological NN potentials. In addition, difficulties in solving the nuclear many-body problem for these potentials prevented progress. When the empirical saturation properties were reproduced quantitatively, it was imposed by adjusting short-range 3N forces, see, e.g., Refs. [25, 26]. However, recently this changed when nuclear matter calculations using soft Hamiltonians, derived

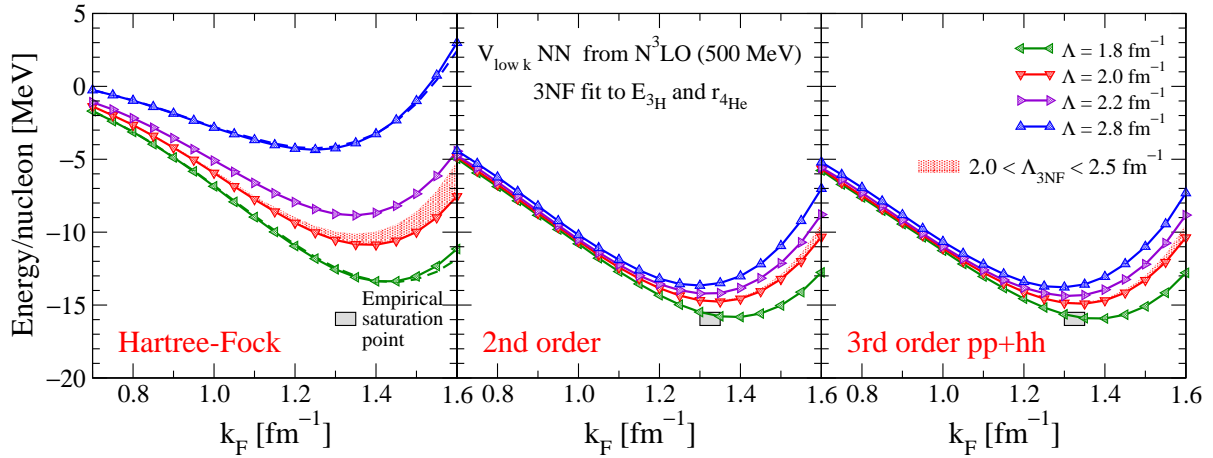


**Figure 1.2:** Energy per nucleon of symmetric nuclear matter plotted as a function of the Fermi momentum  $k_F$  at the Hartree-Fock level (left), and including second-order (middle) and third-order particle-particle/hole-hole contributions (right). The results are based on low-momentum interactions  $V_{\text{low } k}$  obtained from the  $N^3\text{LO}$  NN potential EM 500 MeV [27] supplemented with non-local  $N^2\text{LO}$  3N forces with 3N low-energy couplings adjusted to the  ${}^3\text{H}$  binding energy and  ${}^4\text{He}$  charge radius. Taken from Ref. [28].

from chiral NN+3N interactions with low-energy couplings only fit to few-body ( $A \leq 4$ ) data, reproduced the empirical saturation point within uncertainty estimates [28], as shown in the right panel of Fig. 1.2. While the results in Fig. 1.2 are shown for low-momentum interactions  $V_{\text{low } k}$ , similar results hold for SRG interactions [29].

Atomic nuclei are arranged according to their proton and neutron number in the nuclear chart. While up to now about 3000 nuclei up to proton number  $Z = 120$  have been studied experimentally [30], it was calculated that about 7000 nuclides are bound [31]. The particle stability of a nuclide is primarily determined by its separation energy, which is the amount of energy needed to remove a single neutron ( $S_n$ ) or proton ( $S_p$ ) or two neutrons ( $S_{2n}$ ) or protons ( $S_{2p}$ ). In terms of the binding energy of a nuclide with proton number  $Z$  and neutron number  $N$ ,  $BE(Z, N)$  (defined negatively), the one- and two-neutron separation energies are defined as  $S_n = BE(Z, N - 1) - BE(Z, N)$  and  $S_{2n} = BE(Z, N - 2) - BE(Z, N)$  with the proton separation energies defined analogously. In case the separation energy is positive the nuclide is stable against particle emission, while in case the separation energy is negative it is unstable. Thus, the location of the drip line is determined by  $S_n = 0$  for the one- and  $S_{2n} = 0$  for the

two-neutron drip line. Pairing, which makes nuclides with an even number of nucleons generally more bound than their odd-mass neighbors, has a strong effect on the location of the drip line. This can be seen, e.g., already in the helium isotopic chain with the even-even  ${}^4,6,8\text{He}$  being bound, whereas  ${}^5,7,9\text{He}$  are unbound.

Figure 1.3 shows the status of the nuclear landscape for even values of the proton number  $Z$  and the neutron number  $N$  (status from 2012), including 767 stable (black squares) or radioactive (green squares) isotopes known experimentally. In contrast to the location of the proton drip line, which is well established for all elements oc-

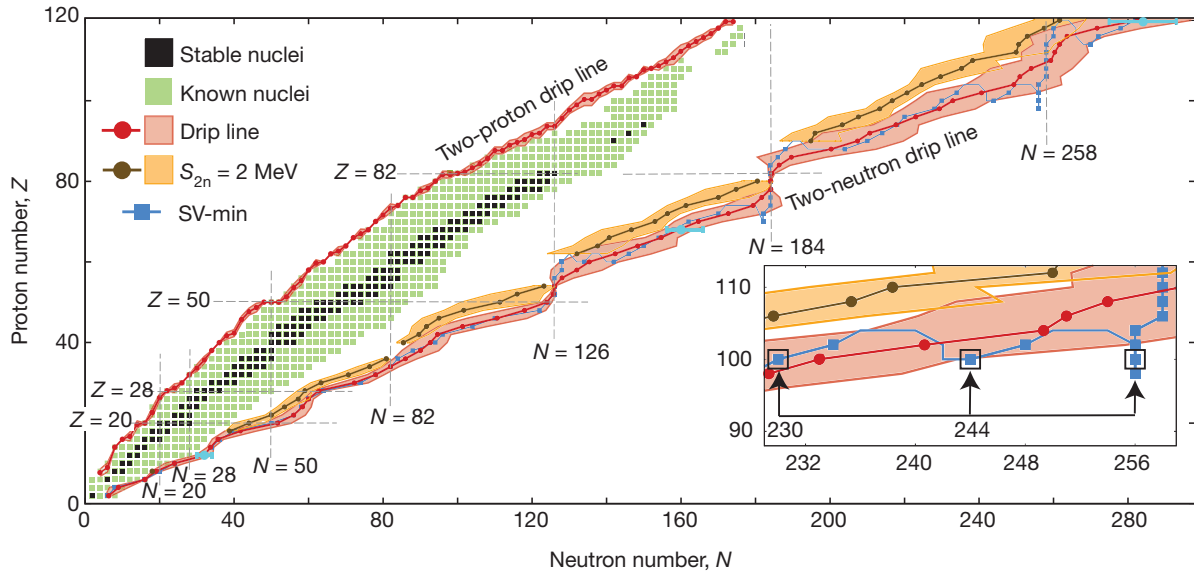


**Figure 1.3:** Status of the nuclear landscape in 2012 as a function of proton number  $Z$  and neutron number  $N$ . The figure includes 767 even-even nuclides known experimentally, represented as black squares for stable and green squares for radioactive isotopes. The red lines show the two-proton and two-neutron drip line when averaging over different EDFs. While the  $S_{2n} = 2 \text{ MeV}$  line is shown in brown, the blue line represents the neutron drip line for another EDF. The inset focuses on the neutron drip line near  $Z = 100$ . Taken from Ref. [31].

curing naturally on earth, the location of the neutron drip line is only known experimentally up to the oxygen isotopic chain. The experimental investigation of neutron-rich nuclei is very challenging due to low production yields and extremely short lifetimes. Since the first successful construction of a particle accelerator by Cockcroft and Walton [32] in 1932, light-ion and heavy-ion accelerators with a successive increase in beam energy allowed to expand the nuclear chart to new regions. Neutron-rich nuclei can be produced by target fragmentation, for which a stable, heavy, neutron-rich nucleus is bombarded with light ions at high energies, inducing fragmentation, spallation, or fission reactions. The inverse process, the fragmentation of heavy projectiles on light-mass targets also allows to produce new neutron-rich nuclides. After their production the nuclides of interest have to be separated and transported to the experimental setup, using the in-flight separation [33] or the isotope separation on line (ISOL) technique [34]. Experimental facilities are, however, currently limited in neutron excess, see, e.g., the recent measurements along the calcium isotopic chain [35–37]. Nevertheless, a great extent of the neutron-rich regime will be accessed by experiments on the way at the Radioactive Isotope Beam Factory (RIBF) at RIKEN in Tokyo (Japan) [38], while the Facility for Antiproton and Ion Research (FAIR) at the GSI Helmholtz-Center for Heavy-Ion Research in Darmstadt [39] and the Facility for Rare Isotope Beams (FRIB) at the Michigan State University in East Lansing (USA) [40] are still under construction. However, even with these future facilities the neutron drip line for heavy elements will not be reached.

Especially neutron-rich nuclei in the medium- to high-mass region far from stability are of interest in nuclear astrophysics, being crucial for the description of heavy-element nucleosynthesis. Heavier elements beyond iron cannot be formed in stellar burning processes, but there exist different nucleosynthesis processes for the formation of heavy elements. One of these is the rapid neutron-capture process (r-process) [41], occurring in extremely dense neutron-rich environments such as core-collapse supernovae or neutron-star mergers. Theoretical simulations of the r-process rely on calculations of neutron capture and photodissociation cross sections as well as fission barriers over a wide mass range only accessible with energy-density functionals (EDF). However, so far EDFs have not

---

been calculated directly from nuclear forces but parametrizations like Skyrme [42] and Gogny [43] have been determined by a fit to experimentally known nuclei. Thus, a comparison of ab initio and EDF results in the medium-mass regime, accessible by both approaches, provides an important test of global EDF models.

The highest densities that can be observed in the cosmos, up to  $\sim 10^{15} \text{ g cm}^{-3}$ , are found in the core of neutron stars. Representing the final stage of a core-collapse supernovae, neutron stars consist mainly of neutrons with a small fraction of protons and electrons [44]. They have one to two times the mass of our sun with the presently upper mass limit determined by relatively recent observations of two-solar-mass neutron stars [45, 46]. Their radius has so far not been measured due to observational difficulties [47], but typical radii are estimated to be in the range of 10-15 km [48]. Theoretical constraints on the properties of neutron stars are obtained by calculations of infinite neutron matter. The energy per particle as a function of density, i.e., the equation of state, of neutron matter can be employed to predict the mass-radius relation of neutron stars [49, 50]. The recent observations of two-solar-mass neutron stars ruled out already many models of nuclear interactions not supporting such heavy neutron stars. Further observations, e.g., the simultaneous measurement of a neutron star's mass and radius, or its moment of inertia will further constrain the nuclear equation of state.

This thesis is organized as follows: In Chapter 2 we introduce chiral EFT for nuclear forces and summarize old and new regularization schemes as well as novel fitting strategies to determine the low-energy couplings. The similarity renormalization group to evolve nuclear forces to lower resolution scales is discussed in Chapter 3. Details about the NN+3N Hamiltonians employed in this work are given in Chapter 4, while we derive the transformation of NN and 3N momentum-space matrix elements into the single-particle harmonic-oscillator basis in Chapter 5. In Chapter 6 we present the many-body approaches used in this work. We explore *sd*-shell nuclei from valence-space interactions derived from many-body perturbation theory in Chapter 7, while we focus on CC calculations of neutron-rich calcium isotopes in Chapter 8. The impact of the saturation properties of nuclear forces on the properties of finite nuclei is investigated by IM-SRG calculations over a wide mass-range in Chapter 9. We conclude in Chapter 10 and give an outlook. The results presented in this thesis have been published in Refs. [12, 37, 51–53].

## 2 Chiral effective field theory for nuclear forces

The derivation of systematic nuclear interactions is a long-lasting endeavor in theoretical nuclear physics. In contrast to prior meson-exchange models or phenomenological interactions chiral effective field theory (EFT) systematically connects the symmetries of the underlying theory, namely quantum chromodynamics (QCD), with nuclear forces. In this section we first discuss the basic principles and symmetries of QCD. Starting from this basis we give an introduction to chiral EFT and summarize its latest developments.

### 2.1 Quantum chromodynamics

The underlying theory of strong interactions, that binds protons and neutrons to nuclei, is quantum chromodynamics (QCD), a local non-Abelian gauge theory. Its fundamental degrees of freedom are the matter fields, called quarks, and the gauge bosons, called gluons. There exist six quark flavors in nature (see Table 2.1). The quarks carry mass and electrical charge and interact via gluon exchanges. In addition, both quarks and gluons, also carry color charge. In nature, these constituents cannot be observed due to their - at least at low temperatures  $T$  and low baryon chemical potential  $\mu_b$  - confinement into color-neutral particles, the hadrons. There exist three color charges: Red (r), green (g) and blue (b). One way of composing color-neutral particles, in analogy to the additive color mixing of light, are baryons which consist of three quarks with different color charges, e.g.,  $u_r u_g d_b$  like the proton. Another way are mesons consisting of a quark and an antiquark, e.g.,  $u_r \bar{d}_r$  like the positively-charged pion  $\pi^+$ . Furthermore, there are indications for four-quark particles (tetraquarks) [54], while a five-quark state, so-called pentaquark, was recently measured at LHCb at the Large Hadron Collider (LHC) at CERN [55]. The pentaquark consists of four quarks and an antiquark.

For low-energy nuclear physics only the three lightest quarks up, down, and strange need to be taken into account, while the remaining three quarks are treated as heavy and are integrated out. The subsequent discussion follows Ref. [56], where further details can be found.

In this light-quark approximation the QCD Lagrangian is given by

$$\mathcal{L}_{\text{QCD}} = \sum_{f=u,d,s} (\bar{q}_f i \not{D} q_f - m_f \bar{q}_f q_f) - \frac{1}{2} \text{Tr}(G_{\mu\nu} G^{\mu\nu}), \quad (2.1)$$

using the Feynman-slash notation for the covariant derivative  $\not{D} \equiv \gamma^\mu D_\mu = \gamma^\mu (\partial_\mu + igA_\mu)$ .  $q_f$  denote the quark fields,  $m_f$  the quark masses and  $A_\mu$  the gluon fields, while the gluon-field-strength tensor is given by

$$G_{\mu\nu}^a = \partial_\mu A_\nu^a - \partial_\nu A_\mu^a + gf^{abc} A_\mu^b A_\nu^c, \quad (2.2)$$

with color indices  $a, b, c = 1, \dots, 8$ , the dimensionless coupling constant of the strong force  $g$ , and the  $SU(3)$  structure constants  $f^{abc}$ . By applying the projection operators  $q_R = (1 + \gamma_5)/2$ ,  $q_L = (1 - \gamma_5)/2$  the kinetic energy in Eq. (2.1) can be represented in terms of left- and right-handed quarks

$$\sum_f \bar{q}_f i \not{D} q_f = \sum_f (\bar{q}_{Lf} i \not{D} q_{Lf} + \bar{q}_{Rf} i \not{D} q_{Rf}). \quad (2.3)$$

This term is symmetric under the rotation of the three flavors of left-handed and right-handed quarks by independent unitary matrices. The  $U(3)_L \times U(3)_R$  symmetry is, however, not a symmetry of the quantum theory due to anomalies in the  $U(1)_A$  transformation. Hence, the remaining symmetry is  $U(1)_V \times SU(3)_L \times SU(3)_R$ . While  $U(1)_V$  just corresponds to baryon number conservation,  $SU(3)_L \times SU(3)_R$ , under which  $q_{Lf} \rightarrow L_{ff'} q_{Lf'}$  and  $q_{Rf} \rightarrow R_{ff'} q_{Rf'}$ , where  $R$  and  $L$  are independent  $SU(3)$  matrices, is called ‘‘chiral symmetry’’. The  $SU(3)_L \times SU(3)_R$  symmetry can be rewritten as  $SU(3)_A \times SU(3)_V = SU(3)_{L-R} \times SU(3)_{L+R}$  in terms of the axial chiral symmetry  $SU(3)_A$  and the vector symmetry  $SU(3)_V$ , which corresponds to the isospin symmetry generalized to three quarks. However, both symmetries  $SU(3)_A$  and  $SU(3)_V$  are explicitly broken due to the small, non-zero quark masses  $m_u \neq 0$ ,  $m_d \neq 0$ ,  $m_s \neq 0$ . The quark mass term may be written as

$$\sum_i m_i \bar{q}_i q_i = \sum_{i,j} \bar{q}_{Ri} M_{ij} q_{Lj} + \text{H.c.}, \quad \text{with} \quad M = \begin{pmatrix} m_u & & \\ & m_d & \\ & & m_s \end{pmatrix}, \quad (2.4)$$

coupling explicitly left- and right-handed quarks.

**Table 2.1:** Masses, electrical charges and additional quantum numbers of the six quark flavors from Particle Data Group (PDG) [57].

symbol	flavor(f)	mass	electric charge	
u	up	$2.3^{+0.7}_{-0.5}$ MeV	+2/3	isospin=+1/2
d	down	$4.8^{+0.5}_{-0.3}$ MeV	-1/3	isospin=-1/2
s	strange	$95 \pm 5$ MeV	-1/3	strangeness=-1
c	charm	$1275 \pm 25$ MeV	+2/3	charm=+1
b	bottom	$4660 \pm 30$ MeV	-1/3	bottom=-1
t	top	$173210 \pm 510 \text{ MeV} \pm 710 \text{ MeV}$	+2/3	top=+1

In addition to this explicit breaking axial chiral symmetry  $SU(3)_A$  is also spontaneously broken, even for vanishing quark masses. If axial chiral symmetry would not be spontaneously broken, there would exist parity doublets in the particle spectrum. These particles would have the same mass and identical quantum numbers but opposite parity. That this is not the case can be deduced from the nucleon  $N(J^\pi = \frac{1}{2}^+)$  with mass  $m_N \approx 940$  MeV and its chiral partner  $N^*(J^\pi = \frac{1}{2}^-)$  with  $m_{N^*} \approx 1535$  MeV. The spontaneous (axial) chiral symmetry breaking by the QCD vacuum gives rise to the formation of the chiral condensate  $\langle 0|\bar{q}q|0\rangle$ . The chiral condensate is the expectation value of a quark-antiquark pair in vacuum and is non-zero when (axial) chiral symmetry is spontaneously broken. It can be seen as the order parameter of spontaneous (axial) chiral symmetry breaking.

Furthermore, spontaneous (axial) chiral symmetry breaking has an important consequence. By Goldstone's theorem there are massless Goldstone bosons - one for each generator of a spontaneously broken continuous symmetry [58]. Pions, kaons, and the eta meson are identified as the Goldstone bosons of spontaneous (axial) chiral symmetry breaking. However, the Goldstone bosons acquire small masses due to the explicit chiral symmetry breaking by the quark masses and are therefore called pseudo-Goldstone bosons. The pions are indeed very light, while the mesons carrying strangeness are heavier because of the stronger breaking of the chiral symmetry in the strange sector. The pseudo-Goldstone bosons are very important for nuclear forces because their long-range parts can be formulated in terms of pion exchanges.

Another characteristic property of QCD is the significant running of the strong coupling constant  $\alpha_s$ . Working in an energy range, where the number of flavors is taken constant, a simple exact analytic expression for the renormalized coupling  $\alpha_s(\mu_R^2)$  as a function of the (unphysical) renormalization scale  $\mu_R$  at the one-loop level [59, 60] is given by

$$\frac{g^2}{4\pi} \equiv \alpha_s(\mu_R^2) = \frac{1}{b_0 \ln\left(\frac{\mu_R^2}{\Lambda^2}\right)}, \quad (2.5)$$

where  $\Lambda$  is a constant of integration, which corresponds to the scale where the perturbatively-defined coupling would diverge, i.e., it is the non-perturbative scale of QCD. The one-loop beta-function coefficient is given by  $b_0 = (33 - 2n_f)/(12\pi)$  with the number of quark flavors  $n_f$ , that are considered light ( $m_f \ll \mu_R$ ), while the remaining heavier quark flavors decouple from the theory. At high momenta the strong coupling constant becomes weaker, resulting in the so-called "asymptotic freedom", that allows for a perturbative treatment of the theory. However, at low momenta of about less than 1 GeV  $\alpha_s$  becomes larger than 1, making QCD non-perturbative in this low-momentum regime. Thus, it is not possible to analytically derive nuclear forces directly from the QCD Lagrangian.

There is, however, an approach to directly obtain low-energy properties of nuclear systems from QCD using lattice Monte-Carlo techniques. In lattice QCD [61] a four-dimensional Euclidean lattice is used to discretize space-time, with the quarks residing on the lattice sites, and the gluon fields residing on the links between the lattice sites. The path integrals can then be evaluated numerically and the results are depending, among other input parameters, on the lattice spacing  $b$ , defining the distance between adjacent lattice sites, and the lattice size  $L$ , determining the volume. Combining calculations for several lattice spacings and lattice sizes, results can be extrapolated to vanishing lattice spacing and infinite volume. Nevertheless, the computational cost of lattice QCD calculations is extremely high. While calculations for baryons are using physical values for the light quark masses as input parameters, calculations for nuclear systems with  $A > 1$  are currently limited to large values for the light quark masses leading to unphysical values of the pion mass.

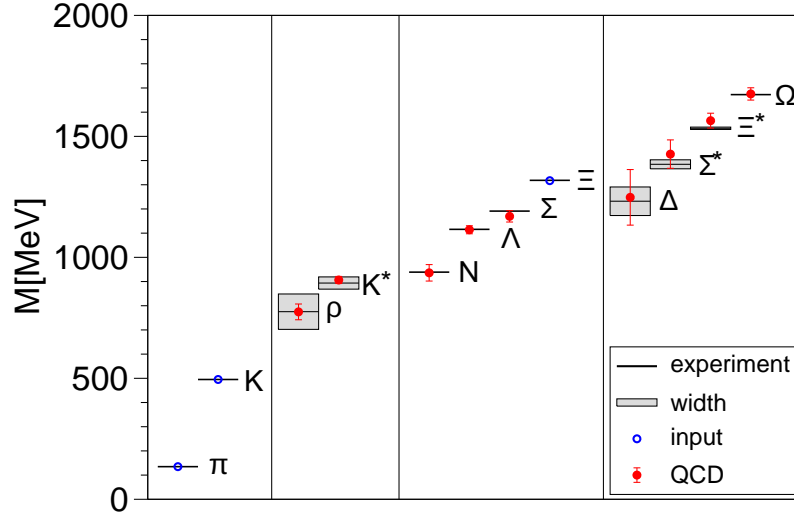


**Figure 2.1:** Results for the spectrum of light hadrons calculated by lattice QCD [65]. Horizontal lines and bands are the experimental values with their decay widths. Red solid circles with vertical error bars correspond to the lattice QCD results and their error estimates. The blue circles mark  $\pi$ ,  $K$  and  $\Xi$  masses that were used to set the light and strange quark masses and the strong coupling constant  $g$ .

One remarkable example of lattice QCD calculations is the prediction of the spectrum of light hadrons, shown in Fig. 2.1, using the  $\pi$ ,  $K$  and  $\Xi$  masses to set the light and strange quark masses and the strong coupling constant  $g$ . Many interesting results for low-energy nuclear physics observables have been obtained for example by the NPLQCD Collaboration, using quark masses corresponding to  $m_\pi \approx 800$  MeV. Examples are the scattering parameters that describe low-energy nucleon-nucleon scattering [62], the binding energies of a range of nuclei and hypernuclei with atomic number  $A \leq 4$  and strangeness  $|s| \leq 2$  [63], and magnetic moments of the lightest nuclei [64]. For more details we refer to a review on lattice QCD [61].

Due to the complicated non-perturbative nature of QCD at low-energies nuclear interactions have been modeled for a long time by meson exchanges, e.g., CD-Bonn [66], or phenomenological potentials, e.g., Argonne  $\nu_{18}$  [67]. These potentials reproduce nucleon-nucleon scattering data very accurately but there is no clear connection to the symmetries of the underlying theory. Effective field theories (EFT), however, allow for the systematic determination of nuclear interactions and currents consistent with the symmetries of QCD. In general, EFT are based on the separation of scales. Therefore we briefly want to discuss the different scales in low-energy nuclear physics.

As stated before, the interaction between nucleons may be formulated in terms of meson exchanges. The lightest mesons, the pions, have an average mass of  $m_\pi \approx 138$  MeV, corresponding to a Compton wavelength of  $\lambda_\pi = 1/m_\pi \approx 1.4$  fm. Comparing this to the two unnaturally large neutron-proton  $S$ -wave scattering lengths

$$a_{np}(^1S_0) = -23.714 \text{ fm}, \quad a_{np}(^3S_1) = 5.42 \text{ fm} \gg \lambda_\pi \quad (2.6)$$

reveals that there already exists a relevant energy scale well below the pion mass. This scale is also manifested in the binding momentum of the lightest nucleus, the loosely-bound deuteron,

$$\Gamma_d = \sqrt{m_N E_d} \approx 46 \text{ MeV} \ll m_\pi, \quad (2.7)$$

with the nucleon mass  $m_N \approx 938.92$  MeV and the binding energy of the deuteron  $E_d = 2.224$  MeV. For large scattering length physics the momentum scale of interest is  $q \sim |a(^1S_0)|^{-1} \approx 8$  MeV  $\ll m_\pi$ , which defines the so-called pion-less EFT [68, 69], whose breakdown scale  $\Lambda_b$  is of the order of the pion mass. When going to higher momenta pions are resolved and need to be included in the EFT explicitly, leading to chiral EFT, whose breakdown scale is around 500 MeV. When comparing the breakdown scale of chiral EFT to the energy separation in the hadron spectrum it may be important to include even heavier particles such as the delta isobar  $\Delta(1232)$ , whose energy separation from the nucleon is only about  $m_\Delta - m_N \approx 293$  MeV. This extension is referred to as  $\Delta$ -full chiral EFT [70].

---

## 2.2 Chiral effective field theory for low-energy QCD

---

### 2.2.1 Basic principles

---

As mentioned above the general idea of effective field theories is the separation of scales. For a physical system of interest one has to choose the relevant degrees of freedom, leaving the symmetry properties of the system unchanged. In the fundamental theory of strong interactions quarks and gluons are the basic degrees of freedom. If a system, however, is probed at low energies or momenta, corresponding to long distances, these basic degrees of freedom are not resolved. Only probes with high energy or momentum would resolve these basic degrees of freedom, necessitating a different choice for the relevant degrees of freedom of the EFT and thereby moving also the breakdown scale to higher energies.

Already in 1979 Steven Weinberg outlined the basic principle of EFT in the following way [71]: “If one writes down the most general possible Lagrangian, including all terms consistent with assumed symmetry principles, and then calculates matrix elements with this Lagrangian to any given order of perturbation theory, the result will simply be the most general possible S-matrix consistent with analyticity, perturbative unitarity, cluster decomposition and the assumed symmetry principles.”

The most general Lagrangian consistent with assumed symmetry principles for a typical low-momentum scale  $q$  with respect to the breakdown scale  $\Lambda_b$  is then given by

$$\mathcal{L} = \sum_{\nu} \left( \frac{q}{\Lambda_b} \right)^{\nu} \mathcal{F}_{\nu}(q, g_i), \quad (2.8)$$

where  $\mathcal{F}_{\nu}$  is a function of order 1 and  $g_i$  are the *a priori* undetermined low-energy constants (LECs). The different terms in Eq. (2.8) are ordered, according to a power-counting scheme, in terms of powers  $\nu$  of the expansion parameter  $q/\Lambda_b < 1$ . The lowest order, or leading order (LO) with  $\nu = 0$ , contains the most important contributions in the expansion, while there are infinitely many higher orders. These include contributions of decreasing importance and are called next-to-leading order (NLO) for  $\nu = 1$ , N<sup>2</sup>LO for  $\nu = 2$ , etc.. The inclusion of higher orders leads to a systematic improvability of the EFT, but also involves the determination of more LECs. In case the number of undetermined LECs exceeds the available data used to fix them, the predictive power of the EFT is limited. This problem should, however, arise only at very high orders in the EFT.

Since high-momentum (energy) degrees of freedom only exist for short distances (times) they are not resolved in a low-energy EFT. Consequently, these high-momentum (energy) degrees of freedom are treated as heavy and are integrated out. Their contribution gets implicitly included by fixing the LECs  $g_i$ , appearing along with contact interactions, to experimental data. These LECs should take values of the order  $\sim 1$ , called natural, so that the convergence behavior of the EFT is not influenced by over- or underestimation of individual terms.

---

### 2.2.2 Chiral effective field theory

---

Chiral effective field theory was introduced in the pioneering work of Weinberg in the early 1990's [4, 72]. The relevant degrees of freedom in chiral EFT are nucleons and pions. The typical low-momentum scale  $q$  in nuclei or nuclear matter is set by nucleon momenta of the order of the pion mass. The high-momentum or breakdown scale  $\Lambda_b$  is obtained by comparing to the energy separation in the hadron spectrum. As mentioned above the inclusion of the delta isobar is still an open question, however, heavier-meson exchanges, e.g., that of the  $\rho$  meson with  $m_{\rho} \approx 770$  MeV, are not resolved. Thus, the breakdown scale is usually assumed to be  $\Lambda_b \sim 500$  MeV. This leads to an expansion parameter  $q/\Lambda_b \sim 1/3$ , so that the uncertainty should be reduced by a factor of 3 when including the next order.

Before introducing a power-counting scheme to set the hierarchy for the importance of terms in the effective Lagrangian, we examine how many powers of  $q$  arise in the one-pion-exchange interaction. The coupling of a pion to non-relativistic nucleons, shown on the left of Fig. 2.2, is given by

$$H_{\text{int}} = -i \frac{g_A}{2f_{\pi}} \int \frac{d^3k d^3k'}{(2\pi)^3} b^{\dagger}(\mathbf{k}', m_{s'}, m_{t'}) b(\mathbf{k}, m_s, m_t) [(\boldsymbol{\sigma})_{m_s, m_{s'}} \cdot \mathbf{q}] (\boldsymbol{\tau}^i)_{m_t, m_{t'}} \frac{1}{\sqrt{2\omega_q}} (a_i^{\dagger}(-\mathbf{q}) + a_i(\mathbf{q})), \quad (2.9)$$

where the coupling strength  $-i \frac{g_A}{2f_{\pi}}$  contains the axial coupling  $g_A$  and the pion decay constant  $f_{\pi}$ .  $b^{\dagger}$  ( $b$ ) denote the creation (annihilation) operator of a nucleon with momentum  $\mathbf{k}$  and spin (isospin) projections  $m_s$  ( $m_t$ ) and  $a_i^{\dagger}$  ( $a_i$ ) correspond to the creation (annihilation) operator of a pion with momentum  $\mathbf{q} = \mathbf{k}' - \mathbf{k}$  and isospin component  $i$ .

---



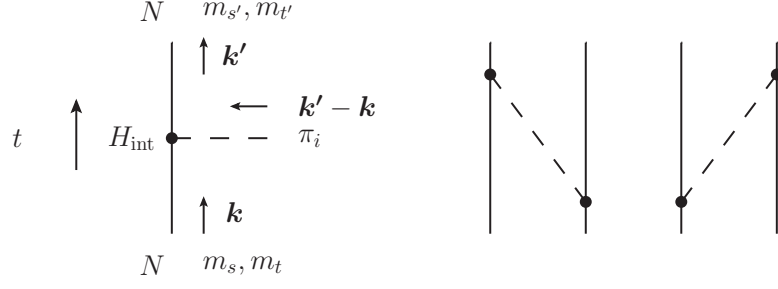


**Figure 2.2:** Interaction vertex  $H_{\text{int}}$  of a pion  $\pi$  with isospin component  $i$  and nucleons  $N$  (left) and contribution from different time orderings to the one-pion-exchange interaction (right).

$\sigma/\tau$  denote the Pauli spin/isospin matrices and the pion energy is given by  $\omega_q = \sqrt{q^2 + m_\pi^2}$ . The sum in the last term of Eq. (2.9) arises due to different time orderings, where  $a_i^\dagger(-\mathbf{q})$  corresponds to the emission and  $a_i(\mathbf{q})$  to the absorption of a pion. Thus, we can derive the one-pion-exchange interaction

$$\langle \mathbf{k}' | V_{\text{OPE}} | \mathbf{k} \rangle = \sum_{n=1} \frac{\langle \mathbf{k}' | H_{\text{int}} | n \rangle \langle n | H_{\text{int}} | \mathbf{k} \rangle}{E_i - E_n}, \quad (2.10)$$

where we have to sum over one pion ( $n = 1$ ) and the energy denominator is given by  $E_i - E_n = -\omega_q$ . Evaluating this and taking into account the two time orderings, shown on the right of Fig. 2.2 leads to

$$\begin{aligned} V_{\text{OPE}}(\mathbf{k}', \mathbf{k}) = V_{\text{OPE}}(\mathbf{q} = \mathbf{k}' - \mathbf{k}) &= \left( -i \frac{g_A}{2f_\pi} \right)^2 \left( \frac{1}{\sqrt{2\omega_q}} \right)^2 \frac{1}{-\omega_q} \tau_1 \cdot \tau_2 [\boldsymbol{\sigma}_1 \cdot \mathbf{q} \boldsymbol{\sigma}_2 \cdot (-\mathbf{q}) + \boldsymbol{\sigma}_1 \cdot (-\mathbf{q}) \boldsymbol{\sigma}_2 \cdot \mathbf{q}] \\ &= - \left( \frac{g_A}{2f_\pi} \right)^2 \frac{(\boldsymbol{\sigma}_1 \cdot \mathbf{q})(\boldsymbol{\sigma}_2 \cdot \mathbf{q})}{q^2 + m_\pi^2} \tau_1 \cdot \tau_2. \end{aligned} \quad (2.11)$$

Having motivated the origin of the powers of the momentum scale  $q$  we want to introduce Weinberg's power-counting scheme [4, 72, 73], based on dimensional analysis, which is most widely used. We outline this scheme, following Ref. [4], in which an interaction of type  $i$  is characterized by the number  $n_i$  of nucleon fields, the number  $p_i$  of pion fields, and the number  $d_i$  of derivatives or pion mass insertions. Each meson field contributes  $-1/2$  powers of  $q$  from  $1/\sqrt{2\omega_q}$  in Eq. (2.9), each derivative one power of  $q$ , and each intermediate state makes a contribution of  $-1$  power of  $q$ . Additionally, each loop is accompanied with an integral over a three-momentum, and hence adds three powers of  $q$ . Combining this, a graph with  $V_i$  vertices of type  $i$ ,  $D$  intermediate states, and  $L$  loops contributes in powers  $\nu$  of  $q/\Lambda_b$

$$\nu = \sum_i V_i (d_i - \frac{1}{2} p_i) - D + 3L. \quad (2.12)$$

Using the following topological identities

$$D = \sum_i V_i - 1, \quad L = I - D, \quad 2I + 2N = \sum_i V_i (p_i + n_i), \quad (2.13)$$

with the number of internal lines  $I$  and the number of nucleons  $N$ , Eq. (2.12) can be rewritten to

$$\nu = 2 - N + 2L + \sum_i V_i (d_i + \frac{1}{2} n_i - 2). \quad (2.14)$$

Additionally, in order to account for the normalization of the  $N$ -nucleon states [74], the factor  $3N - 6$  has to be added to the right-hand side of Eq. (2.14), leading to

$$\nu = -4 + 2N + 2L + \sum_i V_i (d_i + \frac{1}{2} n_i - 2), \quad (2.15)$$

maintaining a rather natural hierarchy of nuclear dynamics. Nucleons interact mainly via two-body forces starting at  $\nu = 0$  (LO), while many-body forces provide small corrections. The natural and consistent emergence of many-nucleon forces in chiral EFT is a fundamental advantage over previous approaches to obtain nuclear interactions. Many-nucleon forces arise due to the fact that nucleons are finite-size composite particles.

Based on the power counting we can now construct the effective Lagrangian order-by-order. The LO and NLO effective Lagrangians, describing vertices  $\Delta_i = d_i + n_i/2 - 2 = 0, 1$ , take the form [74]

$$\begin{aligned} \mathcal{L}^{(0)} &= \frac{1}{2}(\partial_\mu \boldsymbol{\pi} \cdot \partial^\mu \boldsymbol{\pi}) - \frac{1}{2}m_\pi^2 \boldsymbol{\pi}^2 + N^\dagger \left[ i\partial_0 + \frac{g_A}{2f_\pi} \boldsymbol{\tau} \boldsymbol{\sigma} \cdot \boldsymbol{\nabla} \boldsymbol{\pi} - \frac{1}{4f_\pi^2} \boldsymbol{\tau} \cdot (\boldsymbol{\pi} \times \dot{\boldsymbol{\pi}}) \right] N \\ &\quad - \frac{C_S}{2}(N^\dagger N)(N^\dagger N) - \frac{C_T}{2}(N^\dagger \boldsymbol{\sigma} N)(N^\dagger \boldsymbol{\sigma} N) + \dots, \end{aligned} \quad (2.16)$$

$$\begin{aligned} \mathcal{L}^{(1)} &= N^\dagger \left[ 4c_1 m_\pi^2 - \frac{2c_1}{f_\pi^2} m_\pi^2 \boldsymbol{\pi}^2 + \frac{c_2}{f_\pi^2} \dot{\boldsymbol{\pi}}^2 + \frac{c_3}{f_\pi^2} (\partial_\mu \boldsymbol{\pi} \cdot \partial^\mu \boldsymbol{\pi}) - \frac{c_4}{2f_\pi^2} \epsilon_{ijk} \epsilon_{abc} \sigma_i \tau_a (\nabla_j \pi_b) (\nabla_k \pi_c) \right] N \\ &\quad - \frac{D}{4f_\pi} (N^\dagger N)(N^\dagger \boldsymbol{\sigma} \boldsymbol{\tau} N) \cdot \boldsymbol{\nabla} \boldsymbol{\pi} - \frac{E}{2} (N^\dagger N)(N^\dagger \boldsymbol{\tau} N) \cdot (N^\dagger \boldsymbol{\tau} N) + \dots, \end{aligned} \quad (2.17)$$

where  $\boldsymbol{\pi}$  and  $N$  are the pion and nucleon fields, respectively. The LECs are given by  $c_i$ ,  $C_{S,T}$ ,  $D$  and  $E$  and ellipses refer to terms with more pion fields. For more complete expressions of the Lagrangian including higher-order terms we refer to Ref. [74] and references therein.

The derivation of a potential from the effective Lagrangian, which is an intensively studied problem in nuclear physics, is necessary to enable calculations of nuclear observables using nucleonic degrees of freedom. The important conceptual achievements in this field have been made in the 1950's for meson field theory [75]. For a discussion of methods, which have been used in the context of chiral EFT, we again refer to Ref. [74].

The LO and NLO effective Lagrangians in Eqs. (2.16) and (2.17) determine the nuclear potential up to N<sup>2</sup>LO, except for a NN contact term at NLO, which includes a vertex from  $\mathcal{L}^{(2)}$  [76]. In Fig. 2.3 we show the hierarchy of nuclear forces up to N<sup>3</sup>LO and emphasize, that the diagrams do not represent Feynman graphs of the scattering amplitude, but should be understood as a schematic visualization of the irreducible parts of it. In general, there are contact interactions parametrizing the short-range, or high-momentum, physics with LECs usually fit to low-energy nucleon-nucleon scattering data. Moreover, the long- and intermediate-range contributions are due to the exchange of one or more pions and also contain LECs that are determined from low-energy pion-nucleon scattering data.

The contribution at LO (first row) consists of two contact interactions and the one-pion exchange. We give the expression in momentum space here and refer to Refs. [5, 77] for higher-order two-nucleon contributions

$$V_{\text{LO}}(\mathbf{q}) = V_{\text{contact}}^{(0)} + V_{\text{OPE}}^{(0)} = C_S + C_T \boldsymbol{\sigma}_1 \cdot \boldsymbol{\sigma}_2 - \left( \frac{g_A}{2f_\pi} \right)^2 \frac{(\boldsymbol{\sigma}_1 \cdot \mathbf{q})(\boldsymbol{\sigma}_2 \cdot \mathbf{q})}{q^2 + m_\pi^2} \boldsymbol{\tau}_1 \cdot \boldsymbol{\tau}_2, \quad (2.18)$$











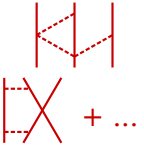
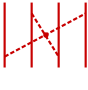
where  $\mathbf{q} = \mathbf{k}' - \mathbf{k}$  is the nucleon momentum transfer with initial and final relative momenta  $\mathbf{k} = (\mathbf{k}_1 - \mathbf{k}_2)/2$ ,  $\mathbf{k}' = (\mathbf{k}'_1 - \mathbf{k}'_2)/2$  and the initial and final single-nucleon momenta  $\mathbf{k}_i$ ,  $\mathbf{k}'_i$ . The LECs are the same as in Eq. (2.16). A NN contact interaction with a  $\Delta_i = 1$  vertex is not allowed due to parity conservation. Hence, NLO contribution have power  $\nu = 2$ , and consist of 7 contacts with a  $\Delta_i = 2$  vertex and two-pion exchange interactions with one loop. At order N<sup>2</sup>LO, one  $\pi N$   $\Delta_i = 0$  vertex in the two-pion exchange with one loop gets replaced by a  $\Delta_i = 1$  vertex. At this order there are no new NN contact interactions. In addition to 15 new NN contacts with a  $\Delta_i = 4$  vertex and two-pion exchange interactions with one loop and two  $\Delta_i = 1$  vertices also three-pion exchanges contribute to order N<sup>3</sup>LO. Furthermore, there are relativistic corrections to the one- ( $1/m^2$ ) and two-pion exchange ( $1/m$ ) interactions.

Following Eq. (2.15) the leading three-nucleon interaction should appear at  $\nu = 2$ , i.e., at NLO, however, those contributions cancel against part of the recoil correction of the iterated two-body potential [78]. Thus, the first non-vanishing 3N force contribution appears at order  $\nu = 3$ , i.e., at N<sup>2</sup>LO. The two-pion-exchange contribution, depending on the low-energy couplings  $c_1$ ,  $c_3$ , and  $c_4$  from the NLO chiral Lagrangian, which are predicted from the NN sector, cf. Eq. (2.17), is given by

$$V_{2\pi}^{(3)} = \frac{1}{2} \left( \frac{g_A}{2f_\pi} \right)^2 \sum_{i \neq j \neq k} \frac{(\boldsymbol{\sigma}_i \cdot \mathbf{q}_i)(\boldsymbol{\sigma}_j \cdot \mathbf{q}_j)}{(q_i^2 + m_\pi^2)(q_j^2 + m_\pi^2)} F_{ijk}^{\alpha\beta} \tau_i^\alpha \tau_j^\beta, \quad (2.19)$$

with the function  $F_{ijk}^{\alpha\beta}$  defined as

$$F_{ijk}^{\alpha\beta} = \delta^{\alpha\beta} \left[ -\frac{4c_1 m_\pi^2}{f_\pi^2} + \frac{2c_3}{f_\pi^2} \mathbf{q}_i \cdot \mathbf{q}_j \right] + \sum_\gamma \frac{c_4}{f_\pi^2} \epsilon^{\alpha\beta\gamma} \tau_k^\gamma \boldsymbol{\sigma}_k \cdot (\mathbf{q}_i \times \mathbf{q}_j).$$

		NN	3N	4N
LO	$\mathcal{O}\left(\frac{q^0}{\Lambda_b^0}\right)$			
NLO	$\mathcal{O}\left(\frac{q^2}{\Lambda_b^2}\right)$			
N <sup>2</sup> LO	$\mathcal{O}\left(\frac{q^3}{\Lambda_b^3}\right)$			
N <sup>3</sup> LO	$\mathcal{O}\left(\frac{q^4}{\Lambda_b^4}\right)$			

**Figure 2.3:** Hierarchy of nuclear forces in chiral effective field theory up to N<sup>3</sup>LO. Solid lines represent nucleons, while dashed lines correspond to pions. The different low-energy couplings are indicated in the vertices. Small dots, large solid dots, solid squares, and empty squares denote vertices of index  $\Delta_i = 0, 1, 2$  and 4, respectively. More details are given in the text.

The contributions from the remaining graphs are a one-pion-exchange contact, and a three-nucleon-contact term, which take the form

$$V_{1\pi, \text{cont}}^{(3)} = -\frac{g_A}{8f_\pi^2} D \sum_{i \neq j \neq k} \frac{\boldsymbol{\sigma}_j \cdot \mathbf{q}_j}{q_j^2 + m_\pi^2} (\boldsymbol{\tau}_i \cdot \boldsymbol{\tau}_j) (\boldsymbol{\sigma}_i \cdot \mathbf{q}_j), \quad V_{\text{cont}}^{(3)} = \frac{E}{2} \sum_{j \neq k} (\boldsymbol{\tau}_j \cdot \boldsymbol{\tau}_k), \quad (2.20)$$

where  $D$  and  $E$  are the corresponding LECs from the Lagrangian of order  $\Delta_i = 1$ , cf. Eq. (2.17). These are related to the constants  $c_D$  and  $c_E$  by

$$D = \frac{c_D}{f_\pi^2 \Lambda_\chi}, \quad E = \frac{c_E}{f_\pi^4 \Lambda_\chi}, \quad (2.21)$$

with  $\Lambda_\chi = 700$  MeV. Thus,  $c_D$  and  $c_E$  are the only new LECs arising in the leading 3N force and have to be adjusted to uncorrelated few-body observables. Different choices for fitting these constants are presented in Secs. 2.4 and 4. Sub-leading 3N forces at N<sup>3</sup>LO have been derived in Refs. [79–81] and can be grouped into five topologies. They contain no new LECs and are predicted from the LO NN sector, since they only depend on the couplings  $C_S$  and  $C_T$ . While the leading 3N forces have been implemented in nuclear structure calculations for some time, a straightforward inclusion of N<sup>3</sup>LO 3N forces has only become possible by the recent partial-wave decomposition of those terms [82]. We will come back to this in Sec. 5.2, describing the implementation of 3N forces in our many-body calculations.

The first non-vanishing 4N forces arise at N<sup>3</sup>LO and have been derived in Refs. [83, 84]. Similar to the sub-leading 3N forces, 4N forces at N<sup>3</sup>LO do not contain new LECs, but only depend on the LO LEC  $C_T$ . Current nuclear-structure calculations do not include chiral 4N forces and it seems to be justified, since neutron and symmetric nuclear matter calculations, including 4N forces in the Hartree-Fock approximation, have shown that their contributions are small [85].

### 2.3 Old and new regularization schemes

Chiral EFT potentials lead to ultraviolet (high-energy) divergences when substituted into the Lippmann-Schwinger (LS) equation [86]. The appearance of these UV divergences is an inherent feature of chiral EFT. A commonly

adopted scheme for the renormalization of the LS equation is based on introducing a finite UV cutoff. The resulting potential  $V(\mathbf{k}, \mathbf{k}')$  is multiplied with a regulator function  $f_{\text{NN}}^\Lambda$ ,

$$V(\mathbf{k}, \mathbf{k}') \rightarrow V_{\text{reg}}(\mathbf{k}, \mathbf{k}') = f_{\text{NN}}^\Lambda(k) V(\mathbf{k}, \mathbf{k}') f_{\text{NN}}^\Lambda(k'), \quad (2.22)$$

where the exponential regulator function

$$f_{\text{NN}}^\Lambda(k) = \exp(-k^m/\Lambda^m), \quad (2.23)$$

with  $m = 6$  was used in the Epelbaum, Glöckle and Meißner [87] (EGM) potentials, while different powers  $m \leq 8$  for different terms in the potential were employed by Entem and Machleidt [6] (EM). The potential is then renormalized by tuning the LECs, accompanying the contact interactions, to scattering data. However, this scheme leads to the appearance of finite-cutoff artefacts as reflected in a residual cutoff dependence of nuclear observables. Necessarily, the UV momentum-space cutoff  $\Lambda$  has to be of the order of the breakdown scale  $\Lambda_b$ .

The most-commonly used  $\text{N}^3\text{LO}$  potential in nuclear-structure calculations employs a UV momentum-space cutoff  $\Lambda = 500 \text{ MeV}$ , denoted EM 500 MeV [27] in the following. Another version of the potential has a momentum-space cutoff  $\Lambda = 600 \text{ MeV}$  [6]. While keeping  $\pi\text{N}$  LECs  $c_1$  [88] and the  $d_i$ 's [89] at the values determined from  $\pi\text{N}$  data,  $c_2$ ,  $c_3$ , and  $c_4$  were varied in addition to the NN LECs. The optimization procedure started with a fit to NN phase shifts and then the fit was refined by minimizing the  $\chi^2$  obtained from a direct comparison with the data.

Recently, Entem, Machleidt and Nosyk [90] published new potentials using three momentum-space cutoffs  $\Lambda = 450, 500, 550 \text{ MeV}$  for all chiral orders from LO up to  $\text{N}^4\text{LO}$ .

Following a different approach in the regularization, EGM obtained a variety of  $\text{N}^2\text{LO}$  [91] and  $\text{N}^3\text{LO}$  [87] potentials with a momentum-space cutoff in the range  $\Lambda = (450 - 600) \text{ MeV}$ . In addition to the momentum-space cutoff  $\Lambda$ , the spectral function of the sub-leading two-pion exchange was also regularized to suppress an unphysically strong attraction caused by the very strong short-range components, using  $\tilde{\Lambda} = (500 - 700) \text{ MeV}$  [92]. The  $\pi\text{N}$  LECs  $c_1$  and  $c_4$  were adopted from Ref. [88], while for  $c_3$  the value  $c_3 = -3.40 \text{ GeV}^{-1}$  was used, which is still consistent with the result  $c_3 = -4.69 \pm 1.34 \text{ GeV}^{-1}$  from Ref. [88]. The remaining  $\pi\text{N}$  LECs  $c_2$  and  $d_i$ 's were taken from Ref. [89]. The NN LECs were adjusted to NN phase shifts up to a laboratory scattering energy of  $T_{\text{Lab}} = 200 \text{ MeV}$  in case of the  $\text{N}^3\text{LO}$  potentials.

Instead of performing a momentum-space regularization used in the  $\text{N}^2\text{LO}$  and  $\text{N}^3\text{LO}$  potentials described above, it is also possible to perform the regularization in coordinate space. This was used recently in the construction of local chiral NN potentials up to  $\text{N}^2\text{LO}$  [93, 94] for quantum Monte Carlo calculations. A local potential just depends on the separation  $\mathbf{r} = \mathbf{r}_1 - \mathbf{r}_2$  between the particles. In the momentum-space formulation of chiral potentials there are two sources of non-localities: The Fourier transformation of the regulator function given in Eq. (2.23) leads to a non-local interaction  $V(\mathbf{r}, \mathbf{r}')$ . In addition, there are genuine non-localities, e.g., in the contact interactions that depend on the momentum transfer in the exchange channel  $\mathbf{q}_{\text{exc}} = (\mathbf{k}' + \mathbf{k})/2$  and also  $\mathbf{q}_{\text{exc}}$ -dependent parts in the one-pion exchange beyond  $\text{N}^2\text{LO}$ . However, the Fourier transformation of terms with the momentum transfer  $\mathbf{q} = \mathbf{k}' - \mathbf{k}$  lead to a local interaction. Both sources of non-locality were eliminated up to  $\text{N}^2\text{LO}$ . Instead of applying the regulator in momentum-space, long-range terms of the interaction got directly regularized in coordinate space using

$$f_{\text{NN, long}}^{R_0}(r) = 1 - \exp(-r^4/R_0^4). \quad (2.24)$$

So,  $R_0$  takes over the role of the momentum-space cutoff  $\Lambda$ . The regulator smoothly cuts off short-range parts of the pion-exchange potentials, for which the chiral expansion does not converge [95], at distances  $r < R_0$ , while leaving the long-range parts unchanged. Similar to the momentum-space interactions a spectral-function regularization was applied, making the two-pion exchange at  $\text{N}^2\text{LO}$  less singular at short distances. The genuine non-localities were avoided by choosing a set of  $\mathbf{q}_{\text{exc}}$ -independent contact operators. This is possible for all contributions up to  $\text{N}^2\text{LO}$ , except for the spin-orbit term that depends on  $\mathbf{q} \times \mathbf{q}_{\text{exc}}$ . The contact interactions were regularized with a local momentum-space regulator  $f_{\text{NN, cont}}(q^2)$  resulting in a smeared out delta function in coordinate space. In the local chiral NN potentials, derived in Ref. [94], a cutoff range  $R_0 = (1.0 - 1.2) \text{ fm}$  ( $R_0 = (0.8 - 1.2) \text{ fm}$  in Ref. [93]) was used and the spectral-function-regularization cutoff was varied in the range  $\tilde{\Lambda} = (1.0 - 1.4) \text{ GeV}$ . These potentials employed the same  $\pi\text{N}$  LECs as the EGM potentials and the NN LECs were determined by a fit to NN phase shifts, using different maximal laboratory scattering energies  $T_{\text{Lab}}^{\text{max}}$  at different chiral orders and values of  $R_0$ .

Although fully-local chiral potentials can only be derived up to  $\text{N}^2\text{LO}$  the idea of locally regularizing the long-range terms was also used in the derivation of higher-order potentials [77, 86]. Epelbaum, Krebs and Meißner (EKM) employed a local coordinate-space regulator function

$$f_{\text{NN, long}}^{R_0}(r) = [1 - \exp(-r^2/R_0^2)]^n, \quad (2.25)$$

with  $n = 6$ . This function is Fourier transformed to momentum space and then multiplied to the long-range terms. Due to the form of the regulator the additional spectral-function regularization of the two-pion exchange contributions is obsolete. This is particularly beneficial for the inclusion of 3N forces at  $N^3\text{LO}$  and  $N^4\text{LO}$  [96, 97], since they were only derived for infinite  $\tilde{\Lambda}$ . The contact operators got regularized with the standard non-local regulator specified in Eq. (2.23) with  $m = 2$ . In order to have a single cutoff scale, the coordinate- and momentum-space cutoffs  $R_0$  and  $\Lambda$  are related by  $\Lambda = 2R_0^{-1}$ . For the regulator  $R_0$ , EKM employed the range  $R_0 = (0.8 - 1.2)$  fm, which corresponds to a range  $\Lambda \simeq (500 - 330)$  MeV for the momentum-space cutoff. In contrast to the fully non-local EGM potentials, EKM adopted the central values of  $\pi\text{N}$  LECs up to  $N^3\text{LO}$  from Refs. [88, 89] without modifications and also fit the NN LECs to NN phase shifts, using different maximal laboratory scattering energies  $T_{\text{Lab}}^{\text{max}}$  at different chiral orders ( $T_{\text{Lab}}^{\text{max}} \leq 25$  MeV at LO,  $T_{\text{Lab}}^{\text{max}} \leq 100$  MeV at NLO and  $N^2\text{LO}$  and  $T_{\text{Lab}}^{\text{max}} \leq 200$  MeV at  $N^3\text{LO}$ ). However, at  $N^3\text{LO}$  further constraints had to be imposed to stabilize the fit in the coupled  $^3S_1$ - $^3D_1$  channel. More specifically, it was imposed that the deuteron binding energy was reproduced correctly, the  $D$ -state probability in the deuteron was within  $P_D = 5\% \pm 1\%$  or Wigner  $SU(4)$  symmetry was not violated too strongly.

## 2.4 Novel fitting strategies for the determination of the low-energy couplings

The quest for higher orders in chiral EFT is important in a systematically improvable expansion and is reflected in the derivation of NN forces up to  $N^4\text{LO}$  [77, 98] and even the dominant contributions at  $N^5\text{LO}$  [99]. As mentioned above, also 3N forces are developed up to  $N^4\text{LO}$  [96, 97]. However, the inclusion of higher orders will only result in higher accuracy if the fit at lower orders was done accurately.

When the fits of the EGM and EM potentials were about a decade old, Ekström *et al.* [100] started to revisit the optimization question, because in the meantime there had been considerable progress in the development of tools for derivative-free nonlinear least-squares optimization. Furthermore, the quantification of theoretical uncertainties in nuclear-structure calculations requires, in principle, a covariance analysis of the LECs with respect to the experimental uncertainties of the scattering data employed in their fit. The  $N^2\text{LO}_{\text{opt}}$  potential used a momentum-space cutoff  $\Lambda = 500$  MeV and a spectral-function regularization with  $\tilde{\Lambda} = 700$  MeV. While for the  $N^2\text{LO}_{\text{opt}}$  potential  $\pi\text{N}$  and NN were optimized with respect to a selected class of phase shifts and the deuteron binding energy, the estimation of the uncertainties of the LECs was the focus of the  $N^2\text{LO}$  potential obtained in Ref. [101]. Thus, the objective function was consisting of experimentally measured cross sections and their associated experimental uncertainties. The relative uncertainties in the LECs were found to be below 1%, except for  $c_1$  and  $C_{1p_1}$  where it was 5.8% and 2.6%, respectively. In addition to a correlation analysis, the uncertainties of the LECs were propagated in the calculation of deuteron observables, phase shifts, and effective range parameters. However, the authors noted the importance of extracting the derivatives of the objective function with higher numerical precision. Instead of using a bivariate spline of the objective function or finite-difference approximations automatic differentiation was suggested to obtain derivatives to machine precision.

Optimization techniques based on automatic differentiation were first employed in a condensed analysis of the statistical uncertainties of all LECs up to  $N^2\text{LO}$  in Ref. [102]. Two different strategies for the fit of the LECs have been pursued: The separate (sep) approach is very similar to the conventional procedure of constraining the LECs. In the first step  $\pi\text{N}$  LECs ( $c_i, d_i, e_i$ ) are optimized to  $\pi\text{N}$  cross sections. Subsequently, the NN LECs are fit to NN cross sections, and finally, 3N forces are determined by fitting  $c_D$  and  $c_E$  to the binding energies and radii of  $^3\text{H}$  and  $^3\text{He}$  as well as the  $\beta$ -decay half-life of  $^3\text{H}$ . In the simultaneous approach, however, all LECs up to a specific order are optimized at the same time with respect to  $\pi\text{N}$  and NN scattering data as well as bound-state observables of  $^2,^3\text{H}$  and  $^3\text{He}$ . The derived potentials employ the non-local NN regulator specified in Eq. (2.23) with  $m = 6$  and a momentum-space cutoff  $\Lambda = 500$  MeV as well as a spectral-function regularization with  $\tilde{\Lambda} = 700$  MeV. In addition, the momentum-space cutoff is varied in the range  $\Lambda = (450 - 600)$  MeV for the simultaneous fit of  $N^2\text{LO}$  potentials. The 3N force is regularized with a non-local 3N regulator of the form

$$f_{3\text{N}}^{\Lambda_{3\text{N}}}(p, q) = \exp[-((p^2 + 3/4q^2)/\Lambda_{3\text{N}}^2)^{n_{3\text{N}}}], \quad (2.26)$$

with the Jacobi momenta  $p$  and  $q$ , the 3N cutoff  $\Lambda_{3\text{N}} = 500$  MeV and  $n_{3\text{N}} = 3$ . The availability of machine-precise first- and second-order derivatives of the objective function with respect to the LECs was used during the optimization, the uncertainty analysis and the error propagation. By comparing the sim and sep approach it was concluded that a simultaneous fit is necessary to identify the optimal set of LECs, capture all relevant correlations, reduce the statistical uncertainty, and attain order-by-order convergence in chiral EFT. However, when performing calculations for all 42  $N^2\text{LO}_{\text{sim}}$  potentials, arising from 7 different momentum-space cutoffs  $\Lambda$  and 6 different maximal NN laboratory scattering energies  $125 \text{ MeV} \leq T_{\text{Lab}}^{\text{max}} \leq 290 \text{ MeV}$  used in the fit, no-core shell-model results for the

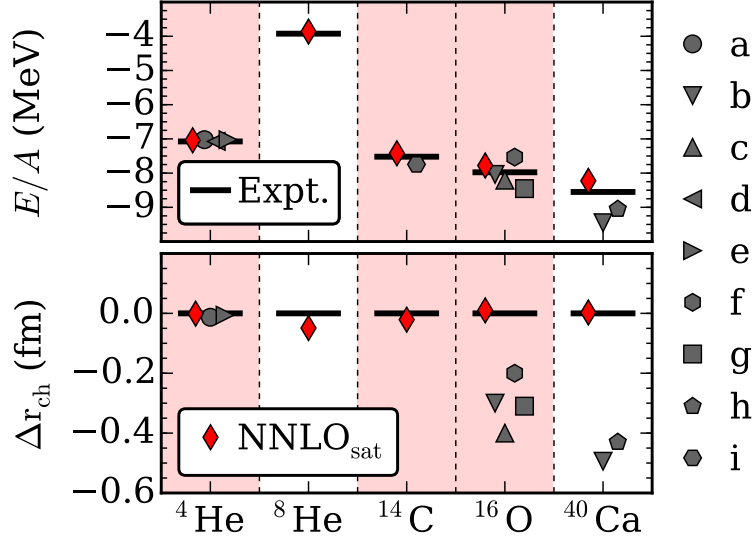


**Figure 2.4:** Ground-state energy per nucleon and difference between computed and experimental charge radii for selected nuclei computed with chiral interactions [103]. The results with  $N^2LO_{\text{sat}}$  are represented by the red diamonds, while other symbols correspond to different theoretical predictions. The marked observables are a subset of many-body properties that were used in the fit of the LECs. Taken from Ref. [103].

ground-state energy of  ${}^4\text{He}$  vary by about 2 MeV and coupled-cluster results for the ground-state energy of  ${}^{16}\text{O}$  even vary by about 35 MeV, respectively. Thus, the spread of  $N^2LO_{\text{sim}}$  results hints at a surprisingly large systematic error when extrapolating to heavier systems, while the corresponding statistical uncertainties are small.

The strategy to simultaneously optimize all LECs up to a specific order has been also used in the construction of the  $N^2LO_{\text{sat}}$  potential [103]. While the optimization did not make use of automatic differentiation it included the properties of nuclei with mass number  $A > 3, 4$ . The set of fit observables included NN scattering data with  $T_{\text{Lab}}^{\text{max}} \leq 35$  MeV, effective range parameters, deuteron properties, the binding energies and charge radii of  ${}^3\text{H}$ ,  ${}^{3,4}\text{He}$ ,  ${}^{14}\text{C}$ , and  ${}^{16}\text{O}$ , as well as binding energies of  ${}^{22,24,25}\text{O}$ , respectively. This potential also employs the non-local NN regulator specified in Eq. (2.23) with  $m = 6$  and a momentum-space cutoff  $\Lambda = 450$  MeV as well as a spectral-function regularization with  $\tilde{\Lambda} = 700$  MeV. Moreover, the 3N regulator is also non local. Coupled-cluster calculations for binding energies and radii of nuclei up to  ${}^{40}\text{Ca}$ , shown in Fig. 2.4, are in very good agreement with experiment, while other ab initio calculations predict too-small radii and too-large binding energies. In addition, coupled-cluster calculations of symmetric nuclear matter using  $N^2LO_{\text{sat}}$  are consistent with the empirical saturation point.

In addition, also the Granada group investigated statistical and systematic uncertainties when fitting  $\delta$ -shell interactions [104] and, more recently, also in the context of chiral EFT interactions [105].

### 3 Similarity renormalization group

Comparing chiral EFT interactions, introduced in Sec. 2.2, to phenomenological high-precision NN interactions like CD-Bonn [66] or Argonne  $v_{18}$  [67], reveals that the former are already quite soft due to the regularization scheme that suppresses high-momentum contributions. Although some nuclear-structure calculations for medium-mass nuclei employ unevolved interactions from chiral EFT, e.g., coupled-cluster calculations using the  $N^2\text{LO}_{\text{sat}}$  interaction in Refs. [12, 37, 103], most configuration-space based many-body approaches can only achieve converged results for light systems using unevolved interactions. Since the coupling of low- and high-lying momenta enables the scattering of nucleon pairs from low- to high-momentum states large many-body model spaces are needed for the representation of the interaction. However, many-body calculations for larger model spaces require increasing computational resources, making a rather fast model-space convergence desirable. A possibility to tame short-range central and tensor correlations, induced by the repulsive core at short distances, using a unitary transformation is the unitary correlation operator method (UCOM) [106]. The correlated interaction  $V_{\text{UCOM}}$  has been prediagonalized to a band-diagonal structure in momentum space, indicating that low and high momenta have been decoupled. Another approach are low-momentum NN interactions  $V_{\text{low}k}$ , introduced to low-energy nuclear physics in the early 2000s [107]. The  $V_{\text{low}k}$  interactions are given by the low-momentum block of a block-diagonal Hamiltonian in momentum space. This decoupling pattern is clearly different from that of the correlated interaction  $V_{\text{UCOM}}$ . The Similarity Renormalization Group (SRG) was independently developed by Glazek and Wilson [108, 109] as well as Wegner [110] in the early 1990s, for applications in light-front quantum field theory and condensed matter physics, respectively. The first application of the SRG in nuclear physics was the evolution of NN potentials by Bogner *et al.* in Ref. [17]. Although starting from a different conceptional background the SRG and the UCOM approach both yield interactions that are band-diagonal in momentum space. However, the behavior of matrix elements in the high-momentum sector is quite different, since UCOM-transformed interactions generate a stronger coupling among high-lying states compared to SRG-evolved interactions [111]. While the UCOM and the  $V_{\text{low}k}$  formalism are, so far, restricted to the two-body space, the SRG has been applied in three- and even in four-body space. In the following we present the basic principles of the SRG, which is nowadays used most widely in low-energy nuclear theory, see Ref. [112] for a recent review.

The basic idea of the SRG is to simplify the structure of the Hamiltonian by a continuous sequence of unitary transformations

$$H_\alpha = U_\alpha H_0 U_\alpha^\dagger, \quad (3.1)$$

where  $H_0$  is the initial, unevolved Hamiltonian and the quantity  $\alpha$  characterizes the unitary transformation and is called flow parameter. The flow parameter  $\alpha$  is related to the resolution scale  $\lambda$  by  $\alpha = \lambda^{-4}$ . Differentiating Eq. (3.1) with respect to  $\alpha$  results in

$$\frac{dH_\alpha}{d\alpha} = \frac{d}{d\alpha}(U_\alpha H_0 U_\alpha^\dagger) = \frac{dU_\alpha}{d\alpha} H_0 U_\alpha^\dagger + U_\alpha \underbrace{\frac{dH_0}{d\alpha}}_{=0} U_\alpha^\dagger + U_\alpha H_0 \frac{dU_\alpha^\dagger}{d\alpha}, \quad (3.2)$$

with the initial Hamiltonian  $H_0$  being independent of the flow parameter. Since  $U_\alpha$  is a unitary operator, i.e.,  $U_\alpha U_\alpha^\dagger = U_\alpha^\dagger U_\alpha = \mathbb{1}$ , differentiating leads to

$$\frac{d}{d\alpha}(U_\alpha U_\alpha^\dagger) = \frac{dU_\alpha}{d\alpha} U_\alpha^\dagger + U_\alpha \frac{dU_\alpha^\dagger}{d\alpha} = \frac{d}{d\alpha} \mathbb{1} = 0, \quad (3.3)$$

which implies

$$\frac{dU_\alpha}{d\alpha} U_\alpha^\dagger = -U_\alpha \frac{dU_\alpha^\dagger}{d\alpha}. \quad (3.4)$$

By inserting  $\mathbb{1}$  and Eq. (3.4) in Eq. (3.2), it can be rewritten to

$$\frac{dH_\alpha}{d\alpha} = \frac{dU_\alpha}{d\alpha} U_\alpha^\dagger U_\alpha H_0 U_\alpha^\dagger + U_\alpha H_0 U_\alpha^\dagger U_\alpha \frac{dU_\alpha^\dagger}{d\alpha} \quad (3.5)$$

$$= \frac{dU_\alpha}{d\alpha} U_\alpha^\dagger H_\alpha - H_\alpha \frac{dU_\alpha}{d\alpha} U_\alpha^\dagger = [\eta_\alpha, H_\alpha]. \quad (3.6)$$

The generator  $\eta_\alpha$  has been defined as

$$\eta_\alpha \equiv \frac{dU_\alpha}{d\alpha} U_\alpha^\dagger, \quad (3.7)$$

and is anti Hermitian, which can be easily shown with Eq. (3.4)

$$\eta_\alpha^\dagger = \left( \frac{dU_\alpha}{d\alpha} U_\alpha^\dagger \right)^\dagger = U_\alpha \frac{dU_\alpha^\dagger}{d\alpha} = -\eta_\alpha. \quad (3.8)$$

In general, any anti-Hermitian operator can be chosen as generator. If we choose  $\eta_\alpha = [G_\alpha, H_\alpha]$ , the operator  $G_\alpha$  has to be Hermitian in order to fulfill the anti-Hermiticity relation in Eq. (3.8). Wegner proposed to take the diagonal matrix elements of  $H_\alpha$

$$G_\alpha = H_\alpha^d = \sum_k \langle k | H_\alpha | k \rangle |k\rangle \langle k|, \quad (3.9)$$

using some generic basis  $\{|k\rangle\}$ . Thus, the evolution will terminate at the fix point, when  $H_\alpha$  is diagonal and the generator  $\eta_\alpha = [H_\alpha^d, H_\alpha]$  vanishes. A choice for the operator  $G_\alpha$  that has been used most widely is the intrinsic kinetic energy  $T_{\text{int}} = T - T_{\text{cm}}$ , leading to the generator

$$\eta_\alpha = \left( \frac{2\mu}{\hbar^2} \right)^2 [T_{\text{int}}, H_\alpha], \quad (3.10)$$

with the reduced mass  $\mu = m_N/2$ . Assuming the intrinsic kinetic energy  $T_{\text{int}}$  to be independent of the flow parameter  $\alpha$ , the flow equation in a two-body partial-wave momentum-space basis is given by

$$\frac{dV_\alpha(k, k')}{d\alpha} = [[T_{\text{int}}, T_{\text{int}} + V_\alpha(k, k')], T_{\text{int}} + V_\alpha(k, k')] \quad (3.11)$$

$$= -(k^2 - k'^2)^2 V_\alpha(k, k') + \frac{2}{\pi} \int_0^\infty q^2 dq (k^2 + k'^2 - 2q^2) V_\alpha(k, q) V_\alpha(q, k'), \quad (3.12)$$

with the normalization condition  $\int_0^\infty \frac{2}{\pi} q^2 dq |q\rangle \langle q| = 1$  and assuming units  $m_N/\hbar^2 = 1$ . Here,  $k = |\mathbf{k}|$  and  $k' = |\mathbf{k}'|$  denote the initial and final relative momenta, respectively. Note that the matrix structure of  $V_\alpha(k, k')$  in coupled channels such as  ${}^3S_1$ - ${}^3D_1$  is implicitly included. For small enough  $\alpha$  the first term on the right-hand side of Eq. (3.12) dominates in the far off-diagonal region, leading to

$$V_\alpha(k, k') \xrightarrow{k \neq k'} V_{\alpha=0}(k, k') \exp[-\alpha(k^2 - k'^2)^2]. \quad (3.13)$$

Thus, the coupling of low- and high-momenta in the far off-diagonal region is driven to zero and the evolved interaction  $V_\alpha(k, k')$  is taking a band-diagonal form. The resolution scale  $\lambda$  measures the “width” of the band-diagonal interaction in momentum space by limiting the momentum transfers between nucleons to

$$|q| = |\mathbf{k}' - \mathbf{k}| \lesssim \lambda. \quad (3.14)$$

While the SRG flow is continuous, we show in Fig. 3.1 momentum-space matrix elements for selected  $\lambda$  values during the SRG evolution of the chiral  $N^3\text{LO}$  NN potentials EM 500 MeV [27] and EGM  $\Lambda/\tilde{\Lambda} = 550/600$  MeV [87] in the  ${}^1S_0$  (top) and  ${}^3S_1$  (bottom) channel. While the resolution scale  $\lambda$  decreases the evolved interaction is taking a band-diagonal form as expected from Eq. (3.13). Note that the axes are the kinetic energy  $k^2$ , so that the width of the band in  $k^2$  is roughly given by  $\lambda^2$ . For the solution of Eq. (3.12) we have used the CVODE solver from the Sundials package [113].

The great flexibility of the SRG is the freedom of choosing appropriate generators to achieve different patterns of decoupling. Block-diagonal forms for the generator were studied in Refs. [116, 117], leading to an analogous decoupling as achieved in low-momentum interactions  $V_{\text{low}k}$ . Variations of the standard kinetic energy were investigated in Ref. [118], enabling the evolution to proceed more efficiently without losing its advantages.

A peculiarity of renormalization methods is, however, that irreducible operators of higher particle rank get induced when solving the flow equation. To understand this we can insert an initial irreducible two-body interaction, e.g., written in second quantization, into the right-hand side of Eq. (3.6). Thus, the evaluation of the commutators induces irreducible contributions beyond the two-body level in each infinitesimal step in the flow parameter. In general, up to  $A$ -nucleon operators arise during the evolution, which are of course only probed in calculations of the  $A$ -nucleon system. If the SRG flow equations are truncated at the two-body level the properties of the two-nucleon system, e.g., the deuteron binding energy, are preserved. Truncations at the three-body level preserve energies of



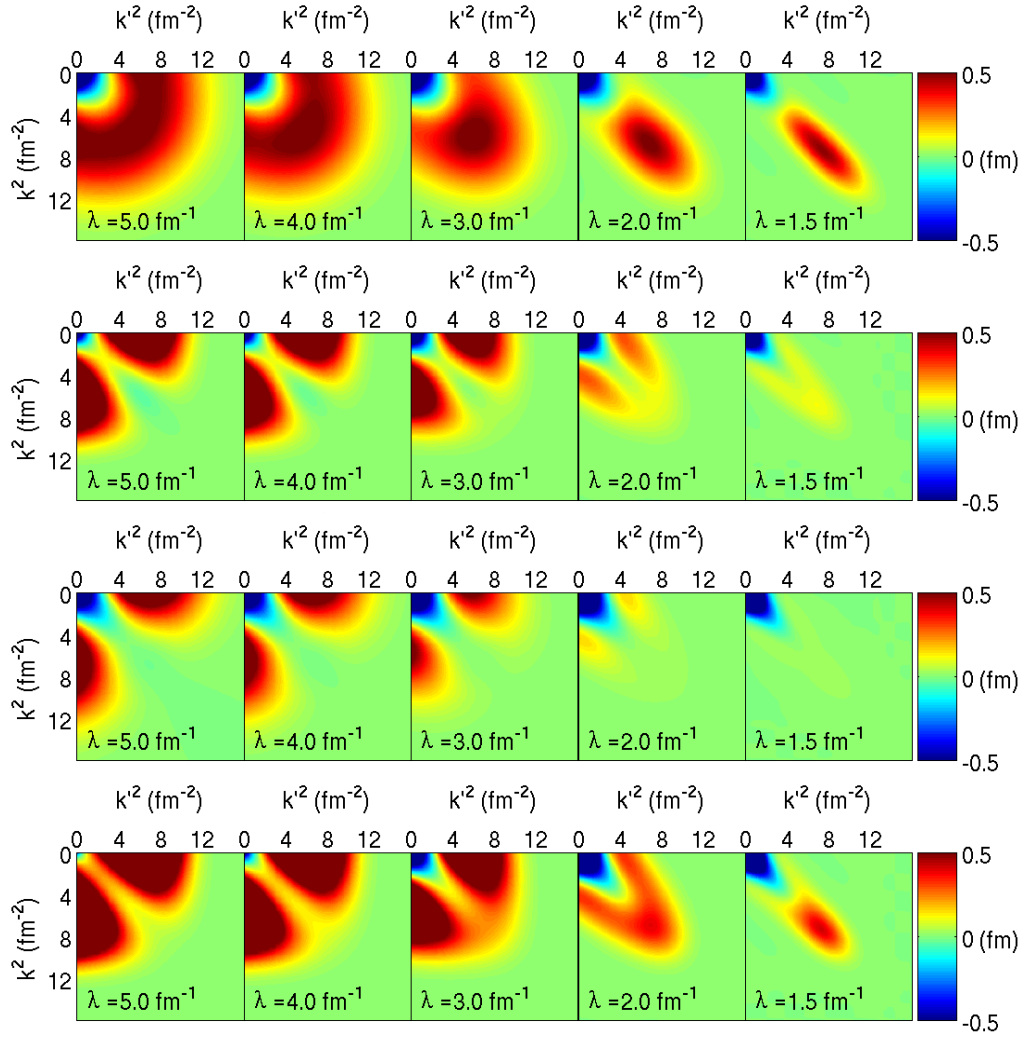


**Figure 3.1:** Momentum-space matrix elements for selected  $\lambda$  values during the SRG evolution of the chiral  $N^3\text{LO}$  NN potentials EM 500 MeV [27] and EGM  $\Lambda/\bar{\Lambda} = 550/600$  MeV [87] in the  $^1S_0$  (top) and  $^3S_1$  (bottom) channel. Note that the axes are the kinetic energy  $k^2$ . Taken from [114] based on [115].

$A = 3$  nuclei, and so on. Truncating the SRG flow equation at particle rank  $i$  causes a violation of unitarity, leading to a resolution-scale dependence of many-body results for mass numbers  $A > i$ .

The SRG evolution in three-body space has been implemented in relative (Jacobi) harmonic oscillator [18, 19], relative-momentum plane-wave [119], and momentum-space hyperspherical-harmonics representations [120]. Results for the ground-state energy of  $^3\text{H}$  as a function of the resolution scale  $\lambda$  are presented in Fig. 3.2, using a chiral  $N^2\text{LO}$  interaction by EGM with  $\Lambda/\bar{\Lambda} = 550/600$  MeV that has been SRG evolved in relative-momentum plane-wave basis [119]. When only the chiral NN interaction is taken into account, while the generator and the flowing Hamiltonian are truncated at the two-body level, the ground-state energy results, denoted NN-only, show a significant resolution-scale dependence due to the violation of unitarity in the three-body system. However, as already explained above the unitarity of the transformation can be restored by truncating the flow equations at the three-body level, taking into account induced 3N interactions, labeled NN+3N-induced. Thus, the ground-state energy does not change for varying resolution scales  $\lambda$ . If the initial NN and 3N forces are consistently SRG evolved at the three-body level the triton ground-state energy, represented by NN+3N-full, is again not depending on the resolution scale  $\lambda$  and reproduces the experimental value, that was used to constrain the low-energy couplings in the leading chiral 3N force at  $N^2\text{LO}$ .

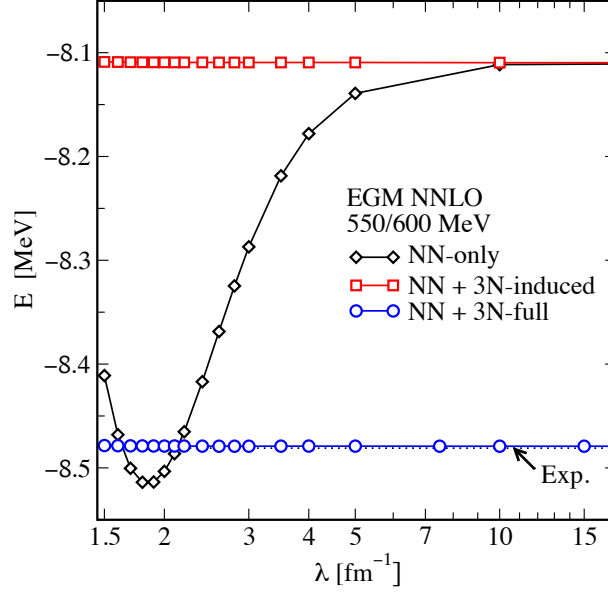


**Figure 3.2:** Ground-state energy of  ${}^3\text{H}$  as a function of the flow parameter  $\lambda$  for a chiral  $\text{N}^2\text{LO}$  NN+3N interaction by EGM with  $\Lambda/\tilde{\Lambda} = 550/600$  MeV. NN-only results, shown by the black curve, discard induced 3N interactions, while those were included in the results labeled NN+3N-induced (red). The blue curve (NN+3N-full) represents results for which NN and 3N forces were consistently SRG evolved at the three-body level. The experimental binding energy is shown by the black dotted line. Figure taken from [121].

So far the discussion was focused on the Hamiltonian, but when aiming at a consistent calculation of other observables the corresponding operators should be evolved as well [122, 123]. The flow equation for a general operator  $O_\alpha$  is given by

$$\frac{dO_\alpha}{d\alpha} = [\eta_\alpha, O_\alpha]. \quad (3.15)$$

Since the generator depends on the evolved Hamiltonian  $H_\alpha$ , the flow equations for the Hamiltonian and for other operators need to be solved simultaneously with initial conditions  $H_{\alpha=0} = H$  and  $O_{\alpha=0} = O$ . It may therefore be more efficient to evolve the unitary transformation  $U_\alpha$  itself

$$\frac{dU_\alpha}{d\alpha} = \eta_\alpha U_\alpha, \quad (3.16)$$

with the initial condition  $U_{\alpha=0} = \mathbb{1}$ . It is also possible to determine  $U_\alpha$  directly from the eigenvectors of the Hamiltonians  $H_{\alpha=0}$  and  $H_\alpha$  by

$$U_\alpha = \sum_i |\psi_i(\alpha)\rangle \langle \psi_i(0)|. \quad (3.17)$$

## 4 Chiral NN+3N Hamiltonians used in this work

In this section we introduce the Hamiltonians used in this work. While the model-space convergence of chiral potentials regularized in momentum space is still rather slow, it can be enhanced by performing a SRG evolution introduced in Sec. 3. In addition, the inclusion of binding energies and charge radii of nuclei with  $A > 3, 4$  in the construction of the  $N^2LO_{\text{sat}}$  potential [103], described in Sec. 2.4, revealed that coupled-cluster calculations of symmetric nuclear matter using this potential are consistent with the empirical saturation point.

The motivation to use rather soft potentials that also reproduce the empirical saturation point within uncertainties was already employed in Ref. [28]. Instead of using unevolved NN potentials in the determination of the  $N^2LO$  3N couplings  $c_D$  and  $c_E$ , these Hamiltonians employed low-momentum NN interactions obtained by SRG evolution of the EM 500 MeV [27] potential to a series of low-resolution scales  $\lambda_{\text{NN}} = 1.8, 2.0, 2.2, 2.8 \text{ fm}^{-1}$ . Taking chiral EFT as a general low-momentum basis and assuming the long-range couplings  $c_i$  to be invariant under the SRG transformation, each SRG-evolved NN interaction was combined with the leading  $N^2LO$  3N force [78, 124], using the non-local 3N regulator specified in Eq. (2.26) with  $n_{3N} = 4$  and  $\Lambda_{3N} = 2.0 \text{ fm}^{-1}$ . In addition, the 3N cutoff was varied to  $\Lambda_{3N} = 2.5 \text{ fm}^{-1}$  for the  $\lambda_{\text{NN}} = 2.0 \text{ fm}^{-1}$  interaction. The  $c_i$  couplings in the two-pion-exchange 3N interaction were taken consistently with the NN interaction:  $c_1 = -0.81 \text{ GeV}^{-1}$ ,  $c_3 = -3.2 \text{ GeV}^{-1}$ ,  $c_4 = 5.4 \text{ GeV}^{-1}$ . To probe uncertainties in the  $c_i$  couplings, 3N forces with the  $c_i$  values obtained from the Nijmegen NN partial wave analysis (PWA):  $c_1 = -0.76 \text{ GeV}^{-1}$ ,  $c_3 = -4.78 \text{ GeV}^{-1}$ ,  $c_4 = 3.96 \text{ GeV}^{-1}$  [125] were used for the  $\lambda_{\text{NN}}/\Lambda_{3N} = 2.0/2.0 \text{ fm}^{-1}$  interaction. For all Hamiltonians, the low-energy couplings  $c_D$ ,  $c_E$  in the 3N one-pion-exchange and 3N contact interaction have been fit to the  ${}^3\text{H}$  binding energy and  ${}^4\text{He}$  charge radius using Faddeev- and Faddeev-Yakubovsky calculations. The resulting LECs and the ground-state energies of  ${}^4\text{He}$  are summarized in Tab. 4.1. Symmetric nuclear-matter calculations, performed at an incomplete third order in many-body perturbation theory omitting third-order particle-hole contributions, using these Hamiltonians reproduce the empirical saturation point within theoretical uncertainties [28, 29], as already mentioned in Sec. 1.

$\lambda_{\text{NN}}/\Lambda_{3N} [\text{fm}^{-1}]$	$c_D$	$c_E$	$E_{4\text{He}} [\text{MeV}]$
1.8/2.0 (EM)	+1.264	-0.120	-29.0660
2.0/2.0 (EM)	+1.271	-0.131	-28.8957
2.0/2.5 (EM)	-0.292	-0.592	-28.9920
2.2/2.0 (EM)	+1.214	-0.137	-28.8147
2.8/2.0 (EM)	+1.278	-0.078	-28.7005
2.0/2.0 (PWA)	-3.007	-0.686	-28.8810

**Table 4.1:** Results for the  $c_D$  and  $c_E$  couplings fit to  $E_{3\text{H}} = -8.482 \text{ MeV}$  and to the point charge radius  $r_{4\text{He}} = 1.464 \text{ fm}$  (based on Ref. [126]) for the NN SRG scales  $\lambda_{\text{NN}}$  and 3N cutoffs  $\Lambda_{3N}$  and different EM/PWA  $c_i$  values used. The last column includes the Faddeev-Yakubovsky results for the ground-state energy of  ${}^4\text{He}$ .

In addition to these chiral NN+3N Hamiltonians, we also employ the  $N^2LO_{\text{sat}}$  potential [103] in our coupled-cluster calculations of calcium isotopes, presented in Sec. 8.



---

## 5 Jacobi-momentum and single-particle harmonic-oscillator bases

---

While some approaches for solving the nuclear many-body problem only rely on the operator structure of the nuclear interaction, e.g., quantum Monte Carlo methods, others employ interaction matrix elements expanded in a plane-wave momentum basis, e.g., Faddeev- and Faddeev-Yakubovsky calculations. For all approaches that rely on a basis expansion of the nuclear Hamiltonian the corresponding basis has to be chosen carefully, so that it covers the relevant physics and also exploits the symmetries of the underlying operators. All many-body methods used in this work employ at some point a basis composed of harmonic-oscillator (HO) eigenstates. It has been proven to be suitable for the calculation of ground- and excited states of nuclei. In this section we discuss the steps to transform the input matrix elements, given with respect to Jacobi momenta, into matrix elements in the HO single-particle basis. The procedure for NN matrix elements is outlined in Sec. 5.1, while details on the transformation of 3N matrix elements are explained in Sec. 5.2.

---

### 5.1 Two-body bases

---

Before going into detail on the different steps to transform NN matrix elements we briefly outline the general idea: The operator structure of chiral NN potentials is usually given in momentum space. Having expanded these operators in a plane-wave momentum basis, the corresponding matrix elements are transformed into the relative HO basis. In a successive step, these relative matrix elements are coupled with the center-of-mass coordinate of the two-body system to obtain NN interaction matrix elements in the single-particle basis.

A general NN interaction can be written in terms of initial and final relative momenta  $\mathbf{k} = (\mathbf{k}_1 - \mathbf{k}_2)/2$ ,  $\mathbf{k}' = (\mathbf{k}'_1 - \mathbf{k}'_2)/2$  as

$$V^{(2)} = V^{(2)}(\mathbf{k}, \mathbf{k}'), \quad (5.1)$$

with initial and final single-nucleon momenta  $\mathbf{k}_i, \mathbf{k}'_i$ . It can be decomposed in a plane-wave partial wave basis by evaluating projection integrals of the form

$$F_{ll'}^{m_l m_{l'}}(k, k') = \int d\hat{\mathbf{k}}' d\hat{\mathbf{k}} Y_{l'm_{l'}}^*(\hat{\mathbf{k}}') Y_{lm_l}(\hat{\mathbf{k}}) V^{(2)}(\mathbf{k}, \mathbf{k}'), \quad (5.2)$$

for fixed values of  $k = |\mathbf{k}|, k' = |\mathbf{k}'|$  and the angular momentum quantum numbers. Since the nucleons also carry spin and isospin, we couple the single-nucleon spins (isospins) to a total spin  $S$  (isospin  $T$ ), leading to partial-wave decomposed matrix elements  $\langle k(lS)JT \mathcal{M}_T | V^{(2)} | k'(l'S)JT \mathcal{M}_T \rangle = \langle (lS)JT \mathcal{M}_T | V(k, k') | (l'S)JT \mathcal{M}_T \rangle$  already used as input for the NN SRG evolution in Sec. 3. Here, we explicitly show the  $\mathcal{M}_T$  dependence distinguishing proton-proton, proton-neutron and neutron-neutron  $T = 1$  matrix elements.

A general basis state in the two-body Jacobi HO basis, suppressing the isospin, is given by

$$|n(lS)J\rangle = \sum_{m_l, m_S} \begin{pmatrix} l & S & J \\ m_l & m_S & m_J \end{pmatrix} \{ |nlm_l\rangle \otimes |Sm_S\rangle \}. \quad (5.3)$$

Thus, we need a relation between the Jacobi HO basis state  $|nlm_l\rangle$  and the plane-wave partial wave basis state  $|klm_l\rangle$ . We start by expressing the Jacobi HO state in terms of momentum states

$$|nlm_l\rangle = \int d^3p |\mathbf{p}\rangle \langle \mathbf{p} | nlm_l \rangle = \int dp p^2 \int d\hat{\mathbf{p}} |\mathbf{p}\rangle \langle \mathbf{p} | nlm_l \rangle, \quad (5.4)$$

where the overlap is the HO wave function [127] in momentum space

$$\Psi_{nlm_l}(\mathbf{p}) = \langle \mathbf{p} | nlm_l \rangle = R_{nl}(p) Y_{lm_l}(\hat{\mathbf{p}}), \quad (5.5)$$

with the radial part given by

$$R_{nl}(p) = (-1)^n \sqrt{\frac{2(n!)b^3}{\Gamma(n+l+\frac{3}{2})}} (pb)^l e^{-\frac{1}{2}(pb)^2} L_n^{l+\frac{1}{2}}((pb)^2). \quad (5.6)$$

Here, we have employed the oscillator parameter  $b = \sqrt{\frac{\hbar c}{m_N \hbar \Omega}}$  and the generalized Laguerre polynomials  $L_n^{l+\frac{1}{2}}((pb)^2)$ . Expanding the momentum states  $|\mathbf{p}\rangle$  in the plane-wave partial wave basis leads to

$$|\mathbf{p}\rangle = \sum_{l', m_{l'}} \int dp' (p')^2 |p' l' m_{l'}\rangle \langle p' l' m_{l'} | \mathbf{p} \rangle \quad (5.7)$$

$$= \sum_{l', m_{l'}} \int dp' (p')^2 \frac{\delta(p' - p)}{p' p} Y_{l' m_{l'}}^*(\hat{\mathbf{p}}) |p' l' m_{l'}\rangle \quad (5.8)$$

$$= \sum_{l', m_{l'}} Y_{l' m_{l'}}^*(\hat{\mathbf{p}}) |p l' m_{l'}\rangle. \quad (5.9)$$

Inserting Eq. (5.9) into Eq. (5.4) reveals the relation between the Jacobi HO basis and the plane-wave partial wave basis

$$|nlm_l\rangle = \sum_{l', m_{l'}} \int dp p^2 R_{nl}(p) \underbrace{\int d\hat{\mathbf{p}} Y_{l' m_{l'}}^*(\hat{\mathbf{p}}) Y_{lm_l}(\hat{\mathbf{p}}) |p l' m_{l'}\rangle}_{=\delta_{ll'} \delta_{m_l m_{l'}}} = \int dp p^2 R_{nl}(p) |plm_l\rangle, \quad (5.10)$$

where we used the orthonormality relation of the spherical harmonics. Thus, we return to Eq. (5.3), which can be rewritten by employing Eq. (5.10) and by recoupling of the angular momenta to

$$\begin{aligned} |n(lS)J\rangle &= \sum_{m_l, m_S} \sum_{J', m_{J'}} \begin{pmatrix} l & S & | & J \\ m_l & m_S & | & m_J \end{pmatrix} \begin{pmatrix} l & S & | & J' \\ m_l & m_S & | & m_{J'} \end{pmatrix} \int dk k^2 R_{nl}(k) |k(lS)J\rangle \\ &= \sum_{J', m_{J'}} \delta_{JJ'} \delta_{m_J m_{J'}} \int dk k^2 R_{nl}(k) |k(lS)J\rangle \\ &= \int dk k^2 R_{nl}(k) |k(lS)J\rangle, \end{aligned} \quad (5.11)$$

where we exploited the orthonormality relation of the Clebsch-Gordan coefficients. Thus, the transformation formula for NN matrix elements from the plane-wave partial wave to the Jacobi HO basis is given by

$$\langle n(lS)JT \mathcal{M}_T | V^{(2)} | n'(l'S)JT \mathcal{M}_T \rangle = \int dk k^2 R_{nl}(k) \int dk' k'^2 R_{n'l'}(k') \langle k(lS)JT \mathcal{M}_T | V^{(2)} | k'(l'S)JT \mathcal{M}_T \rangle, \quad (5.12)$$

which is evaluated on a two-dimensional momentum mesh with  $N_k = N_{k'} \sim 100$  points. In the radial wave function we have to introduce scaling factors  $b_k = \sqrt{2}$  multiplied to the oscillator parameter  $b$  to compensate for the difference in the definition of the relative momentum  $\mathbf{k} = (\mathbf{k}_1 - \mathbf{k}_2)/2$  and the Jacobi momentum  $\mathbf{k} = (\mathbf{k}_1 - \mathbf{k}_2)/\sqrt{2}$ . This step is necessary since the following transformation into the single-particle basis assumes Jacobi coordinates, see Eq. (5.18).

For the transformation into the single-particle basis we start from non-antisymmetrized  $j$ -coupled HO single-particle states  $|n_a(l_a s_a) j_a m_{j_a} m_{t_a}\rangle$  and couple them to the total angular momentum  $\mathcal{J}$  and total isospin  $T$

$$|ab\rangle = |n_a(l_a s_a) j_a m_{j_a} m_{t_a}, n_b(l_b s_b) j_b m_{j_b} m_{t_b}\rangle \quad (5.13)$$

$$\begin{aligned} &= \sum_{\mathcal{J}, \mathcal{M}} \sum_{T, \mathcal{M}_T} \begin{pmatrix} j_a & j_b & | & \mathcal{J} \\ m_{j_a} & m_{j_b} & | & \mathcal{M} \end{pmatrix} \begin{pmatrix} t_a & t_b & | & T \\ m_{t_a} & m_{t_b} & | & \mathcal{M}_T \end{pmatrix} \\ &\quad \times |[n_a(l_a s_a) j_a, n_b(l_b s_b) j_b] \mathcal{J} \mathcal{M}, (t_a t_b) T \mathcal{M}_T\rangle, \end{aligned} \quad (5.14)$$

In a first step we change the coupling scheme of particle 1 and 2 from  $j$ - to  $ls$ -coupling

$$|[n_a(l_a s_a) j_a, n_b(l_b s_b) j_b] \mathcal{J}\rangle \rightarrow |[n_a(l_a) \lambda(s_a s_b) S] \mathcal{J}\rangle, \quad (5.15)$$

with the total orbital angular momentum  $\lambda$  and the total spin  $S$ , by employing a  $9j$ -symbol

$$|[n_a(l_a s_a) j_a, n_b(l_b s_b) j_b] \mathcal{J}\rangle = \sum_{\lambda, S} \hat{j}_a \hat{j}_b \hat{\lambda} \hat{S} \begin{Bmatrix} l_a & s_a & j_a \\ l_b & s_b & j_b \\ \lambda & S & \mathcal{J} \end{Bmatrix} |[n_a(l_a) \lambda(s_a s_b) S] \mathcal{J}\rangle, \quad (5.16)$$

where we have introduced the notation  $\hat{j}_a = \sqrt{2j_a + 1}$ . Therefore, in the second step we can perform the Talmi transformation [127] from the single-particle coordinates  $\mathbf{r}_1, \mathbf{r}_2$  to the center-of-mass coordinate  $\mathbf{cm}_x$  of particles 1 and 2 and the relative Jacobi coordinate  $\mathbf{x}$

$$\mathbf{cm}_x = \frac{\mathbf{r}_1 + \mathbf{r}_2}{\sqrt{2}}, \quad (5.17)$$

$$\mathbf{x} = \frac{\mathbf{r}_1 - \mathbf{r}_2}{\sqrt{2}}. \quad (5.18)$$

This coordinate transformation is obtained by the orthogonal matrix

$$\begin{pmatrix} \mathbf{cm}_x \\ \mathbf{x} \end{pmatrix} = \begin{pmatrix} \sqrt{\frac{d}{d+1}} & \sqrt{\frac{1}{d+1}} \\ \sqrt{\frac{1}{d+1}} & -\sqrt{\frac{d}{d+1}} \end{pmatrix} \begin{pmatrix} \mathbf{r}_1 \\ \mathbf{r}_2 \end{pmatrix}, \quad (5.19)$$

with  $d = 1$  and is represented by a Talmi-Moshinsky bracket [127], also referred to as HO bracket,

$$|[n_a l_a(\mathbf{r}_1) n_b l_b(\mathbf{r}_2)]\lambda\rangle = \sum_{N,L,n,l} \langle NL, nl; \lambda | n_a l_a, n_b l_b \rangle_{d=1} |[NL(\mathbf{cm}_x) nl(\mathbf{x})]\lambda\rangle. \quad (5.20)$$

In step three we reorder the coupling of angular momenta. The relative orbital angular momentum  $l$  of the Jacobi coordinate is coupled with the total spin  $S$  to the relative angular momentum  $J$ , which is successively coupled with the orbital angular momentum  $L$  of the center-of-mass of particles 1 and 2 to the total angular momentum  $\mathcal{J}$ , according to

$$|[L(l)\lambda S]\mathcal{J}\rangle \rightarrow |[L(lS)J]\mathcal{J}\rangle. \quad (5.21)$$

For that, we employ a  $6j$ -symbol

$$\begin{aligned} |[L(l)\lambda S]\mathcal{J}\rangle &= \sum_J \langle [L(lS)J]\mathcal{J} | [L(l)\lambda S]\mathcal{J} \rangle |[L(lS)J]\mathcal{J}\rangle \\ &= \sum_J (-1)^{L+l+S+J} \hat{\lambda} \hat{j} \begin{Bmatrix} L & l & \lambda \\ S & \mathcal{J} & J \end{Bmatrix} |[L(lS)J]\mathcal{J}\rangle. \end{aligned} \quad (5.22)$$

Collecting all terms and decoupling the orbital angular momentum  $L$  of the center-of-mass of particles 1 and 2 and the relative angular momentum  $J$  leads to

$$\begin{aligned} |ab\rangle &= \sum_{\mathcal{J}, \mathcal{M}_T, \mathcal{M}_T} \sum_{\lambda, S} \sum_{N, L, n, l} \sum_J \sum_{m_L, m_J} (-1)^{L+l+S+J} \hat{j}_a \hat{j}_b \hat{\lambda}^2 \hat{S} \hat{J} \\ &\quad \times \begin{pmatrix} j_a & j_b & \mathcal{J} \\ m_{j_a} & m_{j_b} & \mathcal{M} \end{pmatrix} \begin{pmatrix} t_a & t_b & T \\ m_{t_a} & m_{t_b} & \mathcal{M}_T \end{pmatrix} \\ &\quad \times \begin{Bmatrix} l_a & s_a & j_a \\ l_b & s_b & j_b \\ \lambda & S & \mathcal{J} \end{Bmatrix} \langle NL, nl; \lambda | n_a l_a, n_b l_b \rangle_{d=1} \begin{Bmatrix} L & l & \lambda \\ S & \mathcal{J} & J \end{Bmatrix} \\ &\quad \times \begin{pmatrix} L & J & \mathcal{J} \\ m_L & m_J & \mathcal{M} \end{pmatrix} |NLm_L; n(lS)Jm_J T \mathcal{M}_T\rangle. \end{aligned} \quad (5.23)$$

When considering antisymmetrized states  $|ab\rangle_a$  an additional term arises with exchanged single-particle indices, according to

$$|ab\rangle \rightarrow |ab\rangle_a = \sqrt{2} \mathcal{A} |ab\rangle = \frac{1}{\sqrt{2}} (|ab\rangle - |ba\rangle), \quad (5.24)$$

where  $\mathcal{A}$  is the antisymmetrization operator  $\mathcal{A} = \frac{1}{\text{Al}} \sum_{\mathcal{P}} \text{sgn}(\mathcal{P}) \mathcal{P}$  with the permutation operator  $\mathcal{P}$  and the sign of the corresponding permutation  $\text{sgn}(\mathcal{P})$ . Considering this exchange of indices in all terms of Eq. (5.23) leads to phases from the Clebsch-Gordan coefficients  $(-1)^{j_a+j_b-\mathcal{J}}$ ,  $(-1)^{t_a+t_b-T}$ , the  $9j$  symbol  $(-1)^{l_a+l_b+s_a+s_b+j_a+j_b+\lambda+S+\mathcal{J}}$

and the HO bracket  $(-1)^{\lambda-L}$ . Collecting all phases and employing that the HO bracket conserves parity, i.e.,  $(-1)^L = (-1)^{l_a+l_b+l}$ , leads to  $(-1)^{l+S+T}$  and, consequently, to

$$|ab\rangle_a = \frac{1}{\sqrt{2}} (1 - (-1)^{l+S+T}) |ab\rangle. \quad (5.25)$$

Before writing the transformation for two-body matrix elements we consider the properties of a general two-body interaction

$$\begin{aligned} \langle N L m_L; n(l S) J m_J | V^{(2)} | N' L' m_{L'}; n'(l' S') J' m_{J'} \rangle &= \delta_{NN'} \delta_{LL'} \delta_{m_L m_{L'}} \delta_{SS'} \delta_{JJ'} \delta_{m_J m_{J'}} \\ &\times \langle N L m_L; n(l S) J m_J | V^{(2)} | N L m_L; n'(l' S) J m_J \rangle, \end{aligned} \quad (5.26)$$

i.e., that in addition to the isospin quantum numbers also the center-of-mass, the spin and the relative angular momentum quantum numbers are not affected by the interaction. Thus, we can already eliminate the Clebsch-Gordan coefficients

$$\sum_{m_L, m_J} \begin{pmatrix} L & J \\ m_L & m_J \end{pmatrix} \begin{matrix} \mathcal{J} \\ \mathcal{M} \end{matrix} \begin{pmatrix} L & J \\ m_L & m_J \end{pmatrix} \begin{matrix} \mathcal{J} \\ \mathcal{M} \end{matrix} = \delta_{\mathcal{J}\mathcal{J}} \delta_{\mathcal{M}\mathcal{M}}, \quad (5.27)$$

and the transformation to normalized, antisymmetrized  $\mathcal{J}T$ -coupled matrix elements is given by

$$\begin{aligned} {}_a \langle (ab) \mathcal{J} T \mathcal{M}_T | V^{(2)} | (cd) \mathcal{J} T \mathcal{M}_T \rangle_a &= \frac{2}{\sqrt{(1 + \delta_{ab})(1 + \delta_{cd})}} \sum_{\lambda, S} \sum_{N, L, n, l} \sum_J \sum_{\lambda'} \sum_{n', l'} \\ &\times (-1)^{L+l+S+J} \hat{j}_a \hat{j}_b \hat{\lambda}^2 \hat{S} \hat{J} (-1)^{L+l'+S+J} \hat{j}_c \hat{j}_d \hat{\lambda}'^2 \hat{S}' \hat{J}' \\ &\times \begin{Bmatrix} l_a & s_a & j_a \\ l_b & s_b & j_b \\ \lambda & S & \mathcal{J} \end{Bmatrix} \langle N L, n l; \lambda | n_a l_a, n_b l_b \rangle_{d=1} \begin{Bmatrix} L & l & \lambda \\ S & \mathcal{J} & J \end{Bmatrix} \\ &\times \begin{Bmatrix} l_c & s_c & j_c \\ l_d & s_d & j_d \\ \lambda' & S & \mathcal{J}' \end{Bmatrix} \langle N L, n' l'; \lambda' | n_c l_c, n_d l_d \rangle_{d=1} \begin{Bmatrix} L & l' & \lambda' \\ S & \mathcal{J}' & J' \end{Bmatrix} \\ &\times (1 - (-1)^{l+S+T}) \langle n(l S) J T \mathcal{M}_T | V^{(2)} | n'(l' S) J T \mathcal{M}_T \rangle \quad (5.28) \\ &= \frac{2}{\sqrt{(1 + \delta_{ab})(1 + \delta_{cd})}} \sum_{\lambda, S} \sum_{N, L, n, l} \sum_J \sum_{\lambda'} \sum_{n', l'} \hat{j}_a \hat{j}_b \hat{j}_c \hat{j}_d \hat{\lambda}^2 \hat{\lambda}'^2 \hat{S}^2 \hat{J}^2 \\ &\times \begin{Bmatrix} l_a & s_a & j_a \\ l_b & s_b & j_b \\ \lambda & S & \mathcal{J} \end{Bmatrix} \langle N L, n l; \lambda | n_a l_a, n_b l_b \rangle_{d=1} \begin{Bmatrix} L & l & \lambda \\ S & \mathcal{J} & J \end{Bmatrix} \\ &\times \begin{Bmatrix} l_c & s_c & j_c \\ l_d & s_d & j_d \\ \lambda' & S & \mathcal{J}' \end{Bmatrix} \langle N L, n' l'; \lambda' | n_c l_c, n_d l_d \rangle_{d=1} \begin{Bmatrix} L & l' & \lambda' \\ S & \mathcal{J}' & J' \end{Bmatrix} \\ &\times (1 - (-1)^{l+S+T}) \langle n(l S) J T \mathcal{M}_T | V^{(2)} | n'(l' S) J T \mathcal{M}_T \rangle, \quad (5.29) \end{aligned}$$

where we employed that  $l' = l \pm 2$  to eliminate the phase in the second line of Eq. (5.28) and the indices in the delta functions refer to  $\{n_a, l_a, j_a\}$ .

## 5.2 Three-body bases

Similar to the two-body case we outline the different steps to transform 3N matrix elements: The operator structure of chiral 3N forces, see, e.g., Eqs. (2.19) and (2.20) for the contributions at  $N^2\text{LO}$ , is given in momentum space and has to be expanded in a plane-wave momentum basis. The corresponding matrix elements of the Faddeev components are transformed into the relative HO basis. These steps are discussed in Sec. 5.2.1. We continue with the derivation of a basis representation of the antisymmetrizer in the relative HO basis, which is necessary for the antisymmetrization of the Faddeev components, in Sec. 5.2.2. In Sec. 5.2.3 we derive the three-body Talmi Moshinsky transformation to transform the antisymmetrized 3N matrix elements in the relative HO basis to the single-particle basis.



### 5.2.1 Partial-wave decomposition and transformation to relative harmonic oscillator states

A general translationally invariant 3N force can be written as a function of the Jacobi momenta

$$\mathbf{p} = \frac{\mathbf{k}_1 - \mathbf{k}_2}{\sqrt{2}}, \quad (5.30)$$

$$\mathbf{q} = \sqrt{\frac{2}{3}} \left[ \frac{1}{2}(\mathbf{k}_1 + \mathbf{k}_2) - \mathbf{k}_3 \right], \quad (5.31)$$

where  $\mathbf{k}_i$  are the single-nucleon momenta, as

$$V^{(3)} = V^{(3)}(\mathbf{p}, \mathbf{q}, \mathbf{p}', \mathbf{q}'). \quad (5.32)$$

Here, we have distinguished between the Jacobi momenta of the initial  $\mathbf{p}, \mathbf{q}$  and final states  $\mathbf{p}', \mathbf{q}'$ . In analogy to the NN sector it is possible to decompose the 3N force in a plane-wave partial wave basis, which involves the evaluation of projection integrals of the form

$$F_{l_{12}l_3l'_{12}l'_3}^{m_{l_{12}}m_{l_3}m_{l'_{12}}m_{l'_3}}(\mathbf{p}, \mathbf{q}, \mathbf{p}', \mathbf{q}') = \int d\hat{\mathbf{p}}' d\hat{\mathbf{q}}' d\hat{\mathbf{p}} d\hat{\mathbf{q}} Y_{l'_{12}m_{l'_{12}}}^*(\hat{\mathbf{p}}') Y_{l'_3m_{l'_3}}^*(\hat{\mathbf{q}}') Y_{l_{12}m_{l_{12}}}(\hat{\mathbf{p}}) Y_{l_3m_{l_3}}(\hat{\mathbf{q}}) V^{(3)}(\mathbf{p}, \mathbf{q}, \mathbf{p}', \mathbf{q}'), \quad (5.33)$$

for fixed values of  $p = |\mathbf{p}|, q = |\mathbf{q}|, p' = |\mathbf{p}'|, q' = |\mathbf{q}'|$  and the angular momentum quantum numbers. Since we also need to take into account the spin and isospin quantum numbers of the nucleons we employ a  $JT$ -coupled three-body plane-wave basis [128] of the form

$$|pq\alpha\rangle \equiv |pq; [(l_{12}s_{ab})j_{12}(l_3s_c)I_3]J(t_{ab}t_c)T\rangle, \quad (5.34)$$

where  $l_{12}$  denotes the relative orbital angular momentum of particles 1 and 2 with relative momentum  $p$  and  $s_{ab}$ ,  $j_{12}$  and  $t_{ab}$  correspond to spin, total angular momentum and isospin of the pair. Analogously, the orbital angular momentum of particle 3 relative to the center-of-mass of the pair 12 with relative momentum  $q$  is denoted by  $l_3$ , while  $s_c = 1/2$ ,  $I_3$  and  $t_c = 1/2$  correspond to spin, total angular momentum and isospin. The total relative three-body angular momentum and the total isospin are labeled by  $J$  and  $T$ . In Eq. (5.34) we already employed the rotational invariance of the 3N force, i.e., the independence of the projections  $m_J$  and  $\mathcal{M}_T$ , and omitted these quantum numbers in the basis states. Note that the basis states are only partially antisymmetric with respect to the exchange of the first two particles, i.e.,  $(-1)^{l_{12}+s_{ab}+t_{ab}} = 1$ .

In our nuclear structure calculations we include partial waves up to the relative total three-body angular momentum  $J = 9/2$ . In addition, the maximum value of the relative orbital angular momentum  $j_{12}$  is truncated to  $j_{12,\max} = 8$  for partial waves with  $J \leq 5/2$ ,  $j_{12,\max} = 7$  for  $J = 7/2$  and  $j_{12,\max} = 6$  for  $J = 9/2$ . For all partial waves, however, the number of discrete momenta  $p$  and  $q$  is  $N_p = N_q = 15$ .

In general, 3N interactions can be decomposed in terms of Faddeev components

$$V^{(3)} = \langle pq\alpha | V^{(3)} | p'q'\alpha' \rangle = \sum_{i=1}^3 V^{(3),i}, \quad (5.35)$$

with each of the three Faddeev components  $V^{(3),i}$  being symmetric in the second- and third-particle label. These components are related via permutation transformations

$$V^{(3),2} = \mathcal{P}_{123} V^{(3),1} \mathcal{P}_{123}^{-1}, \quad V^{(3),3} = \mathcal{P}_{132} V^{(3),1} \mathcal{P}_{132}^{-1}, \quad (5.36)$$

with the permutation operators  $\mathcal{P}_{123} = \mathcal{P}_{12}\mathcal{P}_{23}$  ( $\mathcal{P}_{132} = \mathcal{P}_{13}\mathcal{P}_{23}$ ), that permute three particles cyclically (anti-cyclically). The inverse of the permutation operator is given by  $\mathcal{P}_{123}^{-1} = \mathcal{P}_{23}\mathcal{P}_{12}$  ( $\mathcal{P}_{132}^{-1} = \mathcal{P}_{23}\mathcal{P}_{13}$ ). In contrast, it is also possible to derive matrix elements of the completely antisymmetrized interaction by

$$V^{(3),\text{as}} = (1 + \mathcal{P}_{123} + \mathcal{P}_{132}) V^{(3),i} (1 + \mathcal{P}_{123} + \mathcal{P}_{132}). \quad (5.37)$$

Nevertheless, the application of the permutation operators in Eq. (5.37) in a momentum partial-wave basis is non-trivial and can induce numerical uncertainties [129]. Although the novel improved implementation of Ref. [82]

provides perfectly stable results even for large values of angular momenta, we transform the Faddeev components  $V^{(3),i}$  to the Jacobi HO basis and perform the antisymmetrization directly in this basis.

A general basis state in the three-body Jacobi HO basis is given by

$$|n_{12}n_3\alpha\rangle \equiv |n_{12}n_3; [(l_{12}s_{ab})j_{12}(l_3 1/2)I_3]J(t_{ab} 1/2)T\rangle, \quad (5.38)$$

which also fulfills the partial antisymmetry with respect to the exchange of the first two particles. Since the transformation is only related to the spatial part we decouple it from the spin part and omit the isospin part for brevity leading to

$$|n_{12}n_3\alpha\rangle = |n_{12}n_3; [(l_{12}s_{ab})j_{12}(l_3 1/2)I_3]J\rangle \quad (5.39)$$

$$= \sum_{m_{j_{12}}, m_{I_3}} \sum_{m_{l_{12}}, m_{l_3}} \sum_{m_{s_{ab}}, m_{s_c}} \begin{pmatrix} j_{12} & I_3 & J \\ m_{j_{12}} & m_{I_3} & m_J \end{pmatrix} \begin{pmatrix} l_{12} & s_{ab} & j_{12} \\ m_{l_{12}} & m_{s_{ab}} & m_{j_{12}} \end{pmatrix} \begin{pmatrix} l_3 & 1/2 & I_3 \\ m_{l_3} & m_{s_c} & m_{I_3} \end{pmatrix} \\ \times \{ \{ |n_{12}l_{12}m_{l_{12}}\rangle \otimes |n_3l_3m_{l_3}\rangle \} \otimes \{ |s_{ab}m_{s_{ab}}\rangle \otimes |1/2m_{s_c}\rangle \} \}. \quad (5.40)$$

Then, the transformation formula for 3N matrix elements from the plane-wave partial wave to the Jacobi HO basis can be obtained in analogy to the NN case, Eq. (5.12), and is given by

$$\langle n_{12}n_3\alpha | V^{(3),i} | n'_{12}n'_3\alpha' \rangle = \int dp p^2 R_{n_{12}l_{12}}(p) \int dq q^2 R_{n_3l_3}(q) \int dp' (p')^2 R_{n'_{12}l'_{12}}(p') \int dq' (q')^2 R_{n'_3l'_3}(q') \\ \times \langle pq\alpha | V^{(3),i} | p'q'\alpha' \rangle, \quad (5.41)$$

which is evaluated by interpolating the 3N force matrix elements from the initial four-dimensional momentum mesh with  $N_p = N_q = N_{p'} = N_{q'} = 15$  by cubic splines onto a finer mesh, on which also the radial wave functions are calculated. Since the 3N matrix elements in the plane-wave partial wave basis are not regularized we regularize them by multiplication with the regulator function Eq. (2.26) after the interpolation, yielding

$$\langle pq\alpha | V^{(3),i,\text{reg}} | p'q'\alpha' \rangle = f^{\Lambda_{3N}}(p, q) \langle pq\alpha | V^{(3),i} | p'q'\alpha' \rangle f^{\Lambda_{3N}}(p', q'). \quad (5.42)$$

While the successive antisymmetrization and the transformation to the single-particle basis employ the definition of the Jacobi momenta given in Eqs. (5.30) and (5.31), the partial-wave decomposition uses a slightly modified version

$$\tilde{\mathbf{p}} = \frac{\mathbf{k}_1 - \mathbf{k}_2}{2}, \quad (5.43)$$

$$\tilde{\mathbf{q}} = \frac{2}{3} \left[ \mathbf{k}_3 - \frac{1}{2}(\mathbf{k}_1 + \mathbf{k}_2) \right]. \quad (5.44)$$

Therefore, we have to introduce scaling factors  $b_p = \sqrt{2}$  and  $b_q = \sqrt{\frac{3}{2}}$  multiplied to the oscillator parameter  $b$  in the evaluation of the radial part of the HO wave function. In addition, the sign change in the Jacobi momentum  $\mathbf{q} = -b_q \tilde{\mathbf{q}}$  leads to a phase  $(-1)^{l_{12}+l'_{12}}$ . Moreover, since the evaluation of 3N matrix elements in momentum space is only determined up to a phase we have to introduce a factor  $i^{l_{12}-l'_{12}+l_3-l'_3}$ .

### 5.2.2 Basis representation of the antisymmetrizer

As mentioned above the Jacobi HO basis states are only partially antisymmetrized with respect to the exchange of particle 1 and 2. In order to obtain fully antisymmetrized basis states with respect to particle exchange we derive a basis representation of the antisymmetrizer  $\mathcal{A}$  in the Jacobi HO basis [130]. Since the antisymmetrizer  $\mathcal{A}$  is a projection operator obeying  $\mathcal{A}^2 = \mathcal{A}$  the diagonalization will yield two eigenspaces. The fully antisymmetrized states have the eigenvalue 1, while spurious states have eigenvalue 0. The antisymmetrizer for three particles is defined as

$$\mathcal{A} = \frac{1}{3!} \sum_{\mathcal{P}} \text{sgn}(\mathcal{P}) \mathcal{P} \quad (5.45)$$

$$= \frac{1}{6} (\mathcal{P}_{123} + \mathcal{P}_{312} + \mathcal{P}_{231} - \mathcal{P}_{213} - \mathcal{P}_{321} - \mathcal{P}_{132}). \quad (5.46)$$

The antisymmetry with respect to the exchange of particle 1 and 2 implies, e.g.,  $\mathcal{P}_{123} = -\mathcal{P}_{213}$  leading to

$$\mathcal{A} = \frac{1}{6}(\mathcal{P}_{123} + \mathcal{P}_{312} + \mathcal{P}_{231} + \mathcal{P}_{123} + \mathcal{P}_{231} + \mathcal{P}_{312}) \quad (5.47)$$

$$= \frac{1}{3}(\mathbb{1} + \mathcal{P}_{312} + \mathcal{P}_{231}) \quad (5.48)$$

$$= \frac{1}{3}(\mathbb{1} + \mathcal{T}_{12}\mathcal{T}_{23} + \mathcal{T}_{23}\mathcal{T}_{12}), \quad (5.49)$$

where we have used  $\mathcal{P}_{123} = 1$  and the representation of permutation operators in terms of transposition operators. Since the partial antisymmetry for the exchange of particle 1 and 2 translates to  $\mathcal{T}_{12} = -1$  we can reduce the three-body antisymmetrizer to the transposition operator  $\mathcal{T}_{23}$

$$\mathcal{A} = \frac{1}{3}(\mathbb{1} - 2\mathcal{T}_{23}). \quad (5.50)$$

Instead of acting with the transposition operator on the  $j$ -coupled Jacobi HO state  $|\alpha\rangle \equiv |n_{12}n_3\alpha\rangle$  it is convenient to transform the basis state to  $LS$  coupling

$$|\alpha\rangle = |n_{12}n_3; [(l_{12}s_{ab})j_{12}(l_3 1/2)I_3]Jm_J(t_{ab} 1/2)T\mathcal{M}_T\rangle \quad (5.51)$$

$$= \sum_{L,m_L} \sum_{S,m_S} \hat{j}_{12}\hat{l}_3\hat{L}\hat{S} \begin{pmatrix} l_{12} & s_{ab} & j_{12} \\ l_3 & 1/2 & I_3 \\ L & S & J \end{pmatrix} \begin{pmatrix} L & S & J \\ m_L & m_S & m_J \end{pmatrix} \\ \times \{ |n_{12}n_3; (l_{12}l_3)Lm_L\rangle \otimes |(s_{ab} 1/2)Sm_S\rangle \otimes |(t_{ab} 1/2)T\mathcal{M}_T\rangle \}. \quad (5.52)$$

Thus, the matrix element of the transposition operator  $\mathcal{T}_{23}$  takes the form

$$\langle \alpha | \mathcal{T}_{23} | \alpha' \rangle = \sum_{L,m_L} \sum_{S,m_S} \sum_{L',m_{L'}} \sum_{S',m_{S'}} \hat{j}_{12}\hat{l}_3\hat{L}\hat{S}\hat{j}'_{12}\hat{l}'_3\hat{L}'\hat{S}' \\ \times \begin{pmatrix} l_{12} & s_{ab} & j_{12} \\ l_3 & 1/2 & I_3 \\ L & S & J \end{pmatrix} \begin{pmatrix} L & S & J \\ m_L & m_S & m_J \end{pmatrix} \begin{pmatrix} l'_{12} & s'_{ab} & j'_{12} \\ l'_3 & 1/2 & I'_3 \\ L' & S' & J' \end{pmatrix} \begin{pmatrix} L' & S' & J' \\ m_{L'} & m_{S'} & m_{J'} \end{pmatrix} \\ \times \langle n_{12}n_3; (l_{12}l_3)Lm_L | \mathcal{T}_{23} | n'_{12}n'_3; (l'_{12}l'_3)L'm_{L'} \rangle \\ \times \langle (s_{ab} 1/2)Sm_S | \mathcal{T}_{23} | (s'_{ab} 1/2)S'm_{S'} \rangle \langle (t_{ab} 1/2)T\mathcal{M}_T | \mathcal{T}_{23} | (t'_{ab} 1/2)T'\mathcal{M}_{T'} \rangle. \quad (5.53)$$

We start with the last term and evaluate the action of the transposition operator  $\mathcal{T}_{23}$  on the ket  $[(t_a t_b)t_{ab}t_c]T\mathcal{M}_T\rangle$

$$\mathcal{T}_{23} |[(t_a t_b)t_{ab}t_c]T\mathcal{M}_T\rangle = |[(t_a t_c)t_{ac}t_b]T\mathcal{M}_T\rangle, \quad (5.54)$$

resulting in the matrix element for the isospin

$$\langle [(t_a t_b)t_{ab}t_c]T\mathcal{M}_T | \mathcal{T}_{23} | [(t_a t_b)t'_{ab}t_c]T'\mathcal{M}_{T'} \rangle = \langle [(t_a t_b)t_{ab}t_c]T\mathcal{M}_T | [(t_a t_c)t'_{ac}t_b]T'\mathcal{M}_{T'} \rangle \\ = \delta_{TT'} \delta_{\mathcal{M}_T \mathcal{M}_{T'}} (-1)^{t_b+t_c+t_{ab}+t'_{ac}} \hat{t}_{ab} \hat{t}'_{ac} \begin{Bmatrix} t_b & t_a & t_{ab} \\ t_c & T & t'_{ac} \end{Bmatrix} \\ = \delta_{TT'} \delta_{\mathcal{M}_T \mathcal{M}_{T'}} (-1)^{1+t_{ab}+t'_{ac}} \hat{t}_{ab} \hat{t}'_{ac} \begin{Bmatrix} 1/2 & 1/2 & t_{ab} \\ 1/2 & T & t'_{ac} \end{Bmatrix}. \quad (5.55)$$

The evaluation of the spin matrix element follows in analogy to the isospin, yielding

$$\langle [(s_a s_b)s_{ab}s_c]Sm_S | \mathcal{T}_{23} | [(s_a s_b)s'_{ab}s_c]S'm_{S'} \rangle = \delta_{SS'} \delta_{m_S m_{S'}} (-1)^{1+s_{ab}+s'_{ac}} \hat{s}_{ab} \hat{s}'_{ac} \begin{Bmatrix} 1/2 & 1/2 & s_{ab} \\ 1/2 & S & s'_{ac} \end{Bmatrix}. \quad (5.56)$$

Finally, we turn to the spatial matrix element by investigating the action of the transposition operator  $\mathcal{T}_{23}$  on the ket  $|n_{12}n_3; [l_{12}(\mathbf{x})l_3(\mathbf{y})]Lm_L\rangle$

$$\mathcal{T}_{23} |n_{12}n_3; [l_{12}(\mathbf{x})l_3(\mathbf{y})]Lm_L\rangle = |n_{12}n_3; [l_{12}(\mathbf{x}')l_3(\mathbf{y}')]Lm_L\rangle, \quad (5.57)$$



**Figure 5.1:** Schematic illustration of the three-particle system represented in single-particle coordinates  $r_1, r_2, r_3$  (left) and Jacobi coordinates  $x, y$ , defined in Eqs. (5.58) and (5.59), and center-of-mass coordinates  $cm, cm_x$ , defined in Eqs. (5.17) and (5.80) (right).

where the Jacobi coordinates

$$\mathbf{x} = \frac{\mathbf{r}_1 - \mathbf{r}_2}{\sqrt{2}}, \quad (5.58)$$

$$\mathbf{y} = \sqrt{\frac{2}{3}} \left[ \frac{1}{2}(\mathbf{r}_1 + \mathbf{r}_2) - \mathbf{r}_3 \right], \quad (5.59)$$

shown in Fig. 5.1, are redefined due to the exchange of single-particle coordinates 2 and 3. The coordinate transformation leads to

$$\begin{aligned} \mathbf{x}' &= \mathcal{T}_{23} \mathbf{x} = \frac{\mathbf{r}_1 - \mathbf{r}_3}{\sqrt{2}}, \\ \mathbf{y}' &= \mathcal{T}_{23} \mathbf{y} = \sqrt{\frac{2}{3}} \left[ \frac{1}{2}(\mathbf{r}_1 + \mathbf{r}_3) - \mathbf{r}_2 \right]. \end{aligned} \quad (5.60)$$

The primed and the original Jacobi momenta can be related by an orthogonal matrix

$$\begin{pmatrix} \mathbf{x}' \\ \mathbf{y}' \end{pmatrix} = \begin{pmatrix} \sqrt{\frac{d}{d+1}} & \sqrt{\frac{1}{d+1}} \\ \sqrt{\frac{1}{d+1}} & -\sqrt{\frac{d}{d+1}} \end{pmatrix} \begin{pmatrix} \mathbf{x} \\ \mathbf{y} \end{pmatrix}, \quad (5.61)$$

with  $d = \frac{1}{3}$ . Thus, we can expand the states with primed coordinates in terms of states with the original coordinates employing a HO bracket [127]

$$|n_{12}n_3; [l_{12}(\mathbf{x}')l_3(\mathbf{y}')]Lm_L\rangle = \sum_{\tilde{n}_{12}, \tilde{n}_3} \sum_{\tilde{l}_{12}, \tilde{l}_3} \langle \tilde{n}_{12} \tilde{l}_{12}, \tilde{n}_3 \tilde{l}_3; L | n_{12} l_{12}, n_3 l_3 \rangle_{d=\frac{1}{3}} | \tilde{n}_{12} \tilde{n}_3; [\tilde{l}_{12}(\mathbf{x}) \tilde{l}_3(\mathbf{y})] Lm_L \rangle. \quad (5.62)$$

Therefore, the spatial matrix element is given by

$$\langle n_{12}n_3; (l_{12}l_3)Lm_L | \mathcal{T}_{23} | n'_{12}n'_3; (l'_{12}l'_3)L'm_{L'} \rangle = \delta_{LL'} \delta_{m_L m_{L'}} \langle n_{12}l_{12}, n_3l_3; L | n'_{12}l'_{12}, n'_3l'_3 \rangle_{d=\frac{1}{3}}. \quad (5.63)$$

Inserting the results for the spatial, spin and isospin matrix element Eqs. (5.63), (5.56), (5.55) into the Eq. (5.53) yields

$$\begin{aligned}
\langle \alpha | \mathcal{T}_{23} | \alpha' \rangle &= \sum_{L, m_L} \sum_{S, m_S} \sum_{L', m_{L'}} \sum_{S', m_{S'}} \delta_{LL'} \delta_{m_L m_{L'}} \delta_{SS'} \delta_{m_S m_{S'}} \delta_{TT'} \delta_{\mathcal{M}_T \mathcal{M}_{T'}} \\
&\times (-1)^{1+s_{ab}+s'_{ac}} (-1)^{1+t_{ab}+t'_{ac}} \hat{j}_{12} \hat{I}_3 \hat{L} \hat{S} \hat{j}'_{12} \hat{I}'_3 \hat{L}' \hat{S}' \hat{s}_{ab} \hat{s}'_{ac} \hat{t}_{ab} \hat{t}'_{ac} \\
&\times \begin{Bmatrix} l_{12} & s_{ab} & j_{12} \\ l_3 & 1/2 & I_3 \\ L & S & J \end{Bmatrix} \begin{pmatrix} L & S & J \\ m_L & m_S & m_J \end{pmatrix} \begin{Bmatrix} l'_{12} & s'_{ab} & j'_{12} \\ l'_3 & 1/2 & I'_3 \\ L' & S' & J' \end{Bmatrix} \begin{pmatrix} L' & S' & J' \\ m_{L'} & m_{S'} & m_{J'} \end{pmatrix} \\
&\times \langle n_{12} l_{12}, n_3 l_3; L | n'_{12} l'_{12}, n'_3 l'_3 \rangle_{d=\frac{1}{3}} \begin{Bmatrix} 1/2 & 1/2 & s_{ab} \\ 1/2 & S & s'_{ac} \end{Bmatrix} \begin{Bmatrix} 1/2 & 1/2 & t_{ab} \\ 1/2 & T & t'_{ac} \end{Bmatrix} \\
&= \sum_{L, S} \delta_{JJ'} \delta_{m_J m_{J'}} \delta_{TT'} \delta_{\mathcal{M}_T \mathcal{M}_{T'}} \\
&\times (-1)^{1+s_{ab}+s'_{ac}} (-1)^{1+t_{ab}+t'_{ac}} \hat{j}_{12} \hat{I}_3 \hat{L}^2 \hat{S}^2 \hat{j}'_{12} \hat{I}'_3 \hat{L}'^2 \hat{S}'^2 \hat{s}_{ab} \hat{s}'_{ac} \hat{t}_{ab} \hat{t}'_{ac} \\
&\times \begin{Bmatrix} l_{12} & s_{ab} & j_{12} \\ l_3 & 1/2 & I_3 \\ L & S & J \end{Bmatrix} \begin{Bmatrix} l'_{12} & s'_{ab} & j'_{12} \\ l'_3 & 1/2 & I'_3 \\ L & S & J' \end{Bmatrix} \\
&\times \langle n_{12} l_{12}, n_3 l_3; L | n'_{12} l'_{12}, n'_3 l'_3 \rangle_{d=\frac{1}{3}} \begin{Bmatrix} 1/2 & 1/2 & s_{ab} \\ 1/2 & S & s'_{ac} \end{Bmatrix} \begin{Bmatrix} 1/2 & 1/2 & t_{ab} \\ 1/2 & T & t'_{ac} \end{Bmatrix}, \tag{5.64}
\end{aligned}$$

$$\begin{aligned}
&\times \langle n_{12} l_{12}, n_3 l_3; L | n'_{12} l'_{12}, n'_3 l'_3 \rangle_{d=\frac{1}{3}} \begin{Bmatrix} 1/2 & 1/2 & s_{ab} \\ 1/2 & S & s'_{ac} \end{Bmatrix} \begin{Bmatrix} 1/2 & 1/2 & t_{ab} \\ 1/2 & T & t'_{ac} \end{Bmatrix}, \tag{5.65}
\end{aligned}$$

where the summations over  $L', m_{L'}, S', m_{S'}$  were carried out first and then the orthonormality relation of the Clebsch-Gordan coefficients was employed. Equation (5.65) states that the transposition operator is not only diagonal in  $m_J$  and  $\mathcal{M}_T$  but independent of the projection quantum numbers. Consequently, as already pointed out before we can eliminate those quantum numbers from the basis states. Moreover, the transposition operator is block-diagonal in the energy quantum number (due to the energy conservation of the HO bracket  $2n_{12} + l_{12} + 2n_3 + l_3 = 2n'_{12} + l'_{12} + 2n'_3 + l'_3$ ), the total relative angular momentum  $J$  and total isospin  $T$ . Thus, we can diagonalize each  $EJT$  block of dimension  $d_{EJT}$  separately, yielding the subspaces of physical and spurious eigenstates. Since the physical subspace within each  $EJT$  block is degenerate we introduce the label  $i$ , so that the expansion of the antisymmetric relative three-particle states in terms of the Jacobi HO states is given by

$$|EJT i\rangle = \sum_{\alpha}^{d_{EJT}} \langle EJT i | \alpha \rangle | \alpha \rangle = \sum_{\alpha}^{d_{EJT}} c_{\alpha, i} | \alpha \rangle. \tag{5.66}$$

Here, we introduced the coefficients of fractional parentage  $c_{\alpha, i}$  [131, 132], that correspond to the eigenvectors obtained by diagonalizing the  $EJT$  block. Then the basis representation of the antisymmetrizer  $\mathcal{A}$  in terms of antisymmetric Jacobi states reads

$$\mathcal{A} = \sum_{E, J, T, i} |EJT i\rangle \langle EJT i|, \tag{5.67}$$

and the antisymmetrized  $JT$ -coupled matrix elements are given by

$$\langle EJT i | V^{(3)} | E'JT i' \rangle = 18 \sum_{\alpha \alpha'} c_{\alpha, i} c_{\alpha', i'} \langle \alpha | V^{(3), i} | \alpha' \rangle, \tag{5.68}$$

with a factor 3 due to the use of the Faddeev components  $V^{(3), i}$  and a factor 6 from the antisymmetrization  $|abc\rangle_{\alpha} = \sqrt{3!} \mathcal{A} |abc\rangle$ .

### 5.2.3 Three-body Talmi Moshinsky transformation

In the following we want to derive the transformation of the 3N matrix elements from the Jacobi HO basis into the single-particle basis. An expression for this transformation was first given in Ref. [131], but it was replaced with

a more efficient version from Ref. [132]. We start from non-antisymmetrized  $j$ -coupled HO single-particle states  $|n_a(l_a s_a)j_a m_{j_a} m_{t_a}\rangle$  and couple them to the total angular momentum  $\mathcal{J}$  and total isospin  $T$

$$|abc\rangle = |n_a(l_a s_a)j_a m_{j_a} t_a m_{t_a}, n_b(l_b s_b)j_b m_{j_b} t_b m_{t_b}, n_c(l_c s_c)j_c m_{j_c} t_c m_{t_c}\rangle \quad (5.69)$$

$$\begin{aligned} &= \sum_{J_{12}, \mathcal{J}} \sum_{t_{ab}, T} \begin{pmatrix} j_a & j_b & & \\ m_{j_a} & m_{j_b} & & \\ & & J_{12} & \\ & & m_{j_a} + m_{j_b} & \end{pmatrix} \begin{pmatrix} J_{12} & j_c & & \\ m_{j_a} + m_{j_b} & m_{j_c} & & \\ & & \mathcal{J} & \\ & & \mathcal{M} & \end{pmatrix} \\ &\times \begin{pmatrix} t_a & t_b & & \\ m_{t_a} & m_{t_b} & & \\ & & t_{ab} & \\ & & m_{t_a} + m_{t_b} & \end{pmatrix} \begin{pmatrix} t_{ab} & t_c & & \\ m_{t_a} + m_{t_b} & m_{t_c} & & \\ & & T & \\ & & m_T & \end{pmatrix} \\ &\times | \{ [n_a(l_a s_a)j_a, n_b(l_b s_b)j_b] J_{12} n_c(l_c s_c)j_c \} \mathcal{J} \mathcal{M}, [(t_a t_b)] t_{ab} t_c \} T m_T \rangle \end{aligned} \quad (5.70)$$

$$\begin{aligned} &= \sum_{J_{12}, \mathcal{J}} \sum_{t_{ab}, T} \begin{pmatrix} j_a & j_b & & \\ m_{j_a} & m_{j_b} & & \\ & & J_{12} & \\ & & m_{j_a} + m_{j_b} & \end{pmatrix} \begin{pmatrix} J_{12} & j_c & & \\ m_{j_a} + m_{j_b} & m_{j_c} & & \\ & & \mathcal{J} & \\ & & \mathcal{M} & \end{pmatrix} \\ &\times \begin{pmatrix} t_a & t_b & & \\ m_{t_a} & m_{t_b} & & \\ & & t_{ab} & \\ & & m_{t_a} + m_{t_b} & \end{pmatrix} \begin{pmatrix} t_{ab} & t_c & & \\ m_{t_a} + m_{t_b} & m_{t_c} & & \\ & & T & \\ & & m_T & \end{pmatrix} \\ &\times \{ \{ |a\rangle |b\rangle \}^{J_{12}} |c\rangle \}^{\mathcal{J} \mathcal{M}}, \end{aligned} \quad (5.71)$$

with  $\mathcal{M} = m_{j_a} + m_{j_b} + m_{j_c}$  and  $m_T = m_{t_a} + m_{t_b} + m_{t_c}$ . In the definition of the ket in Eq. (5.71) we omitted the isospin quantum numbers for brevity. Moreover, the identity of the center-of-mass motion and the relative motion in the Jacobi HO basis

$$\mathbb{1} = \sum_{n_{cm}, l_{cm}, m_{cm}} \sum_{\alpha} |n_{cm} l_{cm} m_{cm}\rangle |\alpha\rangle \langle n_{cm} l_{cm} m_{cm}| \langle \alpha|, \quad (5.72)$$

with the shorthand notation  $\alpha = \{n_{12}, l_{12}, s_{ab}, j_{12}, n_3, l_3, I_3, J, m_J, t_{ab}, T, m_T\}$ , can be rewritten by coupling to the total angular momentum  $\mathcal{J}$  as

$$\mathbb{1} = \sum_{n_{cm}, l_{cm}} \sum_{\alpha} \sum_{\mathcal{J}' \mathcal{M}'} \{ |n_{cm} l_{cm}\rangle |\alpha\rangle \}^{\mathcal{J}' \mathcal{M}'} \{ \langle n_{cm} l_{cm}| \langle \alpha| \}^{\mathcal{J}' \mathcal{M}'}, \quad (5.73)$$

where the shorthand notation  $\alpha$  does not contain  $m_J$  anymore. Inserting Eq. (5.73) into Eq. (5.71) results in

$$\begin{aligned} |abc\rangle &= \sum_{J_{12}, \mathcal{J}} \sum_{n_{cm}, l_{cm}} \sum_{\alpha} \begin{pmatrix} j_a & j_b & & \\ m_{j_a} & m_{j_b} & & \\ & & J_{12} & \\ & & m_{j_a} + m_{j_b} & \end{pmatrix} \begin{pmatrix} J_{12} & j_c & & \\ m_{j_a} + m_{j_b} & m_{j_c} & & \\ & & \mathcal{J} & \\ & & \mathcal{M} & \end{pmatrix} \\ &\times \begin{pmatrix} t_a & t_b & & \\ m_{t_a} & m_{t_b} & & \\ & & t_{ab} & \\ & & m_{t_a} + m_{t_b} & \end{pmatrix} \begin{pmatrix} t_{ab} & t_c & & \\ m_{t_a} + m_{t_b} & m_{t_c} & & \\ & & T & \\ & & m_T & \end{pmatrix} \\ &\times T \{ |n_{cm} l_{cm}\rangle |\alpha\rangle \}^{\mathcal{J} \mathcal{M}}, \end{aligned} \quad (5.74)$$

where we introduced the overlap  $T \equiv \{ \langle n_{cm} l_{cm}| \langle \alpha| \}^{\mathcal{J} \mathcal{M}} \{ \{ |a\rangle |b\rangle \}^{J_{12}} |c\rangle \}^{\mathcal{J} \mathcal{M}}$ . Since the isospin projection quantum numbers obey  $m_T = \mathcal{M}_T$ , the collective summation index simplifies to  $\alpha = \{n_{12}, l_{12}, s_{ab}, j_{12}, n_3, l_3, I_3, J, t_{ab}, T\}$ .

The overlap  $T$  is derived by expanding the state  $\{ \{ |a\rangle |b\rangle \}^{J_{12}} |c\rangle \}^{\mathcal{J} \mathcal{M}}$  in terms of  $\{ |n_{cm} l_{cm}\rangle |\alpha\rangle \}^{\mathcal{J} \mathcal{M}}$ . In a first step we change the coupling scheme of particle 1 and 2 from  $j$ - to  $ls$ -coupling

$$|[(l_a s_a)j_a (l_b s_b)j_b] J_{12}\rangle \rightarrow |[(l_a l_b) L_{12} (s_a s_b) s_{ab}] J_{12}\rangle, \quad (5.75)$$

with the orbital angular momentum  $L_{12}$  and the spin  $s_{ab}$ , by employing a  $9j$ -symbol

$$|[(l_a s_a)j_a (l_b s_b)j_b] J_{12}\rangle = \sum_{L_{12}, s_{ab}} \hat{j}_a \hat{j}_b \hat{L}_{12} \hat{s}_{ab} \begin{Bmatrix} l_a & s_a & j_a \\ l_b & s_b & j_b \\ L_{12} & s_{ab} & J_{12} \end{Bmatrix} |[(l_a l_b) L_{12} (s_a s_b) s_{ab}] J_{12}\rangle. \quad (5.76)$$

Thus, in the second step we can now perform the first Talmi transformation [127] from the single-particle coordinates  $\mathbf{r}_1, \mathbf{r}_2$  to the relative Jacobi coordinate  $\mathbf{x}$  and the center-of-mass coordinate  $\mathbf{cm}_x$  of particles 1 and 2 (cf. Eq. (5.19))

$$|[(l_a s_a)j_a (l_b s_b)j_b] L_{12}\rangle = \sum_{\mathcal{N}_{12}, \mathcal{L}_{12}, n_{12}, l_{12}} \langle \mathcal{N}_{12} \mathcal{L}_{12}, n_{12} l_{12}; L_{12} | n_a l_a, n_b l_b \rangle_{d=1} |[\mathcal{N}_{12} \mathcal{L}_{12}(\mathbf{cm}_x) n_{12} l_{12}(\mathbf{x})] L_{12}\rangle. \quad (5.77)$$

In preparation for the second Talmi transformation our third step is to decouple the  $j$ -coupling of the third nucleon and couple the orbital angular momenta  $L_{12}, l_c$  to  $\mathcal{L}$  and spins  $s_{ab}, s_c$  to  $S_3$ , so that

$$|[(L_{12}s_{ab})J_{12}(l_c s_c)j_c]\mathcal{J}\rangle \rightarrow |[(L_{12}l_c)\mathcal{L}(s_{ab}s_c)S_3]\mathcal{J}\rangle, \quad (5.78)$$

by employing a  $9j$ -symbol

$$|[(L_{12}s_{ab})J_{12}(l_c s_c)j_c]\mathcal{J}\rangle = \sum_{\mathcal{L}, S_3} \hat{J}_{12} \hat{j}_c \hat{\mathcal{L}} \hat{S}_3 \left\{ \begin{array}{ccc} L_{12} & s_{ab} & J_{12} \\ l_c & s_c & j_c \\ \mathcal{L} & S_3 & \mathcal{J} \end{array} \right\} |[(L_{12}l_c)\mathcal{L}(s_{ab}s_c)S_3]\mathcal{J}\rangle. \quad (5.79)$$

Before performing the second Talmi transformation, which relates the center-of-mass coordinate  $\mathbf{cm}_x$  of particles 1 and 2, Eq. (5.17), and the single-particle coordinate of the third nucleon  $\mathbf{r}_3$  to the second Jacobi coordinate  $\mathbf{y}$ , Eq. (5.59), and the total center-of-mass coordinate of the three-particle system

$$\mathbf{cm} = \sqrt{\frac{1}{3}}(\mathbf{r}_1 + \mathbf{r}_2 + \mathbf{r}_3), \quad (5.80)$$

also shown in Fig. 5.1, we perform the fourth step and couple the orbital angular momenta  $\mathcal{L}_{12}, l_c$  to  $\Lambda$  and, successively,  $\Lambda$  with the orbital angular momentum  $l_{12}$  of the relative motion of particles 1 and 2 to the total angular momentum  $\mathcal{L}$  as

$$|[(\mathcal{L}_{12}l_{12})L_{12}l_c]\mathcal{L}\rangle \rightarrow |[(\mathcal{L}_{12}l_c)\Lambda l_{12}]\mathcal{L}\rangle. \quad (5.81)$$

This reordering in the coupling of three angular momenta is obtained by a  $6j$ -symbol

$$\begin{aligned} |[(\mathcal{L}_{12}l_{12})L_{12}l_c]\mathcal{L}\rangle &= \sum_{\Lambda} \langle [(\mathcal{L}_{12}l_c)\Lambda l_{12}]\mathcal{L} | [(\mathcal{L}_{12}l_{12})L_{12}l_c]\mathcal{L} \rangle |[(\mathcal{L}_{12}l_c)\Lambda l_{12}]\mathcal{L}\rangle \\ &= \sum_{\Lambda} (-1)^{l_{12}+l_c+L_{12}+\Lambda} \hat{L}_{12} \hat{\Lambda} \left\{ \begin{array}{ccc} l_{12} & \mathcal{L}_{12} & L_{12} \\ l_c & \mathcal{L} & \Lambda \end{array} \right\} |[(\mathcal{L}_{12}l_c)\Lambda l_{12}]\mathcal{L}\rangle \\ &= \sum_{\Lambda} (-1)^{l_{12}+l_c+L_{12}+\Lambda} \hat{L}_{12} \hat{\Lambda} \left\{ \begin{array}{ccc} l_c & \mathcal{L}_{12} & \Lambda \\ l_{12} & \mathcal{L} & L_{12} \end{array} \right\} |[(\mathcal{L}_{12}l_c)\Lambda l_{12}]\mathcal{L}\rangle, \end{aligned} \quad (5.82)$$

where we used the invariance of the  $6j$ -symbol under interchange of the upper and lower arguments in each of any two columns. Consequently, in step five we can perform the second Talmi transformation [127] described above, which is given by

$$\begin{pmatrix} \mathbf{cm} \\ \mathbf{y} \end{pmatrix} = \begin{pmatrix} \sqrt{\frac{d}{d+1}} & \sqrt{\frac{1}{d+1}} \\ \sqrt{\frac{1}{d+1}} & -\sqrt{\frac{d}{d+1}} \end{pmatrix} \begin{pmatrix} \mathbf{cm}_x \\ \mathbf{r}_3 \end{pmatrix}, \quad (5.83)$$

with  $d = 2$ , or in terms of the HO bracket

$$|[\mathcal{N}_{12}\mathcal{L}_{12}(\mathbf{cm}_x)n_c l_c(\mathbf{r}_3)]\Lambda\rangle = \sum_{n_{cm}, l_{cm}, n_3, l_3} \langle n_{cm} l_{cm}, n_3 l_3; \Lambda | \mathcal{N}_{12}\mathcal{L}_{12}, n_c l_c \rangle_{d=2} | [n_{cm} l_{cm}(\mathbf{cm})n_3 l_3(\mathbf{y})]\Lambda \rangle. \quad (5.84)$$

Since the total center-of-mass angular momentum  $l_{cm}$  of the three-particle system is not part of intermediate angular momentum coupling in the bra  $\{ |n_{cm} l_{cm}\rangle | \alpha \rangle \}^{\mathcal{L}, \mathcal{M}}$  step six and seven are performed to achieve this also for the ket. In step six we reorder the coupling of orbital angular momenta. The orbital angular momenta  $l_{12}, l_3$  of the Jacobi coordinates are coupled to  $L_3$  and, successively,  $L_3$  is coupled with the total center-of-mass angular momentum  $l_{cm}$  of the three-particle system to the total orbital angular momentum  $\mathcal{L}$ , according to

$$|[(l_{cm}l_3)\Lambda l_{12}]\mathcal{L}\rangle \rightarrow |[l_{cm}(l_3 l_{12})L_3]\mathcal{L}\rangle. \quad (5.85)$$

Here, we employ again a  $6j$ -symbol

$$\begin{aligned} |[(l_{cm}l_3)\Lambda l_{12}]\mathcal{L}\rangle &= \sum_{L_3} \langle [l_{cm}(l_3 l_{12})L_3]\mathcal{L} | [(l_{cm}l_3)\Lambda l_{12}]\mathcal{L} \rangle |[l_{cm}(l_3 l_{12})L_3]\mathcal{L}\rangle \\ &= \sum_{L_3} (-1)^{l_{cm}+l_3+l_{12}+\mathcal{L}} \hat{L}_3 \hat{\Lambda} \left\{ \begin{array}{ccc} l_{cm} & l_3 & \Lambda \\ l_{12} & \mathcal{L} & L_3 \end{array} \right\} |[l_{cm}(l_3 l_{12})L_3]\mathcal{L}\rangle. \end{aligned} \quad (5.86)$$

In addition, we change the order of angular momentum coupling from  $(l_3 l_{12})L_3$  to  $(l_{12} l_3)L_3$  introducing a phase  $(-1)^{l_3+l_{12}-L_3}$  arising from the exchange of two columns in the Clebsch-Gordan coefficient. We proceed with step seven in which we separate the total center-of-mass angular momentum  $l_{cm}$  from the total relative orbital angular momentum  $L_3$  and couple  $L_3$  with the total spin  $S_3$  to the total relative angular momentum  $J$ . The total relative angular momentum is adjoined by the total center-of-mass angular momentum  $l_{cm}$  so that

$$|[(l_{cm}L_3)\mathcal{L}S_3]J\rangle \rightarrow |[l_{cm}(L_3S_3)J]J\rangle. \quad (5.87)$$

This recoupling is achieved by application of a  $6j$ -symbol

$$\begin{aligned} |[l_{cm}L_3)\mathcal{L}S_3]J\rangle &= \sum_J \langle [l_{cm}(L_3S_3)J]J | [l_{cm}L_3)\mathcal{L}S_3]J \rangle |[l_{cm}(L_3S_3)J]J\rangle \\ &= \sum_J (-1)^{l_{cm}+L_3+S_3+J} \mathcal{L} \hat{J} \begin{Bmatrix} l_{cm} & L_3 & \mathcal{L} \\ S_3 & J & J \end{Bmatrix} |[l_{cm}(L_3S_3)J]J\rangle. \end{aligned} \quad (5.88)$$

In step eight we change the coupling scheme from  $ls$ - to  $j$ -coupling and thereby introduce the relative angular momenta  $j_{12}$  and  $I_3$

$$|[(l_{12}l_3)L_3(s_{ab}s_c)S_3]J\rangle \rightarrow |[(l_{12}s_{ab})j_{12}(l_3s_c)I_3]J\rangle. \quad (5.89)$$

This is achieved by using a  $9j$ -symbol

$$|[(l_{12}l_3)L_3(s_{ab}s_c)S_3]J\rangle = \sum_{j_{12}, I_3} \hat{L}_3 \hat{S}_3 \hat{J}_{12} \hat{I}_3 \begin{Bmatrix} l_{12} & l_3 & L_3 \\ s_{ab} & s_c & S_3 \\ j_{12} & I_3 & J \end{Bmatrix} |[(l_{12}s_{ab})j_{12}(l_3s_c)I_3]J\rangle. \quad (5.90)$$

Collecting all terms leads to

$$\begin{aligned} \{ \{ |a\rangle |b\rangle \}^{J_{12}} |c\rangle \}^{\mathcal{J}\mathcal{M}} &= \sum_{L_{12}, s_{ab}} \sum_{\substack{\mathcal{N}_{12}, \mathcal{L}_{12} \\ n_{12}, l_{12}}} \sum_{\mathcal{L}, S_3} \sum_{\Lambda} \sum_{\substack{n_{cm}, l_{cm} \\ n_3, l_3}} \sum_{L_3} \sum_J \sum_{j_{12}, I_3} \\ &\times \hat{J}_a \hat{J}_b \hat{L}_{12} \hat{S}_{ab} \begin{Bmatrix} l_a & s_a & j_a \\ l_b & s_b & j_b \\ L_{12} & s_{ab} & J_{12} \end{Bmatrix} \\ &\times \langle \mathcal{N}_{12} \mathcal{L}_{12}, n_{12} l_{12}; L_{12} | n_a l_a, n_b l_b \rangle_{d=1} \\ &\times \hat{J}_{12} \hat{J}_c \mathcal{L} \hat{S}_3 \begin{Bmatrix} L_{12} & s_{ab} & J_{12} \\ l_c & s_c & j_c \\ \mathcal{L} & S_3 & J \end{Bmatrix} \\ &\times (-1)^{l_{12}+l_c+L_{12}+\Lambda} \hat{L}_{12} \hat{\Lambda} \begin{Bmatrix} l_c & \mathcal{L}_{12} & \Lambda \\ l_{12} & \mathcal{L} & L_{12} \end{Bmatrix} \\ &\times \langle n_{cm} l_{cm}, n_3 l_3; \Lambda | \mathcal{N}_{12} \mathcal{L}_{12}, n_c l_c \rangle_{d=2} \\ &\times (-1)^{l_{cm}+l_3+l_{12}+\mathcal{L}} \hat{\Lambda} \hat{L}_3 \begin{Bmatrix} l_{cm} & l_3 & \Lambda \\ l_{12} & \mathcal{L} & L_3 \end{Bmatrix} (-1)^{l_3+l_{12}-L_3} \\ &\times (-1)^{l_{cm}+L_3+S_3+J} \mathcal{L} \hat{J} \begin{Bmatrix} l_{cm} & L_3 & \mathcal{L} \\ S_3 & J & J \end{Bmatrix} \\ &\times \hat{L}_3 \hat{S}_3 \hat{J}_{12} \hat{I}_3 \begin{Bmatrix} l_{12} & l_3 & L_3 \\ s_{ab} & s_c & S_3 \\ j_{12} & I_3 & J \end{Bmatrix} \\ &\times \{ |n_{cm} l_{cm}\rangle |a\rangle \}^{\mathcal{J}\mathcal{M}}, \end{aligned} \quad (5.91)$$

which simplifies when multiplying with the bra  $\{ \langle n'_{cm} l'_{cm} | \alpha' \rangle \}^{\mathcal{J}\mathcal{M}}$ , recalling the quantum numbers represented by the collective index  $\alpha = \{n_{12}, l_{12}, s_{ab}, j_{12}, n_3, l_3, I_3, J, t_{ab}, T\}$ , due to the Kronecker deltas

$$\delta_{n_{cm} n'_{cm}} \delta_{l_{cm} l'_{cm}} \delta_{n_{12} n'_{12}} \delta_{l_{12} l'_{12}} \delta_{s_{ab} s'_{ab}} \delta_{j_{12} j'_{12}} \delta_{n_3 n'_3} \delta_{l_3 l'_3} \delta_{I_3 I'_3} \delta_{JJ'}. \quad (5.92)$$



Thus, the overlap  $T$ , introduced in Eq. (5.74), is given by

$$\begin{aligned}
T = & \sum_{L_{12}} \sum_{\mathcal{N}_{12}, \mathcal{L}_{12}} \sum_{\mathcal{L}, \mathcal{S}_3} \sum_{\Lambda} \sum_{L_3} \\
& \times \hat{j}_a \hat{j}_b \hat{L}_{12} \hat{S}_{ab} \begin{Bmatrix} l_a & s_a & j_a \\ l_b & s_b & j_b \\ L_{12} & s_{ab} & J_{12} \end{Bmatrix} \\
& \times \langle \mathcal{N}_{12} \mathcal{L}_{12}, n_{12} l_{12}; L_{12} | n_a l_a, n_b l_b \rangle_{d=1} \\
& \times \hat{j}_{12} \hat{j}_c \hat{\mathcal{L}} \hat{S}_3 \begin{Bmatrix} L_{12} & s_{ab} & J_{12} \\ l_c & s_c & j_c \\ \mathcal{L} & \mathcal{S}_3 & \mathcal{J} \end{Bmatrix} \\
& \times (-1)^{l_{12}+l_c+L_{12}+\Lambda} \hat{L}_{12} \hat{\Lambda} \begin{Bmatrix} l_c & \mathcal{L}_{12} & \Lambda \\ l_{12} & \mathcal{L} & L_{12} \end{Bmatrix} \\
& \times \langle n_{cm} l_{cm}, n_3 l_3; \Lambda | \mathcal{N}_{12} \mathcal{L}_{12}, n_c l_c \rangle_{d=2} \\
& \times (-1)^{l_{cm}+l_3+l_{12}+\mathcal{L}} \hat{\Lambda} \hat{L}_3 \begin{Bmatrix} l_{cm} & l_3 & \Lambda \\ l_{12} & \mathcal{L} & L_3 \end{Bmatrix} (-1)^{l_3+l_{12}-L_3} \\
& \times (-1)^{l_{cm}+L_3+S_3+\mathcal{J}} \hat{\mathcal{L}} \hat{\mathcal{J}} \begin{Bmatrix} l_{cm} & L_3 & \mathcal{L} \\ S_3 & \mathcal{J} & J \end{Bmatrix} \\
& \times \hat{L}_3 \hat{S}_3 \hat{j}_{12} \hat{I}_3 \begin{Bmatrix} l_{12} & l_3 & L_3 \\ s_{ab} & s_c & S_3 \\ j_{12} & I_3 & J \end{Bmatrix}, \tag{5.93}
\end{aligned}$$

agreeing with the result of Ref. [132] up to the  $\mathcal{N}_{12}$  summation, which may be eliminated by the energy conservation of the HO bracket  $\mathcal{N}_{12} = \frac{1}{2}(2n_a + l_a + 2n_b + l_b - 2n_{12} - l_{12} - \mathcal{L}_{12})$ .

Returning to Eq. (5.74) and decoupling the center-of-mass orbital angular momentum from the relative angular momentum leads to

$$\begin{aligned}
|abc\rangle = & \sum_{J_{12}, \mathcal{J}} \sum_{n_{cm}, l_{cm}} \sum_{\alpha} \sum_{m_{cm}, m_J} \begin{pmatrix} j_a & j_b & J_{12} \\ m_{j_a} & m_{j_b} & m_{j_a} + m_{j_b} \end{pmatrix} \begin{pmatrix} J_{12} & j_c \\ m_{j_a} + m_{j_b} & m_{j_c} \end{pmatrix} \begin{pmatrix} \mathcal{J} \\ \mathcal{M} \end{pmatrix} \\
& \times \begin{pmatrix} t_a & t_b & t_{ab} \\ m_{t_a} & m_{t_b} & m_{t_a} + m_{t_b} \end{pmatrix} \begin{pmatrix} t_{ab} & t_c \\ m_{t_a} + m_{t_b} & m_{t_c} \end{pmatrix} \begin{pmatrix} T \\ m_T \end{pmatrix} \\
& \times T \begin{pmatrix} l_{cm} & J \\ m_{cm} & m_J \end{pmatrix} \begin{pmatrix} \mathcal{J} \\ \mathcal{M} \end{pmatrix} |n_{cm} l_{cm} m_{cm}\rangle |am_J\rangle. \tag{5.94}
\end{aligned}$$

Considering the properties of a general three-body interaction

$$\begin{aligned}
\langle n_{cm} l_{cm} m_{cm}; \alpha m_J | V^{(3)} | n'_{cm} l'_{cm} m'_{cm}; \alpha' m_{J'} \rangle = & \delta_{n_{cm} n'_{cm}} \delta_{l_{cm} l'_{cm}} \delta_{m_{cm} m'_{cm}} \delta_{J J'} \delta_{m_J m_{J'}} \\
& \times \langle n_{cm} l_{cm} m_{cm}; \alpha m_J | V^{(3)} | n_{cm} l_{cm} m_{cm}; \alpha' m_J \rangle, \tag{5.95}
\end{aligned}$$

i.e., that in addition to the total isospin quantum numbers also the center-of-mass and the relative angular momentum quantum numbers are not affected by the interaction. Thus, we can already eliminate the Clebsch-Gordan coefficients

$$\sum_{m_{cm}, m_J} \begin{pmatrix} l_{cm} & J \\ m_{cm} & m_J \end{pmatrix} \begin{pmatrix} \mathcal{J} \\ \mathcal{M} \end{pmatrix} \begin{pmatrix} l_{cm} & J \\ m_{cm} & m_J \end{pmatrix} \begin{pmatrix} \mathcal{J} \\ \mathcal{M} \end{pmatrix} = \delta_{\mathcal{J} \mathcal{J}} \delta_{\mathcal{M} \mathcal{M}}, \tag{5.96}$$

and the transformation to  $\mathcal{J}T$ -coupled matrix elements is given by

$$\begin{aligned}
\langle [(ab)J_{12} t_{abc}] \mathcal{J} T | V^{(3)} | [(a'b')J'_{12} t'_{ab} c'] \mathcal{J} T \rangle = & \sum_{J_{12}, J'_{12}, \mathcal{J}} \sum_{n_{cm}, l_{cm}} \sum_{\alpha, \alpha'} \\
& \times \{ \langle a | \langle b \rangle \}^{J_{12}} \langle c \rangle^{\mathcal{J}} \{ |n_{cm} l_{cm}\rangle | \alpha \rangle \}^{\mathcal{J}} \\
& \times \langle \alpha | V^{(3)} | \alpha' \rangle \\
& \times \{ \langle n_{cm} l_{cm} | \alpha' \rangle \}^{\mathcal{J}} \{ \{ |a'\rangle | b' \rangle \}^{J'_{12}} | c' \rangle \}^{\mathcal{J}}, \tag{5.97}
\end{aligned}$$

where we use 3N matrix elements  $\langle \alpha | V^{(3)} | \alpha' \rangle$  that have been transformed back after the antisymmetrization and the collective indices refer to

$$\begin{aligned}\alpha &= \{n_{12}, l_{12}, s_{ab}, j_{12}, n_3, l_3, I_3, J, t_{ab}, T\} \\ \alpha' &= \{n'_{12}, l'_{12}, s'_{ab}, j'_{12}, n'_3, l'_3, I'_3, t'_{ab}\}.\end{aligned}\tag{5.98}$$

The transformation of 3N matrix elements is computationally very demanding, but optimized caching of the relevant intermediates and the use of Basic Linear Algebra Subprograms (BLAS) for the matrix multiplications allows us to generate 3N matrix elements in 15 major oscillator shells ( $e_{\text{Max}} = 14$ ) and  $e_1 + e_2 + e_3 \leq E_{3\text{Max}} = 18 < 3e_{\text{Max}}$  at moderate computational cost.

## 6 Many-body approaches

In the following section we briefly introduce the many-body methods used throughout this work. Before going into there, we want to give an overview of the different approaches to solve the non-relativistic nuclear many-body problem. The Green's function Monte Carlo approach [7–9], using phenomenological NN+3N interactions and, more recently, also local chiral EFT interactions [133, 134], as well as configuration-interaction (CI) approaches, e.g., the no-core shell model (NCSM) [10], are able to perform quasi-exact calculations of up to  $p$ -shell nuclei. Large-scale NCSM diagonalizations, starting from the initial or a free-space RG evolved Hamiltonian, in a finite model space are, however, limited due to the curse of dimensionality, i.e., the exponential growth of the Slater-determinant basis dimension when enlarging the model space. This limitation can be overcome by importance truncation (IT) [11], allowing to select the many-body basis states according to their importance for the calculation at hand. Thus, also lower  $sd$ -shell isotopic chains like the oxygen isotopes are accessible [135]. Moreover, the advent of chiral EFT interactions and RG transformations, have enabled the development of new many-body methods and the revival of old ones. The increase in reach of ab initio calculations into the medium-mass regime, comparing

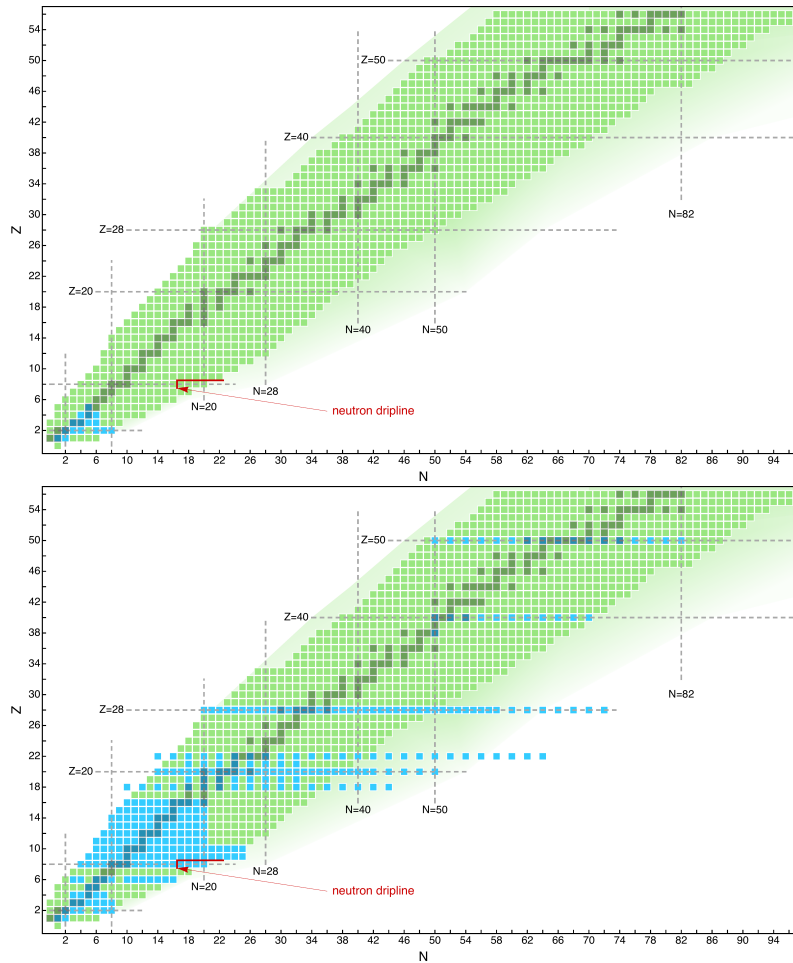


**Figure 6.1:** The chart of nuclides and the reach of ab initio calculations in 2005 (top) and 2015 (bottom). For nuclei marked blue there exist ab initio calculations. Note that the figure is just an illustration and is not intended to be exhaustive. Taken from Ref. [14].

the status in 2005 (top) and 2015 (bottom) in Fig. 6.1, can be attributed to methods for which the numerical cost of solving the nuclear many-body problem scales polynomially in the number of nucleons  $A$ . Those methods are coupled-cluster (CC) theory [13], the In-Medium Similarity Renormalization Group (IM-SRG) [14] and self-consistent Green's function (SCGF) theory [15]. Another approach is nuclear lattice EFT [16], for which the many-body problem of nucleons is solved on a Euclidean space-time lattice. Similar to GFMC and lattice QCD, the energies of the ground and excited states are obtained by propagating the system in imaginary time. Of course all approaches have benefited from ever-increasing computer performance.

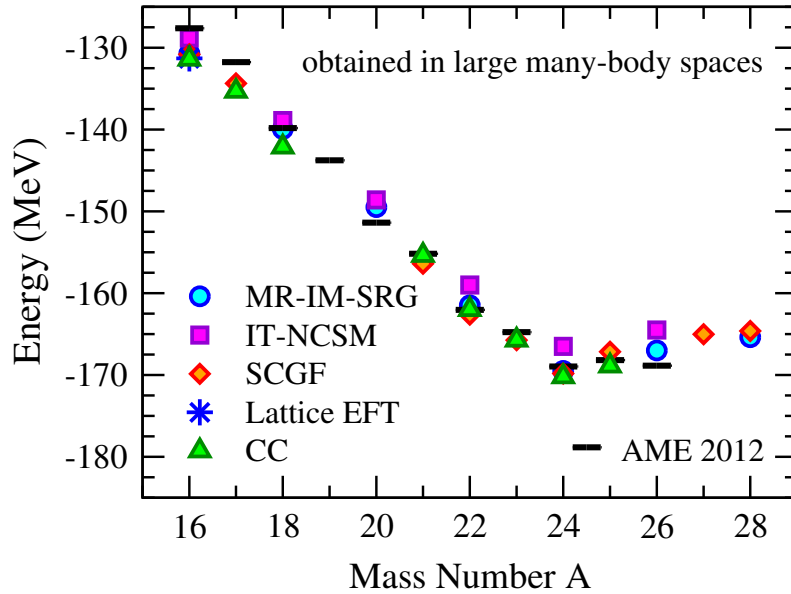


**Figure 6.2:** Ground-state energies of oxygen isotopes obtained in large many-body spaces by the MR-IM-SRG [135], IT-NCSM [135], SCGF [136], CC [137], based on the SRG-evolved NN+3N-full Hamiltonian, and nuclear Lattice EFT [138], based on NN+3N forces at  $N^2$ LO. Taken from [139].

An example that highlights the progress in ab initio nuclear-structure calculations is given in Fig. 6.2, summarizing the results for the ground-state energies of oxygen isotopes obtained in large many-body spaces by the multi-reference IM-SRG (MR-IM-SRG(2)) [135], IT-NCSM [135], SCGF (Dyson ADC(3)) [136], CC ( $\Lambda$ -CCSD(T)) [137], based on the same SRG-evolved NN+3N-full Hamiltonian, and nuclear Lattice EFT [138], based on NN+3N forces at  $N^2$ LO. The results from methods that solve the Schrödinger equation of the  $A$ -body system in an approximate, but systematically improvable, way agree with IT-NCSM diagonalizations within a few percent, when starting from the same Hamiltonian. Clearly, these CC, IM-SRG and SCGF results are obtained at different level of truncation of the many-body expansion and while IT-NCSM results include full 3N matrix elements the other three methods include them in a normal-ordered approximation. Moreover, because of the large number of 3N matrix elements all calculations have to introduce an energy cut on them. Nevertheless, the sum of uncertainties associated with these truncations is on a few percent level, suggesting that the truncations are well controlled. We conclude this discussion by referring to Tab. 6.1, which summarizes the different ab initio many-body approaches and their current, most sophisticated formulations for the calculation of ground and excited states of closed- and open-shell nuclei in the medium-mass regime ( $A > 20$ ). We also specify their ability to derive valence-space interactions, since this is a focus of this thesis.

Since all many-body approaches used throughout this work include normal ordered 3N forces we will give a brief introduction to normal ordering in Sec. 6.1. In Sec. 6.2 we summarize the basic principles of many-body perturbation theory to obtain valence-space interactions. For a long time this approach started only from NN forces, and the agreement to experiment was restored by fitting single-particle energies and monopole matrix elements or single-particle energies and all two-body matrix elements to data. However, the normal-ordering technique enabled the inclusion of normal-ordered 3N forces in the derivation of valence-space interactions. Although the resulting interactions described experimental results well, the restriction to low order in the many-body expansion is hard to overcome due to the increasing number of diagrams arising at higher orders.

An ab initio method used in this work is the IM-SRG, presented in Sec. 6.4. It was developed in the last decade [140] and combines the flow-equation formalism, also used in the free-space SRG, with the normal-ordering technique for solving the many-body Schrödinger equation. In addition, we use CC theory, which, originally developed in nuclear physics but mostly applied in quantum chemistry in the meantime, experienced a revival, which started more than a decade ago. Details on CC theory are given in Sec. 6.5. Since both approaches build correlations between nucleons on top of a reference state, e.g., a Hartree-Fock Slater determinant for closed-shell nuclei, we briefly review the Hartree-Fock method in Sec. 6.3. While both ab initio approaches were first applied to ground states of closed-shell nuclei, their reach has been extended by equation-of-motion (EOM) techniques to excited states of closed-shell nuclei and even further to ground and excited states of open-shell nuclei. In addition, they are

also capable to derive valence-space interactions non-perturbatively. For details we refer to Tab. 6.1 and the given references.

## 6.1 Normal ordering

The starting point of nuclear-structure calculations is the intrinsic nuclear  $A$ -body Hamiltonian containing, in principle, NN, 3N and higher-body interactions,

$$H = \left(1 - \frac{1}{A}\right) T^{(1)} + T^{(2)} + V^{(2)} + V^{(3)} + \dots, \quad (6.1)$$

with the  $A$ -body intrinsic kinetic energy  $T_{\text{int}}$  separated into a one- and two-body contribution

$$T^{(1)} \equiv \sum_i \frac{\mathbf{p}_i^2}{2m}, \quad T^{(2)} \equiv - \sum_{i < j} \frac{\mathbf{p}_i \cdot \mathbf{p}_j}{Am}. \quad (6.2)$$

While the formal inclusion of many-body forces is straightforward in some many-body approaches, e.g., the no-core shell model [152], the extension of others is a non-trivial task, e.g., coupled-cluster theory with explicit 3N interactions [20–22]. Even if the extension of the formalism is easy, the computational cost usually increases by orders of magnitude due to the explicit inclusion of 3N forces. Thus, calculations, especially of heavier nuclei, that are routinely done at the NN level, may be rendered unfeasible. This motivated the development of approximation schemes to include 3N interactions. In the following we will discuss the basic principles of normal ordering, that allows to include contributions of an operator of a given particle rank in lower-particle rank operators. Hence, a many-body method that includes NN forces can include up to two-body contributions of 3N or higher-body forces without additional cost. There is, however, no *a priori* quantification of the amount of information transferred to lower-particle ranks, making benchmarks against calculations including the full 3N interaction explicitly indispensable.

The calculation of the structure of an atomic nucleus of mass  $A$  is done in  $A$ -body Hilbert space, employing a suitable  $A$ -body basis. Since the nucleus is composed of fermions, a natural choice are Slater determinants, i.e., antisymmetrized product states of single-particle wave functions. Starting from the fermionic creation and annihilation operators  $a_i^\dagger$  and  $a_j$ , which satisfy the canonical anticommutation relations

$$\{a_i^\dagger, a_j^\dagger\} = \{a_i, a_j\} = 0, \quad \{a_i^\dagger, a_j\} = \delta_{ij}, \quad (6.3)$$

a generic  $A$ -particle Slater determinant can be constructed as

$$|\Phi_0\rangle = |\varphi_1\rangle \otimes \dots \otimes |\varphi_A\rangle \quad (6.4)$$

$$= \prod_{i=1}^A a_i^\dagger |0\rangle, \quad (6.5)$$

with the particle vacuum  $|0\rangle$ , obeying  $a_j |0\rangle = 0$ . We use here Hartree-Fock single-particle wave functions  $|\varphi_k\rangle$ , obeying  $|\varphi_k\rangle = a_k^\dagger |0\rangle$  with the corresponding fermionic creation operator  $a_k^\dagger$ . For details on the relation between Hartree-Fock and harmonic oscillator single-particle wave functions we refer to Sec. 6.3.

Normal ordering with respect to a reference state  $|\Phi_0\rangle$  is a standard tool in quantum many-body and field theory. An appropriate reference state for the ground state of a closed-shell nucleus is, e.g., the unperturbed harmonic-oscillator Slater determinant [20, 152, 153] or the ground state of a Hartree-Fock [21, 154] calculation. In this work we will focus on single-reference normal ordering, while the generalization to multi-reference states is employed in the calculation of ground [135] and excited states [155] of open-shell nuclei. Since it is very tedious to include the set of creation operators to generate  $|\Phi_0\rangle$  from the particle vacuum  $|0\rangle$ , cf. Eq. (6.5), we define the normal ordering relative to the reference state  $|\Phi_0\rangle$ , called Fermi vacuum. We therefore define quasiparticle operators that create or destroy holes and particles, where holes (particles) are occupied (unoccupied) single-particle states in the reference state. Hole and particle annihilators acting on the reference state result in

$$a_i^\dagger |\Phi_0\rangle = 0, \quad (6.6)$$

$$a_a |\Phi_0\rangle = 0, \quad (6.7)$$

**Table 6.1:** Ab initio many-body approaches and their current, most sophisticated formulations for ground and excited states of closed- and open-shell nuclei in the medium-mass regime ( $A > 20$ ) as well as their ability to derive valence-space interactions.

method	closed-shell nuclei		open-shell nuclei		valence-space interactions
	ground states	excited states	ground states	excited states	
Coupled cluster	$\Lambda$ -CCSD(T)/CR-CC(2,3) based on HF ref. state [141]	Equation of Motion CCSD	particle attached/particle removed EOM-CCSD $A \pm 1, +2$ [142] <sup>a</sup> Bogoliubov CCD	-	effective interaction based on CC [137]
In-medium SRG	IM-SRG(2) [140]/Magnus(2) [143] based on HF ref. state	Equation of Motion IMSRG(2,2) [144]	multi-ref. IM-SRG(2) based on PNP HFB ref. state [135] <sup>b</sup> multi-ref. IM-SRG(2) based on NCSM $N_{\max}^{\text{ref}} = 0$ ref. state [146] <sup>b</sup>	-	effective interaction based on ensemble normal ordering [145]
Self-consistent Green's function	Dyson ADC(3) [136] based on HF ref. state	$A \pm 1$	Gorkov ADC(2) [147] based on HFB ref. state	$A \pm 1$	-
Many-body perturbation theory	HF MBPT(3) [148]	-	multi-configurational PT(2) based on NCSM $N_{\max}^{\text{ref}} = 0, 2, 4$ ref. state [149]	-	-
Nuclear lattice EFT	[150]	-	[151] <sup>b</sup>	-	-

<sup>a</sup> mass number  $A$  is restricted to closed sub-shell nuclei

<sup>b</sup> even-even nuclei only

where the quantum number of hole states are given by  $i, j, k, \dots$ , the quantum numbers of particle states are given by  $a, b, c, \dots$ , and those of generic states by  $p, q, r, \dots$ . A string of quasiparticle operators is in normal order relative to the Fermi vacuum, if all quasiparticle-annihilation operators are standing to the right of all quasiparticle-creation operators. However, standard operator expressions in second quantization, e.g., for a 3N force

$$V^{(3)} = \frac{1}{36} \sum_{p,q,r,s,t,u} \langle pqr | V^{(3)} | stu \rangle a_p^\dagger a_q^\dagger a_r^\dagger a_u a_t a_s, \quad (6.8)$$

with  $\langle pqr | V^{(3)} | stu \rangle$  assumed to be fully antisymmetrized, are generically in normal order with respect to the particle vacuum  $|0\rangle$ . Rewriting a generic string of creation or annihilation operators  $ABCDE \dots$  in normal order with respect to a reference state  $|\Phi_0\rangle$  is accomplished by Wick's theorem [156]

$$\begin{aligned} ABCDE \dots &= :ABCDE \dots :_{|\Phi_0\rangle} + \sum_{\text{single contractions}} \overline{ABCDE \dots} :_{|\Phi_0\rangle} \\ &+ \sum_{\text{double contractions}} \overline{\overline{ABCDE \dots}} :_{|\Phi_0\rangle} \\ &+ \dots \\ &+ \sum_{\text{full contractions}} \overline{\overline{\overline{ABCDE \dots}}} :_{|\Phi_0\rangle}, \end{aligned} \quad (6.9)$$

where  $:ABCDE \dots :_{|\Phi_0\rangle}$  represents the string in normal order with respect to the reference state  $|\Phi_0\rangle$ , which vanishes when taking the reference state expectation value, i.e.,

$$\langle \Phi_0 | :ABCDE \dots :_{|\Phi_0\rangle} | \Phi_0 \rangle = 0. \quad (6.10)$$

The normal-ordered product is given by

$$:ABC \dots :_{|\Phi_0\rangle} = \text{sgn}(\mathcal{P}) HAB \dots, \quad (6.11)$$

with the sign of the permutations  $\mathcal{P}$  needed for re-ordering the operator  $H$  within the operator string. In this work, normal-ordered operators are indicated by  $: \dots :$ , while in the literature other notations, e.g.,  $\mathcal{N}[\dots]$  or  $\{\dots\}$ , are also common. Note that the index, indicating the reference state used to calculate the normal-ordered product, is often omitted for brevity, but the particular reference state is specified in some other way. Furthermore, in the second term of Eq. (6.9) we introduced a contraction, denoted by the bracket connecting two-involved operators, which can be rewritten by

$$:AB \dots \overline{H \dots K} :_{|\Phi_0\rangle} = \text{sgn}(\mathcal{P}) \overline{HK} :AB \dots :_{|\Phi_0\rangle}. \quad (6.12)$$

The sums in Eq. (6.9) run over all possible single, double,  $\dots$ , full contractions within the given string of operators, with the displayed contractions intended as examples.

The evaluation of products of two normal-ordered strings of operators is accomplished by the generalized Wick's theorem

$$\begin{aligned} :ABC \dots :_{|\Phi_0\rangle} :XYZ \dots :_{|\Phi_0\rangle} &= :ABC \dots XYZ \dots :_{|\Phi_0\rangle} + \sum_{\text{single contractions}} \overline{ABC \dots XYZ \dots} :_{|\Phi_0\rangle} \\ &+ \sum_{\text{double contractions}} \overline{\overline{ABC \dots XYZ \dots}} :_{|\Phi_0\rangle} \\ &+ \sum_{\text{triple contractions}} \overline{\overline{\overline{ABC \dots XYZ \dots}}} :_{|\Phi_0\rangle} \\ &+ \dots, \end{aligned} \quad (6.13)$$

where contractions are only evaluated between normal-ordered strings and not within them. The generalized Wick's theorem will be employed in the evaluation of commutators of normal-ordered operators in Sec. 6.4.1.

Wick's theorem, Eq. (6.9), simplifies for the special case of two operators to

$$:\overline{AB}:_{|\Phi_0\rangle} = AB - :AB:_{|\Phi_0\rangle}. \quad (6.14)$$

Inserting the quasiparticle operators into Eq. (6.14) leads only to two non-zero contractions

$$:\overline{a_i^\dagger a_j}:_{|\Phi_0\rangle} = a_i^\dagger a_j - :a_i^\dagger a_j:_{|\Phi_0\rangle} = a_i^\dagger a_j + a_j a_i^\dagger = \delta_{ij}, \quad (6.15)$$

$$:\overline{a_a a_b^\dagger}:_{|\Phi_0\rangle} = a_a a_b^\dagger - :a_a a_b^\dagger:_{|\Phi_0\rangle} = a_a a_b^\dagger + a_b^\dagger a_a = \delta_{ab}, \quad (6.16)$$

$$:\overline{a_i a_j^\dagger}:_{|\Phi_0\rangle} = 0, \quad (6.17)$$

$$:\overline{a_a^\dagger a_b}:_{|\Phi_0\rangle} = 0, \quad (6.18)$$

while other combinations, involving mixed hole and particle indices, are zero due to the Kronecker delta. The 3N interaction in Eq. (6.8), using generic states  $p, q, r, \dots$ , can be rewritten with Wick's theorem to

$$V^{(3)} = \frac{1}{36} \sum_{p,q,r,s,t,u} \langle pqr | V^{(3)} | stu \rangle :a_p^\dagger a_q^\dagger a_r^\dagger a_u a_t a_s:_{|\Phi_0\rangle} \quad (6.19)$$

$$+ \frac{1}{36} \sum_{p,q,r,s,t,u} \langle pqr | V^{(3)} | stu \rangle \sum_{\text{single contractions}} :a_p^\dagger a_q^\dagger a_r^\dagger a_u a_t a_s:_{|\Phi_0\rangle} \quad (6.20)$$

$$+ \frac{1}{36} \sum_{p,q,r,s,t,u} \langle pqr | V^{(3)} | stu \rangle \sum_{\text{double contractions}} :a_p^\dagger a_q^\dagger a_r^\dagger a_u a_t a_s:_{|\Phi_0\rangle} \quad (6.21)$$

$$+ \frac{1}{36} \sum_{p,q,r,s,t,u} \langle pqr | V^{(3)} | stu \rangle \sum_{\text{triple contractions}} :a_p^\dagger a_q^\dagger a_r^\dagger a_u a_t a_s:_{|\Phi_0\rangle}. \quad (6.22)$$

Evaluating all possible contractions with Eqs. (6.15)–(6.18) leads to

$$V^{(3)} = \frac{1}{36} \sum_{p,q,r,s,t,u} \langle pqr | V^{(3)} | stu \rangle :a_p^\dagger a_q^\dagger a_r^\dagger a_u a_t a_s:_{|\Phi_0\rangle} \quad (6.23)$$

$$+ \frac{1}{4} \sum_{i,p,q,s,t} \langle pqi | V^{(3)} | sti \rangle :a_p^\dagger a_q^\dagger a_t a_s:_{|\Phi_0\rangle} \quad (6.24)$$

$$+ \frac{1}{2} \sum_{i,j,p,s} \langle pij | V^{(3)} | sij \rangle :a_p^\dagger a_s:_{|\Phi_0\rangle} \quad (6.25)$$

$$+ \frac{1}{6} \sum_{i,j,k} \langle ijk | V^{(3)} | ijk \rangle \quad (6.26)$$

$$= V_{3B}^{(3)} + V_{2B}^{(3)} + V_{1B}^{(3)} + V_{0B}^{(3)}, \quad (6.27)$$

with the two-body (2B) operator arising from terms with a single contraction and the one (zero)-body operator from doubly (triply) contracted contributions. It is important to notice that, while the sum in the residual three-body (3B) operator is still running over generic indices, part of the summations for lower particle ranks run over hole states only. This provides a significant simplification since the number of hole states is small compared to the number of particle states, reducing the number of required 3N matrix elements.

We have accomplished an operator identity of the 3N interaction in vacuum normal order, Eq. (6.8), and a sum of operators normal ordered with respect to a reference state  $|\Phi_0\rangle$ , Eq. (6.27). Thus, the information solely included in a three-body operator has been transferred to lower particle ranks by normal ordering with respect to a reference state that encodes information on the closed-shell nucleus of interest. Since we are seeking for an approximation scheme to include 3N interactions in many-body approaches, without extending the formalism to the three-body level, the first term in Eq. (6.27) is discarded, defining the so-called normal-ordered two-body (NO2B) approximation

$$V_{\text{NO2B}}^{(3)} \approx V_{0B}^{(3)} + V_{1B}^{(3)} + V_{2B}^{(3)}. \quad (6.28)$$



To include this operator in many-body calculations, e.g., in NCSM calculations, it is transformed back to vacuum normal order by reverse application of Wick's theorem to  $:a_p^\dagger a_q^\dagger a_t a_s:_{|\Phi_0\rangle}$  and  $:a_p^\dagger a_s:_{|\Phi_0\rangle}$  leading to

$$:a_p^\dagger a_q^\dagger a_t a_s:_{|\Phi_0\rangle} = a_p^\dagger a_q^\dagger a_t a_s - \overline{a_p^\dagger a_q^\dagger a_t a_s:_{|\Phi_0\rangle}} - \overline{a_p^\dagger a_q^\dagger a_t a_s:_{|\Phi_0\rangle}} \quad (6.29)$$

$$\begin{aligned} & - :a_p^\dagger a_q^\dagger a_t a_s:_{|\Phi_0\rangle} - :a_p^\dagger a_q^\dagger a_t a_s:_{|\Phi_0\rangle} - \overline{a_p^\dagger a_q^\dagger a_t a_s:_{|\Phi_0\rangle}} - \overline{a_p^\dagger a_q^\dagger a_t a_s:_{|\Phi_0\rangle}} \\ & = a_p^\dagger a_q^\dagger a_t a_s + \overline{a_p^\dagger a_t} :a_q^\dagger a_s:_{|\Phi_0\rangle} - \overline{a_p^\dagger a_s} :a_q^\dagger a_t:_{|\Phi_0\rangle} \end{aligned} \quad (6.30)$$

$$\begin{aligned} & - \overline{a_q^\dagger a_t} :a_p^\dagger a_s:_{|\Phi_0\rangle} + \overline{a_q^\dagger a_s} :a_p^\dagger a_t:_{|\Phi_0\rangle} + \overline{a_p^\dagger a_t a_q^\dagger a_s} - \overline{a_p^\dagger a_s a_q^\dagger a_t} \\ & = a_p^\dagger a_q^\dagger a_t a_s + \overline{a_p^\dagger a_t} \left( a_q^\dagger a_s - \overline{a_q^\dagger a_s} \right) - \overline{a_p^\dagger a_s} \left( a_q^\dagger a_t - \overline{a_q^\dagger a_t} \right) \end{aligned} \quad (6.31)$$

$$\begin{aligned} & - \overline{a_q^\dagger a_t} \left( a_p^\dagger a_s - \overline{a_p^\dagger a_s} \right) + \overline{a_q^\dagger a_s} \left( a_p^\dagger a_t - \overline{a_p^\dagger a_t} \right) + \overline{a_p^\dagger a_t a_q^\dagger a_s} - \overline{a_p^\dagger a_s a_q^\dagger a_t} \\ & = a_p^\dagger a_q^\dagger a_t a_s + \overline{a_p^\dagger a_t a_q^\dagger a_s} - \overline{a_p^\dagger a_s a_q^\dagger a_t} - \overline{a_q^\dagger a_t a_p^\dagger a_s} + \overline{a_q^\dagger a_s a_p^\dagger a_t} + \overline{a_q^\dagger a_t a_p^\dagger a_s} - \overline{a_q^\dagger a_s a_p^\dagger a_t} \end{aligned} \quad (6.32)$$

$$:a_p^\dagger a_s:_{|\Phi_0\rangle} = a_p^\dagger a_s - \overline{a_p^\dagger a_s:_{|\Phi_0\rangle}} = a_p^\dagger a_s - \overline{a_p^\dagger a_s}. \quad (6.33)$$

Inserting Eq. (6.33) into Eq. (6.25) leads to

$$\frac{1}{2} \sum_{i,j,p,s} \langle pij | V^{(3)} | sij \rangle :a_p^\dagger a_s:_{|\Phi_0\rangle} = \frac{1}{2} \sum_{i,j,p,s} \langle pij | V^{(3)} | sij \rangle \left( a_p^\dagger a_s - \overline{a_p^\dagger a_s} \right) \quad (6.34)$$

$$= \frac{1}{2} \sum_{i,j,p,s} \langle pij | V^{(3)} | sij \rangle a_p^\dagger a_s - \frac{1}{2} \sum_{i,j,k} \langle ijk | V^{(3)} | ijk \rangle \quad (6.35)$$

and accordingly inserting Eq. (6.32) into Eq. (6.24) results in

$$\begin{aligned} \frac{1}{4} \sum_{i,p,q,s,t} \langle pqi | V^{(3)} | sti \rangle :a_p^\dagger a_q^\dagger a_t a_s:_{|\Phi_0\rangle} & = \frac{1}{4} \sum_{i,p,q,s,t} \langle pqi | V^{(3)} | sti \rangle a_p^\dagger a_q^\dagger a_t a_s \\ & + \frac{1}{4} \sum_{i,j,q,s} \langle jq i | V^{(3)} | sji \rangle a_q^\dagger a_s - \frac{1}{4} \sum_{i,j,q,t} \langle jq i | V^{(3)} | jti \rangle a_q^\dagger a_t \\ & - \frac{1}{4} \sum_{i,j,p,s} \langle pji | V^{(3)} | sji \rangle a_p^\dagger a_s + \frac{1}{4} \sum_{i,j,p,t} \langle pji | V^{(3)} | jti \rangle a_p^\dagger a_t \\ & + \frac{1}{4} \sum_{i,j,k} \langle jki | V^{(3)} | jki \rangle - \frac{1}{4} \sum_{i,j,k} \langle kji | V^{(3)} | jki \rangle \\ & = \frac{1}{4} \sum_{i,p,q,s,t} \langle pqi | V^{(3)} | sti \rangle a_p^\dagger a_q^\dagger a_t a_s - \sum_{i,j,p,s} \langle pij | V^{(3)} | sij \rangle a_p^\dagger a_s \\ & + \frac{1}{2} \sum_{i,j,k} \langle ijk | V^{(3)} | ijk \rangle. \end{aligned} \quad (6.37)$$

By combining the results for the one- and two-body part with the zero-body part from Eq. (6.26), the 3N interaction in NO2B approximation in vacuum normal order takes the form

$$V_{\text{NO2B}}^{(3)} = \frac{1}{6} \sum_{i,j,k} \langle ijk | V^{(3)} | ijk \rangle \quad (6.38)$$

$$- \frac{1}{2} \sum_{i,j,p,s} \langle pij | V^{(3)} | sij \rangle a_p^\dagger a_s \quad (6.39)$$

$$+ \frac{1}{4} \sum_{i,p,q,s,t} \langle pqi | V^{(3)} | sti \rangle a_p^\dagger a_q^\dagger a_t a_s. \quad (6.40)$$

The quality of the NO2B approximation was first investigated in coupled-cluster calculations using a harmonic oscillator Slater determinant as reference state [20].

---

## 6.2 Many-body perturbation theory for valence-space interactions

---

While many-body perturbation theory (MBPT) can be formulated to calculate ground and excited states of closed- and open-shell nuclei we employ it as a diagrammatic framework to calculate valence-space interactions. This approach has been pursued for more than five decades, see, e.g., [157–159]. Before focusing on how to calculate these interactions within the framework of time-dependent degenerate or nearly degenerate Rayleigh-Schrödinger (RS) perturbation theory in Sec. 6.2.2 we want to outline the basic idea of valence-space calculations and the concept of the effective interaction in Sec. 6.2.1. The discussion follows the reviews [160, 161].

---

### 6.2.1 Basics

---

The large-scale diagonalization of the  $A$ -body Schrödinger equation

$$H |\Psi_\alpha\rangle = E_\alpha |\Psi_\alpha\rangle, \quad (6.41)$$

using the intrinsic nuclear  $A$ -body Hamiltonian given in Eq. (6.1), to obtain the eigenstates  $|\Psi_\alpha\rangle$  and the corresponding energies  $E_\alpha$  is limited due the exponential growth of the Slater-determinant basis dimension when enlarging the model space. Thus, these no-core CI calculations, employing the initial or a free-space RG evolved Hamiltonian, are limited to  $p$ - and lower  $sd$ -shell nuclei. Valence-space methods however reduce the number of degrees of freedom by treating the nucleus as a many-body system comprised of a closed-shell core and additional nucleons occupying a truncated single-particle (valence) space. For this it is customary to rewrite the  $A$ -body Hamiltonian in terms of a one-body potential  $U$ , e.g., the harmonic oscillator potential

$$U = \sum_i \frac{1}{2} m \omega r_i^2 \quad (6.42)$$

to

$$H = T + V = (T + U) + (V - U) = H_0 + H_1, \quad (6.43)$$

where  $T$  is the kinetic energy,  $V$  includes two- and, in general, also higher-body interactions and  $H_0$  is the unperturbed Hamiltonian with eigenfunctions  $|\psi_i\rangle$  and the corresponding eigenvalues  $\epsilon_i$

$$H_0 |\psi_i\rangle = \epsilon_i |\psi_i\rangle. \quad (6.44)$$

The infinitely many degrees of freedom of the Hilbert space are reduced to the valence space by the projection operator  $P$  and its complement  $Q$ , defined as

$$P = \sum_{i=1}^d |\psi_i\rangle \langle \psi_i|, \quad (6.45)$$

$$Q = \sum_{i=d+1}^{\infty} |\psi_i\rangle \langle \psi_i| = 1 - P, \quad (6.46)$$

with the dimension of the valence space denoted as  $d$ . The projection operator fulfill the relations  $PQ = QP = 0$ ,  $P^2 = P$  and  $Q^2 = Q$ . Thus, we can formally reduce the  $A$ -body eigenvalue problem of Eq. (6.41) to the valence space with the Hamiltonian  $H_{\text{eff}}$

$$PH_{\text{eff}}P |\Psi_\alpha\rangle = E_\alpha P |\Psi_\alpha\rangle. \quad (6.47)$$

The goal is to derive the valence-space interaction from the original Hamiltonian  $H$ , so that the diagonalization in the valence space reproduces a subset of eigenvalues  $E_\alpha$  of the full  $A$ -body Hamiltonian. Since valence-space calculations give binding energies relative to the core, e.g.,  $^{16}\text{O}$  for the  $sd$ -shell, for which all single-particle orbitals are filled

$$|c\rangle = \prod_{l=1}^{A_c} a_l^\dagger |0\rangle, \quad (6.48)$$

the eigenvalue problem is modified to

$$PH'_{\text{eff}}P |\Psi_\alpha\rangle = (E_\alpha - E_c)P |\Psi_\alpha\rangle, \quad (6.49)$$


---

where  $E_c$  is the energy of the core. Valence-space states, e.g., for two valence nucleons, are defined as

$$|\Psi_i^M\rangle = \sum_{\alpha<\beta}^d C_{\alpha\beta}^{(i)} a_\alpha^\dagger a_\beta^\dagger |c\rangle, \quad (6.50)$$

where we use greek indices  $\alpha, \beta, \dots$  for valence-space orbitals, while upper case roman indices  $I, J, \dots$  indicate core and lower case roman indices  $i, j, \dots$  higher-lying (unoccupied) orbitals, respectively. The superscript  $(i)$  specifies the quantum number of the states. The effective Hamiltonian  $H'_{\text{eff}}$ , given by

$$H'_{\text{eff}} = \sum_{\alpha=1}^d \varepsilon_\alpha a_\alpha^\dagger a_\alpha + V_{\text{eff}}, \quad (6.51)$$

is composed of the single-particle energies (SPEs)  $\varepsilon_\alpha$  of the  $d$  orbitals in the valence space and the two-body effective interaction  $V_{\text{eff}}$  between valence nucleons. The SPEs can be determined empirically by taking the binding-energy difference between the appropriate state in the nucleus with one additional nucleon to closed shells and the ground-state energy of the closed-shell nucleus (core). Moreover, the effective two-body interaction can also be adjusted to reproduce experimental ground- and excited-state energies. An example for phenomenological  $sd$ -shell interactions are the USD Hamiltonians developed by Brown and Richter [162].

However, our aim is to calculate  $H_{\text{eff}}$ , where we start from the definition of the effective interaction including the core energy  $E_c$ . We define the projection of the  $A$ -body eigenstate  $|\Psi_\alpha\rangle$  onto the model space as  $|\Psi_\alpha^M\rangle = P|\Psi_\alpha\rangle$  and the wave operator  $\Omega$  that transforms the model-space eigenstates back to the  $A$ -body eigenstates by  $|\Psi_\alpha\rangle = \Omega|\Psi_\alpha^M\rangle$ . This latter transformation is however not trivial as it states the existence of a one-to-one correspondence between  $d$  valence and  $A$ -body eigenstates. If we assume that the inverse of the wave operator exists, we can similarity transform the Hamiltonian  $H$  to  $\mathcal{H} = \Omega^{-1}H\Omega$  and its eigenstates  $|\Psi_\alpha\rangle$  to  $|\Psi_\alpha^M\rangle = \Omega^{-1}|\Psi_\alpha\rangle$ . This results in

$$\Omega^{-1}H\Omega\Omega^{-1}|\Psi_\alpha\rangle = E_\alpha\Omega^{-1}|\Psi_\alpha\rangle \quad (6.52)$$

$$\mathcal{H}|\Psi_\alpha^M\rangle = E_\alpha|\Psi_\alpha^M\rangle, \quad (6.53)$$

where the eigenvalues are unaffected by the similarity transformation. The similarity transformed Hamiltonian  $\mathcal{H}$  can be rewritten in terms of the projection operators  $P$  and  $Q$  to

$$\mathcal{H} = P\mathcal{H}P + P\mathcal{H}Q + Q\mathcal{H}P + Q\mathcal{H}Q, \quad (6.54)$$

which, when inserted in Eq. (6.53), leads to the decoupling equation

$$Q\mathcal{H}P = 0. \quad (6.55)$$

This implies that we can define the valence-space effective Hamiltonian  $H_{\text{eff}}$  by

$$H_{\text{eff}} = P\mathcal{H}P = P\Omega^{-1}H\Omega P. \quad (6.56)$$

It is important to note that there is no unique representation of the wave operator  $\Omega$ . Since in practical calculations the perturbative expansion is truncated at a given order, the different choices for the wave operator  $\Omega$  give different results for the effective interaction. Even the same defining equation for the wave operator might be solved by different iterative schemes. We choose the wave operator  $\Omega$  to have the form

$$\Omega = 1 + \chi, \quad (6.57)$$

with the correlation operator  $\chi$ . Since  $\Omega$  obeys  $P\Omega P = P$  and the term  $\Omega Q$  does not appear in the theory, the correlation operator  $\chi$  has the properties

$$P\chi P = 0, \quad Q\Omega P = \underbrace{QP}_{=0} + Q\chi P = (1-P)\chi P = \chi P, \quad (6.58)$$

$$Q\chi Q = 0, \quad P\chi Q = 0. \quad (6.59)$$

Thus, we choose  $\chi$  as

$$\chi = Q\chi P. \quad (6.60)$$

For the next steps in the derivation the following relations are helpful

$$\chi = Q\chi P = Q\chi(1-Q) = Q\chi - \underbrace{Q\chi Q}_{=0} = Q\chi, \quad (6.61)$$

$$\chi = Q\chi P = (1-P)\chi P = \chi P - \underbrace{P\chi P}_{=0} = \chi P. \quad (6.62)$$

This enables us to rewrite Eq. (6.55) in terms of the wave operator  $\Omega = 1 + \chi$  and its inverse  $\Omega^{-1} = 1 - \chi$  to

$$0 = Q\mathcal{H}P = Q\Omega^{-1}H\Omega P = Q(1-\chi)H(1+\chi)P \quad (6.63)$$

$$= QHP - Q\chi HP + QH\chi P - Q\chi H\chi P \quad (6.64)$$

$$= QHP - Q\chi(P+Q)HP + QH(P+Q)\chi P - Q\chi(P+Q)H(P+Q)\chi P \quad (6.65)$$

$$= QHP - \underbrace{Q\chi P HP}_{=\chi} - \underbrace{Q\chi Q HP}_{=0} + \underbrace{QH P \chi P}_{=0} + \underbrace{QH Q \chi P}_{=\chi} - Q\chi(P+Q)H(P+Q)\chi P \quad (6.66)$$

$$= QHP - \chi HP + QH\chi - \chi H\chi, \quad (6.67)$$

which determines the correlation operator  $\chi$ . In the following we employ the partitioning of  $H = H_0 + H_1$  and since we are working in a degenerate model space we define

$$PH_0P = \omega P, \quad (6.68)$$

with the unperturbed model space eigenvalue  $\omega$ . Thus, Eq. (6.67) is modified to

$$0 = \underbrace{QH_0P}_{=0} + QH_1P - \chi H_0P - \chi H_1P + QH_0\chi + QH_1\chi - \chi H_0\chi - \chi H_1\chi \quad (6.69)$$

$$= QH_1P - \chi \underbrace{PH_0P}_{=\omega P} - \chi PH_1P + QH_0Q\chi + QH_1Q\chi - \chi \underbrace{PH_0Q\chi}_{=0} - \chi PH_1Q\chi, \quad (6.70)$$

where we have used Eqs. (6.61) and (6.62) as well as the diagonal nature of  $H_0$ . By rearranging terms we arrive at

$$(\omega - QH_0Q - QH_1Q)\chi = QH_1P - \chi PH_1P - \chi PH_1Q\chi, \quad (6.71)$$

which yields an equation for the correlation operator  $\chi$

$$\chi = Q \frac{1}{\omega - QH_0Q} QH_1P - \frac{1}{\omega - QH_0Q} \chi (PH_1P + PH_1Q\chi P). \quad (6.72)$$

In the first term on the right-hand side we have used  $Q^2 = Q$  and in the last term we have again employed Eq. (6.62). Inserting the ansatz for the wave operator  $\Omega$  into the effective Hamiltonian, Eq. (6.56), we find

$$H_{\text{eff}} = P\Omega^{-1}H\Omega P = P(1-\chi)H(1+\chi)P \quad (6.73)$$

$$= PHP - \underbrace{P\chi HP}_{PQ\chi PHP=0} + PH\chi P - \underbrace{P\chi H\chi P}_{PQ\chi PH\chi P=0} \quad (6.74)$$

$$= PH_0P + PH_1P + \underbrace{PH_0Q\chi P}_{=0} + PH_1Q\chi P \quad (6.75)$$

$$= PH_0P + V_{\text{eff}}(\chi), \quad (6.76)$$

where we have defined  $V_{\text{eff}}(\chi) = PH_1P + PH_1Q\chi P$ . Inserting this relation into Eq. (6.72) results in

$$\chi = Q \frac{1}{\omega - QH_0Q} QH_1P - \frac{1}{\omega - QH_0Q} \chi V_{\text{eff}}(\chi), \quad (6.77)$$

which, when multiplied on both sides with  $PH_1$  and adding  $PH_1P$  to both sides, leads to

$$PH_1P + PH_1\chi = PH_1P + PH_1Q \frac{1}{\omega - QHQ} QH_1P - PH_1 \frac{1}{\omega - QHQ} \chi V_{\text{eff}}(\chi). \quad (6.78)$$

We now want to define the so-called  $\widehat{Q}$ -box as

$$\widehat{Q}(\omega) = PH_1P + PH_1Q \frac{1}{\omega - QHQ} QH_1P. \quad (6.79)$$

The diagrammatic content of the  $\widehat{Q}$ -box is discussed in Sec. 6.2.2 on time-dependent RS perturbation theory. We anticipate that the  $\widehat{Q}$ -box consists of non-folded diagrams which are irreducible and valence linked. An irreducible diagram has between each pair of interaction vertices at least one hole line or a particle line beyond the valence space. In valence-linked diagrams the interactions are linked to at least one valence line. Note that there are connected (consisting of a single piece) and disconnected valence-linked diagrams. However, when including folded diagrams the disconnected diagrams cancel.

Identifying  $V_{\text{eff}}(\chi)$  on the left and the expression for the  $\widehat{Q}$ -box on the right of Eq. (6.78) leads to

$$V_{\text{eff}}(\chi) = \widehat{Q}(\omega) - PH_1 \frac{1}{\omega - QHQ} \chi V_{\text{eff}}(\chi). \quad (6.80)$$

Equation (6.80) is solved by an iteration scheme, where  $\chi_n$  and  $V_{\text{eff}}^{(n)} = V_{\text{eff}}(\chi_n)$  are determined from  $\chi_{n-1}$  and  $V_{\text{eff}}^{(n-1)}$ . While there are several iteration methods we want to focus on the method by Kuo and Krenciglowa. For that we write Eq. (6.80) as

$$V_{\text{eff}}^{(n)} = \widehat{Q}(\omega) - PH_1 \frac{1}{\omega - QHQ} \chi_n V_{\text{eff}}^{(n-1)}. \quad (6.81)$$

The solution takes the form

$$V_{\text{eff}}^{(n)} = \widehat{Q} + \sum_{m=1}^{\infty} \frac{1}{m!} \left( \frac{d^m \widehat{Q}}{d\omega^m} \right) (V_{\text{eff}}^{(n-1)})^m, \quad (6.82)$$

which converges when  $V_{\text{eff}}^{(n)} \approx V_{\text{eff}}^{(n-1)}$ . For  $n \rightarrow \infty$  the solution  $V_{\text{eff}}^{(\infty)}$  equals the formal solution

$$V_{\text{eff}}^{(\infty)} = \sum_{m=0}^{\infty} \frac{1}{m!} \left( \frac{d^m \widehat{Q}}{d\omega^m} \right) (V_{\text{eff}}^{(\infty)})^m. \quad (6.83)$$

---

## 6.2.2 Time-dependent Rayleigh-Schrödinger perturbation theory

---

As pointed out above, we want to derive a valence-linked diagram expansion for both SPEs and  $V_{\text{eff}}$  from degenerate time-dependent RS perturbation theory. In a first step we introduce the time-evolution operator  $U(t, t')$  and discuss its properties. Then we focus on the propagation of a two-body valence state in imaginary time, addressing the factorization into different contributions through the decomposition theorem. Based on these preliminaries we want to derive an expression for the model-space effective interaction.

The relation

$$U^\dagger(t, t')U(t, t') = U(t, t')U^\dagger(t, t') = 1 \quad (6.84)$$

implies that the time-evolution operator is unitary, i.e.,  $U^\dagger(t, t') = U^{-1}(t, t')$ . In addition, we conclude from

$$U(t, t')U(t', t'') = U(t, t''), \quad (6.85)$$

$$U(t, t')U(t', t) = 1, \quad (6.86)$$

that

$$U(t, t') = U^\dagger(t', t). \quad (6.87)$$

In our discussion of time-dependent RS perturbation theory we employ the complex time approach for the time-development operator  $U$ , i.e., the time  $t$  is rotated by a small angle  $\epsilon$  into the complex plane. Thus, the complex

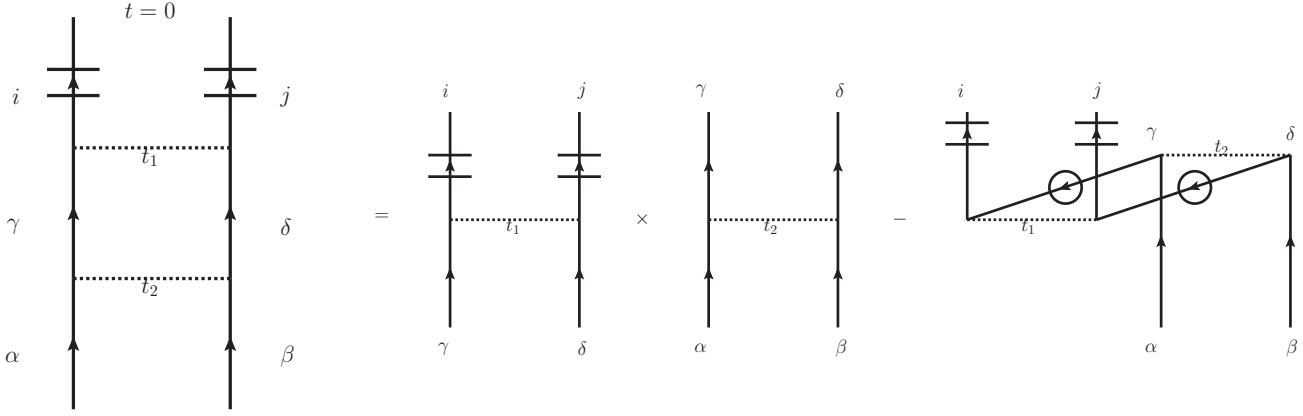


**Figure 6.3:** On the left we show a second-order contribution to the wave function with time ordering  $0 > t_1 > t_2 > -\infty$ . Greek indices and the corresponding lines represent valence-space orbitals, while railed lines and lower case latin indices belong to the  $Q$ -space. In the middle we have factorized the left diagram in two pieces with time orderings  $0 > t_1 > -\infty$  and  $0 > t_2 > -\infty$ . On the right we subtract the folded diagram with time ordering  $0 > t_2 > t_1 > -\infty$ , where the down-going lines with a circle correspond to valence-space orbitals (folded lines).

time  $t$  is converted to the real time  $\tilde{t}$  by  $t = \tilde{t}(1 - i\epsilon)$ . The time-evolution operator in the interaction picture is then given by

$$U(0, -\infty) = \lim_{\epsilon \rightarrow 0^+} \lim_{t \rightarrow -\infty(1-i\epsilon)} U(0, t) = \lim_{\epsilon \rightarrow 0^+} \lim_{t \rightarrow -\infty(1-i\epsilon)} \sum_{n=0}^{\infty} (-i)^n \int_{t'}^0 dt_1 \int_{t'}^{t_1} dt_2 \cdots \int_{t'}^{t_{n-1}} dt_n \times H_1(t_1)H_1(t_2) \cdots H_1(t_n), \quad (6.88)$$

or in terms of the time-ordering operator  $T[\dots]$

$$U(0, -\infty) = \lim_{\epsilon \rightarrow 0^+} \lim_{t \rightarrow -\infty(1-i\epsilon)} \sum_{n=0}^{\infty} \frac{(-i)^n}{n!} \int_{t'}^0 dt_1 \int_{t'}^0 dt_2 \cdots \int_{t'}^0 dt_n T[H_1(t_1)H_1(t_2) \cdots H_1(t_n)], \quad (6.89)$$

where  $H_1(t)$  is defined as  $H_1(t) = e^{iH_0 t} H_1 e^{-iH_0 t}$ .

The action of the time-evolution operator on the unperturbed wave function of two valence nucleons on top of a closed-shell core is given by

$$U(0, -\infty) a_\alpha^\dagger a_\beta^\dagger |c\rangle, \quad (6.90)$$

with an example for a contribution to the exact wave function shown in the left part of Fig. 6.3. The diagram consists of two ( $n = 2$ ) successive interactions at times  $t_2$  and  $t_1$ . At time  $t_2$  the nucleons in valence-space states  $\alpha$ ,  $\beta$  are scattered into valence states  $\gamma$ ,  $\delta$ . While at  $t_1$  valence states  $\gamma$ ,  $\delta$  are propagated to higher-lying orbitals  $i$ ,  $j$  from the excluded  $Q$ -space. This diagram, assuming for convenience  $H_1 = V$  instead of  $H_1 = V - U$ , results in the following expression

$$a_i^\dagger a_j^\dagger |c\rangle \times v_{ij\gamma\delta}^{(2)} v_{\gamma\delta\alpha\beta}^{(2)} \times I, \quad (6.91)$$

with the abbreviation  $v_{ij\gamma\delta}^{(2)}$  for fully antisymmetrized two-body matrix elements and the integral  $I$  is given by

$$I = \lim_{\epsilon \rightarrow 0^+} \lim_{t \rightarrow -\infty(1-i\epsilon)} (-i)^2 \int_{t'}^0 dt_1 \int_{t'}^{t_1} dt_2 e^{-i(\epsilon_\gamma + \epsilon_\delta - \epsilon_i - \epsilon_j)t_1} e^{-i(\epsilon_\alpha + \epsilon_\beta - \epsilon_\gamma - \epsilon_\delta)t_2}. \quad (6.92)$$

In a degenerate or a nearly degenerate valence space the vanishing exponent  $\epsilon_\alpha + \epsilon_\beta - \epsilon_\gamma - \epsilon_\delta \approx 0$  leads to a divergent integral  $I$ . In the following discussion we will show how to factorize out such divergencies. In the middle part of Fig. 6.3 we have rewritten the left diagram as a factorization of two independent pieces, given by

$$a_i^\dagger a_j^\dagger |c\rangle \times v_{ij\gamma\delta}^{(2)} v_{\gamma\delta\alpha\beta}^{(2)} \times I_1, \quad (6.93)$$

with the integral  $I_1$

$$I_1 = \lim_{\epsilon \rightarrow 0^+} \lim_{t \rightarrow -\infty(1-i\epsilon)} (-i)^2 \int_{t'}^0 dt_1 \int_{t'}^0 dt_2 e^{-i(\epsilon_\gamma + \epsilon_\delta - \epsilon_i - \epsilon_j)t_1} e^{-i(\epsilon_\alpha + \epsilon_\beta - \epsilon_\gamma - \epsilon_\delta)t_2}, \quad (6.94)$$

where the factorization implies that the two time integrations are independent of each other. Nevertheless the  $t_2$  integral is also divergent. Because of the different time-integration limits, the factorized diagram contains a time-incorrect contribution, which is given by the folded diagram on the right of Fig. 6.3. While down-going lines usually represent hole orbitals, we introduce the convention of down-going lines with a circle for valence-space orbitals (folded lines). The folded-diagram contribution reads

$$-a_i^\dagger a_j^\dagger |c\rangle \times v_{ij\gamma\delta}^{(2)} v_{\gamma\delta\alpha\beta}^{(2)} \times I_2, \quad (6.95)$$

with the integral  $I_2$

$$I_2 = I_1 - I = \lim_{\epsilon \rightarrow 0^+} \lim_{t \rightarrow -\infty(1-i\epsilon)} (-i)^2 \int_{t'}^0 dt_1 \int_{t_1}^0 dt_2 e^{-i(\epsilon_\gamma + \epsilon_\delta - \epsilon_i - \epsilon_j)t_1} e^{-i(\epsilon_\alpha + \epsilon_\beta - \epsilon_\gamma - \epsilon_\delta)t_2}, \quad (6.96)$$

which is finite, even though  $I$  and  $I_1$  are infinite. Substituting the integrals to

$$\int_{t'}^0 dt_1 \int_{t_1}^0 dt_2 = \int_{t'}^0 dt_2 \int_{t'}^{t_2} dt_1, \quad (6.97)$$

we can perform the integrations

$$I_2 = \lim_{\epsilon \rightarrow 0^+} \lim_{t \rightarrow -\infty(1-i\epsilon)} (-i) \int_{t'}^0 dt_2 e^{-i(\epsilon_\alpha + \epsilon_\beta - \epsilon_\gamma - \epsilon_\delta)t_2} \frac{1}{\epsilon_\gamma + \epsilon_\delta - \epsilon_i - \epsilon_j} (e^{-i(\epsilon_\gamma + \epsilon_\delta - \epsilon_i - \epsilon_j)t_2} - e^{-i(\epsilon_\gamma + \epsilon_\delta - \epsilon_i - \epsilon_j)t'}) \quad (6.98)$$

$$= \frac{1}{\epsilon_\gamma + \epsilon_\delta - \epsilon_i - \epsilon_j} \lim_{\epsilon \rightarrow 0^+} \lim_{t \rightarrow -\infty(1-i\epsilon)} (-i) \int_{t'}^0 dt_2 e^{-i(\epsilon_\alpha + \epsilon_\beta - \epsilon_i - \epsilon_j)t_2} \quad (6.99)$$

$$= \frac{1}{\epsilon_\gamma + \epsilon_\delta - \epsilon_i - \epsilon_j} \frac{1}{\epsilon_\alpha + \epsilon_\beta - \epsilon_i - \epsilon_j}. \quad (6.100)$$

The combined expression for the folded diagram reads

$$-a_i^\dagger a_j^\dagger |c\rangle \times v_{ij\gamma\delta}^{(2)} v_{\gamma\delta\alpha\beta}^{(2)} \frac{1}{\epsilon_\gamma + \epsilon_\delta - \epsilon_i - \epsilon_j} \frac{1}{\epsilon_\alpha + \epsilon_\beta - \epsilon_i - \epsilon_j}, \quad (6.101)$$

which can be further simplified in the case of a degenerate model space with  $\epsilon_\alpha + \epsilon_\beta = \epsilon_\gamma + \epsilon_\delta = \omega$  to

$$-a_i^\dagger a_j^\dagger |c\rangle \times v_{ij\gamma\delta}^{(2)} v_{\gamma\delta\alpha\beta}^{(2)} \frac{1}{(\omega - \epsilon_i - \epsilon_j)^2}, \quad (6.102)$$

or in terms of the derivative with respect to  $\omega$

$$-a_i^\dagger a_j^\dagger |c\rangle \times v_{ij\gamma\delta}^{(2)} \frac{d}{d\omega} \left( \frac{1}{(\omega - \epsilon_i - \epsilon_j)} \right) v_{\gamma\delta\alpha\beta}^{(2)}. \quad (6.103)$$

Having discussed the above diagram as an example out of infinitely many possible diagrams arising in the propagation of the wave function we now want to turn to a more general way of removing the unwanted divergencies. We again start from two valence particles propagated in imaginary time

$$U(0, -\infty) a_\alpha^\dagger a_\beta^\dagger |c\rangle, \quad (6.104)$$

where the decomposition theorem allows to factorize diagrams of  $n$ -th order into two groups

1. one group of diagrams with  $\mu$  vertices linked to one or both valence lines  $U_V(0, -\infty) a_\alpha^\dagger a_\beta^\dagger |c\rangle$ ,

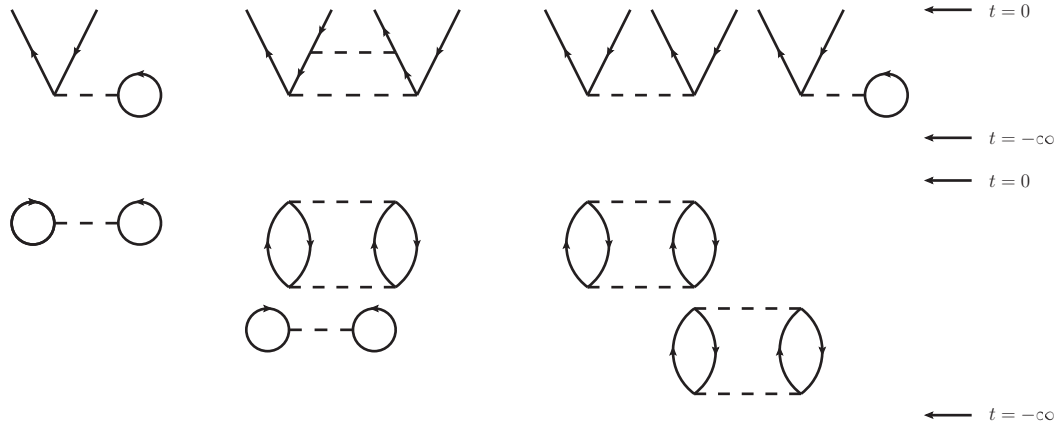


**Figure 6.4:** The upper diagrams are all connected to the  $t = 0$  boundary via fermion lines and give contributions proportional to the ground-state wave function of the core  $U_Q(0, -\infty)|c\rangle$ . The lower diagrams correspond to vacuum fluctuations and are denoted  $\langle c|U(0, -\infty)|c\rangle$ .

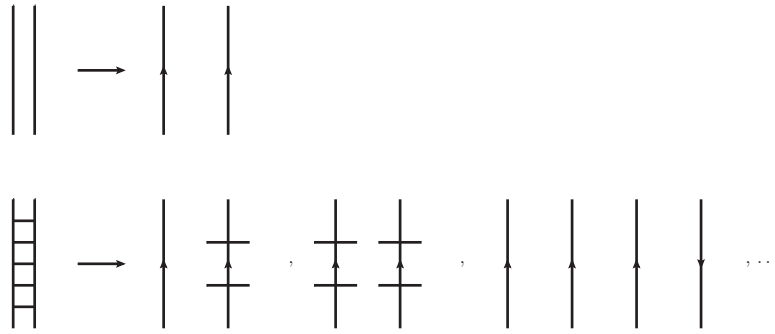


**Figure 6.5:** Active states (top) are solely composed of valence-particle ( $P$ -space) lines, while passive states contain at least one  $Q$ -space line.

2. one group of diagrams with  $\nu = n - \mu$  vertices that are not linked to any valence state  $U(0, -\infty)|c\rangle$ .

Starting with the second term, which can be expanded into a sum of all diagrams with  $n$   $H_1$  vertices as

$$U(0, -\infty)|c\rangle = \sum_{n=0}^{\infty} U^{(n)}(0, -\infty)|c\rangle. \quad (6.105)$$

Similarly to the aforementioned distinction, there are  $\mu$  vertices that are connected, directly or indirectly, to the  $t = 0$  time boundary via fermion lines, while there are  $\nu = n - \mu$  vertices not connected to this boundary. The class of diagrams containing  $\mu$  vertices corresponds to contributions proportional to the ground-state wave function of the core  $U_Q(0, -\infty)|c\rangle$ , with examples shown in the upper part of Fig. 6.4. The class of diagrams consisting of  $\nu$  vertices are vacuum-fluctuation diagrams  $\langle c|U(0, -\infty)|c\rangle$ , with examples shown in the lower part of Fig. 6.4.

Also the first term,  $U_V(0, -\infty)a_\alpha^\dagger a_\beta^\dagger|c\rangle$ , can be factorized in a similar manner. For that we define an active state as being solely composed of valence-particle ( $P$ -space) lines, shown in the upper part of Fig. 6.5, and a passive state as being composed of at least one  $Q$ -space line, shown in the lower part of Fig. 6.5. Acting with  $U_V(0, -\infty)$  on a general  $P$ -space basis vector  $|\psi_\alpha\rangle \equiv a_\alpha^\dagger a_\beta^\dagger|c\rangle$  either terminates in an active or a passive state at  $t = 0$ . Thus, we can write

$$U_V(0, -\infty)|\psi_\alpha\rangle = |\chi_\alpha^P\rangle + |\chi_\alpha^Q\rangle. \quad (6.106)$$

The diagrams contributing to these two terms are conveniently expressed in terms of chains of  $\hat{Q}$ -boxes as shown in Fig. 6.6. Note that the intermediate active states between two successive  $\hat{Q}$ -boxes correspond to a summation over all  $P$ -space states. While the  $\hat{Q}$ -box was briefly introduced in Sec. 6.2.1, we want to remind that it consists of



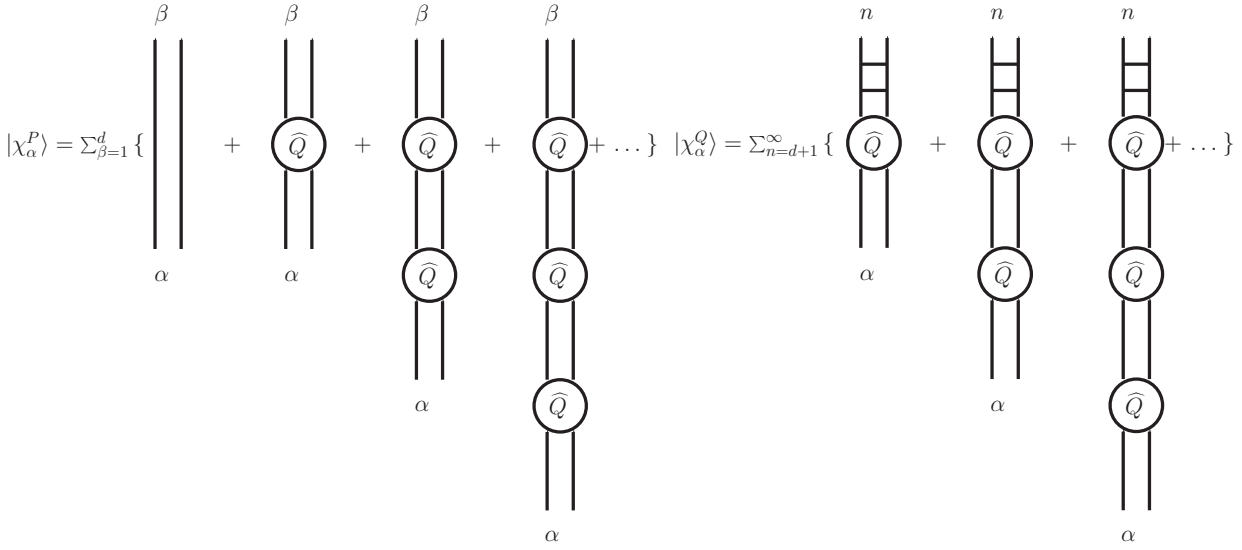


**Figure 6.6:** Schematic representation of  $|\chi_\alpha^P\rangle$  (left) and  $|\chi_\alpha^Q\rangle$  (right), with  $t = 0$  set at the top of the diagram.

non-folded diagrams which are irreducible and valence linked and contain at least one  $H_1$  vertex. An irreducible diagram has between each pair of interaction vertices at least one hole line or a particle line beyond the valence space. In valence-linked diagrams the interactions are linked to at least one valence line. This corresponds to the definition of the  $\widehat{Q}$ -box with incoming and outgoing active states, shown in the upper part of Fig. 6.7. However, for the  $|\chi_\alpha^Q\rangle$  term we need a  $\widehat{Q}$ -box with incoming active and outgoing passive states, like the diagrams shown in the lower part of Fig. 6.7.

Noting that certain terms in  $|\chi_\alpha^Q\rangle$  give rise to divergencies, e.g., the left diagram in Fig. 6.3, we can factorize these out by the folding operation. Thereby it is possible to extract out of each term in  $|\chi_\alpha^Q\rangle$  a contribution that is belonging to  $|\chi_\alpha^P\rangle$ . Thus, we can rewrite  $U_V(0, -\infty)|\psi_\alpha\rangle$  to

$$U_V(0, -\infty)|\psi_\alpha\rangle = \sum_{\beta=1}^d U_{VQ}(0, -\infty)|\psi_\beta\rangle\langle\psi_\beta|U_V(0, -\infty)|\psi_\alpha\rangle, \quad (6.107)$$

with the diagrammatic representation of  $U_{VQ}(0, -\infty)|\psi_\beta\rangle$  shown in the upper part of Fig. 6.8, where the folding operation is denoted by the integration sign, while  $\langle\psi_\beta|U_V(0, -\infty)|\psi_\alpha\rangle$  is shown in the lower part of Fig. 6.8. Note that the  $\beta$  sum over the first term in  $U_{VQ}(0, -\infty)|\psi_\beta\rangle$  times  $\langle\psi_\beta|U_V(0, -\infty)|\psi_\alpha\rangle$  is equal to  $|\chi_\alpha^P\rangle$ .

Thus, by collecting all terms we can rewrite Eq. (6.104) to

$$U(0, -\infty)|\psi_\alpha\rangle = U_Q(0, -\infty)|c\rangle\langle c|U(0, -\infty)|c\rangle \times \sum_{\beta=1}^d U_{VQ}(0, -\infty)|\psi_\beta\rangle\langle\psi_\beta|U_V(0, -\infty)|\psi_\alpha\rangle. \quad (6.108)$$

With the above preliminaries we can now derive the model-space equation

$$PH_{\text{eff}}P|\Psi_\lambda\rangle = E_\lambda P|\Psi_\lambda\rangle, \quad (6.109)$$

with  $\lambda = 1, \dots, d$ , the eigenvectors  $|\Psi_\lambda\rangle$  and the corresponding energies  $E_\lambda$  of the full  $A$ -body Hamiltonian  $H$ . We therefore need a one-to-one correspondence between the  $d$ -parent states  $|\rho_\lambda\rangle$  in the model space and the true eigenstates  $|\Psi_\lambda\rangle$  given by

$$\frac{U(0, -\infty)|\rho_\lambda\rangle}{\langle\rho_\lambda|U(0, -\infty)|\rho_\lambda\rangle} = \frac{|\Psi_\lambda\rangle}{\langle\rho_\lambda|\Psi_\lambda\rangle}, \lambda = 1, \dots, d, \quad (6.110)$$

where we now use the Schrödinger representation for convenience, while all results also hold in the interaction representation. Employing that  $|\Psi_\lambda\rangle$  are eigenstates with the corresponding energies  $E_\lambda$ , Eq. (6.110) implies

$$H \frac{U(0, -\infty)|\rho_\lambda\rangle}{\langle\rho_\lambda|U(0, -\infty)|\rho_\lambda\rangle} = E_\lambda \frac{U(0, -\infty)|\rho_\lambda\rangle}{\langle\rho_\lambda|U(0, -\infty)|\rho_\lambda\rangle}, \lambda = 1, \dots, d. \quad (6.111)$$

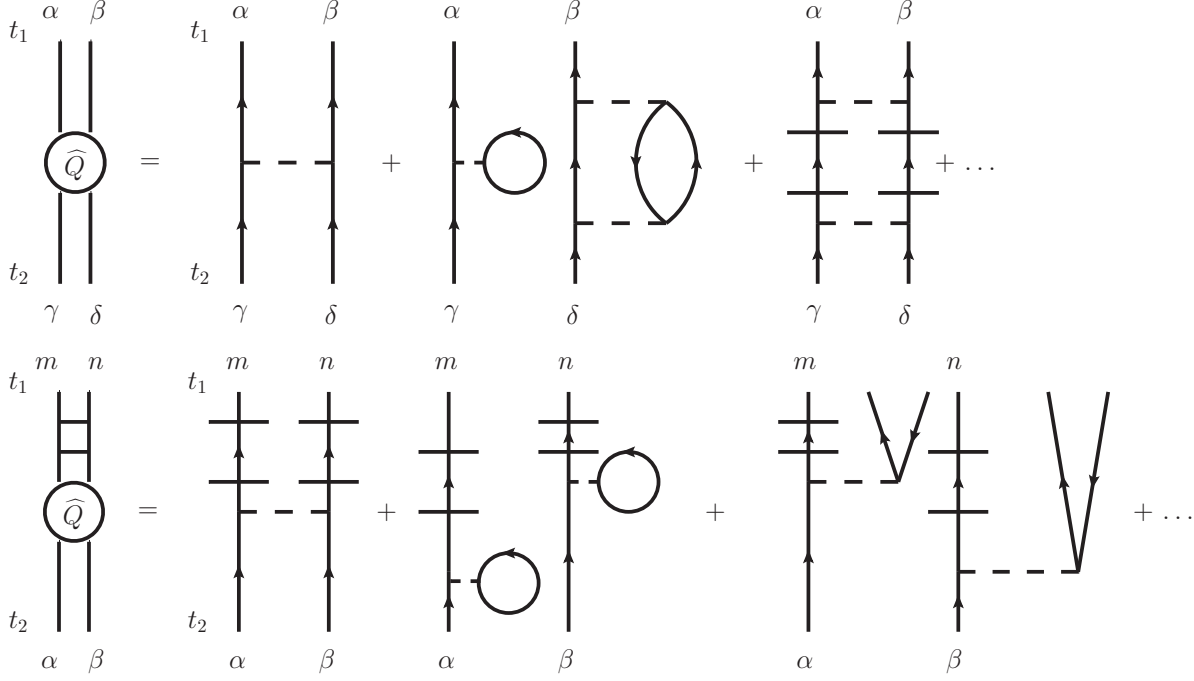


**Figure 6.7:** Diagrams contributing to the  $\widehat{Q}$ -box with incoming and outgoing active states (top) and with incoming active and outgoing passive states (bottom).

We assume that the projections  $P|\Psi_\lambda\rangle$  of  $d$  eigenstates of the full Hamiltonian  $H$  onto the model space are known and they are linearly independent. By expanding the parent states  $|\rho_\lambda\rangle$  in terms of  $P$ -space basis states  $|\psi_\alpha\rangle$  we arrive at

$$|\rho_\lambda\rangle = \sum_{\alpha=1}^d C_\alpha^{(\lambda)} |\psi_\alpha\rangle, \quad (6.112)$$

and they fulfill

$$\langle \rho_\lambda | \Psi_\mu \rangle = \langle \rho_\lambda | P | \Psi_\mu \rangle = 0, \lambda \neq \mu = 1, \dots, d. \quad (6.113)$$

The first equality holds because  $|\rho_\lambda\rangle$  is contained only in  $P$ -space, while the second equality is true because the projections  $P|\Psi_\lambda\rangle$  are linearly independent. Note that in general

$$|\rho_\lambda\rangle \neq P|\Psi_\lambda\rangle, \quad (6.114)$$

$$\langle \Psi_\lambda | P P | \Psi_\mu \rangle \neq 0, \lambda \neq \mu, \quad (6.115)$$

$$\langle \rho_\lambda | \rho_\mu \rangle \neq 0, \lambda \neq \mu. \quad (6.116)$$

However, the parent states  $|\rho_\lambda\rangle$  are a pure mathematical device to derive  $H_{\text{eff}}$  since their construction assumes knowledge of  $P|\Psi_\lambda\rangle$  which is not available until  $H_{\text{eff}}$  is known. Consequently, the final expression for  $H_{\text{eff}}$  should be independent of  $|\rho_\lambda\rangle$ .

Inserting the expansion of the parent states Eq. (6.112) into Eq. (6.111) leads to

$$\sum_{\alpha=1}^d C_\alpha^{(\lambda)} \frac{HU(0, -\infty)|\psi_\alpha\rangle}{\langle \rho_\lambda | U(0, -\infty) | \rho_\lambda \rangle} = \sum_{\beta=1}^d C_\beta^{(\lambda)} \frac{E_\lambda U(0, -\infty)|\psi_\beta\rangle}{\langle \rho_\lambda | U(0, -\infty) | \rho_\lambda \rangle}, \quad (6.117)$$

which can be rewritten using the decomposition theorem, Eq. (6.108), to

$$\sum_{\gamma=1}^d b_\gamma^{(\lambda)} HU_Q(0, -\infty)|c\rangle U_{VQ}(0, -\infty)|\psi_\gamma\rangle = \sum_{\sigma=1}^d b_\sigma^{(\lambda)} E_\lambda U_Q(0, -\infty)|c\rangle U_{VQ}(0, -\infty)|\psi_\sigma\rangle, \quad (6.118)$$

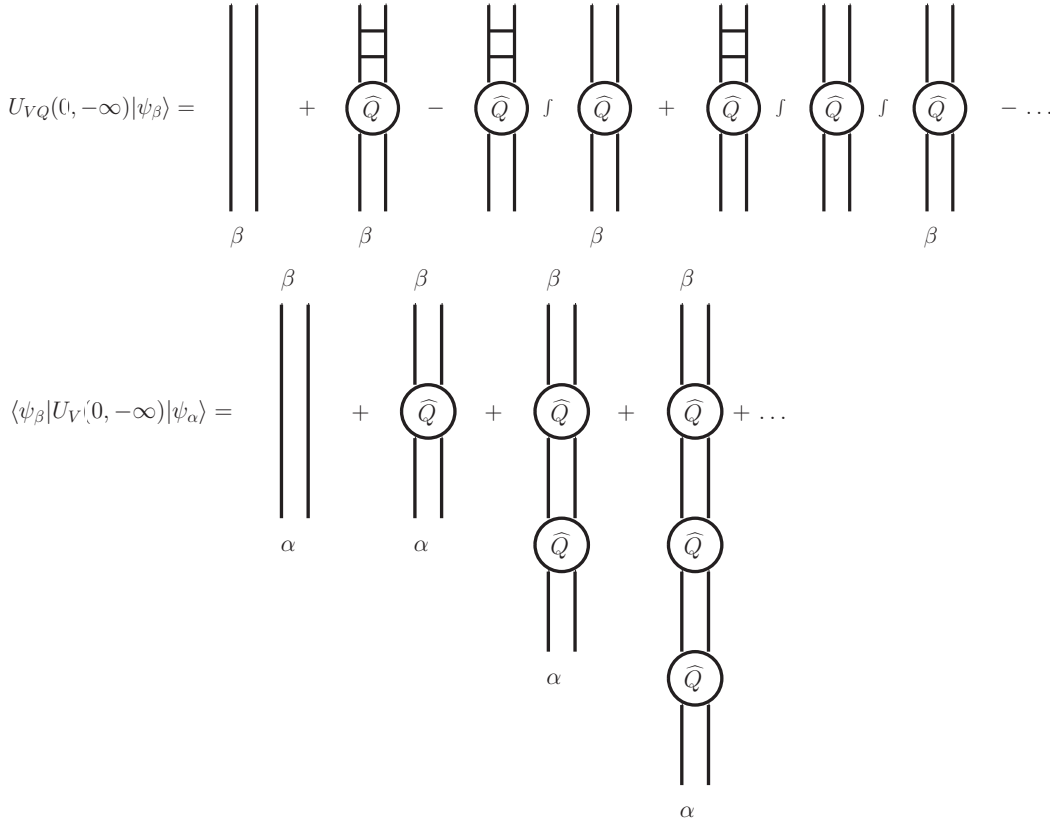


**Figure 6.8:** Schematic representation of wave-function diagrams  $U_{VQ}(0, -\infty)|\psi_\beta\rangle$  (top), where the integration sign denotes the folding operation, and matrix elements  $\langle\psi_\beta|U_Q(0, -\infty)|\psi_\alpha\rangle$  (bottom).

with the definition

$$b_\sigma^{(\lambda)} = \sum_{\beta=1}^d C_\beta^{(\lambda)} \frac{\langle c|U(0, -\infty)|c\rangle \langle \psi_\sigma|U_V(0, -\infty)|\psi_\beta\rangle}{\langle \rho_\lambda|U(0, -\infty)|\rho_\lambda\rangle}. \quad (6.119)$$

Since the only  $P$ -space contribution in  $U_Q(0, -\infty)|c\rangle U_{VQ}(0, -\infty)|\psi_\beta\rangle$  is  $|\psi_\beta\rangle$ , cf. top part of Fig. 6.8, it follows that

$$\langle \psi_\theta|U_{VQ}(0, -\infty)|\psi_\sigma\rangle = \delta_{\theta\sigma}, \quad (6.120)$$

and, hence, multiplying Eq. (6.118) with  $\langle \psi_\theta|$  results in

$$\sum_{\gamma=1}^d \langle \psi_\theta|H_{\text{eff}}|\psi_\gamma\rangle b_\gamma^{(\lambda)} = E_\lambda b_\theta^{(\lambda)}, \quad (6.121)$$

with  $H_{\text{eff}} = HU_Q(0, -\infty)U_{VQ}(0, -\infty)$ . Comparing this result to Eq. (6.47) suggests to identify  $b_\gamma^{(\lambda)}$  with the projection of the true eigenstate onto the model space  $P|\Psi_\lambda\rangle$ . To prove this we multiply Eq. (6.110) with  $\langle \psi_\gamma|$  and insert the expansion of the parent states, Eq. (6.112), and the decomposition theorem, Eq. (6.108), leading to

$$\frac{\langle \psi_\gamma|\Psi_\lambda\rangle}{\langle \rho_\lambda|\Psi_\lambda\rangle} = \sum_{\alpha,\beta=1}^d C_\alpha^{(\lambda)} \frac{\langle \psi_\gamma|U_{VQ}(0, -\infty)|\psi_\beta\rangle \langle c|U(0, -\infty)|c\rangle \langle \psi_\beta|U_V(0, -\infty)|\psi_\alpha\rangle}{\langle \rho_\lambda|U(0, -\infty)|\rho_\lambda\rangle} \quad (6.122)$$

$$= \sum_{\alpha,\beta=1}^d C_\alpha^{(\lambda)} \frac{\delta_{\gamma\beta} \langle c|U(0, -\infty)|c\rangle \langle \psi_\beta|U_V(0, -\infty)|\psi_\alpha\rangle}{\langle \rho_\lambda|U(0, -\infty)|\rho_\lambda\rangle} \quad (6.123)$$

$$= \sum_{\alpha=1}^d C_\alpha^{(\lambda)} \frac{\langle c|U(0, -\infty)|c\rangle \langle \psi_\gamma|U_V(0, -\infty)|\psi_\alpha\rangle}{\langle \rho_\lambda|U(0, -\infty)|\rho_\lambda\rangle} = b_\gamma^{(\lambda)}. \quad (6.124)$$

Thus, the only dependence of the model-space eigenvalue problem on the parent state  $|\rho_\lambda\rangle$  is via the coefficient  $b_\gamma^{(\lambda)}$ . Since we have obtained the correct formal structure of a model-space eigenvalue problem in Eq. (6.121), we are not interested in  $|\rho_\lambda\rangle$  any more, but we may solve the eigenvalue problem directly for  $b_\gamma^{(\lambda)}$ . For a known  $b_\gamma^{(\lambda)}$ , Eq. (6.124) ensures that the parent states  $|\rho_\lambda\rangle$  can be indeed constructed as the projection of the true eigenstate onto the model space.

By defining the model-space eigenstate  $|b_\lambda\rangle$  as

$$|b_\lambda\rangle = \sum_{\gamma=1}^d b_\gamma^{(\lambda)} |\psi_\gamma\rangle = \frac{P|\Psi_\lambda\rangle}{\langle\rho_\lambda|\Psi_\lambda\rangle}, \quad (6.125)$$

we arrive at

$$PH_{\text{eff}}P|b_\lambda\rangle = E_\lambda P|b_\lambda\rangle, \quad (6.126)$$

Although the true eigenvectors are orthogonal, i.e.,

$$\langle\Psi_\lambda|\Psi_\mu\rangle = \delta_{\lambda\mu}, \quad (6.127)$$

the projections of the true eigenvectors onto the model space do, in general, not preserve orthogonality

$$\langle b_\lambda|b_\mu\rangle \neq \delta_{\lambda\mu}. \quad (6.128)$$

Consequently, Eq. (6.128) implies that the effective Hamiltonian  $H_{\text{eff}}$  is, in general, not Hermitian. This is overcome by defining bi-orthogonal wave functions

$$|\bar{b}_\lambda\rangle = \sum_{\gamma=1}^d \bar{b}_\gamma^{(\lambda)} |\psi_\gamma\rangle, \quad (6.129)$$

that obey

$$\langle\bar{b}_\lambda|b_\mu\rangle = \delta_{\lambda\mu}. \quad (6.130)$$

For the evaluation of the matrix elements of  $H_{\text{eff}}$  we study the contributions from

$$\langle\psi_\theta|H_{\text{eff}}|\psi_\gamma\rangle = \langle\psi_\theta|HU_Q(0, -\infty)U_{VQ}(0, -\infty)|\psi_\gamma\rangle, \quad (6.131)$$

where for the second factor all interactions have to be linked to at least one valence line, whereas in the first factor no valence lines are involved. We start with the contributions from  $H_0$ , for which  $|\psi_\theta\rangle$  is an eigenstate and the only  $P$ -space component of  $U_{VQ}(0, -\infty)|\psi_\gamma\rangle$  is  $|\psi_\gamma\rangle$  itself, resulting in

$$\langle\psi_\theta|H_0U_Q(0, -\infty)U_{VQ}(0, -\infty)|\psi_\gamma\rangle = \langle\psi_\theta|H_0|\psi_\gamma\rangle = \langle\psi_\theta|H_0(C) + H_0(V)|\psi_\gamma\rangle = \delta_{\theta\gamma}(\epsilon_V + \epsilon_C). \quad (6.132)$$

This term represents the unperturbed energies with the contributions split into a core and a valence-space component. Similarly, we can decompose the interaction term into  $H_1 = H_1(C) + H_1(V)$ , where  $H_1(C)$  gives rise to diagrams in which  $H_1$  is not linked to any valence line at the time  $t = 0$  and  $H_1(V)$  to all the other diagrams. Summing all contributions from  $H_1(C)$  yields

$$\langle\psi_\theta|H_1(C)U_Q(0, -\infty)U_{VQ}(0, -\infty)|\psi_\gamma\rangle = \delta_{\theta\gamma}\langle c|H_1(C)U_Q(0, -\infty)|c\rangle = \delta_{\theta\gamma}(E_C - \epsilon_C), \quad (6.133)$$

with the core energy  $E_C$ . Thus, the core part was successfully separated out of the eigenvalue problem

$$\sum_{\gamma=1}^d \langle\psi_\theta|(H_0(V) + H_1(V))U_Q(0, -\infty)U_{VQ}(0, -\infty)|\psi_\gamma\rangle b_\gamma^{(\lambda)} = (E_\lambda - E_C)b_\theta^{(\lambda)}, \quad (6.134)$$

and we can now turn to a prescription to calculate

$$\langle\psi_\theta|H'_{\text{eff}}|\psi_\gamma\rangle = \langle\psi_\theta|H_1(V)U_Q(0, -\infty)U_{VQ}(0, -\infty)|\psi_\gamma\rangle. \quad (6.135)$$

Assuming the simplified structure  $U_Q(0, -\infty)|c\rangle = |c\rangle H'_{\text{eff}}$  can be written as

$$H'_{\text{eff}} = \widehat{Q} - \widehat{Q}' \int \widehat{Q} + \widehat{Q}' \int \widehat{Q} \int \widehat{Q} - \dots, \quad (6.136)$$

with both  $\widehat{Q}$ -boxes consisting of irreducible diagrams with vertices linked to at least one valence line and the integral sign representing the general folding operation. However,  $\widehat{Q}'$  has at least two  $H_1$  vertices, one from  $H_1(V)$  and the other from  $U_{VQ}(0, -\infty)|\psi_\gamma\rangle$ , while  $\widehat{Q}$  starts with first order terms from the  $H_1(V)$  vertex. Consequently,  $\widehat{Q}'$  is obtained from  $\widehat{Q}$  by dropping the terms with less than two vertices and folded diagrams in  $H'_{\text{eff}}$  contain at least three interaction vertices. Taking into account higher-order terms in  $U_Q(0, -\infty)|c\rangle$  introduces subtle differences between the  $\widehat{Q}'$ - and  $\widehat{Q}$ -boxes and necessitates a definition of a third  $\widehat{Q}$ -box  $\widehat{Q}_1$ , while the functional form of Eq. (6.136) is preserved.

While we briefly investigated the calculation of folded diagrams already, it is possible to rewrite folded terms in  $H'_{\text{eff}}$  as

$$-\widehat{Q}' \int \widehat{Q} = \frac{d\widehat{Q}'(\omega)}{d\omega} \widehat{Q}(\omega), \quad (6.137)$$

$$\widehat{Q}' \int \widehat{Q} \int \widehat{Q} = \frac{1}{2!} \frac{d^2\widehat{Q}'(\omega)}{d\omega^2} \widehat{Q}(\omega) \widehat{Q}(\omega) + \frac{d\widehat{Q}'(\omega)}{d\omega} \frac{d\widehat{Q}(\omega)}{d\omega} \widehat{Q}(\omega), \quad (6.138)$$

leading to the general expression of an  $n$ -folded  $\widehat{Q}$ -box with  $n + 1$   $\widehat{Q}$ -boxes

$$\widehat{Q}' \int \widehat{Q} \int \widehat{Q} \dots \int \widehat{Q} = \sum_{m_1 m_2 \dots m_n} \frac{1}{m_1!} \frac{d^{m_1}\widehat{Q}'(\omega)}{d\omega^{m_1}} P \frac{1}{m_2!} \frac{d^{m_2}\widehat{Q}(\omega)}{d\omega^{m_2}} P \dots \frac{1}{m_n!} \frac{d^{m_n}\widehat{Q}(\omega)}{d\omega^{m_n}} P \widehat{Q}(\omega). \quad (6.139)$$

The constraints for this expression are  $m_1 + m_2 + \dots + m_n = n$ ,  $m_1 \geq 1$ ,  $m_2, m_3, \dots, m_n \geq 0$  and  $m_k \leq n - k + 1$ , with the last one due to the fact that there are only  $n - k + 1$   $\widehat{Q}$ -boxes to the right of the  $k$ -th  $\widehat{Q}$ -box such that it can be differentiated at most  $n - k + 1$  times. On the right of Eq. (6.139) we have inserted  $P$ -space projection operators between the  $\widehat{Q}$ -box terms to indicate that model space intermediate states are summed over. Note that all the  $\widehat{Q}$ -boxes and  $\widehat{Q}$ -box derivatives are evaluated at the degenerate model-space energy  $\omega$ . Moreover, since  $\widehat{Q}'$  is differentiated at least once and with the relation  $\frac{d\widehat{Q}'(\omega)}{d\omega} = \frac{d\widehat{Q}(\omega)}{d\omega} \widehat{Q}'$  can be eliminated in the above equations. Thus, it can be shown that a possible solution is given by

$$V_{\text{eff}}^{(n)} = \widehat{Q} + \sum_{m=1}^{\infty} \frac{1}{m!} \left( \frac{d^m \widehat{Q}}{d\omega^m} \right) \left( V_{\text{eff}}^{(n-1)} \right)^m. \quad (6.140)$$

Thus, the effective interaction is obtained through an iterative procedure requiring the evaluation of the  $\widehat{Q}$ -box and its energy derivatives. It is worth noting that the operator  $H'_{\text{eff}}$  includes both one- and two-body contributions since our derivation started from a state with two-valence nucleons. The corresponding set of one-body diagrams is denoted  $\widehat{S}$ -box. To obtain the single-particle energies, we solve the coupled Dyson equations,

$$\varepsilon_\alpha^{(k)} = \langle \alpha | H_0 | \alpha \rangle + \widehat{S}(\varepsilon_\alpha^{(k-1)}), \quad (6.141)$$

by iteration starting from  $\varepsilon_\alpha^{(0)} = \omega$  until  $\varepsilon_\alpha^{(k)} \approx \varepsilon_\alpha^{(k-1)}$ . Because the  $\varepsilon_\alpha$  depend on relative shifts in the unperturbed harmonic-oscillator spectrum, we also update the unperturbed valence-space energy to be the centroid of the converged SPEs and iterate until the centroid of the final SPEs is equal to the unperturbed value.

Note that in the case of  $N_V$  valence nucleons  $H'_{\text{eff}}$  will contain, in general, many-body forces of rank  $n$  with  $n \leq N_V$  although  $V$  is only a two-body interaction. These many-body forces in MBPT have been addressed in Ref. [163].

While the formal definition of the  $\widehat{Q}$ -box includes  $H_1$  vertices up to infinite order, practical calculations are done at finite order in the interaction. In Sec. 7 we present results which include contributions up to second and third order in  $H_1$ . Third-order calculations represent the current state-of-the-art, while higher-order calculations are prohibited by the increasing number of diagrams. For calculations at a given order it has to be ensured that the effective interaction  $H'_{\text{eff}}$  is converged with respect to excitations out of the valence space. These excitations are only allowed up to some finite energy  $N\hbar\Omega$ , which is ultimately limited by the size of the single-particle basis. For our MBPT

calculations we add to the isospin-symmetry breaking NN forces from chiral EFT electromagnetic interactions, i.e., the Coulomb force and higher-order electromagnetic corrections. In addition to the two-body interaction we include normal-ordered one- and two-body terms of chiral 3N forces. These normal-ordered 3N forces are obtained by normal ordering the 3N force with respect to the harmonic-oscillator Slater determinant of the closed-shell core  $|c\rangle$ . Their inclusion in MBPT calculations of valence-space interactions was key for the understanding of the structure of medium-mass nuclei, the evolution to the neutron and proton drip lines [153, 164] and the formation of shell structure [35, 165–167]. The MBPT calculations are performed with a Fortran code developed by Morten Hjorth-Jensen [161].

### 6.3 Hartree-Fock method

The Hartree-Fock (HF) method is an independent-particle or mean-field method. The nuclear many-body problem with  $A$  interacting nucleons is approximated by a one-body operator, assuming that the nucleons move independently of each other in the mean-field potential. Since the HF method does not include residual interactions between the nucleons, there are no correlations between particles and, thus, the many-body wave function is given by a single Slater determinant. It is determined by minimizing its energy expectation value according to the variational principle, by optimizing the single-particle orbitals from which the Slater determinant is constructed. Therefore, the HF method itself is a many-body method, selecting the best approximation for the ground state of a closed-shell nucleus from a set of Slater determinants. Moreover, the Slater determinant, constructed from optimized single-particle orbitals, provides a starting point for more sophisticated many-body methods, e.g., CC or IM-SRG calculations, in which it is used as a reference state to normal order 3N forces.

The starting point of the energy minimization is the Hartree-Fock Slater determinant describing the  $A$ -body system

$$|\Phi_{\text{HF}}\rangle = |\varphi_1\rangle \otimes \cdots \otimes |\varphi_A\rangle, \quad (6.142)$$

where  $|\varphi_p\rangle$  denote the Hartree-Fock single-particle wave functions. To perform the variational calculation we have to choose a complete and orthogonal set of single-particle wave functions. For nuclear-structure calculations the spherical harmonic-oscillator basis with single-particle wave functions  $|\chi_s\rangle$  and creation operator  $c_s^\dagger$  provides a convenient choice. In general, other choices for the single-particle basis are possible. We can expand  $|\varphi_p\rangle$  and the corresponding creation operator  $a_p^\dagger$  in the chosen basis

$$|\varphi_p\rangle = \sum_s D_{sp} |\chi_s\rangle, \quad (6.143)$$

$$a_p^\dagger = \sum_s D_{sp} c_s^\dagger, \quad (6.144)$$

with the overlap coefficients  $D_{sp} = \langle \chi_s | \varphi_p \rangle$ . Since both sets of single-particle wave functions  $\{|\varphi_p\rangle\}$  and  $\{|\chi_s\rangle\}$  are complete and orthogonal, the basis transformation has to be unitary, i.e.,  $DD^\dagger = D^\dagger D = \mathbb{1}$ . Any unitary transformation that does not mix hole and particle states leaves the HF Slater determinant  $|\Phi_{\text{HF}}\rangle$  unchanged up to a phase. Thus, it is more convenient to work in terms of the one-body density matrix

$$\rho_{sp}^{(1)} = \langle \Phi_{\text{HF}} | c_p^\dagger c_s | \Phi_{\text{HF}} \rangle = \sum_{q,t} D_{pq} D_{st}^* \langle \Phi_{\text{HF}} | a_q^\dagger a_t | \Phi_{\text{HF}} \rangle = \sum_i D_{si} D_{pi}^*. \quad (6.145)$$

In the last step we employed that the one-body density matrix is diagonal in the HF basis

$$\rho_{ab}^{(1)} = n_a \delta_{ab}, \quad n_a \in \{0, 1\}, \quad (6.146)$$

with the occupation numbers one for hole (occupied) and zero for particle (unoccupied) states. Moreover, the idempotence of the one-body density matrix

$$(\rho^{(1)})^2 = \rho^{(1)} \quad (6.147)$$

assures that  $\rho^{(1)}$  is a projector onto the subspace spanned by hole states  $|\varphi_i\rangle$ .

For the derivation of the HF equations we start from the intrinsic nuclear  $A$ -body Hamiltonian in the harmonic-oscillator basis, containing the kinetic energy, NN and 3N interactions

$$H = T^{(1)} + V^{(2)} + V^{(3)} \quad (6.148)$$

$$= \sum_{p,s} \langle p | T^{(1)} | s \rangle c_p^\dagger c_s + \frac{1}{4} \sum_{p,q,s,t} \langle pq | V^{(2)} | st \rangle c_p^\dagger c_q^\dagger c_t c_s + \frac{1}{36} \sum_{p,q,r,s,t,u} \langle pqr | V^{(3)} | stu \rangle c_p^\dagger c_q^\dagger c_r^\dagger c_u c_t c_s \quad (6.149)$$

$$= \sum_{p,s} t_{ps}^{(1)} c_p^\dagger c_s + \frac{1}{4} \sum_{p,q,s,t} v_{pqst}^{(2)} c_p^\dagger c_q^\dagger c_t c_s + \frac{1}{36} \sum_{p,q,r,s,t,u} v_{pqrstu}^{(3)} c_p^\dagger c_q^\dagger c_r^\dagger c_u c_t c_s, \quad (6.150)$$

where the abbreviations  $v_{pqst}^{(2)}$  and  $v_{pqrstu}^{(3)}$  denote fully antisymmetrized matrix elements of the NN and 3N interactions. We calculate the HF energy by taking the expectation value of the Hamiltonian in the HF Slater determinant  $|\Phi_{\text{HF}}\rangle$

$$E_{\text{HF}} = \langle \Phi_{\text{HF}} | T^{(1)} + V^{(2)} + V^{(3)} | \Phi_{\text{HF}} \rangle \quad (6.151)$$

$$= \sum_{p,s} t_{ps}^{(1)} \langle \Phi_{\text{HF}} | c_p^\dagger c_s | \Phi_{\text{HF}} \rangle + \frac{1}{4} \sum_{p,q,s,t} v_{pqst}^{(2)} \langle \Phi_{\text{HF}} | c_p^\dagger c_q^\dagger c_t c_s | \Phi_{\text{HF}} \rangle + \frac{1}{36} \sum_{p,q,r,s,t,u} v_{pqrstu}^{(3)} \langle \Phi_{\text{HF}} | c_p^\dagger c_q^\dagger c_r^\dagger c_u c_t c_s | \Phi_{\text{HF}} \rangle. \quad (6.152)$$

By introducing the two- and three-body density matrix

$$\rho_{stpq}^{(2)} = \langle \Phi_{\text{HF}} | c_p^\dagger c_q^\dagger c_t c_s | \Phi_{\text{HF}} \rangle, \quad (6.153)$$

$$\rho_{stupqr}^{(3)} = \langle \Phi_{\text{HF}} | c_p^\dagger c_q^\dagger c_r^\dagger c_u c_t c_s | \Phi_{\text{HF}} \rangle, \quad (6.154)$$

we can rewrite the HF energy as a functional of the density matrices

$$E_{\text{HF}}[\rho^{(1)}, \rho^{(2)}, \rho^{(3)}] = \sum_{p,s} t_{ps}^{(1)} \rho_{sp}^{(1)} + \frac{1}{4} \sum_{p,q,s,t} v_{pqst}^{(2)} \rho_{stpq}^{(2)} + \frac{1}{36} \sum_{p,q,r,s,t,u} v_{pqrstu}^{(3)} \rho_{stupqr}^{(3)}. \quad (6.155)$$

Since we are dealing with a single Slater determinant we can use Wick's theorem, introduced in Sec. 6.1, to derive factorization formulas for the two- and three-body density matrix by full contractions of all operators

$$\rho_{stpq}^{(2)} = \langle \Phi_{\text{HF}} | c_p^\dagger c_q^\dagger c_t c_s | \Phi_{\text{HF}} \rangle = : \overline{c_p^\dagger c_q^\dagger c_t c_s} : | \Phi_{\text{HF}} \rangle + : c_p^\dagger c_q^\dagger c_t c_s : | \Phi_{\text{HF}} \rangle = \rho_{tq}^{(1)} \rho_{sp}^{(1)} - \rho_{tp}^{(1)} \rho_{sq}^{(1)}, \quad (6.156)$$

$$\rho_{stupqr}^{(3)} = \langle \Phi_{\text{HF}} | c_p^\dagger c_q^\dagger c_r^\dagger c_u c_t c_s | \Phi_{\text{HF}} \rangle \quad (6.157)$$

$$= : \overline{c_p^\dagger c_q^\dagger c_r^\dagger c_u c_t c_s} : | \Phi_{\text{HF}} \rangle + : c_p^\dagger c_q^\dagger c_r^\dagger c_u c_t c_s : | \Phi_{\text{HF}} \rangle + : c_p^\dagger c_q^\dagger c_r^\dagger c_u c_t c_s : | \Phi_{\text{HF}} \rangle + : c_p^\dagger c_q^\dagger c_r^\dagger c_u c_t c_s : | \Phi_{\text{HF}} \rangle + : c_p^\dagger c_q^\dagger c_r^\dagger c_u c_t c_s : | \Phi_{\text{HF}} \rangle + : c_p^\dagger c_q^\dagger c_r^\dagger c_u c_t c_s : | \Phi_{\text{HF}} \rangle \quad (6.158)$$

$$= \rho_{ur}^{(1)} \left( \rho_{tq}^{(1)} \rho_{sp}^{(1)} - \rho_{tp}^{(1)} \rho_{sq}^{(1)} \right) + \rho_{tr}^{(1)} \left( \rho_{up}^{(1)} \rho_{sq}^{(1)} - \rho_{uq}^{(1)} \rho_{sp}^{(1)} \right) + \rho_{sr}^{(1)} \left( \rho_{uq}^{(1)} \rho_{tp}^{(1)} - \rho_{tq}^{(1)} \rho_{up}^{(1)} \right). \quad (6.159)$$

Inserting the factorization formulas into Eq. (6.155) leads to

$$\frac{1}{4} \sum_{p,q,s,t} v_{pqst}^{(2)} \left( \rho_{tq}^{(1)} \rho_{sp}^{(1)} - \rho_{tp}^{(1)} \rho_{sq}^{(1)} \right) = \frac{1}{4} \sum_{p,q,s,t} \left( v_{pqst}^{(2)} \rho_{tq}^{(1)} \rho_{sp}^{(1)} - v_{qpst}^{(2)} \rho_{tq}^{(1)} \rho_{sp}^{(1)} \right) \quad (6.160)$$

$$= \frac{1}{4} \sum_{p,q,s,t} \left( v_{pqst}^{(2)} \rho_{tq}^{(1)} \rho_{sp}^{(1)} + v_{pqst}^{(2)} \rho_{tq}^{(1)} \rho_{sp}^{(1)} \right) \quad (6.161)$$

$$= \frac{1}{2} \sum_{p,q,s,t} v_{pqst}^{(2)} \rho_{tq}^{(1)} \rho_{sp}^{(1)}, \quad (6.162)$$

$$\frac{1}{36} \sum_{p,q,r,s,t,u} v_{pqrstu}^{(3)} \left[ \rho_{ur}^{(1)} \left( \rho_{tq}^{(1)} \rho_{sp}^{(1)} - \rho_{tp}^{(1)} \rho_{sq}^{(1)} \right) + \rho_{tr}^{(1)} \left( \rho_{up}^{(1)} \rho_{sq}^{(1)} - \rho_{uq}^{(1)} \rho_{sp}^{(1)} \right) + \rho_{sr}^{(1)} \left( \rho_{uq}^{(1)} \rho_{tp}^{(1)} - \rho_{tq}^{(1)} \rho_{up}^{(1)} \right) \right] \quad (6.163)$$

$$= \frac{1}{36} \sum_{p,q,r,s,t,u} \left[ v_{pqrstu}^{(3)} \rho_{ur}^{(1)} \rho_{tq}^{(1)} \rho_{sp}^{(1)} - v_{qprstu}^{(3)} \rho_{ur}^{(1)} \rho_{tq}^{(1)} \rho_{sp}^{(1)} + v_{qprsut}^{(3)} \rho_{ur}^{(1)} \rho_{tq}^{(1)} \rho_{sp}^{(1)} - v_{pqrstus}^{(3)} \rho_{ur}^{(1)} \rho_{tq}^{(1)} \rho_{sp}^{(1)} \right. \\ \left. + v_{pqrtus}^{(3)} \rho_{ur}^{(1)} \rho_{tq}^{(1)} \rho_{sp}^{(1)} - v_{pqruts}^{(3)} \rho_{ur}^{(1)} \rho_{tq}^{(1)} \rho_{sp}^{(1)} \right] \quad (6.164)$$

$$= \frac{1}{36} \sum_{p,q,r,s,t,u} \left[ v_{pqrstu}^{(3)} \rho_{ur}^{(1)} \rho_{tq}^{(1)} \rho_{sp}^{(1)} + v_{pqrstu}^{(3)} \rho_{ur}^{(1)} \rho_{tq}^{(1)} \rho_{sp}^{(1)} + v_{pqrstu}^{(3)} \rho_{ur}^{(1)} \rho_{tq}^{(1)} \rho_{sp}^{(1)} + v_{pqrstu}^{(3)} \rho_{ur}^{(1)} \rho_{tq}^{(1)} \rho_{sp}^{(1)} \right. \\ \left. + v_{pqrstu}^{(3)} \rho_{ur}^{(1)} \rho_{tq}^{(1)} \rho_{sp}^{(1)} + v_{pqrstu}^{(3)} \rho_{ur}^{(1)} \rho_{tq}^{(1)} \rho_{sp}^{(1)} \right] \quad (6.165)$$

$$= \frac{1}{6} \sum_{p,q,r,s,t,u} v_{pqrstu}^{(3)} \rho_{ur}^{(1)} \rho_{tq}^{(1)} \rho_{sp}^{(1)}, \quad (6.166)$$

where we only exchanged indices and used the antisymmetry of two- and three-body matrix elements  $v_{pqst}^{(2)}$  and  $v_{pqrstu}^{(3)}$ , respectively. Thus, the HF energy is now only a function of the one-body density matrix

$$E_{\text{HF}}[\rho] = \sum_{p,s} t_{ps}^{(1)} \rho_{sp} + \frac{1}{2} \sum_{p,q,s,t} v_{pqst}^{(2)} \rho_{tq} \rho_{sp} + \frac{1}{6} \sum_{p,q,r,s,t,u} v_{pqrstu}^{(3)} \rho_{ur} \rho_{tq} \rho_{sp}. \quad (6.167)$$

We employ the variational principle to determine the stationary point of  $E_{\text{HF}}[\rho]$  under variation of  $\rho$

$$\delta E_{\text{HF}}[\rho] = E_{\text{HF}}[\rho + \delta\rho] - E_{\text{HF}}[\rho] \quad (6.168)$$

$$\approx \sum_{p,s} t_{ps}^{(1)} \delta\rho_{sp} + \sum_{p,q,s,t} v_{pqst}^{(2)} \rho_{tq} \delta\rho_{sp} + \frac{1}{2} \sum_{p,q,r,s,t,u} v_{pqrstu}^{(3)} \rho_{ur} \rho_{tq} \delta\rho_{sp}, \quad (6.169)$$

where terms of higher order in  $\delta\rho$  have been omitted. This can be rewritten by separating the variation of the one-body density matrix

$$\delta E_{\text{HF}}[\rho] = \sum_{p,s} \left( t_{ps}^{(1)} + \sum_{q,t} v_{pqst}^{(2)} \rho_{tq} + \frac{1}{2} \sum_{q,r,t,u} v_{pqrstu}^{(3)} \rho_{ur} \rho_{tq} \right) \delta\rho_{sp} \quad (6.170)$$

$$\equiv \sum_{p,s} h_{ps}[\rho] \delta\rho_{sp}. \quad (6.171)$$

In Eq. (6.171) we have introduced a one-body operator  $h[\rho]$ , which is called the HF single-particle or mean-field Hamiltonian. It contains, besides the kinetic energy  $t$ , a one-body potential that averages over all two- and three-body interactions in the nucleus.

The determination of the HF energy requires the solution of the stationary condition

$$\delta E_{\text{HF}}[\rho] = 0, \quad (6.172)$$

with the constraint that the variation  $\rho + \delta\rho$  has to be idempotent again, i.e.,

$$(\rho + \delta\rho)^2 = \rho + \delta\rho. \quad (6.173)$$

When neglecting terms of higher order in  $\delta\rho$  this condition simplifies to

$$\delta\rho = \rho\delta\rho + \delta\rho\rho, \quad (6.174)$$

or, equivalently

$$\rho\delta\rho\rho = (1 - \rho)\delta\rho(1 - \rho) = 0, \quad (6.175)$$

which means that the hole-hole (hh) and particle-particle (pp) block of  $\delta\rho$  have to vanish. Consequently, variations of  $\delta\rho$  are restricted to hp ( $\delta\rho_{ia}$ ) and ph ( $\delta\rho_{ai}$ ) matrix elements, leading to the stationary condition

$$\delta E_{\text{HF}}[\rho] = \sum_{p,s} h_{ps}[\rho] \delta\rho_{sp} = \sum_{i,a} h_{ai}[\rho] \delta\rho_{ia} + \text{H.c.} = 0, \quad (6.176)$$



which means that ph matrix elements of  $h[\rho]$  have to vanish. We can recast the problem into a commutator

$$[h[\rho], \rho] = 0, \quad (6.177)$$

which states that there exists a simultaneous eigenbasis of  $h[\rho]$  and  $\rho$  that can be obtained by solving the eigenvalue problem for the HF single-particle Hamiltonian

$$h[\rho]|\varphi_w\rangle = \epsilon_w |\varphi_w\rangle. \quad (6.178)$$

Here,  $|\varphi_w\rangle$  denotes the HF eigenstates and  $\epsilon_w$  the corresponding HF single-particle energies. Because the HF single-particle Hamiltonian depends on the one-body density matrix, i.e., on the solution of the eigenvalue problem, Eq. (6.178), this nonlinear problem has to be solved iteratively. Transforming the eigenvalue problem to the HO basis yields

$$\sum_s \left( t_{ps}^{(1)} + \sum_i \sum_{q,t} v_{pqst}^{(2)} D_{ti} D_{qi}^* + \frac{1}{2} \sum_{i,j} \sum_{q,r,t,u} v_{pqrst}^{(3)} D_{uj} D_{rj}^* D_{ti} D_{qi}^* \right) D_{sw} = \epsilon_w D_{pw}. \quad (6.179)$$

Employing the diagonal form of the one-body density matrix in the HF basis, the summations in the mean-field Hamiltonian can be restricted to hole states  $j$  and  $k$

$$h_{ps}[\rho] = t_{ps}^{(1)} + \sum_j v_{pjsj}^{(2)} + \frac{1}{2} \sum_{j,k} v_{pjksjk}^{(3)}, \quad (6.180)$$

and for the HF single-particle energies we obtain

$$\epsilon_w = t_{ww}^{(1)} + \sum_j v_{wjwj}^{(2)} + \frac{1}{2} \sum_{j,k} v_{wjkwjk}^{(3)}. \quad (6.181)$$

The HF ground-state energy is given by the sum over hole states  $i, j, k$

$$E_{\text{HF}} = \sum_i t_{ii}^{(1)} + \frac{1}{2} \sum_{i,j} v_{ijij}^{(2)} + \frac{1}{6} \sum_{i,j,k} v_{ijkijk}^{(3)}, \quad (6.182)$$

which can also be expressed in terms of the HF single-particle energies, Eq. (6.181),

$$E_{\text{HF}} = \sum_i \epsilon_i - \frac{1}{2} \sum_{i,j} v_{ijij}^{(2)} - \frac{1}{3} \sum_{i,j,k} v_{ijkijk}^{(3)}, \quad (6.183)$$

which is different from the results in the HO basis, Eq. (6.167). In summary, we have derived the ground-state energy of a closed-shell nucleus in HF approximation, taking into account a full three-body interaction. This extension to a full three-body interaction was, e.g., used in Ref. [154].

---

#### 6.4 In-medium similarity renormalization group

---

The In-Medium Similarity Renormalization Group (IM-SRG) unites the basic ideas of the renormalization-group evolution, discussed in Sec. 3, and normal ordering, introduced in Sec. 6.1. Instead of performing the evolution of free-space interactions in a two- or three-body basis, the term in-medium refers to the fact that the Schrödinger equation of an  $A$ -body system is solved in an approximate, but systematically improvable, way. The IM-SRG was first employed in the calculation of ground states of closed-shell nuclei [140, 154], while ground and excited states of open-shell nuclei were first accessible through the decoupling of valence-space interactions [168, 169]. Moreover, the generalization of the normal ordering to multi-reference states, such as particle-number projected Hartree-Fock Bogoliubov states, enabled calculations of ground states of even-even, open-shell nuclei [135]. Recently, normal ordering has also been performed with respect to  $N_{\text{max}}^{\text{ref}} = 0$  no-core shell model reference states for even-even, open-shell nuclei. The corresponding in-medium decoupled Hamiltonian is then used in subsequent no-core shell model calculations of ground and excited states [146]. While both valence and no-core shell model may ultimately be limited by the dimension of the largest diagonalizations possible, even with importance truncation, excited states of closed-shell nuclei have been recently calculated by applying EOM techniques to the ground-state-decoupled IM-SRG Hamiltonian [144]. However, in this work we will focus on ground-state properties of closed-shell nuclei. In Sec. 6.4.1 we will outline the basic concepts and derive the  $m$ -scheme flow equations for the single-reference case, while in Sec. 6.4.2 we will present the generators, employed to achieve decoupling. Since we are not only interested in the ground-state energy, but also in other observables, e.g., charge radii, which need to be evolved simultaneously with the Hamiltonian, we will present the Magnus formulation, that directly aims at the construction of the unitary transformation itself. Our discussion follows the review [14], where further details can be found. For a review on multi-reference IM-SRG calculations we refer to [121].

### 6.4.1 Basics and flow equations

Similar to the SRG evolution of the initial Hamiltonian, discussed in Sec. 3, the IM-SRG also employs a continuous sequence of unitary transformations

$$H_s = U_s H_0 U_s^\dagger \quad (6.184)$$

to evolve the normal-ordered Hamiltonian, resulting in the same differential flow-equation

$$\frac{dH_s}{ds} = [\eta_s, H_s], \quad (6.185)$$

where we have used the flow parameter  $s$  to discriminate between free-space, for which the flow parameter is denoted  $\alpha$ , and in-medium SRG. While both methods start from renormalization-group ideas, the goals are conceptually different.

The free-space SRG aims at a unitary transformation to decouple low- and high momentum scales, accelerating the convergence of many-body calculations. However, it is not the goal to evolve the input Hamiltonian to  $\alpha \rightarrow \infty$ , which is equivalent to a full diagonalization yielding momentum eigenstates. In this limit induced terms of higher particle rank, that arise from the evaluation of the commutator in every step of the evolution, would become unnaturally large, degrading the hierarchy of nuclear forces. Thus, the focus is unambiguously on the prediagonalization of nuclear interactions, although the optimal flow parameter range for a given generator, yielding improved convergence and only modest induced higher-body forces, is *a priori* unknown.

The IM-SRG aims, however, at the decoupling of the reference state from its particle-hole excitations. Starting from a single Slater determinant as the reference state  $|\Phi_0\rangle$  the intrinsic nuclear  $A$ -body Hamiltonian Eq. (6.1) can be rewritten exactly in terms of normal-ordered operators, as detailed in Sec. 6.1 for a 3N interaction,

$$H = E + \sum_{p,s} f_{ps} :a_p^\dagger a_s :_{|\Phi_0\rangle} + \frac{1}{4} \sum_{p,q,s,t} \Gamma_{pqst} :a_p^\dagger a_q^\dagger a_t a_s :_{|\Phi_0\rangle} + \frac{1}{36} \sum_{p,q,r,s,t,u} W_{pqrst} :a_p^\dagger a_q^\dagger a_r^\dagger a_u a_t a_s :_{|\Phi_0\rangle}. \quad (6.186)$$

In the following we employ the eigenbasis of the one-body density matrix, obtained by solving the eigenvalue problem for the HF single-particle Hamiltonian, so that

$$\rho_{ab} = n_a \delta_{ab}, \quad n_a \in \{0, 1\}, \quad (6.187)$$

which renders the distinction of hole ( $i, j, k, \dots$ ), particle ( $a, b, c, \dots$ ) and generic indices ( $p, q, r, \dots$ ) obsolete. The different terms in Eq. (6.186) are

$$E = \left(1 - \frac{1}{A}\right) \sum_a \langle a | T^{(1)} | a \rangle n_a + \frac{1}{2} \sum_{a,b} \langle ab | T^{(2)} + V^{(2)} | ab \rangle n_a n_b + \frac{1}{6} \sum_{a,b,c} \langle abc | V^{(3)} | abc \rangle n_a n_b n_c, \quad (6.188)$$

$$f_{ps} = \left(1 - \frac{1}{A}\right) \langle p | T^{(1)} | s \rangle + \sum_a \langle pa | T^{(2)} + V^{(2)} | sa \rangle n_a + \frac{1}{2} \sum_{a,b} \langle pab | V^{(3)} | sab \rangle n_a n_b, \quad (6.189)$$

$$\Gamma_{pqst} = \langle pq | T^{(2)} + V^{(2)} | st \rangle + \sum_a \langle pqa | V^{(3)} | sta \rangle n_a, \quad (6.190)$$

$$W_{pqrst} = \langle pqr | V^{(3)} | stu \rangle, \quad (6.191)$$

where only hole (occupied) states contribute in the summation over occupation numbers in Eqs. (6.188)–(6.190).

Inserting the normal-ordered Hamiltonian, Eq. (6.186), into the IM-SRG flow equation, Eq. (6.185), yields an exact unitary transformation in  $A$ -body space. Since the evaluation of the commutator increases the particle rank in every step of the flow  $\eta_s$  and  $H_s$  are  $A$ -body operators, although they initially have a lower particle rank at  $s = 0$ . In contrast to the free-space SRG, the induced contributions will contribute to terms in  $H_s$  with lower particle rank in successive integration steps. This will become clear in the following when deriving the  $m$ -scheme flow equations. Obviously, it is not feasible to include contributions up to the  $A$ -body level, so that a definition of a truncation scheme is required to close the set of IM-SRG flow equations. Due to the computational demands associated with handling three-body operators,  $\eta_s$  and  $H_s$  are truncated to particle rank  $n = 2$ , leading to the IM-SRG(2) approximation. Thus, for each flow parameter  $s$  we truncate  $H_s$  and  $\eta_s$  to

$$H_s \approx E(s) + f(s) + \Gamma(s), \quad (6.192)$$

$$\eta_s \approx \eta^{(1)}(s) + \eta^{(2)}(s), \quad (6.193)$$

employing the NO2B approximation of the Hamiltonian introduced in Sec. 6.1. Inserting this into Eq. (6.185) leads to

$$\frac{d(E(s) + f(s) + \Gamma(s))}{ds} = [\eta^{(1)}(s) + \eta^{(2)}(s), E(s) + f(s) + \Gamma(s)] \quad (6.194)$$

$$= [\eta^{(1)}(s), f(s)] + [\eta^{(1)}(s), \Gamma(s)] + [\eta^{(2)}(s), f(s)] + [\eta^{(2)}(s), \Gamma(s)]. \quad (6.195)$$

The evaluation of the commutator for two general normal-ordered operators of rank  $M$  and  $N$  results in contributions of rank  $|M - N|, \dots, M + N - 1$ ,

$$[A^{(M)}, B^{(N)}] = \sum_{k=|M-N|}^{M+N-1} C^{(k)}. \quad (6.196)$$

By employing this property we can evaluate the commutators in Eq. (6.195) to

$$[\eta^{(1)}(s), f(s)] = [\eta^{(1)}(s), f(s)]^{(0)} + [\eta^{(1)}(s), f(s)]^{(1)}, \quad (6.197)$$

$$[\eta^{(1)}(s), \Gamma(s)] = [\eta^{(1)}(s), \Gamma(s)]^{(1)} + [\eta^{(1)}(s), \Gamma(s)]^{(2)}, \quad (6.198)$$

$$[\eta^{(2)}(s), f(s)] = [\eta^{(2)}(s), f(s)]^{(1)} + [\eta^{(2)}(s), f(s)]^{(2)}, \quad (6.199)$$

$$[\eta^{(2)}(s), \Gamma(s)] = [\eta^{(2)}(s), \Gamma(s)]^{(0)} + [\eta^{(2)}(s), \Gamma(s)]^{(1)} + [\eta^{(2)}(s), \Gamma(s)]^{(2)} + \underbrace{[\eta^{(2)}(s), \Gamma(s)]^{(3)}}_{=0, \text{ due to IM-SRG(2)}}, \quad (6.200)$$

where the last term contributes to particle rank  $k = 3$ , which exceeds the truncation of the IM-SRG(2) approximation. Since we do not distinguish hole and particle indices any longer, the contraction between two hole, Eq. (6.15), and two particle, Eq. (6.16), states is modified, using the eigenbasis of the one-body density matrix, Eq. (6.187), to

$$\overline{a_a^\dagger a_b} \equiv \langle \Phi_0 | a_a^\dagger a_b | \Phi_0 \rangle \equiv \rho_{ba} = n_b \delta_{ba}, \quad (6.201)$$

$$\overline{a_a a_b^\dagger} \equiv \langle \Phi_0 | a_a a_b^\dagger | \Phi_0 \rangle = \delta_{ab} - \rho_{ab} = (1 - n_a) \delta_{ab}. \quad (6.202)$$

Thus, the summation over Eq. (6.201) only contributes for hole (occupied) states, while the summation over Eq. (6.202) only contributes for particle (unoccupied) states. Therefore, we can simplify the commutators by applying the generalized Wick's theorem, Eq. (6.13), to

$$[\eta^{(1)}(s), f(s)]^{(0)} = \sum_{a,b,p,s} \eta_{ab} f_{ps} : \overline{a_a^\dagger a_b a_p^\dagger a_s} :_{|\Phi_0\rangle} - f_{ps} \eta_{ab} : \overline{a_p^\dagger a_s a_a^\dagger a_b} :_{|\Phi_0\rangle} \quad (6.203)$$

$$= \sum_{a,b,p,s} \eta_{ab} f_{ps} \rho_{sa} (\delta_{bp} - \rho_{bp}) - f_{ps} \eta_{ab} \rho_{bp} (\delta_{sa} - \rho_{sa}) \quad (6.204)$$

$$= \sum_{a,b,p,s} \eta_{ab} f_{ps} \rho_{sa} \delta_{bp} - \eta_{ab} f_{ps} \rho_{sa} \rho_{bp} - f_{ps} \eta_{ab} \rho_{bp} \delta_{sa} + f_{ps} \eta_{ab} \rho_{bp} \rho_{sa} \quad (6.205)$$

$$= \sum_{a,b,p,s} \eta_{ab} f_{ps} n_s \delta_{sa} \delta_{bp} - f_{ps} \eta_{ab} n_b \delta_{bp} \delta_{sa} \quad (6.206)$$

$$= \sum_{a,b} \eta_{ab} f_{ba} (n_a - n_b), \quad (6.207)$$

$$[\eta^{(1)}(s), f(s)]^{(1)} = \sum_{a,b,p,s} \eta_{ab} f_{ps} : \overline{a_a^\dagger a_b a_p^\dagger a_s} :_{|\Phi_0\rangle} - f_{ps} \eta_{ab} : \overline{a_p^\dagger a_s a_a^\dagger a_b} :_{|\Phi_0\rangle} + \eta_{ab} f_{ps} : a_a^\dagger \overline{a_b a_p^\dagger} a_s :_{|\Phi_0\rangle} - f_{ps} \eta_{ab} : a_p^\dagger \overline{a_s a_a^\dagger} a_b :_{|\Phi_0\rangle} \quad (6.208)$$

$$= \sum_{a,b,p,s} \eta_{ab} f_{ps} \rho_{sa} : a_b a_p^\dagger :_{|\Phi_0\rangle} - f_{ps} \eta_{ab} \rho_{bp} : a_s a_a^\dagger :_{|\Phi_0\rangle} + \eta_{ab} f_{ps} (\delta_{bp} - \rho_{bp}) : a_a^\dagger a_s :_{|\Phi_0\rangle} - f_{ps} \eta_{ab} (\delta_{sa} - \rho_{sa}) : a_p^\dagger a_b :_{|\Phi_0\rangle} \quad (6.209)$$

$$= \sum_{a,b,p,s} \eta_{ab} f_{ps} \delta_{bp} : a_a^\dagger a_s :_{|\Phi_0\rangle} - f_{ps} \eta_{ab} \delta_{sa} : a_p^\dagger a_b :_{|\Phi_0\rangle} \quad (6.210)$$

$$= \sum_{a,p,s} \eta_{ap} f_{ps} : a_a^\dagger a_s :_{|\Phi_0\rangle} - \sum_{b,p,s} f_{ps} \eta_{sb} : a_p^\dagger a_b :_{|\Phi_0\rangle} \quad (6.211)$$

$$= \sum_{a,p,s} \eta_{pa} f_{as} : a_p^\dagger a_s :_{|\Phi_0\rangle} - \sum_{a,p,s} f_{pa} \eta_{as} : a_p^\dagger a_s :_{|\Phi_0\rangle} \quad (6.212)$$

$$= \sum_{a,p,s} (\eta_{pa} f_{as} - f_{pa} \eta_{as}) : a_p^\dagger a_s :_{|\Phi_0\rangle} = \sum_{a,p,s} (1 + P_{ps}) \eta_{pa} f_{as} : a_p^\dagger a_s :_{|\Phi_0\rangle}, \quad (6.213)$$

where we used the permutation symbol  $P_{ps}$ , which interchanges the attached indices in any expression except for the normal-ordered operator string, i.e.,

$$P_{ps} g(\dots, p, \dots, s) \equiv g(\dots, s, \dots, p). \quad (6.214)$$

Evaluation of the remaining commutators and rearranging the results according to their particle rank leads to a set of coupled ordinary differential equations (ODE) for  $E(s)$ ,  $f(s)$  and  $\Gamma(s)$

$$\frac{dE}{ds} = \sum_{a,b} (n_a - n_b) \eta_{ab} f_{ba} + \frac{1}{2} \sum_{a,b,c,d} \eta_{abcd} \Gamma_{cdab} n_a n_b \bar{n}_c \bar{n}_d, \quad (6.215)$$

$$\begin{aligned} \frac{df_{ps}}{ds} &= \sum_a (1 + P_{ps}) \eta_{pa} f_{as} + \sum_{a,b} (n_a - n_b) (\eta_{ab} \Gamma_{bpas} - f_{ab} \eta_{bpas}) \\ &+ \frac{1}{2} \sum_{a,b,c} (n_a n_b \bar{n}_c + \bar{n}_a \bar{n}_b n_c) (1 + P_{ps}) \eta_{cpab} \Gamma_{abcs}, \end{aligned} \quad (6.216)$$

$$\begin{aligned} \frac{d\Gamma_{pqst}}{ds} &= \sum_a \{ (1 - P_{pq}) (\eta_{pa} \Gamma_{aqst} - f_{pa} \eta_{aqst}) - (1 - P_{st}) (\eta_{as} \Gamma_{pqat} - f_{as} \eta_{pqat}) \} \\ &+ \frac{1}{2} \sum_{a,b} (1 - n_a - n_b) (\eta_{pqab} \Gamma_{abst} - \Gamma_{pqab} \eta_{abst}) - \sum_{a,b} (n_a - n_b) (1 - P_{pq}) (1 - P_{st}) \eta_{bqat} \Gamma_{apbs}, \end{aligned} \quad (6.217)$$

with  $\bar{n}_a = 1 - n_a$ , and the  $s$ -dependence suppressed for brevity. The ground-state energy is obtained by integrating Eqs. (6.215)–(6.217) from  $s = 0$  to  $s \rightarrow \infty$ , with the initial condition at  $s = 0$  given by the normal-ordered Hamiltonian in Eqs. (6.188)–(6.190). To perform the integration we have to specify the generator  $\eta$ , which is done in Sec. 6.4.2. While we here only discussed the  $m$ -scheme flow equations, it is numerically beneficial to use  $J$ -scheme flow equations for systems with explicit spherical symmetry, e.g., for closed-shell nuclei. In this case the rotational symmetry of the Hamiltonian is preserved and the flow equations are block-diagonal in angular momentum and independent of the angular momentum projection.

## 6.4.2 Generators

The goal of a single-reference IM-SRG calculations is the extraction of the ground-state energy of a closed-shell nucleus. By representing the starting Hamiltonian  $H_{s=0}$  in terms of  $A$ -particle- $A$ -hole (ApAh) excitations of the reference state  $|\Phi_0\rangle$ , employed to perform the normal ordering, we obtain a schematic representation shown in Fig. 6.9. Here, we start from a two-body Hamiltonian. According to Slater-Condon rules, which simplify the calculation of matrix elements  $\langle \Phi' | O_N | \Phi \rangle$  of  $N$ -body operators  $O_N$  in an  $A$ -body Slater determinant basis to contributions for

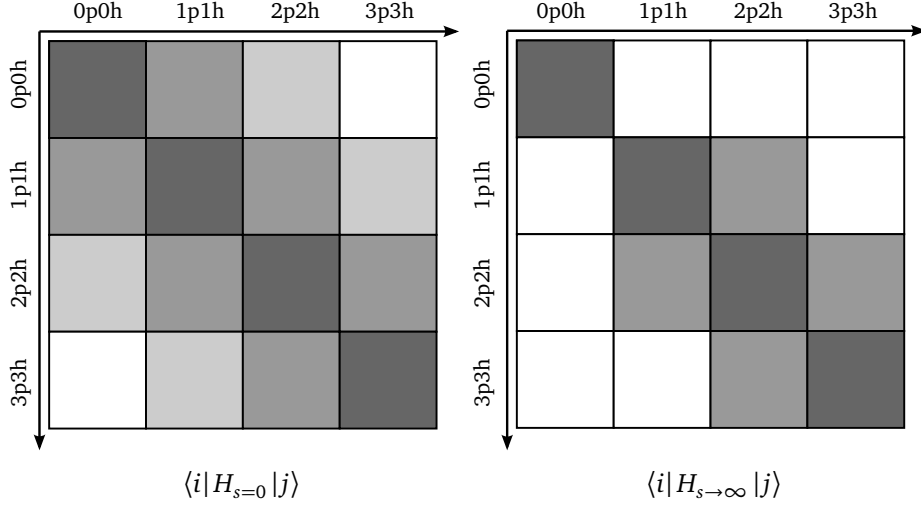


**Figure 6.9:** Initial,  $H_{s=0}$ , and final,  $H_{s \rightarrow \infty}$ , nuclear many-body Hamiltonian at the two-body level, represented in terms of particle-hole excitations of the reference state  $|\Phi_0\rangle$ . Taken from Ref. [14].

which bra  $\langle \Phi' |$  and ket  $|\Phi\rangle$  differ in at most  $N$  orbitals. Thus, a two-body Hamiltonian can only connect  $nph$  to  $(n \pm 2)p(n \pm 2)h$  blocks. Thus,  $0p0h$ - $3p3h$  or  $1p1h$ - $4p4h$  blocks are zero. To obtain the ground-state energy we, therefore, need to decouple the  $0p0h$  block from  $1p1h$  and  $2p2h$  excitations

$$\langle \Phi_0 | H_0 : a_p^\dagger a_h : | \Phi_0 \rangle = f_{ph}, \quad (6.218)$$

$$\langle \Phi_0 | H_0 : a_p^\dagger a_{p'}^\dagger a_{h'} a_h : | \Phi_0 \rangle = \Gamma_{pp'hh'}, \quad (6.219)$$

which define with their Hermitian conjugates the off-diagonal part of the Hamiltonian.

$$H_s^{od} = \sum_{p,h} f_{ph} : a_p^\dagger a_h : | \Phi_0 \rangle + \frac{1}{4} \sum_{p,p',h,h'} \Gamma_{pp'hh'} : a_p^\dagger a_{p'}^\dagger a_{h'} a_h : | \Phi_0 \rangle + \text{H.c.} \quad (6.220)$$

Note that for a Hartree-Fock reference state the  $0p0h$ - $1p1h$  block of  $H_0$  is zero due to Brillouin's theorem, stating that

$$\langle \Phi_0 | H_0 : a_p^\dagger a_h : | \Phi_0 \rangle = 0. \quad (6.221)$$

This is due to the fact that the hole-particle  $f_{hp}$  and particle-hole  $f_{ph}$  matrix elements have to vanish to fulfill the stationary condition given in Eq. (6.176).

The virtue of the IM-SRG, similar to the free-space SRG, is its flexibility in choosing different generators to achieve the decoupling. In the following we will discuss three standard choices for the generator and their decoupling behavior.

The first choice for the generator  $\eta_s$  is similar to the form employed in the free-space SRG proposed by Wegner [110]

$$\eta_s = [H_s^d, H_s^{od}]. \quad (6.222)$$

Inserting the definition of the off-diagonal Hamiltonian, Eq. (6.220), and evaluating the same commutators as for the IM-SRG(2) flow equations, results in

$$\begin{aligned} \eta_{ph} &= \sum_a (1 - P_{ph}) f_{pa}^d f_{ah}^{od} + \sum_{a,b} (n_a - n_b) (f_{ab}^d \Gamma_{bpah}^{od} - f_{ab}^{od} \Gamma_{bpah}^d) \\ &+ \frac{1}{2} \sum_{a,b,c} (n_a n_b \bar{n}_c + \bar{n}_a \bar{n}_b n_c) (1 - P_{ph}) \Gamma_{cpab}^d \Gamma_{abch}^{od}, \end{aligned} \quad (6.223)$$

$$\begin{aligned} \eta_{pp'hh'} &= \sum_a \left\{ (1 - P_{pp'}) (f_{pa}^d \Gamma_{ap'hh'}^{od} - f_{pa}^{od} \Gamma_{ap'hh'}^d) - (1 - P_{hh'}) (f_{ah}^d \Gamma_{pp'ah'}^{od} - f_{ah}^{od} \Gamma_{pp'ah'}^d) \right\} \\ &+ \frac{1}{2} \sum_{a,b} (1 - n_a - n_b) (\Gamma_{pp'ab}^d \Gamma_{abhh'}^{od} - \Gamma_{pp'ab}^{od} \Gamma_{abhh'}^d) - \sum_{a,b} (n_a - n_b) (1 - P_{pp'}) (1 - P_{hh'}) \Gamma_{bp'ah'}^d \Gamma_{apbh}^{od}. \end{aligned} \quad (6.224)$$

These equations are identical to the flow equations, Eqs. (6.216)–(6.217), up to signs, which arise from the anti-Hermiticity of the generator. There are two scenarios for the flow equation to reach a fixed point, i.e.,  $\eta_s$  vanishes:  $H_s^d$  and  $H_s^{od}$  can commute at finite  $s$ , or  $H_s^{od} \rightarrow 0$  for  $s \rightarrow \infty$  as desired. Since off-diagonal matrix elements between states with large energy differences are eliminated first

$$\langle i | H_s^{od} | j \rangle \approx \langle i | H_{s_0}^{od} | j \rangle e^{-(E_i - E_j)^2 (s - s_0)}, \quad s > s_0, \quad (6.225)$$

the flow has a proper RG character. Furthermore, the non-existence of energy denominators, which might become small as for the White generator discussed below, is useful. In numerical applications, however, the Wegner generator is less efficient than other choices. The construction of the generator is as expensive as the evaluation of the flow equation,  $\mathcal{O}(N^6)$  in a single-particle basis of dimension  $N$ , and cubic terms in  $f$  or  $\Gamma$  on the right-hand side of Eqs. (6.215)–(6.217) result in a stiff flow equation. Thus, the adequate ODE solvers for these flow equations have higher memory demands due to the storage of several copies of the solution vector and need more intermediate steps, leading to longer runtimes, than for non-stiff or weakly stiff cases.

The second choice for  $\eta_s$  is motivated by the work of White on canonical transformations in quantum chemistry [170]

$$\eta_s^{A/B} \equiv \sum_{p,h} \frac{f_{ph}}{\Delta_{A/B}^{ph}} : a_p^\dagger a_h : |\Phi_0\rangle + \frac{1}{4} \sum_{p,p',h,h'} \frac{\Gamma_{pp'hh'}}{\Delta_{A/B}^{pp'hh'}} : a_p^\dagger a_{p'}^\dagger a_{h'} a_h : |\Phi_0\rangle - \text{H.c.} \quad (6.226)$$

Since  $f$  and  $\Gamma$  are part of the Hamiltonian and therefore Hermitian, the energy denominators have to induce a sign change under transposition to fulfill the anti-Hermiticity of  $\eta_s$ . The superscripts  $A$  and  $B$  in the definition of the White generator correspond to two different choices for the energy denominators. The Epstein-Nesbet case is constructed from diagonal matrix elements of the Hamiltonian in particle-hole representation

$$\Delta_{ph}^A \equiv f_{pp} - f_{hh} + (n_p - n_h) \Gamma_{phph} = -\Delta_{hp}^A, \quad (6.227)$$

$$\Delta_{pp'hh'}^A \equiv f_{pp} + f_{p'p'} - f_{hh} - f_{h'h'} + (1 - n_p - n_{p'}) \Gamma_{pp'pp'} - (1 - n_h - n_{h'}) \Gamma_{hh'hh'} \\ + (n_p - n_h) \Gamma_{phph} + (n_{p'} - n_{h'}) \Gamma_{p'h'p'h'} + (n_p - n_{h'}) \Gamma_{ph'p'h'} + (n_{p'} - n_h) \Gamma_{p'h'p'h} \quad (6.228)$$

$$= -\Delta_{hh'pp'}^A. \quad (6.229)$$

The Møller-Plesset case is defined as

$$\Delta_{ph}^B \equiv f_{pp} - f_{hh} = -\Delta_{hp}^B, \quad (6.230)$$

$$\Delta_{pp'hh'}^B \equiv f_{pp} + f_{p'p'} - f_{hh} - f_{h'h'} = -\Delta_{hh'pp'}^B. \quad (6.231)$$

The White generator equally suppresses all off-diagonal matrix elements

$$\langle i | H_s^{od} | j \rangle \approx \langle i | H_{s_0}^{od} | j \rangle e^{-(s - s_0)}, \quad s > s_0, \quad (6.232)$$

which does not lead to a proper RG flow. Since we are only interested in the limit  $s \rightarrow \infty$ , for which all unitary transformations suppressing  $H^{od}$  are equivalent up to differences caused by the truncation of the IM-SRG flow equation, the character of the RG flow is not considered further. In numerical applications it is beneficial that the construction of the White generator scales like  $\mathcal{O}(N_h^2 N_p^2)$  with the number of holes (particles)  $N_h$  ( $N_p$ ). Furthermore, since the generator is constructed from energy ratios, inserting it on the right-hand side of Eqs. (6.215)–(6.217) preserves the linearity in  $f$  or  $\Gamma$ . This significantly decreases the stiffness of the flow equations compared to those for the canonical Wegner generator and, therefore, also lowers the number of integration steps, required to solve the IM-SRG flow equations. However, the drawback of the White generator are the energy denominators, which might become small or even vanish. This can be tamed by employing an alternative ansatz, also inspired by White [170]

$$\eta_s^{A/B} \equiv \frac{1}{2} \sum_{p,h} \arctan \frac{2f_{ph}}{\Delta_{A/B}^{ph}} : a_p^\dagger a_h : |\Phi_0\rangle + \frac{1}{8} \sum_{p,p',h,h'} \arctan \frac{2\Gamma_{pp'hh'}}{\Delta_{A/B}^{pp'hh'}} : a_p^\dagger a_{p'}^\dagger a_{h'} a_h : |\Phi_0\rangle - \text{H.c.} \quad (6.233)$$

Thus, the fractions in the generator  $\eta_s$  are regularized by the arctan function, and explicitly limited to the interval  $]-\frac{\pi}{2}, \frac{\pi}{2}[$ . The initial ansatz for the White generator, Eq. (6.226), is recovered when expanding the arctan function for small arguments.

The third choice for the generator is inspired by imaginary-time evolution techniques, used in quantum Monte Carlo methods, and is defined as

$$\eta_s^{A/B} \equiv \sum_{p,h} \text{sgn}(\Delta_{ph}^{A/B}) f_{ph} : a_p^\dagger a_h : |\Phi_0\rangle + \frac{1}{4} \sum_{p,p',h,h'} \text{sgn}(\Delta_{pp'hh'}^{A/B}) \Gamma_{pp'hh'} : a_p^\dagger a_{p'}^\dagger a_h a_{h'} : |\Phi_0\rangle - \text{H.c.}, \quad (6.234)$$

employing again two different choices for  $\Delta$ . Here, the use of fractions, and thereby small or vanishing energy denominators, is explicitly avoided, while the sign functions are needed to ensure that off-diagonal matrix elements are suppressed instead of enhanced during the flow. Inserting the imaginary-time generator into the right-hand side of the IM-SRG(2) flow equations, Eqs. (6.215)–(6.217), leads to quadratic terms in  $f$  or  $\Gamma$ , resulting in a mild increase in the stiffness compared to the use of the White generator. The effort for the construction of the imaginary-time generator scales like  $\mathcal{O}(N_h^2 N_p^2)$ , which is identical to the White generator. The imaginary-time generator, however, generates a proper RG flow, linearly suppressing off-diagonal matrix elements between states with large energy differences first

$$\langle i | H_s^{od} | j \rangle \approx \langle i | H_{s_0}^{od} | j \rangle e^{-|E_i - E_j|(s - s_0)}, \quad s > s_0. \quad (6.235)$$

### 6.4.3 General observables and Magnus formulation

So far, our discussion was focused on the evolution of the Hamiltonian to obtain the ground-state energy of a closed-shell nucleus. For the evaluation of other observables we have to normal order the operator  $O_s$  with respect to the same reference state  $|\Phi_0\rangle$ , used for the Hamiltonian, and evaluate the flow equation

$$\frac{dO_s}{ds} = [\eta_s, O_s], \quad (6.236)$$

with the same generator  $\eta_s$  as in the flow equation of the Hamiltonian. The flow equation for other observables is also truncated at the two-body level to be consistent with the IM-SRG(2) truncation scheme. Thus, we obtain a full set of flow-equations for every other observable, that has to be evolved alongside with the Hamiltonian, leading to a considerable increase in memory demands when being interested in several observables. In addition, each operator may have a different decay pattern compared to the Hamiltonian, leading to ODEs becoming stiff.

In contrast to the free-space SRG, where the unitary transformation is recovered from the eigenvectors of the unevolved and evolved Hamiltonians, Eq. (3.17), in the two- or three-body system, the exact diagonalization of the Hamiltonian for the  $A$ -body problem is prohibited by the computational cost, increasing factorially with the size of the single-particle basis. The use of large-scale no-core shell model calculations is also not valuable because only the lowest eigenstates are obtained via Lanczos methods.

An alternative approach, also suggested for the free-space SRG, is the evolution of the unitary transformation  $U_s$  itself

$$\frac{dU_s}{ds} = \eta_s U_s, \quad (6.237)$$

with the initial condition  $U_{s=0} = \mathbb{1}$ . Magnus [171] proposed, however, to write the unknown operators  $U_s$  as a matrix exponential

$$U_s = e^{\Omega_s}, \quad (6.238)$$

with the anti-Hermitian operator  $\Omega_s$ , i.e.,  $\Omega_s^\dagger = -\Omega_s$ , and the initial condition  $\Omega_{s=0} = 0$ . The formally exact derivative yields

$$\frac{d\Omega_s}{ds} = \sum_{k=0}^{\infty} \frac{B_k}{k!} ad_{\Omega_s}^k(\eta_s), \quad (6.239)$$

where  $B_k$  denotes the Bernoulli numbers and  $ad_{\Omega_s}^k(\eta_s)$  the recursively defined nested commutators

$$ad_{\Omega_s}^0(\eta_s) = \eta_s, \quad (6.240)$$

$$ad_{\Omega_s}^k(\eta_s) = [\Omega_s, ad_{\Omega_s}^{k-1}(\eta_s)], \quad k \geq 1. \quad (6.241)$$

Integration of Eq. (6.239) by Picard iteration leads to an infinite series for  $\Omega_s$ , the so-called Magnus series,

$$\Omega_s = \sum_{n=1}^{\infty} \Omega_{s,n}. \quad (6.242)$$

To determine the formulas for the first terms in the series we introduce some parameter  $\epsilon$ .  $\eta_s$  is linear in  $\epsilon$ , while  $\Omega_{s,n}$  is supposed to be of order  $\epsilon^n$ , leading to

$$\Omega_s = \sum_{n=1}^{\infty} \epsilon^n \Omega_{s,n}. \quad (6.243)$$

Obviously, the Magnus series, Eq. (6.242), is recovered by taking  $\epsilon = 1$ . Inserting the modified series in Eq. (6.239) results in

$$\begin{aligned} \frac{d(\epsilon\Omega_{s,1} + \epsilon^2\Omega_{s,2} + \dots)}{ds} &= \epsilon\eta_s - \frac{1}{2}[\epsilon\Omega_{s,1} + \epsilon^2\Omega_{s,2} + \dots, \epsilon\eta_s] \\ &+ \frac{1}{12}[\epsilon\Omega_{s,1} + \epsilon^2\Omega_{s,2} + \dots, [\epsilon\Omega_{s,1} + \epsilon^2\Omega_{s,2} + \dots, \epsilon\eta_s]] + \dots, \end{aligned} \quad (6.244)$$

and equating powers of  $\epsilon$  leads to the first three terms

$$\frac{d\Omega_{s,1}}{ds} = \eta_s, \quad (6.245)$$

$$\frac{d\Omega_{s,2}}{ds} = -\frac{1}{2}[\Omega_{s,1}, \eta_s], \quad (6.246)$$

$$\frac{d\Omega_{s,3}}{ds} = -\frac{1}{2}[\Omega_{s,2}, \eta_s] + \frac{1}{12}[\Omega_{s,1}, [\Omega_{s,1}, \eta_s]]. \quad (6.247)$$

The final result after integration reads

$$\Omega_{s,1} = \int_0^s ds_1 \eta_{s_1}, \quad (6.248)$$

$$\Omega_{s,2} = \frac{1}{2} \int_0^s ds_1 \int_0^{s_1} ds_2 [\eta_{s_1}, \eta_{s_2}], \quad (6.249)$$

$$\Omega_{s,3} = \frac{1}{6} \int_0^s ds_1 \int_0^{s_1} ds_2 \int_0^{s_2} ds_3 \{[\eta_{s_1}, [\eta_{s_2}, \eta_{s_3}]] + [[\eta_{s_1}, \eta_{s_2}], \eta_{s_3}]\}. \quad (6.250)$$

For more mathematical details and some applications of the Magnus expansion we refer to Ref. [172].

An improved formulation of the IM-SRG, utilizing the Magnus expansion, was presented in Ref. [143]. The virtue of the Magnus expansion is due to the fact that, even if  $\Omega_s$  is truncated to low-orders in  $\eta_s$ , the resulting transformation in Eq. (6.238) using the approximate  $\Omega_s$  is unitary. This also results in a computational advantage of the Magnus formulation. The flow equations for  $\Omega_s$ , Eq. (6.239), can be solved numerically using a simple first-order Euler step method and, although sizable time-step errors accumulate in  $\Omega_s$  with a first-order method, upon exponentiation the transformation, Eq. (6.238), is still unitary. The use of a first-order Euler step method leads to substantial memory savings, while in the conventional integration of the flow equations time-step errors accumulate directly in the evolved  $H_s$ , requiring the use of a high-order solver to sustain an acceptable level of accuracy.

Having determined the unitary transformation, Eq. (6.238), the Hamiltonian and any other operator of interest can be transformed by applying the Baker-Campbell-Hausdorff (BCH) formula,

$$H_s = e^{\Omega_s} H_0 e^{-\Omega_s} = \sum_{k=0}^{\infty} \frac{1}{k!} ad_{\Omega_s}^k(H_0), \quad (6.251)$$

$$O_s = e^{\Omega_s} O_0 e^{-\Omega_s} = \sum_{k=0}^{\infty} \frac{1}{k!} ad_{\Omega_s}^k(O_0). \quad (6.252)$$



Since Eq. (6.251) and Eq. (6.252) consist of an infinite-order series of nested commutators, generating up to  $A$ -body operators, a truncation scheme has to be introduced. In the Magnus(2) truncation  $H_s$ ,  $O_s$ ,  $\eta_s$  and  $\Omega_s$  as well as all commutators are truncated at the NO2B level. Even in this scheme, expressions for  $\frac{d\Omega_s}{ds}$ , Eq. (6.239), and  $H_s$  or  $O_s$ , Eq. (6.251) or Eq. (6.252), consist of an infinite number of terms. Truncating Eq. (6.251) at the  $N$ -th term leads to

$$H_s = \sum_{k=0}^N \frac{1}{k!} ad_{\Omega_s}^k(H_0) + \sum_{k=N+1}^{\infty} \frac{1}{k!} ad_{\Omega_s}^k(H_0), \quad (6.253)$$

defining the remainder of the series to be

$$\delta H_N \equiv \sum_{k=N+1}^{\infty} \frac{1}{k!} ad_{\Omega_s}^k(H_0). \quad (6.254)$$

Since we are interested in the size of  $\delta H_N$  we take the norm

$$\|\delta H_N\| = \sum_{k=N+1}^{\infty} \frac{1}{k!} \|ad_{\Omega_s}^k(H_0)\|, \quad (6.255)$$

and estimate the upper bound on the size of the nested commutator by

$$\|ad_{\Omega_s}^k(H_0)\| \leq 2\|\Omega_s\| \cdot \|ad_{\Omega_s}^{k-1}(H_0)\|. \quad (6.256)$$

Inserting this into the expression for the error we obtain

$$\|\delta H_N\| \leq \sum_{k=N+1}^{\infty} \frac{1}{k!} (2\|\Omega_s\|)^{k-N} \|ad_{\Omega_s}^N(H_0)\| \quad (6.257)$$

$$= \frac{\|ad_{\Omega_s}^N(H_0)\|}{(2\|\Omega_s\|)^N} \sum_{k=N+1}^{\infty} \frac{1}{k!} (2\|\Omega_s\|)^k. \quad (6.258)$$

In the last line we can identify the remainder for the Taylor expansion of  $e^{2\|\Omega_s\|}$ . Inserting the Lagrange form of the remainder gives

$$\|\delta H_N\| \leq \frac{\|ad_{\Omega_s}^N(H_0)\|}{(2\|\Omega_s\|)^N} \frac{e^{2\|\Omega_s\|}}{(N+1)!} (2\|\Omega_s\|)^{N+1} \quad (6.259)$$

$$= \|ad_{\Omega_s}^N(H_0)\| \frac{e^{2\|\Omega_s\|}}{(N+1)!} 2\|\Omega_s\|. \quad (6.260)$$

By introducing a threshold  $\epsilon_{\text{th}}$  such that  $\|\delta H_N\| \leq \epsilon_{\text{th}}\|H_0\|$  we arrive at the convergence criterion

$$\|ad_{\Omega_s}^N(H_0)\| \leq e^{-2\|\Omega_s\|} \frac{\epsilon_{\text{th}}\|H_0\|}{2\|\Omega_s\|} (N+1)!, \quad (6.261)$$

i.e., when the norm of the  $N$ -th nested commutator is below the convergence criterion the evaluation of the BCH expansion terminates.

---

## 6.5 Coupled-cluster method

---

The Coupled-Cluster Method was developed by Coester [173] and Coester and Kümmel [174] in the late 1950s and was originally denoted exp(S)-Method. While it became a widely used method in quantum chemistry, it was only scarcely used in nuclear theory, e.g., Kümmel *et al.* computed nuclear matter and the doubly-magic nuclei  ${}^4\text{He}$ ,  ${}^{16}\text{O}$ , and  ${}^{40}\text{Ca}$  using a formulation particularly suited to deal with the hard core of local NN interactions. Their calculations also revealed the relevance of 3N forces as stated in their review [175]. However, with the advent of chiral EFT and RG-evolved nuclear interactions CC theory has seen a renaissance, starting more than a decade ago [176]. Similar to the IM-SRG approach CC calculations do not obey the variational principle, however they are size extensive and exhibit a polynomial scaling in the model space size. In Sec. 6.5.1 we will discuss the basic concepts and derive the Coupled-Cluster equations for ground-state calculations of closed-shell nuclei. The extension to excited states of closed-shell nuclei as well as ground and excited states of  $A \pm 1$  and  $A + 2$  [142] systems near closed-sub shells by EOM techniques is introduced in Sec. 6.5.2. Since we are also interested in other observables, e.g., charge radii, we explain how these are obtained in Sec. 6.5.3. Our discussion follows the review [13] and Ref. [177], as well as references therein.

### 6.5.1 Coupled-cluster theory for closed-shell nuclei

The Coupled-Cluster Method employs, similar to the IM-SRG, an uncorrelated reference state  $|\Phi_0\rangle$  for the  $A$ -nucleon system, either obtained by naive filling of the HO orbitals or by a HF calculation. The exponential ansatz for the correlated CC wave function is given by

$$|\Psi^A\rangle = e^T |\Phi_0\rangle, \quad (6.262)$$

with the cluster operator  $T = T_1 + T_2 + T_3 + \dots + T_A$ . The different ranks  $k$  of the cluster operator correspond to different particle-hole (ph) excitation levels of the reference state

$$T_1 = \frac{1}{(1!)^2} \sum_{i,a} t_i^a :a_a^\dagger a_i: |\Phi_0\rangle, \quad (6.263)$$

$$T_2 = \frac{1}{(2!)^2} \sum_{i,j,a,b} t_{ij}^{ab} :a_a^\dagger a_b^\dagger a_j a_i: |\Phi_0\rangle, \quad (6.264)$$

⋮

$$T_k = \frac{1}{(k!)^2} \sum_{\substack{i_1, \dots, i_k \\ a_1, \dots, a_k}} t_{i_1 \dots i_k}^{a_1 \dots a_k} :a_{a_1}^\dagger \dots a_{a_k}^\dagger a_{i_k} \dots a_{i_1}: |\Phi_0\rangle, \quad (6.265)$$

where  $i, j, k, \dots$  denote hole and  $a, b, c, \dots$  particle states and the undetermined cluster amplitudes are given by

$$t = \left( \{t_i^a\}, \{t_{ij}^{ab}\}, \dots, \{t_{i_1 \dots i_k}^{a_1 \dots a_k}\} \right). \quad (6.266)$$

These are defined to be antisymmetric in hole and separately in particle indices,

$$t_{\mathcal{P}(i_1 \dots i_k)}^{\mathcal{P}'(a_1 \dots a_k)} = (-1)^{\text{sgn}(\mathcal{P}) + \text{sgn}(\mathcal{P}')} t_{i_1 \dots i_k}^{a_1 \dots a_k}, \quad (6.267)$$

with the permutation operators  $\mathcal{P}$ ,  $\mathcal{P}'$  and the corresponding signs of the permutation  $\text{sgn}(\mathcal{P})$ ,  $\text{sgn}(\mathcal{P}')$ .

Neglecting the residual three-body term in the normal-ordered Hamiltonian, Eq. (6.186), the eigenvalue problem for the  $A$ -nucleon system in NO2B approximation is written as

$$H |\Psi^A\rangle = E |\Psi^A\rangle. \quad (6.268)$$

However, in CC theory the ground-state energy is split into the energy of the reference state  $E_{\text{ref}}$  and the correlation energy  $\Delta E$ , given by

$$\Delta E = E - E_{\text{ref}}. \quad (6.269)$$

Thus, we can rewrite the eigenvalue problem in terms of the Hamiltonian  $H_N = F_N + V_N$ , consisting of the normal-ordered one-body Fock operator  $F_N$  and the normal-ordered two-body interaction operator  $V_N$ , to

$$H_N |\Psi^A\rangle = (H - E_{\text{ref}}) |\Psi^A\rangle = \Delta E |\Psi^A\rangle. \quad (6.270)$$

Multiplication with  $e^{-T}$  and insertion of the exponential ansatz, Eq. (6.262), result in

$$e^{-T} H_N |\Psi^A\rangle = e^{-T} H_N e^T |\Phi_0\rangle \equiv \bar{H} |\Phi_0\rangle = e^{-T} \Delta E e^T |\Phi_0\rangle = \Delta E |\Phi_0\rangle, \quad (6.271)$$

where we introduced the similarity-transformed Hamiltonian  $\bar{H}$ . Note that the cluster operator  $T$  is not anti-Hermitian, i.e.,  $T^\dagger \neq -T$ . While  $T$  and  $-T$  both correspond to excitations,  $T^\dagger$  describes de-excitations. Thus, the transformation  $U = e^T$  is not unitary and consequently the similarity-transformed Hamiltonian  $\bar{H} = U^{-1} H_N U$  is not Hermitian. Nevertheless, the spectrum of the original Hamiltonian is unchanged. Due to the non-Hermiticity of  $\bar{H}$  the expression for the energy

$$\langle \Phi_0 | e^{-T} H_N e^T | \Phi_0 \rangle = \Delta E \quad (6.272)$$

is asymmetric.

Instead of solving the eigenvalue problem for the similarity-transformed Hamiltonian  $\bar{H}$  CC theory can also be seen from a bi-variational perspective, minimizing the energy functional

$$E(T, \Lambda) \equiv \langle \Phi_0 | (\mathbb{1} + \Lambda) e^{-T} H_N e^T | \Phi_0 \rangle = \langle \Phi_0 | (\mathbb{1} + \Lambda) \bar{H} | \Phi_0 \rangle, \quad (6.273)$$

with respect to  $T$  and  $\Lambda$ . The different ranks  $k$  of the de-excitation operator  $\Lambda = \Lambda_1 + \Lambda_2 + \dots + \Lambda_A$  describe the different ph de-excitation levels

$$\Lambda_1 = \frac{1}{(1!)^2} \sum_{i,a} \lambda_a^i : a_i^\dagger a_a : | \Phi_0 \rangle, \quad (6.274)$$

$$\Lambda_2 = \frac{1}{(2!)^2} \sum_{i,j,a,b} \lambda_{ab}^{ij} : a_i^\dagger a_j^\dagger a_b a_a : | \Phi_0 \rangle, \quad (6.275)$$

$\vdots$

$$\Lambda_k = \frac{1}{(k!)^2} \sum_{\substack{i_1, \dots, i_k \\ a_1, \dots, a_k}} \lambda_{a_1 \dots a_k}^{i_1 \dots i_k} : a_{i_1}^\dagger \dots a_{i_k}^\dagger a_{a_k} \dots a_{a_1} : | \Phi_0 \rangle. \quad (6.276)$$

The variation of the energy functional can be understood as an independent variation of the bra state  $\langle \tilde{\Psi}^A | = \langle \Phi_0 | (\mathbb{1} + \Lambda) e^{-T}$  and the ket state  $|\Psi^A\rangle = e^T | \Phi_0 \rangle$ , which fulfill the biorthonormality condition

$$\langle \tilde{\Psi}^A | \Psi^A \rangle = \langle \Phi_0 | (\mathbb{1} + \Lambda) e^{-T} e^T | \Phi_0 \rangle = \langle \Phi_0 | \Phi_0 \rangle = 1, \quad (6.277)$$

since  $\Lambda_k | \Phi_0 \rangle = 0$  for  $k \geq 1$ .

Since it is not possible to include all cluster ranks up to the ApAh level, the cluster operator is usually truncated at some rank  $M$  leading to

$$T^{(M)} = \sum_{i=1}^M T_i. \quad (6.278)$$

By expanding the exponential in Eq. (6.262) in a Taylor series

$$|\Psi^A\rangle = e^T | \Phi_0 \rangle = | \Phi_0 \rangle + T_1 | \Phi_0 \rangle + \left( \frac{1}{2!} T_1^2 + T_2 \right) | \Phi_0 \rangle + \left( \frac{1}{3!} T_1^3 + T_1 T_2 + T_3 \right) | \Phi_0 \rangle + \dots \quad (6.279)$$

it is, however, obvious that higher-order excitations are generated from products of the included cluster operators. Terms of the form  $T_m | \Phi_0 \rangle$  in the expansion above are called connected clusters, while terms involving products of cluster operators, such as  $T_1^2$  or  $T_1 T_2$ , are called disconnected clusters. The similarity-transformed Schrödinger equation for the exact case, Eq. (6.271), is modified for a truncated CC method to

$$\bar{H}^{(M)} | \Phi \rangle = e^{-T^{(M)}} H_N e^{T^{(M)}} | \Phi \rangle = \Delta E^{(M)} | \Phi \rangle, \quad (6.280)$$

where we introduced  $|\Phi\rangle = |\Phi_0\rangle$  for brevity. The coupled set of equations for the determination of the cluster amplitudes

$$t^{(M)} = \left( \{t_i^a\}, \{t_{ij}^{ab}\}, \dots, \{t_{i_1 \dots i_M}^{a_1 \dots a_M}\} \right) \quad (6.281)$$

is obtained by left-projecting Eq. (6.280) onto excited bra states  $\left\{ \{ \langle \Phi_i^a | \}, \{ \langle \Phi_{ij}^{ab} | \}, \dots, \{ \langle \Phi_{i_1 \dots i_M}^{a_1 \dots a_M} | \} \right\}$ , i.e.,

$$\langle \Phi | \bar{H}^{(M)} | \Phi \rangle = \Delta E^{(M)} \quad (6.282)$$

$$\langle \Phi_i^a | \bar{H}^{(M)} | \Phi \rangle = 0 \quad \forall i, a, \quad (6.283)$$

$$\langle \Phi_{ij}^{ab} | \bar{H}^{(M)} | \Phi \rangle = 0 \quad \forall i, j, a, b, \quad (6.284)$$

$\vdots$

$$\langle \Phi_{i_1 \dots i_M}^{a_1 \dots a_M} | \bar{H}^{(M)} | \Phi \rangle = 0 \quad \forall i_1, \dots, i_M, a_1, \dots, a_M. \quad (6.285)$$

An equivalent way for obtaining this set of algebraic equations is by also truncating the de-excitation operator  $\Lambda^{(M)} = \sum_{i=1}^M \Lambda_i$  at the same rank  $M$  as the cluster operator  $T^{(M)}$  and then vary the energy functional, Eq. (6.273), with respect to  $\Lambda^{(M)}$ .

For the computation of the similarity-transformed Hamiltonian  $\bar{H}^{(M)}$  the BCH expansion, also used in Eq. (6.251), can be employed

$$\bar{H}^{(M)} = \sum_{k=0}^{\infty} \frac{1}{k!} ad_{-T^{(M)}}^k(H_N). \quad (6.286)$$

Since the individual terms of  $T^{(M)}$  commute with themselves, the commutators in Eq. (6.286) ensure that each  $T^{(M)}$  connects to the similarity-transformed Hamiltonian  $H_N$  by at least one contraction. Since we are working in NO2B approximation the BCH expansion terminates at fourfold nested commutators ( $k_{\max} = 4$ ), while for a three-body Hamiltonian up to sixfold nested commutators ( $k_{\max} = 6$ ) are possible. Thus, the similarity transformation can be evaluated exactly and the commutator expansion can be simplified even further to

$$\bar{H}^{(M)} = \left( H_N e^{T^{(M)}} \right)_C, \quad (6.287)$$

with the subscript  $C$  denoting connected terms, that have at least one contraction between the similarity-transformed Hamiltonian  $H_N$  and each  $T^{(M)}$ .

Before specifying the maximum rank  $M$  of the cluster operator a few comments are in order: For CC calculations in the HF basis the lowest order contribution to the cluster operator  $T_1$ , called singles, and the corresponding amplitudes  $\{t_i^a\}$  have small absolute values. This can be understood by Brillouin's theorem, given in Eq. (6.221), stating that in the HF basis the Hamiltonian does not connect the HF state to its 1p1h excitations. In general, CC calculations including singles are relatively insensitive to the choice of  $|\Phi\rangle$  and the single-particle orbitals, i.e., using HF or non-HF Slater determinants as input should yield the same results up to numerical effects. This can be understood from Thouless' theorem [178], stating that any two Slater determinants  $|\Phi_A\rangle$ ,  $|\Phi_B\rangle$  that are non-orthogonal and therefore have non-vanishing overlap can be, up to a normalization constant and a phase factor, related by a similarity transformation

$$|\Phi_B\rangle \sim \exp\left(\sum_{i,a} t_i^a : a_a^\dagger a_i :_{|\Phi_A}\right) |\Phi_A\rangle \equiv e^{T_1} |\Phi_A\rangle. \quad (6.288)$$

Due to the exponential ansatz for the correlated wave function, Eq. (6.262), Thouless' theorem is directly incorporated in the CC formalism. The next two terms beyond singles  $T_2$  and  $T_3$ , called doubles and triples, give important contributions and are dominating compared to terms such as  $T_1^2$  or  $T_1 T_2$ . Higher-order cluster operators  $T_4$  or  $T_5$  should become less relevant than  $T_2$  and  $T_3$ , since they describe a simultaneous correlation of four or five nucleons.

In the following we will assume  $M = 2$

$$T^{(\text{CCSD})} = T_1 + T_2, \quad (6.289)$$

leading to CC calculations including singles and doubles, abbreviated by CCSD. By expanding the exponential function in Eq. (6.287) into a Taylor series, the energy and amplitude equations are given by

$$\langle \Phi | \left[ H_N (T_1 + T_2 + \frac{1}{2!} T_1^2) \right]_C | \Phi \rangle = \Delta E^{(\text{CCSD})} \quad (6.290)$$

$$\langle \Phi_i^a | \left[ H_N (1 + T_1 + T_2 + \frac{1}{2!} T_1^2 + T_1 T_2 + \frac{1}{3!} T_1^3) \right]_C | \Phi \rangle = 0 \quad \forall i, a, \quad (6.291)$$

$$\langle \Phi_{ij}^{ab} | \left[ H_N (1 + T_1 + T_2 + \frac{1}{2!} T_1^2 + T_1 T_2 + \frac{1}{3!} T_1^3 + \frac{1}{2!} T_1^2 T_2 + \frac{1}{2!} T_2^2 + \frac{1}{3!} T_1^4) \right]_C | \Phi \rangle = 0 \quad \forall i, j, a, b. \quad (6.292)$$

Note that cluster operator products with excitation ranks being too high for the Hamiltonian  $H_N$  to de-excite the resulting determinants to the states the equations are projected on have been left out. The evaluation of Eqs. (6.290)–(6.292) in terms of matrix elements of  $H_N$  and  $T_k$  is usually accomplished by diagrammatic techniques [177]. The amplitude equations are usually converted into a fixed-point problem and solved iteratively. The correlation energy, Eq. (6.290), is then obtained by inserting the results for the cluster amplitudes  $(\{t_i^a\}, \{t_{ij}^{ab}\})$ . It is notably that in case of a two-body Hamiltonian the algebraic form of the energy equation is valid for all closed-shell coupled-cluster truncations, e.g., CCSDT, CCSDTQ, ..., since it only ever depends on the singles and doubles

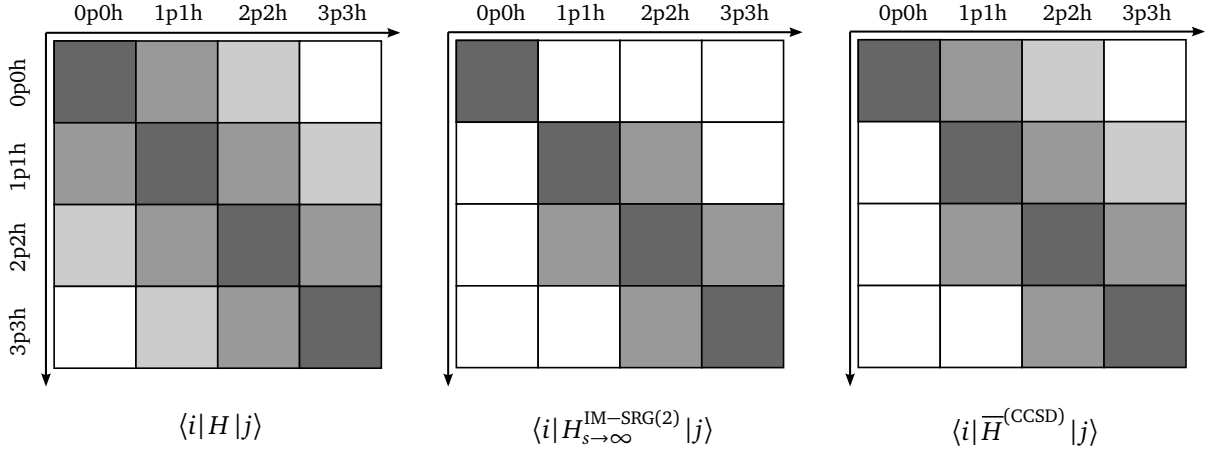


**Figure 6.10:** Comparison of the initial,  $H$ , the IM-SRG(2)-decoupled,  $H_{s \rightarrow \infty}^{\text{IM-SRG}(2)}$ , and the CCSD similarity-transformed,  $\bar{H}^{(\text{CCSD})}$ , nuclear many-body Hamiltonian at the two-body level, represented in terms of particle-hole excitations of the reference state  $|\Phi\rangle$ . Taken from Ref. [14].

amplitudes. This is due to the fact that no closed diagrams can be constructed from a two-body Hamiltonian and cluster operators beyond  $T_2$ . Of course, the correlation energy depends implicitly on the  $T_3, T_4, \dots$  amplitudes through the solution of the amplitude equations. In summary, the CCSD equations demand that the reference state  $|\Phi\rangle$  is an eigenstate of the similarity-transformed Hamiltonian in the space of all 1p1h and 2p2h excited states, shown in the right panel of Fig. 6.10.

Moreover, having determined the cluster amplitudes it is possible to explicitly construct the similarity-transformed Hamiltonian

$$\bar{H}^{(\text{CCSD})} = e^{-T^{(\text{CCSD})}} H_N e^{T^{(\text{CCSD})}} \quad (6.293)$$

by evaluating Eq. (6.286) up to fourfold commutators in case  $H_N$  contains at most a two-body interaction. Thus, the similarity-transformed Hamiltonian  $\bar{H}^{(\text{CCSD})}$  will contain up to six-body operator terms,

$$\bar{H}^{(\text{CCSD})} = \bar{H}_0 + \bar{H}_1 + \bar{H}_2 + \bar{H}_3 + \bar{H}_4 + \bar{H}_5 + \bar{H}_6 \quad (6.294)$$

$$\equiv \bar{H}_0 + \bar{H}_{\text{open}}^{(\text{CCSD})}, \quad (6.295)$$

where we separated closed diagrams, denoted  $\bar{H}_0$ , from diagrams with open Fermion lines, labeled  $\bar{H}_{\text{open}}^{(\text{CCSD})}$ . Clearly, the closed diagrams  $\bar{H}_0$ , that have no external lines, are equal to the correlation energy in Eq. (6.290), while open diagrams  $\bar{H}_{\text{open}}^{(\text{CCSD})}$  enter in the amplitude equations Eqs. (6.291)–(6.292).

In addition to the CCSD equations we briefly discuss the  $\Lambda$ -CCSD equations, which are an important ingredient for an approximative inclusion of triples in the  $\Lambda$ -CCSD(T) approach and in the calculation of observables other than the energy. The  $\Lambda$ -CCSD equations are obtained from the left-eigenvalue problem

$$\langle \Phi | (\mathbb{1} + \Lambda_1 + \Lambda_2) \bar{H}^{(\text{CCSD})} = \Delta E^{(\text{CCSD})} \langle \Phi | (\mathbb{1} + \Lambda_1 + \Lambda_2), \quad (6.296)$$

which can be cast into an energy-independent form by using the distinction of the similarity transformed Hamiltonian into diagrams with,  $\bar{H}_{\text{open}}^{(\text{CCSD})}$ , and without,  $\bar{H}_0 = \Delta E^{(\text{CCSD})}$ , external Fermion lines, leading to

$$\langle \Phi | (\mathbb{1} + \Lambda_1 + \Lambda_2) \bar{H}_{\text{open}}^{(\text{CCSD})} = 0. \quad (6.297)$$

By right-projecting Eq. (6.297) onto excited ket states  $\left\{ \left\{ |\Phi_i^a\rangle \right\}, \left\{ |\Phi_{ij}^{ab}\rangle \right\} \right\}$  we arrive at a system of linear equations

$$\langle \Phi | (\mathbb{1} + \Lambda_1 + \Lambda_2) \bar{H}_{\text{open}}^{(\text{CCSD})} |\Phi_i^a\rangle = 0 \quad \forall i, a, \quad (6.298)$$

$$\langle \Phi | (\mathbb{1} + \Lambda_1 + \Lambda_2) \bar{H}_{\text{open}}^{(\text{CCSD})} |\Phi_{ij}^{ab}\rangle = 0 \quad \forall i, j, a, b. \quad (6.299)$$

This is in contrast to the  $T$  amplitude equations, which are nonlinear. Still the corresponding set of algebraic  $\Lambda$  equations is solved iteratively for  $(\{\lambda_a^i\}, \{\lambda_{ab}^{ij}\})$ , because of the sets' size.

Since the inclusion of full triples, denoted CCSDT ( $M = 3$ ), is usually computationally too expensive for all but the lightest nuclei, triples corrections are taken into account perturbatively. While there are several approaches we focus on the  $\Lambda$ -CCSD(T) non-iterative energy correction [179]. The corrected total energy is given by

$$E^{(\Lambda\text{-CCSD(T)})} = E_{\text{ref}} + \Delta E^{(\text{CCSD})} + \delta E^{(\Lambda\text{-CCSD(T)})}, \quad (6.300)$$

with the  $\Lambda$ -CCSD(T) energy correction of the form

$$\delta E^{(\Lambda\text{-CCSD(T)})} = \frac{1}{(3!)^2} \sum_{ijkabc} \langle \Phi | \Lambda (F_N^{\text{od}} + V_N) | \Phi_{ijk}^{abc} \rangle \frac{1}{\varepsilon_{ijk}^{abc}} \langle \Phi_{ijk}^{abc} | (V_N T_2)_C | \Phi \rangle. \quad (6.301)$$

Here,  $F_N^{\text{od}}$  is the off-diagonal part of the normal-ordered Fock operator  $F_N$ , which vanishes in the Hartree-Fock basis since  $F_N$  is diagonal, while  $|\Phi_{ijk}^{abc}\rangle$  is a 3p3h excitation of the reference  $|\Phi\rangle$ , and  $\varepsilon_{ijk}^{abc}$  is given by diagonal matrix elements of the Fock operator

$$\varepsilon_{ijk}^{abc} = f_{ii} + f_{jj} + f_{kk} - f_{aa} - f_{bb} - f_{cc}. \quad (6.302)$$

Before introducing EOM techniques a comment on the numerical efficiency of CC calculations is in order. The  $m$ -scheme formulation of Coupled-Cluster theory, discussed so far, allowed CCSD computations using low-momentum NN interactions for, e.g.,  $^{40}\text{Ca}$  in a single-particle basis of up to 9 major harmonic oscillator shells [180]. Similarly to IM-SRG calculations it is beneficial to exploit spherical symmetry when one is interested in closed-shell nuclei. In this case the cluster operator is a rank-zero spherical tensor operator and, consequently, already the first CCSD implementation was able to perform calculations for  $^{40,48}\text{Ca}$  and  $^{48}\text{Ni}$  in a single-particle basis of up to 15 major harmonic oscillator shells, starting from unevaluated chiral NN forces [181]. The CCSD amplitude equations can be solved at the cost  $\mathcal{O}(N_h^2 N_p^4)$ , where the number of hole states  $N_h$  is typically much smaller than the number of particle states  $N_p$ , while the construction of the CCSD effective Hamiltonian from the amplitudes requires  $\mathcal{O}(N^6)$  in a single-particle basis of dimension  $N$ .

## 6.5.2 Equation-of-motion techniques

In addition to ground-state wave functions and energies also excited states of closed-shell nuclei can be accessed within CC theory by employing EOM techniques, abbreviated by excitation energy EOM (EE-EOM) in quantum chemistry [182]. Excited states  $|\Psi_\mu^A\rangle$  ( $\mu > 0$ ) of the  $A$ -particle system are obtained by applying the linear excitation operator  $R_\mu^A$  to the correlated CC ground-state wave function  $|\Psi^A\rangle$

$$|\Psi_\mu^A\rangle = R_\mu^A |\Psi^A\rangle = R_\mu^A e^T |\Phi_0\rangle. \quad (6.303)$$

The excitation operator  $R_\mu^A$  for the calculation of excited states in closed-shell nuclei takes the form

$$R_\mu^A = (r_\mu)_0 + \sum_{i,a} (r_\mu)_i^a : a_a^\dagger a_i :_{|\Phi_0\rangle} + \frac{1}{4} \sum_{i,j,a,b} (r_\mu)_{ij}^{ab} : a_a^\dagger a_b^\dagger a_j a_i :_{|\Phi_0\rangle} + \dots, \quad (6.304)$$

generating 1p1h, 2p2h, 3p3h, ... excitations on the ground state of the  $A$ -nucleon system. The constant term  $(r_\mu)_0$  is required for the description of excited states of the same symmetry as the ground state. If the two states have different symmetry then  $(r_\mu)_0 = 0$ .

Moreover, ground and excited states  $|\Psi_\mu^{A\pm k}\rangle$  ( $\mu \geq 0$ ) of the  $A \pm k$ -particle ( $k > 0$ ) system are calculated by acting with the particle-attaching/particle-removing (PA/PR) operator  $R_\mu^{A\pm k}$  on the ground state of the closed-shell nucleus

$$|\Psi_\mu^{A\pm k}\rangle = R_\mu^{A\pm k} |\Psi^A\rangle = R_\mu^{A\pm k} e^T |\Phi_0\rangle. \quad (6.305)$$

Note that  $R_\mu^{A\pm k}$  is a particle number non-conserving operator. For  $k = 1$  the PA and PR operator  $R_\mu^{A\pm 1}$  are given by

$$R_\mu^{A+1} = \sum_a (r_\mu)_a^a a_a^\dagger + \frac{1}{2} \sum_{i,a,b} (r_\mu)_i^{ab} : a_a^\dagger a_b^\dagger a_i :_{|\Phi_0\rangle} + \dots, \quad (6.306)$$

$$R_\mu^{A-1} = \sum_i (r_\mu)_i a_i + \frac{1}{2} \sum_{i,j,a} (r_\mu)_{ij}^a : a_a^\dagger a_j a_i :_{|\Phi_0\rangle} + \dots. \quad (6.307)$$

Thus, the PA(PR)-EOM-CC method adds (removes) a particle to (from) a closed-shell nucleus with  $A$  nucleons by creating 1p, 2p1h, 3p2h, ... (1h, 1p2h, 2p3h, ...) excitations on the ground state of the  $A$ -body system. The two particle-attaching operator takes the form

$$R_\mu^{A+2} = \frac{1}{2} \sum_{a,b} (r_\mu)^{ab} : a_a^\dagger a_b^\dagger : |\Phi_0\rangle + \frac{1}{6} \sum_{i,a,b,c} (r_\mu)_i^{abc} : a_a^\dagger a_b^\dagger a_c^\dagger a_i : |\Phi_0\rangle + \dots \quad (6.308)$$

for states in the  $A + 2$ -nucleus. The corresponding EOM formulations in quantum chemistry are denoted electron attachment (EA-EOM) and ionization potential (IP-EOM).

While the discussion above was general we restrict the following to EOM-CCSD, truncated at singles and doubles. In this case the excitation operator is truncated at the 2p2h level

$$R_\mu^{A,(\text{CCSD})} = (r_\mu)_0 + \sum_{i,a} (r_\mu)_i^a : a_a^\dagger a_i : |\Phi\rangle + \frac{1}{4} \sum_{i,j,a,b} (r_\mu)_{ij}^{ab} : a_a^\dagger a_b^\dagger a_j a_i : |\Phi\rangle, \quad (6.309)$$

and generates excited states by acting on the CCSD ground state

$$|\Psi_\mu^{A,(\text{CCSD})}\rangle = R_\mu^{A,(\text{CCSD})} |\Psi_\mu^{A,(\text{CCSD})}\rangle = R_\mu^{A,(\text{CCSD})} e^{T^{(\text{CCSD})}} |\Phi\rangle, \quad (6.310)$$

where we again use  $|\Phi\rangle = |\Phi_0\rangle$  for brevity. The corresponding Schrödinger equation for excited states  $|\Psi_\mu^{A,(\text{CCSD})}\rangle$  reads

$$H_N R_\mu^{A,(\text{CCSD})} e^{T^{(\text{CCSD})}} |\Phi\rangle = \Delta E_\mu^{A,(\text{CCSD})} R_\mu^{A,(\text{CCSD})} e^{T^{(\text{CCSD})}} |\Phi\rangle, \quad (6.311)$$

with the correlation energy of excited states  $\Delta E_\mu^{A,(\text{CCSD})}$ . Since  $T^{(\text{CCSD})}$  and  $R_\mu^{A,(\text{CCSD})}$  commute, it can be rewritten, in analogy to the ground-state calculation, in terms of the similarity transformed Hamiltonian  $\overline{H}^{(\text{CCSD})}$  to

$$\overline{H}^{(\text{CCSD})} R_\mu^{A,(\text{CCSD})} |\Phi\rangle = \Delta E_\mu^{A,(\text{CCSD})} R_\mu^{A,(\text{CCSD})} |\Phi\rangle. \quad (6.312)$$

By multiplying the ground-state Schrödinger equation  $\overline{H}^{(\text{CCSD})} |\Phi\rangle = \Delta E^{(\text{CCSD})} |\Phi\rangle$  from the left with  $R_\mu^{A,(\text{CCSD})}$  and subtracting it from Eq. (6.312) results in

$$[\overline{H}^{(\text{CCSD})}, R_\mu^{A,(\text{CCSD})}] |\Phi\rangle = \omega_\mu^{A,(\text{CCSD})} R_\mu^{A,(\text{CCSD})} |\Phi\rangle, \quad (6.313)$$

with the excitation energy relative to the ground state

$$\omega_\mu^{A,(\text{CCSD})} = \Delta E_\mu^{A,(\text{CCSD})} - \Delta E^{(\text{CCSD})}. \quad (6.314)$$

Employing that the similarity transformed Hamiltonian  $\overline{H}^{(\text{CCSD})}$  consists of a part without,  $\overline{H}_0 = \Delta E^{(\text{CCSD})}$ , and with open Fermion lines,  $\overline{H}_{\text{open}}^{(\text{CCSD})}$ , the commutator  $[\overline{H}_0, R_\mu^{A,(\text{CCSD})}]$  vanishes and the EOM-CCSD eigenvalue problem can be further simplified to

$$\left( \overline{H}_{\text{open}}^{(\text{CCSD})} R_\mu^{A,(\text{CCSD})} \right)_C |\Phi\rangle = \omega_\mu^{A,(\text{CCSD})} R_\mu^{A,(\text{CCSD})} |\Phi\rangle. \quad (6.315)$$

By left-projecting Eq. (6.315) onto excited bra states  $\left\{ \langle \Phi_i^a | \right\}, \left\{ \langle \Phi_{ij}^{ab} | \right\}$  we arrive at a set of equations for the amplitudes  $\left\{ (r_\mu)_i^a \right\}, \left\{ (r_\mu)_i^{abc} \right\}$

$$\langle \Phi_i^a | \left( \overline{H}_{\text{open}}^{(\text{CCSD})} R_\mu^{A,(\text{CCSD})} \right)_C |\Phi\rangle = \omega_\mu^{A,(\text{CCSD})} (r_\mu)_i^a \quad \forall i, a, \quad (6.316)$$

$$\langle \Phi_{ij}^{ab} | \left( \overline{H}_{\text{open}}^{(\text{CCSD})} R_\mu^{A,(\text{CCSD})} \right)_C |\Phi\rangle = \omega_\mu^{A,(\text{CCSD})} (r_\mu)_{ij}^{ab} \quad \forall i, j, a, b. \quad (6.317)$$

The constant amplitudes  $\left\{ (r_\mu)_0 \right\}$  are determined from the solution of Eqs. (6.316)–(6.317) by calculating

$$\langle \Phi | \left( \overline{H}_{\text{open}}^{(\text{CCSD})} R_\mu^{A,(\text{CCSD})} \right)_C |\Phi\rangle = \omega_\mu^{A,(\text{CCSD})} (r_\mu)_0. \quad (6.318)$$

Excited bra states  $\langle \tilde{\Psi}_\mu^{A,(\text{CCSD})} |$  can be parametrized by the ansatz

$$\langle \tilde{\Psi}_\mu^{A,(\text{CCSD})} | = \langle \Phi | L_\mu^{A,(\text{CCSD})} e^{-T^{(\text{CCSD})}}, \quad (6.319)$$

using the truncated de-excitation operator

$$L_\mu^{A,(\text{CCSD})} = (l_\mu)_0 + \sum_{i,a} (l_\mu)_a^i a_i^\dagger a_a + \frac{1}{4} \sum_{i,j,a,b} (l_\mu)_{ab}^{ij} a_i^\dagger a_j^\dagger a_b a_a. \quad (6.320)$$

The corresponding Schrödinger equation for  $\langle \Psi_\mu^{A,(\text{CCSD})} |$  is given by

$$\langle \Phi | L_\mu^{A,(\text{CCSD})} e^{-T^{(\text{CCSD})}} H_N = \Delta E_\mu^{A,(\text{CCSD})} \langle \Phi | L_\mu^{A,(\text{CCSD})} e^{-T^{(\text{CCSD})}}, \quad (6.321)$$

which can be reformulated in terms of the similarity transformed Hamiltonian

$$\langle \Phi | L_\mu^{A,(\text{CCSD})} \bar{H}^{(\text{CCSD})} = \Delta E_\mu^{A,(\text{CCSD})} \langle \Phi | L_\mu^{A,(\text{CCSD})}. \quad (6.322)$$

The left eigenvalue problem can, similarly to the right one, directly provide the excitation energy  $\omega_\mu^{A,(\text{CCSD})}$  by employing the distinction in a part without,  $\bar{H}_0 = \Delta E^{(\text{CCSD})}$ , and with open Fermion lines,  $\bar{H}_{\text{open}}^{(\text{CCSD})}$ , resulting in

$$\langle \Phi | L_\mu^{A,(\text{CCSD})} \bar{H}_{\text{open}}^{(\text{CCSD})} = \omega_\mu^{A,(\text{CCSD})} \langle \Phi | L_\mu^{A,(\text{CCSD})}. \quad (6.323)$$

A system of equations to determine  $\left( \{ (l_\mu)_a^i \}, \{ (l_\mu)_{ab}^{ij} \} \right)$  is obtained by right-projecting Eq. (6.323) onto excited ket states  $\left\{ \{ |\Phi_i^a\rangle \}, \{ |\Phi_{ij}^{ab}\rangle \} \right\}$ , leading to

$$\langle \Phi | L_\mu^{A,(\text{CCSD})} \bar{H}_{\text{open}}^{(\text{CCSD})} |\Phi_i^a\rangle = \omega_\mu^{A,(\text{CCSD})} (l_\mu)_a^i \quad \forall i, a, \quad (6.324)$$

$$\langle \Phi | L_\mu^{A,(\text{CCSD})} \bar{H}_{\text{open}}^{(\text{CCSD})} |\Phi_{ij}^{ab}\rangle = \omega_\mu^{A,(\text{CCSD})} (l_\mu)_{ab}^{ij} \quad \forall i, j, a, b. \quad (6.325)$$

For the determination of  $\{ (l_\mu)_0 \}$  we come back to the biorthogonality relation already discussed for the ground state. By solving the left and right eigenvalue problem for excited states we have obtained two sets of normalized eigenvectors

$$\mathbf{r}_\mu^{A,(\text{CCSD})} = \left( \{ (r_\mu)_0 \}, \{ (r_\mu)_i^a \}, \{ (r_\mu)_{ij}^{ab} \} \right)^T, \quad (6.326)$$

$$\mathbf{l}_\mu^{A,(\text{CCSD})} = \left( \{ (l_\mu)_0 \}, \{ (l_\mu)_a^i \}, \{ (l_\mu)_{ab}^{ij} \} \right), \quad (6.327)$$

which have the same eigenvalues, but are otherwise distinct. They are not orthogonal among themselves, but fulfill a biorthogonality relation

$$\mathbf{l}_\mu^{A,(\text{CCSD})} \cdot \mathbf{r}_\nu^{A,(\text{CCSD})} = \delta_{\mu\nu}, \quad (6.328)$$

or, in terms of operators

$$\langle \tilde{\Psi}_\mu^{A,(\text{CCSD})} | \Psi_\nu^{A,(\text{CCSD})} \rangle = \langle \Phi | L_\mu^{A,(\text{CCSD})} e^{-T^{(\text{CCSD})}} R_\nu^{A,(\text{CCSD})} e^{T^{(\text{CCSD})}} | \Phi \rangle = \langle \Phi | L_\mu^{A,(\text{CCSD})} R_\nu^{A,(\text{CCSD})} | \Phi \rangle = \delta_{\mu\nu}, \quad (6.329)$$

for which the originally normalized left eigenvector  $\mathbf{l}_\mu^{A,(\text{CCSD})}$  is rescaled by

$$\mathbf{l}_\mu^{A,(\text{CCSD})} \rightarrow \frac{1}{\mathbf{l}_\mu^{A,(\text{CCSD})} \cdot \mathbf{r}_\mu^{A,(\text{CCSD})}} \mathbf{l}_\mu^{A,(\text{CCSD})}. \quad (6.330)$$

The choice of scaling the left eigenvector is made to retain consistency with the treatment of the ground state [182], for which  $R_0^{A,(\text{CCSD})} = \mathbb{1}$  and  $L_0^{A,(\text{CCSD})} = \mathbb{1} + \Lambda_1 + \Lambda_2$  and the corresponding sets of eigenvectors are

$$\mathbf{r}_0^{A,(\text{CCSD})} = (1, \{0\}, \{0\})^T, \quad (6.331)$$

$$\mathbf{l}_0^{A,(\text{CCSD})} = \left( 1, \{ \lambda_a^i \}, \{ \lambda_{ab}^{ij} \} \right). \quad (6.332)$$



Inserting the ground-state property  $R_0^{A,(\text{CCSD})} = \mathbb{1}$  into Eq. (6.329) leads to

$$\langle \Phi | L_\mu^{A,(\text{CCSD})} | \Phi \rangle = \delta_{\mu 0}, \quad (6.333)$$

and, thus, we can determine  $(l_\mu)_0 = 0$  for excited states  $\mu$  [177].

We briefly want to outline particle-number changing PA/PR-EOM-CCSD calculations, for which the corresponding operators are truncated at the 2p1h and 1p2h level, leading to

$$R_\mu^{A+1,(\text{CCSD})} = \sum_a (r_\mu)^a a_a^\dagger + \frac{1}{2} \sum_{i,a,b} (r_\mu)_i^{ab} : a_a^\dagger a_b^\dagger a_i : | \Phi_0 \rangle, \quad (6.334)$$

$$R_\mu^{A-1,(\text{CCSD})} = \sum_i (r_\mu)_i a_i + \frac{1}{2} \sum_{i,j,a} (r_\mu)_{ij}^a : a_a^\dagger a_j a_i : | \Phi_0 \rangle. \quad (6.335)$$

The 1p and 2p1h amplitudes  $(r_\mu)^a$  and  $(r_\mu)_i^{ab}$  are obtained by solving the PA-EOM-CCSD amplitude equations, and, similarly, the 1h and 1p2h amplitudes  $(r_\mu)_i$  and  $(r_\mu)_{ij}^a$  are determined by solving the PR-EOM-CCSD amplitude equations, respectively. Since the intrinsic Hamiltonian depends on the mass number  $A$ , a comment for number-changing EOM operators is in order [13]. For PR-EOM CC calculations, the normal-ordered intrinsic Hamiltonian with the mass number  $A-1$  is used, when solving the CCSD equations for the correlated reference state with mass  $A$  in the first step. Therefore, the Hamiltonian will not fully capture the intrinsic physics of the  $A$ -body problem. However, when solving the eigenvalue problem of the PR-EOM, the resulting solution approximately factorizes into the intrinsic and the center-of-mass wave function. Similarly, in the case of PA-EOM CC calculations the mass number  $A+1$  is used in the normal-ordered intrinsic Hamiltonian when computing the similarity-transformed CCSD Hamiltonian for the  $A$ -body reference.

### 6.5.3 General observables

For the calculation of ground-state observables other than the energy we have to evaluate expectation values for the corresponding normal-ordered operator  $O$ , i.e.,

$$\langle O \rangle \equiv \frac{\langle \Psi^A | O | \Psi^A \rangle}{\langle \Psi^A | \Psi^A \rangle} = \frac{\langle \Phi_0 | e^{T^\dagger} O e^T | \Phi_0 \rangle}{\langle \Phi_0 | e^{T^\dagger} e^T | \Phi_0 \rangle}. \quad (6.336)$$

This is obviously more complicated than for many-body methods that employ a linear ansatz for the wave function. In analogy to the energy we may separate the expectation value of a general operator  $O$  into the reference and the correlation part

$$\langle O \rangle = O_{\text{ref}} + \Delta O = \langle \Phi_0 | O | \Phi_0 \rangle + \langle O_N \rangle, \quad (6.337)$$

where the evaluation of the correlation part can be simplified to [183]

$$\langle O_N \rangle = \frac{\langle \Phi_0 | e^{T^\dagger} O_N e^T | \Phi_0 \rangle}{\langle \Phi_0 | e^{T^\dagger} e^T | \Phi_0 \rangle} = \frac{\langle \Phi_0 | e^{T^\dagger} e^T | \Phi_0 \rangle \langle \Phi_0 | (e^{T^\dagger} O_N e^T)_C | \Phi_0 \rangle}{\langle \Phi_0 | e^{T^\dagger} e^T | \Phi_0 \rangle} = \langle \Phi_0 | (e^{T^\dagger} O_N e^T)_C | \Phi_0 \rangle. \quad (6.338)$$

The factorization in the numerator, however, introduces terms that prevent the expansion from terminating, since multiple excitations or de-excitations of the same hole state may now occur. Thus, an exact determination of the expectation value is prevented and the evaluation of the expectation value in this way requires truncation at some level.

When we choose the operator  $O_N$  to be the Hamiltonian  $H_N$ , the correlation energy is given by

$$\Delta E = \langle H_N \rangle = \frac{\langle \Phi_0 | e^{T^\dagger} H_N e^T | \Phi_0 \rangle}{\langle \Phi_0 | e^{T^\dagger} e^T | \Phi_0 \rangle} = \langle \Phi_0 | (e^{T^\dagger} H_N e^T)_C | \Phi_0 \rangle, \quad (6.339)$$

while it was determined to  $\Delta E = \langle \Phi_0 | e^{-T} H_N e^T | \Phi_0 \rangle = \langle \Phi_0 | (H_N e^T)_C | \Phi_0 \rangle$  in Eq. (6.272). The equivalence between the relations can be shown by inserting  $e^T (P+Q) e^{-T} = \mathbb{1}$ , with the operators  $P$  and  $Q$  projecting onto the reference space and its complement, into the expectation value

$$\Delta E = \frac{\langle \Phi_0 | e^{T^\dagger} H_N e^T | \Phi_0 \rangle}{\langle \Phi_0 | e^{T^\dagger} e^T | \Phi_0 \rangle} = \frac{\langle \Phi_0 | e^{T^\dagger} e^T (P+Q) e^{-T} H_N e^T | \Phi_0 \rangle}{\langle \Phi_0 | e^{T^\dagger} e^T | \Phi_0 \rangle} \quad (6.340)$$

$$= \frac{\langle \Phi_0 | e^{T^\dagger} e^T | \Phi_0 \rangle \langle \Phi_0 | e^{-T} H_N e^T | \Phi_0 \rangle}{\langle \Phi_0 | e^{T^\dagger} e^T | \Phi_0 \rangle} = \langle \Phi_0 | e^{-T} H_N e^T | \Phi_0 \rangle. \quad (6.341)$$

Here, we have employed that the CC amplitude equations require  $Q\bar{H}|\Phi_0\rangle = 0$ , which is only valid when  $T$  is the solution of the untruncated CC equations. Assume we truncate  $T$  to  $T_1 + T_2$ , then the amplitude equations for higher cluster operators, e.g.,  $T_3$ , is not fulfilled and, therefore,  $Q\bar{H}|\Phi_0\rangle = 0$  is not strictly valid.

For the evaluation of general operators it is more convenient to work in terms of reduced density matrices. The normal-ordered part of the one-body reduced density matrix is given by

$$\gamma_N = \sum_{p,s} |s\rangle (\gamma_N)_{sp} \langle p|, \quad (6.342)$$

with the corresponding matrix elements

$$(\gamma_N)_{sp} = \langle \Phi_0 | \left( e^{T^\dagger} : a_p^\dagger a_s :_{|\Phi_0\rangle} e^T \right)_C | \Phi_0 \rangle. \quad (6.343)$$

Thus, the correlation part of the expectation value of any normal-ordered one-body operator can be obtained by

$$\langle O_N^{(1)} \rangle = \sum_{p,s} \langle p| o |s\rangle (\gamma_N)_{sp}, \quad (6.344)$$

while the reference part can be included by employing a modified density matrix  $\gamma_{sp} = \langle \Phi_0 | \left( e^{T^\dagger} a_p^\dagger a_s e^T \right)_C | \Phi_0 \rangle$ , leading to

$$\langle O^{(1)} \rangle = \sum_{p,s} \langle p| o |s\rangle \gamma_{sp}, \quad \gamma_{sp} \equiv \begin{cases} (\gamma_N)_{sp} + \delta_{sp}, & p, s \in \text{holes} \quad (\text{cf. Eq. (6.15)}) \\ (\gamma_N)_{sp}, & \text{else.} \end{cases}$$

By application of Wick's theorem the two-body density matrix can be rewritten in terms of the normal-ordered one- and two-body reduced density matrices and the reference contribution

$$\begin{aligned} \gamma_{stpq} &= (\gamma_N)_{stpq} + \delta_{sp} \delta_{p \in \text{holes}} (\gamma_N)_{tq} - \delta_{tp} \delta_{p \in \text{holes}} (\gamma_N)_{sq} + \delta_{tq} \delta_{q \in \text{holes}} (\gamma_N)_{sp} - \delta_{sq} \delta_{q \in \text{holes}} (\gamma_N)_{tp} \\ &+ \delta_{tq} \delta_{sp} \delta_{p \in \text{holes}} \delta_{q \in \text{holes}} - \delta_{tp} \delta_{sq} \delta_{p \in \text{holes}} \delta_{q \in \text{holes}}, \end{aligned} \quad (6.345)$$

with the matrix elements of the two-body reduced density matrix

$$(\gamma_N)_{stpq} = \langle \Phi_0 | \left( e^{T^\dagger} : a_p^\dagger a_q^\dagger a_t a_s :_{|\Phi_0\rangle} e^T \right)_C | \Phi_0 \rangle. \quad (6.346)$$

Thus, the expectation value for a general two-body operator in terms of density matrix elements is

$$\langle O^{(2)} \rangle = \frac{1}{4} \sum_{p,q,s,t} \langle pq| o |st\rangle (\gamma_N)_{stpq} + \sum_{p,s} \left( \sum_i \langle pi| o |si\rangle \right) (\gamma_N)_{sp} + \frac{1}{2} \sum_{i,j} \langle ij| o |ij\rangle. \quad (6.347)$$

However, it is beneficial to replace the factor  $e^{T^\dagger}$  in Eq. (6.343) and (6.346) with  $(1 + \Lambda)e^{-T}$ , obtained by solving the  $\Lambda$ -CC equations, to arrive at finite expression for the evaluation of expectation values. This replacement leads to [177]

$$(\gamma_N)_{sp} = \langle \Phi_0 | (1 + \Lambda) e^{-T} : a_p^\dagger a_s :_{|\Phi_0\rangle} e^T | \Phi_0 \rangle = \langle \Phi_0 | \left[ (1 + \Lambda) \left( : a_p^\dagger a_s :_{|\Phi_0\rangle} e^T \right)_C \right] | \Phi_0 \rangle, \quad (6.348)$$

$$(\gamma_N)_{stpq} = \langle \Phi_0 | \left[ (1 + \Lambda) \left( : a_p^\dagger a_q^\dagger a_t a_s :_{|\Phi_0\rangle} e^T \right)_C \right] | \Phi_0 \rangle. \quad (6.349)$$

Excited-state properties are obtained in EOM-CCSD, using the excited-state generalization of the ground-state density matrix  $\gamma_N^\mu$  with matrix elements

$$(\gamma_N)_{sp}^\mu = \langle \Phi_0 | L_\mu^{A,(\text{CCSD})} e^{-T} : a_p^\dagger a_s :_{|\Phi_0\rangle} e^T R_\mu^{A,(\text{CCSD})} | \Phi_0 \rangle, \quad (6.350)$$

while transitions are calculated from the transition density matrix  $\gamma_N^{\mu\nu}$  with matrix elements

$$(\gamma_N)_{sp}^{\mu\nu} = \langle \Phi_0 | L_\mu^{A,(\text{CCSD})} e^{-T} : a_p^\dagger a_s :_{|\Phi_0\rangle} e^T R_\nu^{A,(\text{CCSD})} | \Phi_0 \rangle. \quad (6.351)$$

## 7 Exploring $sd$ -shell nuclei

In this section we study ground- and excited-state properties of all  $sd$ -shell nuclei with neutron and proton numbers  $8 \leq N, Z \leq 20$ . We derive effective valence-space Hamiltonians, as outlined in Sec. 6.2, using the set of low-resolution two- and three-nucleon interactions introduced in Sec. 4, that predict realistic saturation properties of symmetric nuclear matter. We focus on estimating the theoretical uncertainties due to variation of the resolution scale in NN forces and the low-energy 3N couplings. In addition, we also explore the uncertainty associated due to the many-body calculations. While all valence-space interactions derived from MBPT so far were based on a single chiral NN+3N interaction this study of ground-state energies, two-neutron and two-proton separation energies, and first excited  $2_1^+$  energies overcomes this limitation. The results discussed here have been published in Ref. [51].

We employ five different chiral NN+3N Hamiltonians, which are denoted as 1.8/2.0 (EM), 2.0/2.0 (EM), 2.2/2.0 (EM), 2.0/2.5 (EM), 2.0/2.0 fm<sup>-1</sup> (EM+PWA), where the values  $\lambda_{\text{NN}}/\Lambda_{\text{3N}}$  indicate the SRG resolution scale and the cutoff in the 3N regulator. The label in parentheses denotes the  $c_i$  couplings used in the NN/3N sector. Based on these interactions, we construct effective valence-space Hamiltonians

$$H'_{\text{eff}} = \sum_{\alpha=1}^d \varepsilon_{\alpha} a_{\alpha}^{\dagger} a_{\alpha} + V_{\text{eff}}, \quad (7.1)$$

where  $\varepsilon_{\alpha}$  denote the single-particle energies (SPEs), and  $V_{\text{eff}}$  is the effective two-body interaction for valence nucleons. With  $H'_{\text{eff}}$  we perform valence shell-model calculations, where the many-body problem is solved exactly for the particles in the valence space on top of a closed core. Taking into account many-body processes outside the valence space, valence-space interactions derived from MBPT have been used successfully for shell-model calculations in many regions of the nuclear chart, see, e.g., Refs. [184–186]. At third order, MBPT based on RG/SRG-evolved interactions with low cutoffs shows a reasonable order-by-order convergence for SPEs and  $V_{\text{eff}}$  in medium-mass nuclei [187]. To explore uncertainties associated with MBPT, we study valence-shell Hamiltonians obtained at second- and third-order in MBPT. In contrast to phenomenological interactions, such as USDA/B [162] that fit both SPEs and  $V_{\text{eff}}$  to experimental  $sd$ -shell data, our results are without adjustments. Therefore, we do not expect to reach accuracies comparable to the best fit USD interactions.

Studies of oxygen [188, 189] and calcium [35, 166, 187] isotopes showed that extending the valence space beyond one major shell provides additional binding and can lead to improvements for neutron-rich systems. However, since our main interest is to perform a comprehensive study of  $sd$ -shell nuclei, estimating the theoretical uncertainty associated with the initial Hamiltonians, we limit our valence space to the  $sd$  shell ( $d_{5/2}$ ,  $d_{3/2}$ , and  $s_{1/2}$  proton and neutron single-particle orbitals on top of a <sup>16</sup>O core). We work in a harmonic-oscillator basis with  $\hbar\Omega = 13.53$  MeV, appropriate for the  $sd$  shell, and scale all matrix elements of  $V_{\text{eff}}$  and bound SPEs by  $A^{-1/3}$  to correct for the increase in nuclear size. For all  $\lambda_{\text{NN}}$  considered, the calculations are converged in a basis consisting of 13 major shells ( $e_{\text{Max}} = 12$ ) for NN forces [187]. For 3N forces, we allow a total energy of the three single-particle states up to  $12\hbar\Omega$  ( $E_{\text{3Max}} = 12$ ) in a basis of 13 major shells. The SPEs for the five NN+3N interactions are summarized in Tab. 7.1 for second and in Tab. 7.2 for third order.

Orbital	1.8/2.0 (EM)		2.0/2.0 (EM)		2.0/2.5 (EM)		2.2/2.0 (EM)		2.0/2.0 (EM+PWA)	
	p	n	p	n	p	n	p	n	p	n
$d_{5/2}$	-1.413	-4.315	-1.121	-4.041	-0.901	-3.728	-0.802	-3.651	-0.473	-3.276
$s_{1/2}$	0.561	-2.454	1.068	-1.976	1.346	-1.583	1.568	-1.375	2.883	0.038
$d_{3/2}$	4.191	1.658	4.436	1.928	5.103	2.298	5.216	2.385	6.380	3.491

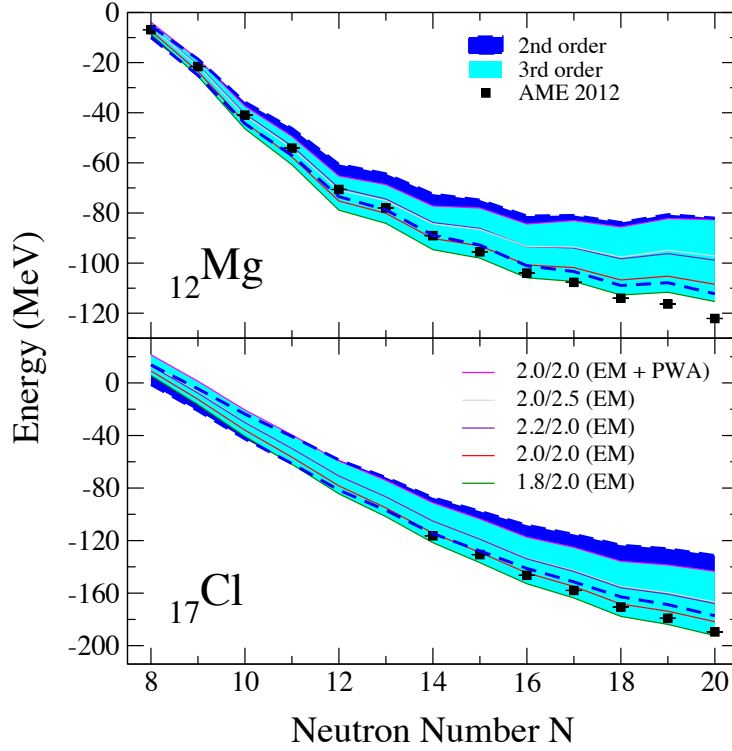
**Table 7.1:** Calculated proton (p) and neutron (n)  $sd$ -shell SPEs in MeV for the five input Hamiltonians at second order in MBPT.

Figure 7.1 shows the ground-state energies of magnesium and chlorine isotopes compared to the Atomic Mass Evaluation (AME 2012) [190]. The second- and third-order MBPT results are represented by the blue, darker and the cyan, lighter bands, respectively, where the width of each band is spanned by the five different NN+3N interactions considered.

The experimental ground-state energies for magnesium isotopes are generally within our uncertainty band, with neutron-rich isotopes at the lower side. Only the most neutron-rich isotopes are underbound in our calculations. On the other hand, the ground-state energies of all chlorine isotopes are in good agreement with our uncertainty

Orbital	1.8/2.0 (EM)		2.0/2.0 (EM)		2.0/2.5 (EM)		2.2/2.0 (EM)		2.0/2.0 (EM+PWA)	
	p	n	p	n	p	n	p	n	p	n
$d_{5/2}$	-1.188	-3.834	-0.873	-3.617	-0.541	-3.072	-0.501	-3.098	-0.221	-2.723
$s_{1/2}$	0.652	-2.254	1.189	-1.787	1.551	-1.214	1.769	-1.025	2.864	0.207
$d_{3/2}$	4.370	1.949	4.799	2.326	5.343	2.990	5.490	3.022	6.760	3.839

**Table 7.2:** Calculated proton (p) and neutron (n)  $sd$ -shell SPEs in MeV for the five input Hamiltonians at third order in MBPT.



**Figure 7.1:** Ground-state energies of the magnesium (top) and chlorine isotopes (bottom panel) relative to  $^{16}\text{O}$  at second (blue, darker band) and third order (cyan, lighter band) in MBPT and compared to the Atomic Mass Evaluation (AME 2012) [190]. The uncertainty bands are spanned by the five different NN+3N interactions (see text for details). The ordering in the legend is with decreasing ground-state energies.

band, and they are typically within the lower side of the third-order MBPT band, defined by the  $\lambda_{\text{NN}}/\Lambda_{3\text{N}} = 1.8/2.0, 2.0/2.0, 2.2/2.0, 2.0/2.5 \text{ fm}^{-1}$  interactions. In general we find better agreement between our results and experiment for the isotopic chains of heavier elements, which suggests a somewhat too weak neutron-neutron interaction in our  $sd$ -shell calculations. This was also observed in Refs. [188, 189] for the oxygen isotopes.

The estimated uncertainties in calculated ground-state energies are dominated by the different input Hamiltonians. Specifically, the resolution-scale dependence by varying  $\lambda_{\text{NN}}$  from  $1.8 - 2.2 \text{ fm}^{-1}$  with  $\Lambda_{3\text{N}} = 2.0 \text{ fm}^{-1}$  is somewhat larger than the  $\Lambda_{3\text{N}}$  dependence from  $2.0 - 2.5 \text{ fm}^{-1}$  for  $\lambda_{\text{NN}} = 2.0 \text{ fm}^{-1}$ . This results in a combined resolution-scale dependence of approximately  $1.0 \text{ MeV}$  per valence particle in  $^{32}\text{Mg}$  and  $^{37}\text{Cl}$ . When also including the PWA  $c_i$  values in 3N forces, the uncertainty roughly doubles to about  $2.0 \text{ MeV}$  per valence particle. For both second- and third-order MBPT bands, the  $2.0/2.0 \text{ fm}^{-1}$  (EM+PWA) interactions generally define the least bound calculations (for ground-state energies, the upper end of the bands).

The difference between second- and third-order MBPT results is relatively small compared to the width of each band, indicating a reasonable, but still incomplete convergence of the MBPT approach in this region. For magnesium and chlorine, third-order results are more bound because of more attractive proton-neutron interactions, whereas for oxygen (not shown), second-order results are more bound than at third order mainly due to the neutron single-

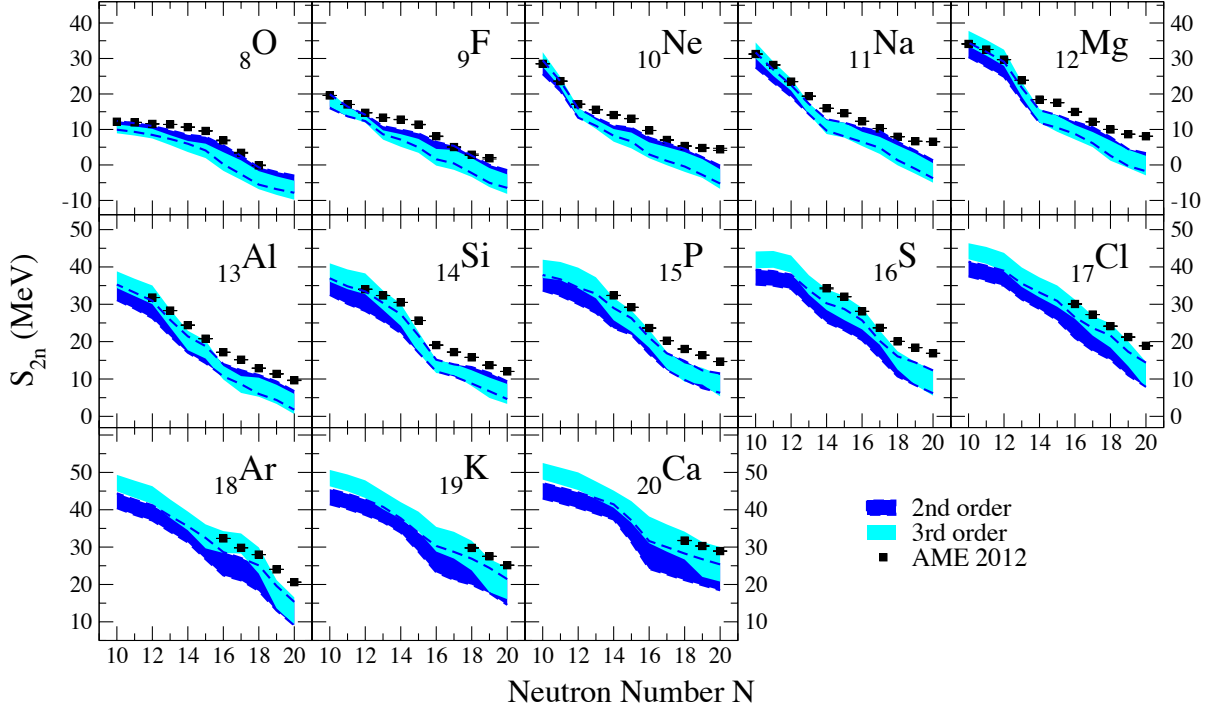


**Figure 7.2:** Uncertainty estimates for the two-neutron separation energies  $S_{2n}$  of  $sd$ -shell isotopic chains at second (blue, darker band) and third order (cyan, lighter band) in MBPT and compared to the Atomic Mass Evaluation (AME 2012) [190].

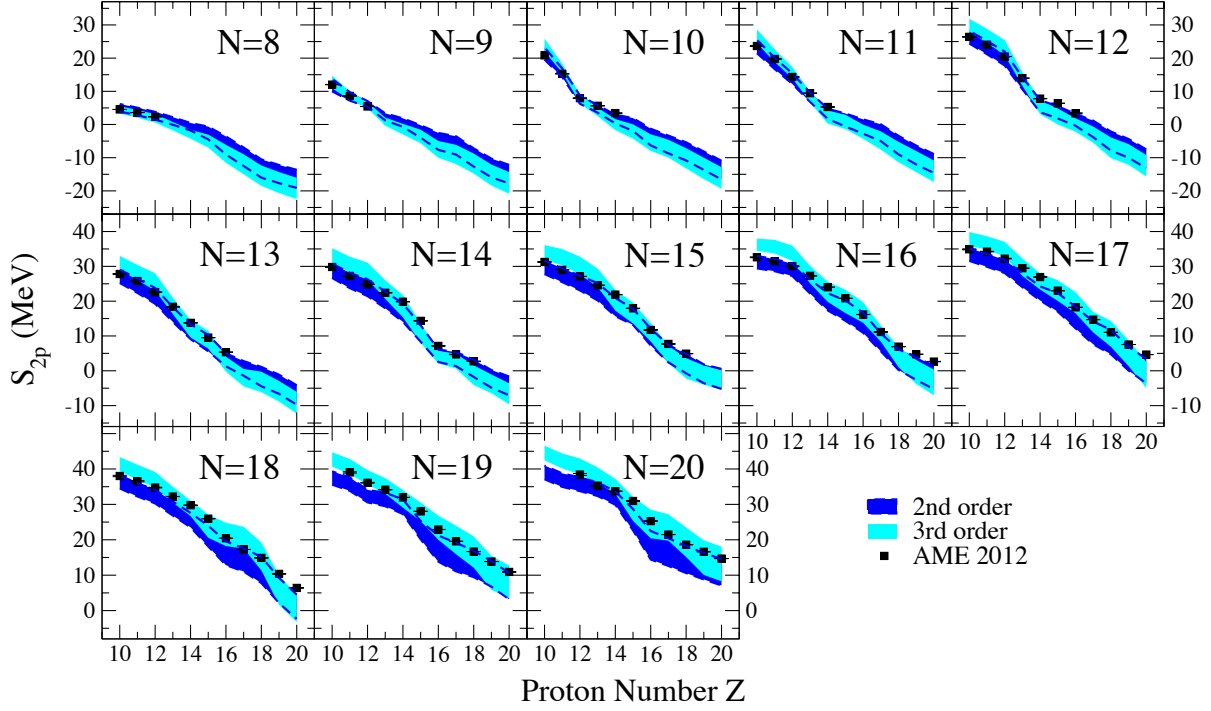
particle energies, cf. Tabs. 7.1 and 7.2. When the uncertainty associated to the MBPT is also included, the total uncertainty increases to 2.1 MeV and 2.8 MeV per valence particle in  $^{32}\text{Mg}$  and  $^{37}\text{Cl}$ , respectively.

Figure 7.2 compares theoretical and experimental two-neutron separation energies  $S_{2n}$  for all isotopic chains from oxygen to calcium ( $Z = 8 - 20$ ). The theoretical calculations describe the overall experimental trends reasonably well, but in general our uncertainty bands underestimate the empirical values. This is especially the case in lighter elements and for the most neutron-rich nuclei for all isotopic chains. This is probably related to the underbinding of the  $sd$ -shell calculations when valence neutron-neutron interactions are dominant. We also note that around  $N = 20$ , the ground states of  $^{29,30}\text{Ne}$  [191, 192],  $^{30,31}\text{Na}$  [193, 194], and  $^{31,32}\text{Mg}$  [195, 196] are dominated by deformed configurations not captured in our  $sd$ -shell calculations (this is the so-called island of inversion). Consequently, our bands do not reproduce the change in slope of  $S_{2n}$  around  $N = 20$  for Ne, Na, or Mg.

Similar to the ground-state energies, the dominant uncertainties arise from the different Hamiltonians, with smaller differences between second- and third-order MBPT results. Typically the uncertainty range for  $S_{2n}$  is  $\sim 5$  MeV. The exceptions are  $N < Z$  isotopes, more visible in heavier elements, where the difference between second- and third-order results is comparable to the uncertainty between input Hamiltonians, due to too weak proton-neutron interactions at second-order MBPT, adding up to a total uncertainty of  $\sim 10$  MeV.

In Fig. 7.3 we show the two-proton separation energy  $S_{2p}$  for all isotonic chains from  $N = 8$  to  $N = 20$ . Our results agree very well with experiment in all cases, and remarkably most experimental values fall within the third-order MBPT band. Only in few proton-deficient and very proton-rich nuclei do experimental  $S_{2p}$  lie within the second-order band. Since there are fewer proton-rich nuclei known experimentally than neutron-rich nuclei,  $S_{2p}$  are in general informative about proton-neutron interactions. The much better agreement in  $S_{2p}$  than for  $S_{2n}$  compared to experiment suggests that the different Hamiltonians considered capture better (mostly isoscalar) proton-neutron interactions than neutron-neutron interactions. Again, the sensitivity to the input Hamiltonians dominates the theoretical  $S_{2p}$  uncertainties (with a similar range of  $\sim 5$  MeV), except for proton-deficient nuclei where the MBPT uncertainty is comparable (with a total uncertainty of  $\sim 10$  MeV).

Finally in Fig. 7.4, the calculated first excited  $2_1^+$  energies are compared to experimental data for all even-even  $sd$ -shell isotopes. The spread of the uncertainty band is typically smaller than  $\sim 500$  keV, with generally reasonable agreement to experiment. However, in the cases with high-lying  $2_1^+$  states, indicative of shell closures ( $^{22}\text{O}$ ,  $^{24}\text{O}$ ,  $^{22}\text{Si}$ ,  $^{34}\text{Si}$ ,  $^{34}\text{Ca}$ ), the uncertainty can be as large as  $\sim 1$  MeV. This means that, while our bands in general



**Figure 7.3:** Uncertainty estimates for two-proton separation energies  $S_{2p}$  of  $sd$ -shell isotonic chains at second (blue, darker band) and third order (cyan, lighter band) in MBPT and compared to the Atomic Mass Evaluation (AME 2012) [190].

predict shell closures consistently, the actual excitation of the  $2_1^+$  state is very sensitive to the details of the input Hamiltonian. The width of the uncertainty band is mostly due to the  $2.0/2.0 \text{ fm}^{-1}$  (EM+PWA) interaction, which is also responsible for the unusually large uncertainty band in  $^{36}\text{Ar}$ . In general, the second- and third-order MBPT bands mostly overlap, except for  $N \sim Z$  argon and calcium isotopes, where only third-order MBPT results are in agreement to experiment. Similar to the case of  $S_{2n}$ , we also note that the  $2_1^+$  states within the island of inversion, the  $N = 20$  isotopes  $^{30}\text{Ne}$  [192] and  $^{32}\text{Mg}$  [196], are deformed, and their relatively low excitation energies cannot be well described in our  $sd$ -shell calculations.

As a first application of the different Hamiltonians with realistic saturation properties, we have explored ground-state energies,  $S_{2n}$ ,  $S_{2p}$ , and first excited  $2_1^+$  energies for all  $sd$ -shell nuclei: isotopic chains from oxygen to calcium and isotonic chains from  $N = 8$  to  $N = 20$ . This is based on NN+3N Hamiltonians that have been fitted only to  $A = 3, 4$  nuclei that predict realistic saturation properties of nuclear matter, without additional adjustments. We have focused on estimating the theoretical uncertainties due to the different input Hamiltonians and associated with the many-body calculations. We find reasonable agreement to experimental data, especially in nuclei dominated by valence proton-neutron interactions. For neutron-rich systems, calculations in extended valence spaces are needed, due to too weak neutron-neutron interactions in the  $sd$  shell.

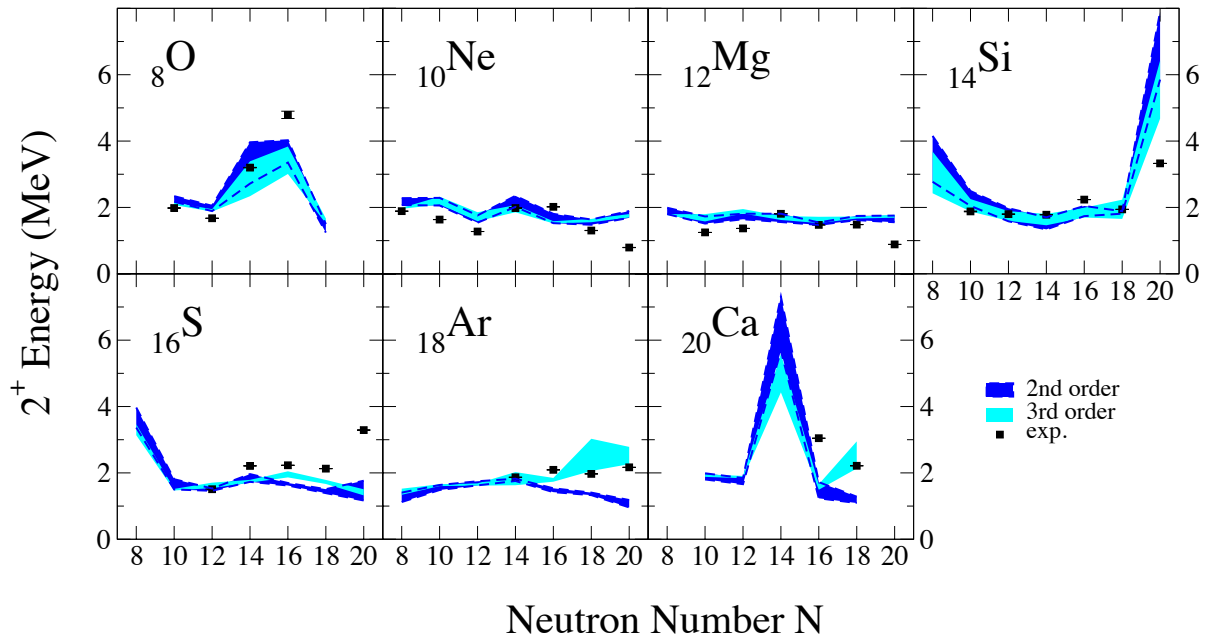


**Figure 7.4:** Uncertainty estimates for excitation energies of the first  $2_1^+$  states in even-even  $sd$ -shell isotopes at second (blue, darker band) and third order (cyan, lighter band) and compared to experimental data from ENSDF [197].





## 8 Calcium isotopic chain

In this section we want to focus on the calcium isotopes that have gained an increased interest in the last years both from experiment and theory. The calcium isotopic chain ( $Z = 20$ ) is a unique nuclear system to study how protons and neutrons interact inside the atomic nucleus. Two of its stable isotopes are magic in both their proton and neutron number ( $^{40}\text{Ca}$  and  $^{48}\text{Ca}$ ), and experimental evidence of doubly magic features in two short-lived calcium isotopes have been reported recently, based on precision measurements of nuclear masses for  $^{52}\text{Ca}$  ( $N = 32$ ) [35] and  $2^+$  excitation energies for  $^{54}\text{Ca}$  ( $N = 34$ ) [36].

Having investigated  $sd$ -shell nuclei in Sec. 7 based on the  $\text{NN}+3\text{N}$  Hamiltonians introduced in Sec. 4, we used the same set of Hamiltonians as well as the  $\text{N}^2\text{LO}_{\text{sat}}$  potential [103], discussed in Sec. 2.4, to perform coupled-cluster calculations of neutron-rich calcium isotopes within a larger theory collaboration.

While the electric charge distributions in atomic nuclei were measured accurately already half a century ago, the knowledge of the distribution of neutrons is still deficient. Therefore, we performed coupled-cluster calculations of the neutron distribution of the neutron-rich nucleus  $^{48}\text{Ca}$ , showing that the neutron skin (difference between the radii of the neutron and proton distributions) is significantly smaller than previously thought. In addition, we made predictions for the electric dipole polarizability and the weak form factor, quantities that, in the meantime, have [198] or will be targeted [199] by precision measurements. These results have been published in Ref. [12]. Moreover, the first measurements of the charge radii of  $^{49,51,52}\text{Ca}$  by collinear laser spectroscopy experiments at ISOLDE, CERN revealed a large and unexpected increase of the size of the neutron-rich calcium isotopes beyond  $N = 28$ , challenging the doubly magic nature of  $^{52}\text{Ca}$ . This measurement provided a benchmark for our ab initio calculations, opening new intriguing questions on the evolution of nuclear sizes away from stability. The results have been published jointly with experimentalists in Ref. [37].

### 8.1 Coupled-cluster calculations of energies, radii and charge densities

Before discussing results we want to specify the coupled-cluster truncations employed in the calculation of energies, radii and charge densities. A HF calculation in a single-particle basis consisting of 15 major harmonic oscillator shells ( $e_{\text{Max}} = 14$ ) with an oscillator frequency of  $\hbar\Omega = 22\text{ MeV}$ , and  $3\text{N}$  matrix elements truncated to the three-particle energy  $E_{3\text{Max}} \leq 18$  for  $\text{N}^2\text{LO}_{\text{sat}}$  and  $E_{3\text{Max}} \leq 16$  for the chiral Hamiltonians presented in Sec. 4, yields the reference state for the coupled-cluster computation. The Hamiltonian is normal ordered with respect to the HF reference state, employing the normal-ordered two-body approximation for the  $3\text{N}$  force introduced in Sec. 6.1. Coupled-cluster theory performs, as outlined in Sec. 6.5.1, the similarity transform  $\bar{H} = e^{-T} H_N e^T$  of the normal-ordered Hamiltonian  $H_N$  using the cluster operator  $T$  that consists of a linear expansion in particle-hole excitation operators. Approximations are introduced by truncating the operator  $T$  to a lower particle-hole rank, and the most commonly used approximation is coupled-cluster with single and double excitations (CCSD). For the computation of the binding energy of  $^{48}\text{Ca}$  we include the perturbative triples correction  $\Lambda\text{-CCSD(T)}$ , given in Eq. (6.300). The neutron separation energies  $S_n$  of  $^{48}\text{Ca}$  and  $^{49}\text{Ca}$  are computed with the particle-removed/attached equation-of-motion coupled-cluster method truncated at the one-particle-two-hole/two-particle-one-hole excitation, cf. Eq. (6.335) and (6.334) in Sec. 6.5.2. The three-point mass difference,  $\Delta = (S_n(^{48}\text{Ca}) - S_n(^{49}\text{Ca}))/2$ , is computed as the difference between two separation energies. The similarity transformed Hamiltonian is non-Hermitian and we compute its right  $R_0^A |\Phi\rangle$  and left  $\langle\Phi| L_0^A$  ground states. Expectation values of one- and two-body operators  $\langle O^{(1)} \rangle$ ,  $\langle O^{(2)} \rangle$  are then obtained from expectation values of the reduced density matrices  $(\gamma_N)_{sp}$ ,  $(\gamma_N)_{stpq}$ , cf. Eq. (6.348) and (6.349). Here, we truncate  $R_0^A(\text{CCSD}) |\Phi\rangle$  and  $\langle\Phi| L_0^A(\text{CCSD})$  at the CCSD level.

For the computation of the root mean square (r.m.s.) point-neutron radius (that is, the radius of the neutron distribution)  $R_n$  and the r.m.s. point-proton radius  $R_p$  we start from the intrinsic operators (see, e.g., Ref. [200])

$$R_n^2 = \frac{1}{N} \sum_i^A (\mathbf{r}_i - \mathbf{R})^2 \frac{1 - \tau^3}{2}, \quad (8.1)$$

and

$$R_p^2 = \frac{1}{Z} \sum_i^A (\mathbf{r}_i - \mathbf{R})^2 \frac{1 + \tau^3}{2}, \quad (8.2)$$

with the number of nucleons  $A$ , the number of neutrons  $N$ , the number of protons  $Z$ , the nucleon coordinates  $\mathbf{r}_i$ , the center-of-mass coordinate  $\mathbf{R}$ , and the third component of the isospin  $\tau^3$  of the  $i$ th nucleon, respectively. As  $R_{n,p}^2$  is a two-body operator, we compute its expectation value by employing the two-body density matrix in the CCSD

approximation. While the radii of closed-(sub-)shell isotopes  $^{40,48,52,54}\text{Ca}$  are accessible in single-reference coupled-cluster calculations, the radii of neighboring isotopes  $^{39,47,51,53}\text{Ca}$  and  $^{41,49,53}\text{Ca}$  have to be computed by the particle-removed/attached equation-of-motion coupled-cluster method truncated at the one-particle-two-hole/two-particle-one-hole excitation, see Sec. 6.5.2. For the intrinsic r.m.s. point-neutron and r.m.s. point-proton densities we first compute the corresponding one-body densities in the laboratory system at the CCSD level. The coupled-cluster wave function factorizes approximately into an intrinsic part times a Gaussian center-of-mass wave function [201]. A deconvolution with respect to the Gaussian center-of-mass wave function [202] yields the intrinsic one-body density. The intrinsic r.m.s. point-neutron and r.m.s. point-proton form factors are obtained from Fourier transforms of the one-body densities; folding these with the nucleon form factors given in Ref. [203] yields the intrinsic (weak-) charge form factors. The Fourier transform of the (weak-) charge form factor yields the corresponding intrinsic (weak-) charge density.

In our ab initio calculations we compute  $R_p$ , which is related to the charge radius  $R_{\text{ch}}$  by

$$R_{\text{ch}}^2 = R_p^2 + \langle r_p^2 \rangle + \frac{N}{Z} \langle r_n^2 \rangle + \frac{3}{4m_p^2 c^4} + \langle r^2 \rangle_{\text{so}}. \quad (8.3)$$

Here  $\langle r_p^2 \rangle = 0.769 \text{ fm}^2$  is the mean squared charge radius of a single proton,  $\langle r_n^2 \rangle = -0.116 \text{ fm}^2$  is that of a single neutron,  $\frac{3}{4m_p^2 c^4} = 0.033 \text{ fm}^2$  is the relativistic Darwin-Foldy correction, and  $\langle r^2 \rangle_{\text{so}}$  is the spin-orbit correction. The spin-orbit correction [204] is calculated from

$$\langle r^2 \rangle_{\text{so}} = \frac{1}{Z} \sum_{i=1}^A \langle r_i^2 \rangle_{\text{so}} = -\frac{1}{Z} \sum_i \frac{\mu_i}{M^2} (\kappa_i + 1), \quad (8.4)$$

with the magnetic moments of the proton,  $\mu_p = 2.793\mu_N$ , and the neutron,  $\mu_n = -1.913\mu_N$ , and the definition

$$\kappa = \begin{cases} l, & j = l - \frac{1}{2} \\ -(l+1), & j = l + \frac{1}{2}. \end{cases} \quad (8.5)$$

For  $^{48}\text{Ca}$  we obtain  $\langle r^2 \rangle_{\text{so}} = -0.090(1) \text{ fm}^2$ , which is slightly smaller in magnitude than the relativistic mean-field estimates [57] due to configuration mixing. Similarly the weak-charge radius  $R_W$  is computed from [57]

$$R_W^2 = \frac{Z}{Q_W} [Q_W^p (R_p^2 + \langle \tilde{r}_p^2 \rangle)] + \frac{N}{Q_W} [Q_W^n (R_n^2 + \langle \tilde{r}_n^2 \rangle)] + \langle \tilde{r}^2 \rangle_{\text{so}}. \quad (8.6)$$

Here  $Q_W = NQ_W^n + ZQ_W^p$  is the total weak charge of the nucleus;  $Q_W^n = -0.9878$  and  $Q_W^p = 0.0721$  are the neutron and proton weak charges (the uncertainty of the weak charge of the neutron and proton are discussed in Ref. [57]), respectively;  $R_{p,n}^2$  is the mean square point-proton/neutron radius;  $\langle \tilde{r}_p^2 \rangle = 2.358 \text{ fm}^2$  and  $\langle \tilde{r}_n^2 \rangle = 0.777 \text{ fm}^2$  are the weak mean squared radii of the proton and neutron; and  $\langle \tilde{r}^2 \rangle_{\text{so}}$  is the spin-orbit correction to the weak-charge radius. We compute  $\langle \tilde{r}^2 \rangle_{\text{so}}$  using the coupled-cluster method in the CCSD approximation and we obtain  $\langle \tilde{r}^2 \rangle_{\text{so}} = 0.069(1) \text{ fm}^2$ . The spin-orbit corrections to the charge and weak-charge radii are taken as the mean value resulting from all the interactions considered in this work, and we estimate an uncertainty of  $0.001 \text{ fm}^2$  from the dependence of  $\langle \tilde{r}^2 \rangle_{\text{so}}$  on the employed interaction. This is comparable to the relativistic mean-field (RMF) estimate  $\langle \tilde{r}^2 \rangle_{\text{so}} \approx 0.077 \text{ fm}^2$  of Ref. [205].

---

## 8.2 Neutron and weak-charge distributions of the $^{48}\text{Ca}$ nucleus

---

Owing to their electric charge, the distribution of protons in a nucleus can be accurately measured and is well known for many atomic nuclei [206]. In contrast, neutron densities are poorly known. An accurate knowledge of neutron distributions in atomic nuclei is crucial for understanding neutron-rich systems, which determine the limits of the nuclear landscape [31] and give rise to exotic structures and novel phenomena in rare isotopes [35, 36, 207]. Because of its fundamental importance, experimental efforts worldwide have embarked on an ambitious programme of measurements of neutron distributions in nuclei using different probes, including hadronic scattering [208], pion photoproduction [209], and parity-violating electron scattering [210]. As neutrons have no electric charge, elastic electron scattering primarily probes the proton distribution, whereas parity-violating electron scattering can

occur only via the weak interaction and is sensitive to the distribution of weak charge. As the weak charge of the neutron,  $Q_W^n \approx -0.99$ , is much larger than that of the proton,  $Q_W^p \approx 0.07$ , a measurement of the parity-violating asymmetry  $A_{pv}$  [211] offers an opportunity to probe the neutron distribution.

Regardless of the probe used, direct measurements of neutron distributions in nuclei are extremely difficult. For this reason, experiments have also focused on other observables related to neutron distributions, such as the electric dipole polarizability  $\alpha_D$ . Recently,  $\alpha_D$  was accurately determined in  $^{208}\text{Pb}$  [212],  $^{120}\text{Sn}$  [213] and  $^{68}\text{Ni}$  [214], and, very recently, after publication of our prediction, in  $^{48}\text{Ca}$  [198]. For this medium-mass nucleus, the calcium radius experiment (CREX) at Jefferson Lab [199] also aims at a measurement of the radius of the weak-charge distribution.

So far, much of the theoretical understanding of proton and neutron distributions in atomic nuclei like  $^{208}\text{Pb}$ ,  $^{120}\text{Sn}$  and  $^{68}\text{Ni}$  came from nuclear density functional theory (DFT) [215]. This method employs energy density functionals that are primarily constrained by global nuclear properties such as binding energies and radii, and it provides us with a coarse-grained description of nuclei across the nuclear chart. Calculations within nuclear DFT generally describe charge radii, and suggest that  $\alpha_D$  is strongly correlated with the neutron skin [203, 216, 217], thereby relating this quantity to the neutron radius. The medium-mass nucleus  $^{48}\text{Ca}$  is of particular interest because it can be accessed by both DFT and ab initio methods, providing results that are well converged in terms of model-space truncations (see Sec. 9.1 for a convergence analysis of IM-SRG calculations). Thus, it provides an exciting opportunity to bridge both approaches. In the process, surprises are expected. For instance, as discussed in the following, ab initio calculations show that the neutron skin of  $^{48}\text{Ca}$  is significantly smaller than estimated by nuclear DFT models. This result not only gives us an important insight into the nuclear size, but also provides an opportunity to inform global DFT models by more refined ab initio theories.

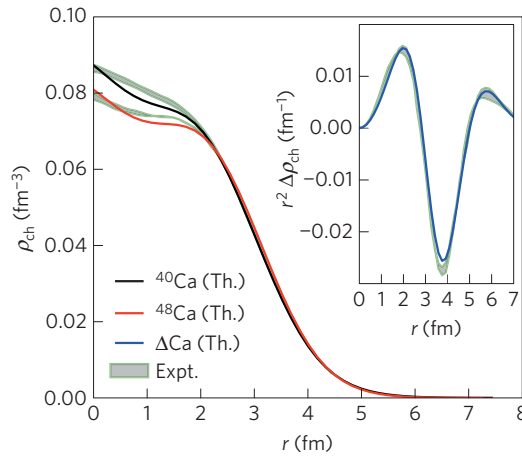


**Figure 8.1:** Charge densities of  $^{40}\text{Ca}$  (black line) and  $^{48}\text{Ca}$  (red line), obtained from coupled-cluster calculations using the  $N^2\text{LO}_{\text{sat}}$  Hamiltonian, compared to experiment [218] (shaded area). Inset:  $r^2$  multiplied by the difference between the computed charge densities of  $^{40}\text{Ca}$  and  $^{48}\text{Ca}$  (blue line) compared to experiment (shaded area). Taken from [12].

The  $N^2\text{LO}_{\text{sat}}$  predictions for the electric charge densities  $\rho_{\text{ch}}$  in  $^{40}\text{Ca}$  and  $^{48}\text{Ca}$  from coupled-cluster calculations are shown in Fig. 8.1. The agreement of theoretical charge densities with experiment [218], especially in the surface region, is most encouraging. The difference between the charge densities of  $^{40}\text{Ca}$  and  $^{48}\text{Ca}$ , shown in the inset of Fig. 8.1, is even better reproduced by theory, as systematic errors at short distances cancel out. The striking similarity of the measured charge radii of  $^{40}\text{Ca}$  and  $^{48}\text{Ca}$ , 3.478(2) fm and 3.477(2) fm, respectively, has been a long-standing challenge for microscopic nuclear structure models. The  $N^2\text{LO}_{\text{sat}}$  results for the charge radii are 3.49(3) fm for  $^{40}\text{Ca}$  and 3.48(3) fm for  $^{48}\text{Ca}$ ; these are the first ab initio calculations to successfully reproduce this observable in both nuclei. The distribution of the electric charge in a nucleus profoundly impacts the electric dipole polarizability  $\alpha_D$ . For the computation of this property we used the Lorentz integral transform combined with the coupled-cluster method to properly take the continuum into account [219]. Moreover, it was necessary to extend the formalism of Ref. [220] to accommodate 3N forces. To validate our model, we computed the dipole polarizabilities of  $^{16}\text{O}$  and  $^{40}\text{Ca}$ , for which experimental data exist [221]. We find an excellent agreement with experiment for  $^{16}\text{O}$ ,  $\alpha_D = 0.57(1) \text{ fm}^3$  compared to  $\alpha_{D,\text{exp}} = 0.58(1) \text{ fm}^3$ . Our result for  $^{40}\text{Ca}$ ,  $\alpha_D = 2.11(4) \text{ fm}^3$ , is only slightly below the experimental value  $\alpha_{D,\text{exp}} = 2.23(3) \text{ fm}^3$ .

We now turn to our main objective and present our predictions for the r.m.s. point-neutron radius  $R_n$ , r.m.s. point-proton radius  $R_p$ , neutron skin  $R_{\text{skin}} = R_n - R_p$ , and electric dipole polarizability in  $^{48}\text{Ca}$ . To estimate systematic uncertainties on computed observables, in addition to  $\text{N}^2\text{LO}_{\text{sat}}$ , we consider five different chiral NN+3N Hamiltonians, which are denoted as 1.8/2.0 (EM), 2.0/2.0 (EM), 2.2/2.0 (EM), 2.8/2.0 (EM), 2.0/2.0  $\text{fm}^{-1}$  (PWA), where the labeling indicates  $\lambda_{\text{NN}}/\Lambda_{3\text{N}}$  and the  $c_i$  couplings used. Similar to  $\text{N}^2\text{LO}_{\text{sat}}$ , these interactions consist of soft nucleon-nucleon and non-local 3N forces. Their 3N forces were adjusted to the binding energy of  $^3\text{H}$  and the charge radius of  $^4\text{He}$  only, and - within EFT uncertainties - yield a realistic saturation point of nuclear matter. A main difference between these interactions and  $\text{N}^2\text{LO}_{\text{sat}}$  is that they have not been constrained by experimental data on heavier nuclei, and they include  $\text{N}^3\text{LO}$  nucleon-nucleon contributions.

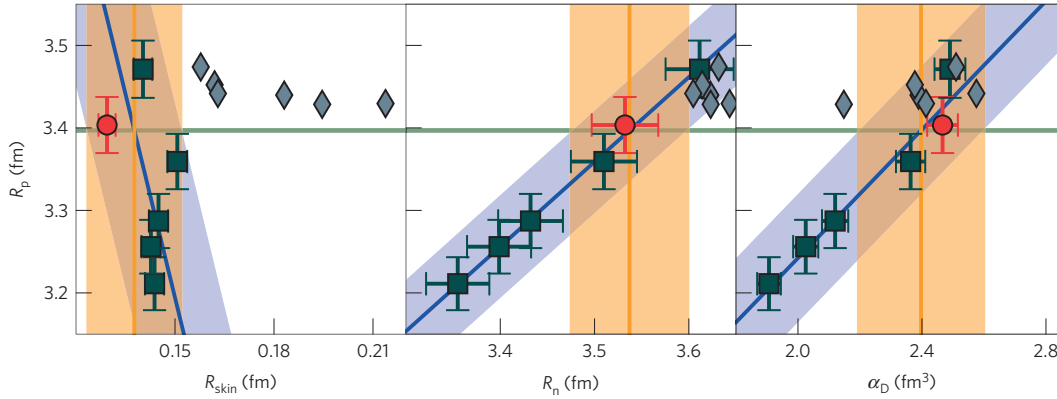


**Figure 8.2:** Predictions for the neutron skin  $R_{\text{skin}}$  (left), r.m.s. point-neutron radius  $R_n$  (middle) and electric dipole polarizability  $\alpha_D$  (right) of  $^{48}\text{Ca}$  plotted against its r.m.s. point-proton radius  $R_p$ . The coupled-cluster results for  $\text{N}^2\text{LO}_{\text{sat}}$  (red circles) and the five chiral NN+3N Hamiltonians (squares) are compared to the DFT results with the energy density functionals SkM\*, SkP, Sly4, SV-min, UNEDF0 and UNEDF1 [217] (diamonds). This is a representative subset of DFT results; for other DFT predictions, we refer to Ref. [217]. The theoretical error bars estimate uncertainties from truncations of the employed method and model space. The blue line represents a linear fit to the data. The blue band encompasses all error bars and estimates systematic uncertainties. The horizontal green line marks the experimental value of  $R_p$ . Its intersection with the blue line and the blue band yields the vertical orange line and orange band, respectively, giving the predicted range for the ordinate. Taken from [12].

Figure 8.2 shows the predicted values of  $R_{\text{skin}}$ ,  $R_n$  and  $\alpha_D$  as functions of  $R_p$ . In all three panels of Fig. 8.2, the blue line represents a linear fit to our ab initio results obtained with the set of chiral forces considered. The blue bands provide an estimate of systematic uncertainties. They encompass the error bars on the computed data points and are symmetric around the linear fit (blue line). The charge radius of  $^{48}\text{Ca}$  is known precisely, and the horizontal green line marks the corresponding  $R_p$ . The intersection between this line and the blue band provides a range for these observables (shown as vertical orange bands) consistent with our set of interactions. Our prediction for the neutron skin in  $^{48}\text{Ca}$  is  $0.12 \lesssim R_{\text{skin}} \lesssim 0.15$  fm. The left panel of Fig. 8.2 shows two remarkable features. First, the ab initio calculations yield neutron skins that are almost independent of the employed interaction. This is due to the strong correlation between the  $R_n$  and  $R_p$  in this nucleus (middle panel of Fig. 8.2). In contrast, DFT models exhibit practically no correlation between  $R_{\text{skin}}$  and  $R_p$ . Second, the ab initio calculations predict a significantly smaller neutron skin than the DFT models. The predicted range is also appreciably lower than the combined DFT estimate of  $0.176(18)$  fm [217] and is well below the relativistic DFT value of  $R_{\text{skin}} = 0.22(2)$  fm [217]. To shed light on the lower values of  $R_{\text{skin}}$  predicted by ab initio theory, we computed the neutron separation energy  $S_n$  and the three-point binding energy difference  $\Delta$  in  $^{48}\text{Ca}$  (both being indicators of the  $N = 28$  shell gap). Our results, summarized in Tab. 8.1, are consistent with experiment and indicate the pronounced magicity of  $^{48}\text{Ca}$ , whereas DFT results usually significantly underestimate the  $N = 28$  shell gap [222]. The shortcoming of DFT for  $^{48}\text{Ca}$  is also reflected in  $R_p$ . Although many nuclear energy density functionals are constrained to the  $R_p$  of  $^{48}\text{Ca}$  [215, 222], the results of DFT models shown in the left panel of Fig. 8.2 overestimate this quantity.

For  $R_n$ , shown in the middle panel of Fig. 8.2, we find  $3.47 \lesssim R_n \lesssim 3.60$  fm. Most of the DFT results for  $R_n$  are outside this range, but fall within the blue band. Comparing the left and middle panel of Fig. 8.2 suggests that a measurement of a small neutron skin in  $^{48}\text{Ca}$  would provide a critical test for ab initio models. For the electric dipole polarizability, shown in the right panel of Fig. 8.2, our prediction  $2.19 \lesssim \alpha_D \lesssim 2.60$   $\text{fm}^3$  is consistent with

Interaction	$BE$	$S_n$	$\Delta$	$R_{ch}$	$R_W$
$N^2LO_{sat}$	404(3)	9.5	2.69	3.48	3.65
1.8/2.0 (EM)	420(1)	10.1	2.69	3.30	3.47
2.0/2.0 (EM)	396(2)	9.3	2.66	3.34	3.52
2.2/2.0 (EM)	379(2)	8.8	2.61	3.37	3.55
2.8/2.0 (EM)	351(3)	8.0	2.41	3.44	3.62
2.0/2.0 (PWA)	346(4)	7.8	2.82	3.55	3.72
Experiment	415.99	9.995	2.399	3.477	

**Table 8.1:** Coupled-cluster results for the binding energy  $BE$ , the neutron separation energy  $S_n$ , the three-point-mass difference  $\Delta$ , the electric-charge radius  $R_{ch}$ , and the weak-charge radius  $R_W$  of  $^{48}\text{Ca}$  in comparison with experiment. Energies are given in MeV and radii in fm. See text for details on the different truncations in coupled-cluster theory used to obtain these results. The error in the calculated  $BE$ s are estimated from the change in  $BE$  from  $E_{3\text{Max}} \leq 16$  to  $E_{3\text{Max}} \leq 18$  for  $N^2LO_{sat}$  and  $E_{3\text{Max}} \leq 14$  to  $E_{3\text{Max}} \leq 16$  for the chiral Hamiltonians presented in Sec. 4. For the computed radii we estimate an error of 1%.

the DFT value of  $2.306(89) \text{ fm}^3$  [217]. Again, most of the DFT results fall within the ab initio uncertainty band. The experimental result for  $\alpha_{D,\text{exp}}$  has been determined very recently from an inelastic proton-scattering experiment at RCNP, Osaka (Japan) to  $2.07(22) \text{ fm}^3$  [198], slightly below our prediction. The excellent correlation between  $R_p$ ,  $R_n$  and  $\alpha_D$  seen in the middle and right panel of Fig. 8.2 demonstrates the usefulness of  $R_n$  and  $\alpha_D$  as probes of the neutron density.

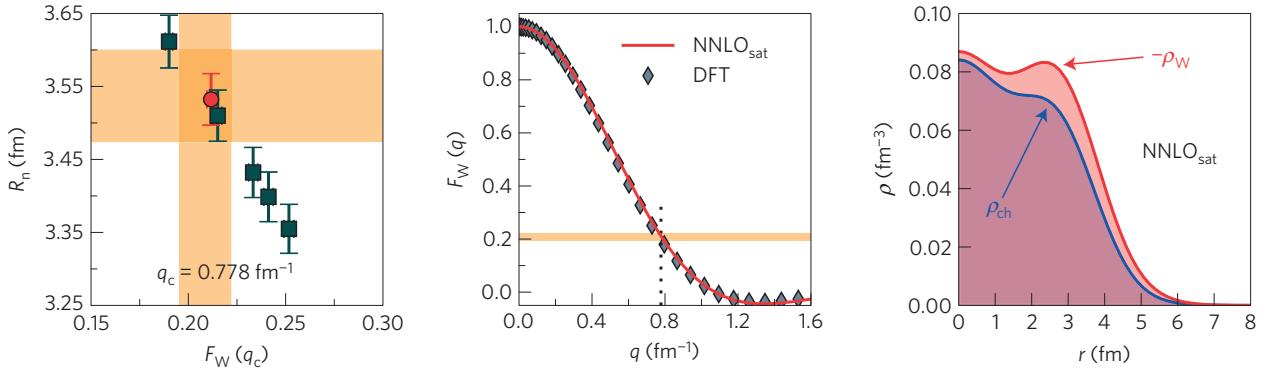


**Figure 8.3:** In the left panel we show the r.m.s. point-neutron radius  $R_n$  in  $^{48}\text{Ca}$  plotted against the weak-charge form factor  $F_W(q_c)$  at the CREX momentum  $q_c = 0.778 \text{ fm}^{-1}$  obtained in coupled-cluster calculations with  $N^2LO_{sat}$  (red circle) and the five chiral NN+3N Hamiltonians introduced in Sec. 4 (squares). The theoretical error bars estimate uncertainties from truncations of the employed method and model space. The width of the horizontal orange band shows the predicted range for  $R_n$  and is taken from the middle panel of Fig. 8.2. The width of the vertical orange band is taken from the right panel of Fig. 8.4 and shows the predicted range for  $F_W(q_c)$ . The weak-charge form factor  $F_W(q)$  as a function of momentum transfer  $q$  with  $N^2LO_{sat}$  (red line) and DFT with the energy density functional SV-min [203] (diamonds) is shown in the middle panel. The orange horizontal band shows  $F_W(q_c)$ . The right panel includes the charge density  $\rho_{ch}$  (blue line) and the (negative of) the weak-charge density  $\rho_W$  (red line). The weak-charge density extends well beyond  $\rho_{ch}$  as it is strongly weighted by the neutron distribution. The weak charge of  $^{48}\text{Ca}$ , obtained by integrating the weak-charge density is  $Q_W = -26.22$ . Taken from [12].

The weak-charge radius  $R_W$  is another quantity that characterizes the size of the nucleus. The CREX experiment will measure the parity-violating asymmetry  $A_{pv}$  in electron scattering on  $^{48}\text{Ca}$  at the momentum transfer  $q_c = 0.778 \text{ fm}^{-1}$ . This observable is proportional to the ratio of the weak-charge and electromagnetic charge form factors  $F_W(q_c)/F_{ch}(q_c)$  [211]. Making some assumptions about the weak-charge form factor, one can deduce  $R_W$  and  $R_n$  from the single CREX data point [199]. The left panel of Fig. 8.3 shows that a strong correlation exists between  $R_n$  and  $F_W(q_c)$ , and this allows us to estimate  $0.195 \lesssim F_W(q_c) \lesssim 0.222$  (cf. right panel of Fig. 8.4), which is consistent with the DFT expectation [203]. The momentum dependence of the weak-charge form factor, shown in the middle

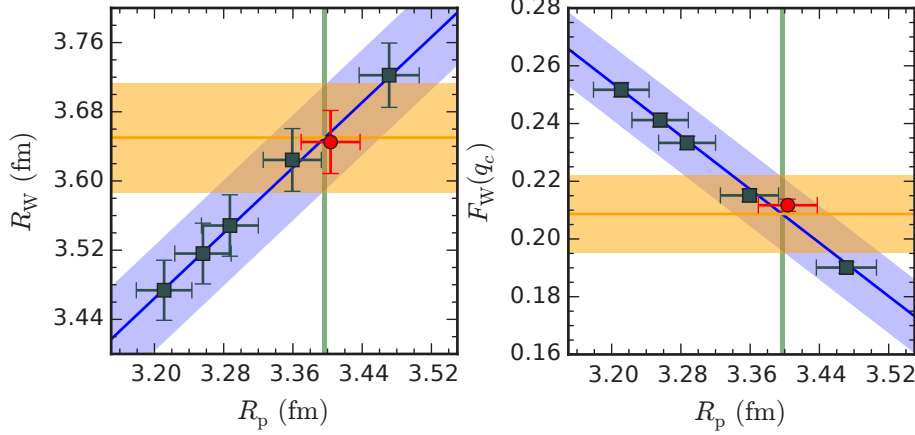


**Figure 8.4:** Correlation between the weak charge radius  $R_W$  (left) and the weak charge form-factor  $F_W(q_c)$  at the CREX momentum transfer  $q_c = 0.778 \text{ fm}^{-1}$  (right) and the r.m.s. point-proton radius  $R_p$  for  $^{48}\text{Ca}$  from the different chiral interactions. The symbols and lines are as in Fig. 8.2. Taken from [12].

panel of Fig. 8.3, is also close to the DFT result. This good agreement again emphasizes the role of  $^{48}\text{Ca}$  as a key isotope for bridging nuclear ab initio and DFT approaches. Exploiting the strong correlation between  $R_W$  and  $R_p$ , shown in the left panel of Fig. 8.4, we find  $3.59 \lesssim R_W \lesssim 3.71 \text{ fm}$ . The weak-charge density  $\rho_W(r)$  is the Fourier transform of the weak-charge form factor  $F_W(q)$ . As seen in the right panel of Fig. 8.3, the spatial extent of  $\rho_W$  in  $^{48}\text{Ca}$  is appreciably greater than that of the electric charge density  $\rho_{\text{ch}}$ , essentially because the former depends mainly on the neutron distribution and there is an excess of eight neutrons over protons in  $^{48}\text{Ca}$ .

### 8.3 Unexpectedly large charge radii of neutron-rich calcium isotopes

Having investigated the properties of the stable calcium isotopes  $^{40,48}\text{Ca}$ , that are magic in both their proton and neutron number, we now want to turn to short-lived, neutron-rich calcium isotopes for which experimental evidence of doubly magic features has been reported recently, based on precision measurements of nuclear masses [35] and  $2^+$  excitation energies [36]. As a local change in the behavior of the charge radius is expected in doubly magic nuclei [223], it is important to pin down the charge radius in these exotic isotopes to understand how shell structure evolves and impacts the limits of stability.

Although the average distance between the electrons and the nucleus in an atom is about 5,000 times larger than the nuclear radius, the size of the nuclear charge distribution is manifested as a perturbation of the atomic energy levels. A change in size between two isotopes gives rise to a shift of the atomic hyperfine structure levels. This shift between two isotopes, commonly known as the isotope shift,  $\delta \nu^{A,A'}$ , includes a part that is proportional to the change in the nuclear mean-square charge radii,  $\delta \langle r_{\text{ch}}^2 \rangle^{A,A'}$ , which is given by

$$\delta \langle r_{\text{ch}}^2 \rangle^{A,A'} = \langle r_{\text{ch}}^2 \rangle^{A'} - \langle r_{\text{ch}}^2 \rangle^A = \frac{1}{F} \left( \delta \nu^{A,A'} - K_{\text{MS}} \frac{M_{A'} - M_A}{M_A M_{A'}} \right). \quad (8.7)$$

Here,  $F$  denotes the electronic field factor and  $K_{\text{MS}}$  the mass shift. It is given by the sum of the normal mass shift,  $K_{\text{NMS}}$ , and the specific mass shift,  $K_{\text{SMS}}$ . Isotope shifts of stable Ca isotopes have been extensively studied in the literature [224], revealing the unusual evolution of their charge radii. Despite an excess of eight neutrons,  $^{48}\text{Ca}$  exhibits the striking feature that it has essentially the same charge radius as  $^{40}\text{Ca}$ , reproduced for the first time in ab initio calculations presented in Sec. 8.2.

A first estimate for the charge radius of the radioactive  $^{49}\text{Ca}$  isotope was based on a failure to observe its resonance in a dedicated measurement of its isotope shift. The resulting conclusion that  $\delta \nu^{48,49} \leq 50 \text{ MHz}$  suggested an enormous increase of the charge radius  $\delta \langle r_{\text{ch}}^2 \rangle^{48,49} \geq 0.5 \text{ fm}^2$  [225], reflecting the strong magicity of  $^{48}\text{Ca}$ . So far, the only charge radius measured beyond  $^{48}\text{Ca}$  has been for  $^{50}\text{Ca}$ , resulting in a large increase of  $\delta \langle r_{\text{ch}}^2 \rangle^{48,50} = 0.293(37) \text{ fm}^2$  [226]. These results raised even more exciting questions on the charge radii evolution of Ca isotopes. It suggested that the prominent odd-even staggering of their charge radii could be even more pronounced beyond  $^{48}\text{Ca}$  because a reduction of the nuclear charge radius for  $^{52}\text{Ca}$  would be expected as a consequence of a suggested doubly magic nature of this isotope. Thus, the experimental determination of the charge

radii of  $^{49,51,52}\text{Ca}$  not only addresses fundamental questions regarding the size of atomic nuclei, but are also important for understanding the possible doubly magic character of  $^{52}\text{Ca}$ . By using high-resolution bunched-beam collinear laser spectroscopy at ISOLDE, CERN, changes in the charge radii for  $^{43-52}\text{Ca}$  isotopes were obtained from the measured optical isotope shifts.

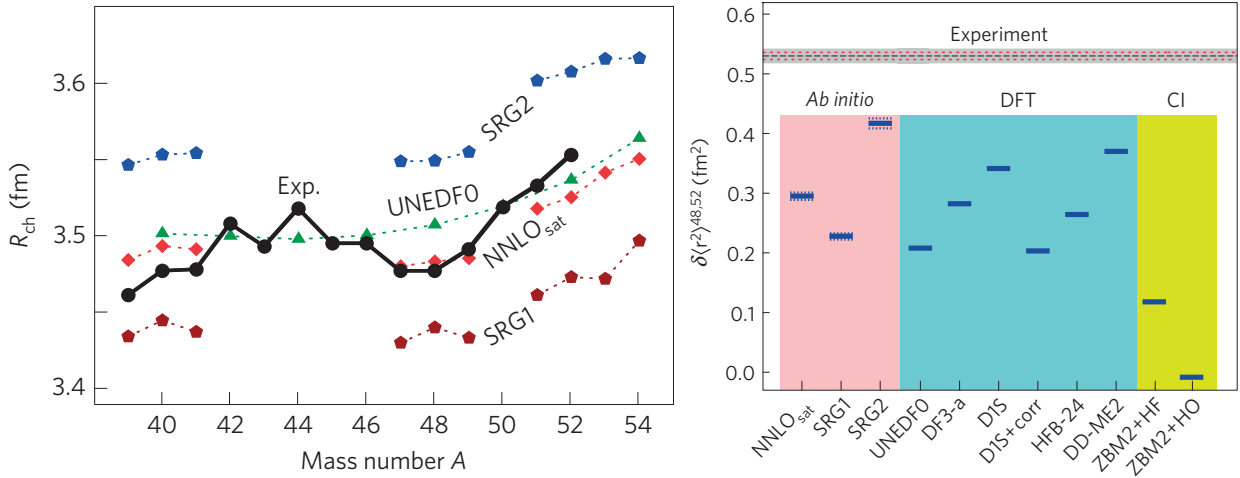


**Figure 8.5:** Experimental charge radii  $R_{\text{ch}}$  of Ca isotopes compared to coupled-cluster calculations with chiral EFT interactions  $\text{N}^2\text{LO}_{\text{sat}}$  SRG1 (2.8/2.0 (EM)), SRG2 (2.0/2.0 (PWA)), as well as DFT calculations with the UNEDF0 functional (left). Experimental error bars are smaller than the symbols. The absolute values were obtained from the reference radius of  $^{40}\text{Ca}$  [227] ( $R_{\text{ch}} = 3.478(2)\text{fm}$ ). The values of  $^{39}\text{Ca}$  and  $^{41,42}\text{Ca}$  are taken from Refs. [228, 229], respectively. A systematic theoretical uncertainty of 1% is estimated for the absolute values due to the truncation level of the coupled-cluster method and the finite basis space employed in the computation. In the right panel we show the experimental r.m.s. charge radius in  $^{52}\text{Ca}$  relative to that in  $^{48}\text{Ca}$  compared to the ab initio results as well as those of representative density functional theory (DFT) and configuration interaction (CI) calculations. The systematic uncertainties in the theoretical predictions are largely canceled when the differences between r.m.s. charge radii are calculated (dotted horizontal blue lines). Experimental uncertainties are represented by the horizontal red lines (statistical) and the gray shaded band (systematic). Taken from [37].

The experimental results for the root-mean-square (r.m.s.) charge radii, shown in the left panel of Fig. 8.5, yield a considerable increase for the charge radius of  $^{49}\text{Ca}$  with respect to  $^{48}\text{Ca}$ ,  $\delta\langle r_{\text{ch}}^2 \rangle^{48,49} = 0.097(4)\text{fm}^2$ , but much smaller than previously suggested [225]. The increase continues towards  $N = 32$ , resulting in a very large charge radius for  $^{52}\text{Ca}$ , with an increase relative to  $^{48}\text{Ca}$  of  $\delta\langle r_{\text{ch}}^2 \rangle^{48,52} = 0.530(5)\text{fm}^2$ .

This increase observed beyond a neutron number  $N = 28$  is as large as the values observed for open-shell nuclei like Fe [227], where there is no sizeable shell gap at  $N = 32$ . Thus, the charge radius of  $^{52}\text{Ca}$  is found to be much larger than expected for a doubly magic nucleus.

In addition to the experimental results we show the charge radii obtained by our ab initio calculations and by other theoretical predictions in the left panel of Fig. 8.5. The coupled-cluster calculations correctly yield similar charge radii for  $^{40}\text{Ca}$  and  $^{48}\text{Ca}$  for the chiral EFT interactions employed. As explained in Sec. 8.1 single-reference coupled-cluster calculations can be extended by equation-of-motion techniques to at most one or two nucleons outside a closed (sub-) shell. Thus, we do not give theoretical results for the mid-shell isotopes  $^{42-46}\text{Ca}$  and  $^{50}\text{Ca}$ . We note that absolute values of charge radii are very well reproduced by  $\text{N}^2\text{LO}_{\text{sat}}$ . The interactions SRG1 (2.8/2.0 (EM)) and SRG2 (2.0/2.0 (PWA)) also reproduce well the overall trend, but as they were not optimized for saturation properties they can give either slightly too low or too high saturation densities, corresponding to larger or smaller charge radii. Also shown are nuclear DFT results obtained with the Skyrme energy density functional UNEDF0 [230], which fails to describe the fine details of the experimental trend.

In the right panel of Fig. 8.5 we show the difference in r.m.s. charge radii between  $^{52}\text{Ca}$  and  $^{48}\text{Ca}$  predicted with different methods and models; all being representative of modern approaches to charge radii. In general, for neutron-rich isotopes beyond  $^{48}\text{Ca}$ , our ab initio calculations consistently predict an increase in charge radii for  $^{50,52}\text{Ca}$ , but fall short of describing the data. Similarly, DFT predictions with various models [31, 231–235]; configuration interaction (CI) calculations [235] obtained from large-scale shell-model calculations with the ZBM2 interaction [236, 237] using Skyrme-Hartree-Fock (ZBM2+HF) and harmonic-oscillator (ZBM2+HO) wa-

---

ve functions, all considerably underestimate the large charge radius of  $^{52}\text{Ca}$ . The standard explanation involving quadrupolar correlations [235, 236] does not seem to improve this, as can be seen by comparing the D1S and D1S plus quadrupolar correlations (D1S+corr) results [232] in the right panel of Fig. 8.5. Thus, our experimental results are truly unexpected. Speculating about the reason for these theoretical shortcomings we note that all theoretical approaches are lacking in the description of deformed intruder states associated with complex configurations. In addition to the Fayans functional DF3-a, shown in the right panel of Fig. 8.5, another Fayans functional FaNDF<sup>0</sup> [238] is used to interpret the very recent charge-radii measurement for the neutron deficient iron isotopes  $^{52,53}\text{Fe}$  [239]. While DFT calculations with the FaNDF<sup>0</sup> functional predict a larger increase in the charge radii towards  $^{52}\text{Ca}$  compared to results from DF3-a, the experimental value is still underestimated.

While we focus here on the unexpectedly large charge radius of  $^{52}\text{Ca}$ , the situation is indeed different for the lighter isotopes  $^{39-48}\text{Ca}$ . Here our ab initio calculations with  $\text{N}^2\text{LO}_{\text{sat}}$  capture the mass dependence around  $^{40}\text{Ca}$  and only slightly overestimate the absolute charge radii of these isotopes. Some of the models shown in the right panel of Fig. 8.5 perform better for lighter Ca isotopes. For instance, shell-model calculations (ZBM2) [235, 236] and DFT results (DF3-a) [231, 240], FaNDF<sup>0</sup> [238] (not shown) and D1S [232] describe experiments in the lighter calcium isotopes, but cannot reproduce the large increase in  $R_{\text{ch}}$  for  $^{52}\text{Ca}$ .

To assess the impact of core breaking effects, which turned out to be important for the description of electromagnetic moments in this region [241], we studied the proton occupancies of natural orbitals above the naively filled  $Z = 20$  shell. Our ab initio calculations show a weak, but gradual erosion of the proton core as neutrons are added. Although this defies the simple pattern of a rigid proton core expected for the magic Ca isotopes, the estimated magnitude of core breaking effects, including coupling to the neutrons, is not sufficient to explain the large charge radius of  $^{52}\text{Ca}$ .

These results open intriguing questions on the evolution of charge radii away from stability and constitute a major challenge in the search of a unified description of the atomic nucleus. It will be interesting to compare to future experiments, aiming at an extension of the current studies to isotopes even further away from stability, especially for the possibly doubly magic nucleus  $^{54}\text{Ca}$  [36].



---

## 9 In-medium similarity renormalization group calculations of nuclei

---

In this section we explore the impact of nuclear matter saturation on the properties and systematics of finite nuclei across the nuclear chart. Using the ab initio IM-SRG, introduced in Sec. 6.4, we study ground-state energies and charge radii of closed-shell nuclei from  ${}^4\text{He}$  to  ${}^{78}\text{Ni}$  in Sec. 9.1, based on the set of low-resolution two- and three-nucleon interactions introduced in Sec. 4, that predict realistic saturation properties. We first investigate in detail the convergence properties of these Hamiltonians with respect to model-space truncations for both two- and three-body interactions. We find one particular interaction that reproduces well the ground-state energies of all closed-shell nuclei studied. As expected from their saturation points relative to this interaction, the other Hamiltonians underbind nuclei, but lead to a remarkably similar systematics of ground-state energies. In Sec. 9.2 we explore the convergence properties of these Hamiltonians for ground-state energies in the vicinity of  $A \sim 100$ , which currently constitutes the frontier of our calculations due to the impact of the model-space truncations for both two- and three-body interactions. In Sec. 9.3 we extend our calculations to complete isotopic chains in the  $sd$  and  $pf$  shells with the valence-space IM-SRG, showing that the one particular interaction reproduces not only experimental ground states but two-neutron-separation energies and first excited  $2^+$  states. We also calculate radii with the valence-space IM-SRG for the first time. Since this particular interaction saturates at too high density, charge radii are still too small compared with experiment. Except for this underprediction, the radii systematics is, however, well reproduced. The results discussed here have been published in Ref. [52], except for the convergence studies of the heaviest nuclei for  $A \sim 100$ .

We employ four different chiral NN+3N Hamiltonians, which are denoted as 1.8/2.0 (EM), 2.0/2.0 (EM), 2.2/2.0 (EM), 2.0/2.0 fm $^{-1}$  (PWA), where the labeling indicates  $\lambda_{\text{NN}}/\Lambda_{3\text{N}}$  and the  $c_i$  couplings used. These chiral NN+3N Hamiltonians were first employed to study symmetric [28] and, more recently, also asymmetric nuclear matter [29, 242]. The first application to finite nuclei was in a valence-space study of  $sd$ -shell isotopes [51], discussed in Sec. 7, and in coupled-cluster calculations of calcium isotopes [12, 37], discussed in Sec. 8, as well as Ni isotopes [243]. Of particular importance to this work is that in symmetric nuclear matter the 1.8/2.0 (EM) interaction yields an energy per particle in good agreement with the empirical value (at saturation density with a Hartree-Fock spectrum slightly too bound [29]), although at a somewhat too high density. The other interactions 2.0/2.0 (EM), 2.2/2.0 (EM), 2.0/2.0 (PWA) saturate at decreasingly smaller energy and density [29]. Note that the nuclear-matter calculations of Ref. [29] are performed at an incomplete third order in many-body perturbation theory omitting third-order particle-hole contributions. Due to this inconsistency and the unknown many-body convergence beyond third order, we restrict our comparison of infinite nuclear matter and finite-nuclei results to a qualitative level.

In this study we use the Magnus formulation, presented in Sec. 6.4.3, to generate explicitly a unitary transformation that decouples the reference state from particle-hole excitations. This transformation can subsequently be applied to any operator, in particular the radius operator discussed below. For calculations of open-shell nuclei, we use the valence-space formulation of the IM-SRG (VS-IM-SRG) [168, 169, 244] based on the ensemble normal-ordering discussed in Ref. [145], which captures the bulk effects of residual 3N forces among valence nucleons. A valence-space Hamiltonian is then produced specifically for each nucleus, which is diagonalized with the NuShellX shell-model code [245] to obtain ground- and excited-state energies in the valence space. In both, ground-state and VS-IM-SRG calculations we employ the arctan variant of the White generator, see Eq. (6.233).

---

### 9.1 Closed-shell nuclei from ${}^4\text{He}$ to ${}^{78}\text{Ni}$

---

In this section, we analyze the model-space convergence of closed-shell nuclei based on the four chiral NN+3N interactions mentioned above. In the calculations we employ an angular-momentum-coupled basis built from single-particle spherical harmonic-oscillator (HO) states with quantum numbers  $e = 2n + l \leq e_{\text{Max}}$ . We employ partial-wave decomposed 3N matrix elements in a Jacobi-momentum basis and include partial waves up to the total three-body angular momentum  $\mathcal{J} \leq 9/2$ . Furthermore in order to manage computational storage requirements, we introduce an additional cut  $e_1 + e_2 + e_3 \leq E_{3\text{Max}} < 3e_{\text{Max}}$  for 3N matrix elements. For the analysis of the convergence behavior presented below, we study  $e_{\text{Max}}/E_{3\text{Max}} = 10/14, 12/14, 14/14, 14/16, \text{ and } 14/18$ .

In addition to ground-state energies, we also investigate the convergence behavior of charge radii. These results are obtained by normal-ordering and evolving the intrinsic proton mean-square radius operator  $R_p^2$ , defined in Eq. (8.2). Note that the proton mean-square radius operator is not free-space SRG evolved, consistent with the determination of the 3N couplings to the charge radius of  ${}^4\text{He}$ . We obtain charge radii by applying the corrections arising from the mean-square charge radii of the proton  $\langle r_p^2 \rangle$  and the neutron  $\langle r_n^2 \rangle$  as well as the relativistic Darwin-Foldy and spin-orbit corrections, see Eq. (8.3). The spin-orbit correction  $\langle r^2 \rangle_{\text{so}}$  is calculated as given in Eq. (8.4),

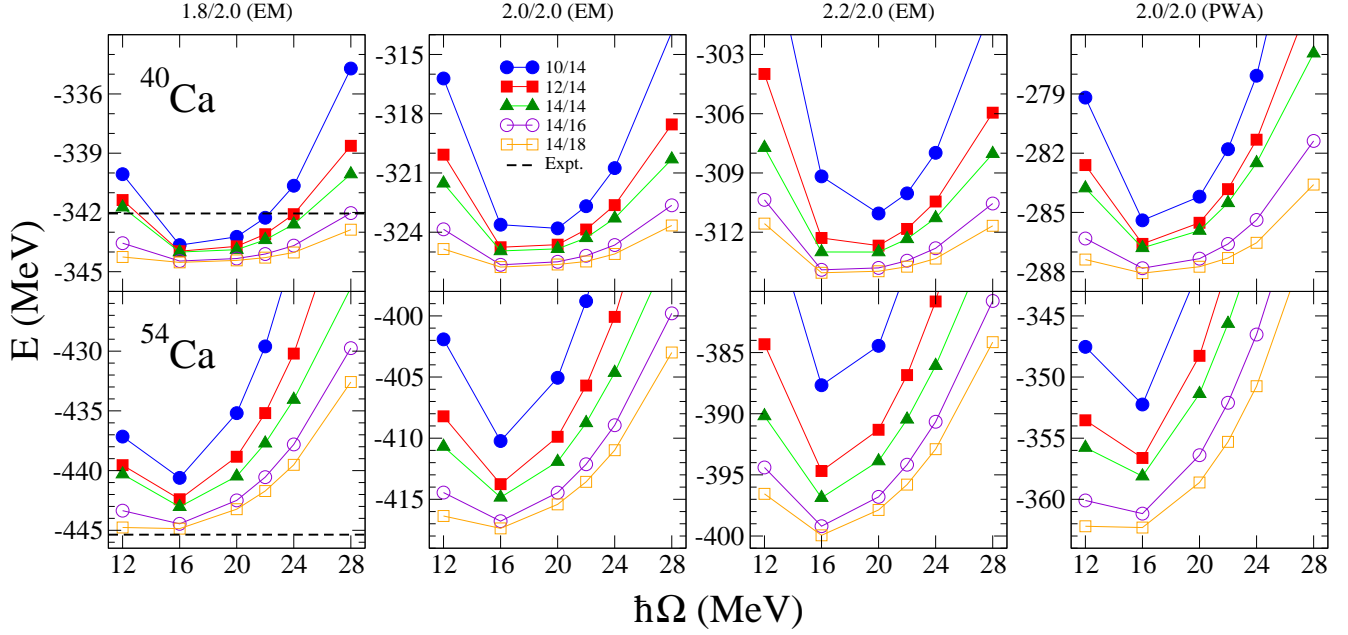


**Figure 9.1:** Convergence of ground-state energies for  $^{40}\text{Ca}$  (top panels) and  $^{54}\text{Ca}$  (bottom panels) calculated with the closed-shell IM-SRG. The column heading specifies the input Hamiltonian:  $\lambda_{\text{NN}}/\Lambda_{3\text{N}} = 1.8/2.0$  (EM) (left),  $2.0/2.0$  (EM) (middle-left),  $2.2/2.0$  (EM) (middle-right), and  $2.0/2.0$  (PWA) (right). In each panel, we show results obtained for harmonic-oscillator frequencies  $\hbar\Omega = (12 - 28)$  MeV and different truncations of the single-particle basis  $e_{\text{Max}}/E_{3\text{Max}} = 10/14$  (filled circles),  $12/14$  (filled squares),  $14/14$  (filled triangles),  $14/16$  (empty circles), and  $14/18$  (empty squares). The experimental ground-state energies from the atomic mass evaluation (AME) 2012 [190] are given by the dashed lines.

Hamiltonian	$^{54}\text{Ca}$				$^{78}\text{Ni}$			
	(10→12)/14	(12→14)/14	14/(14→16)	14/(16→18)	(10→12)/14	(12→14)/14	14/(14→16)	14/(16→18)
1.8/2.0 (EM)	1.8	0.6	1.4	0.4	3.3	0.9	4.4	2.0
2.0/2.0 (EM)	3.5	1.1	1.9	0.6	7.4	2.1	5.7	2.8
2.2/2.0 (EM)	7.0	2.2	2.3	0.7	14.7	5.0	6.6	3.4
2.0/2.0 (PWA)	4.4	1.5	3.1	1.1	9.2	3.0	9.6	5.0

**Table 9.1:** Convergence of ground-state energies of  $^{54}\text{Ca}$  and  $^{78}\text{Ni}$  for the four Hamiltonians considered. The table lists the change in the ground-state energy when increasing  $e_{\text{Max}} \rightarrow e_{\text{Max}} + 2$  ( $E_{3\text{Max}} \rightarrow E_{3\text{Max}} + 2$ ) at fixed  $E_{3\text{Max}}$  ( $e_{\text{Max}}$ ) for harmonic-oscillator frequency  $\hbar\Omega = 16$  MeV.

while values of  $\langle r_p^2 \rangle$  and  $\langle r_n^2 \rangle$  are taken from Ref. [246]. Additionally, two-body currents, due to the coupling of the photon to pions and to two nucleons, contribute to the charge radius, but this correction is neglected here.

In Fig. 9.1, we show the model-space convergence for ground-state energies of  $^{40}\text{Ca}$  and  $^{54}\text{Ca}$ . The energy minima are almost independent of the four different NN+3N interactions, typically located near  $\hbar\Omega = 16$  MeV. While the ground-state energy of  $^{40}\text{Ca}$  is well converged for the different Hamiltonians, in  $^{54}\text{Ca}$  convergence from  $e_{\text{Max}}/E_{3\text{Max}} = 10/14$  to  $14/14$  is only obtained for the interactions with lower resolution scales  $\lambda_{\text{NN}} = 1.8$  and  $2.0 \text{ fm}^{-1}$ . In Table 9.1, we list the change in the ground-state energy with increasing  $e_{\text{Max}}/E_{3\text{Max}}$ . We clearly see the  $1.8/2.0$  (EM) interaction is better converged from  $e_{\text{Max}}/E_{3\text{Max}} = 12/14$  to  $14/14$ , where the energy decreases by only  $0.6 \text{ MeV}$  total, compared with the  $2.2/2.0$  (EM) interaction, where this decrease is  $2.2 \text{ MeV}$ .

In addition, we investigate the impact of increasing the 3N cut  $E_{3\text{Max}} = 14 \rightarrow 18$  for  $e_{\text{Max}} = 14$  both in Fig. 9.1 and Table 9.1. In the case of the  $1.8/2.0$  (EM) interaction, the ground-state energy of  $^{54}\text{Ca}$  decreases by  $0.4 \text{ MeV}$  for  $E_{3\text{Max}} = 16 \rightarrow 18$ , while this decrease of  $0.7 \text{ MeV}$  is only slightly larger for the  $2.2/2.0$  (EM) interaction, indicating both are relatively well converged in terms of  $E_{3\text{Max}}$ . The largest impact is seen with the  $2.0/2.0$  (PWA) interaction, where the difference amounts to  $1.1 \text{ MeV}$ . While the ground-state energies calculated with the  $1.8/2.0$  (EM)

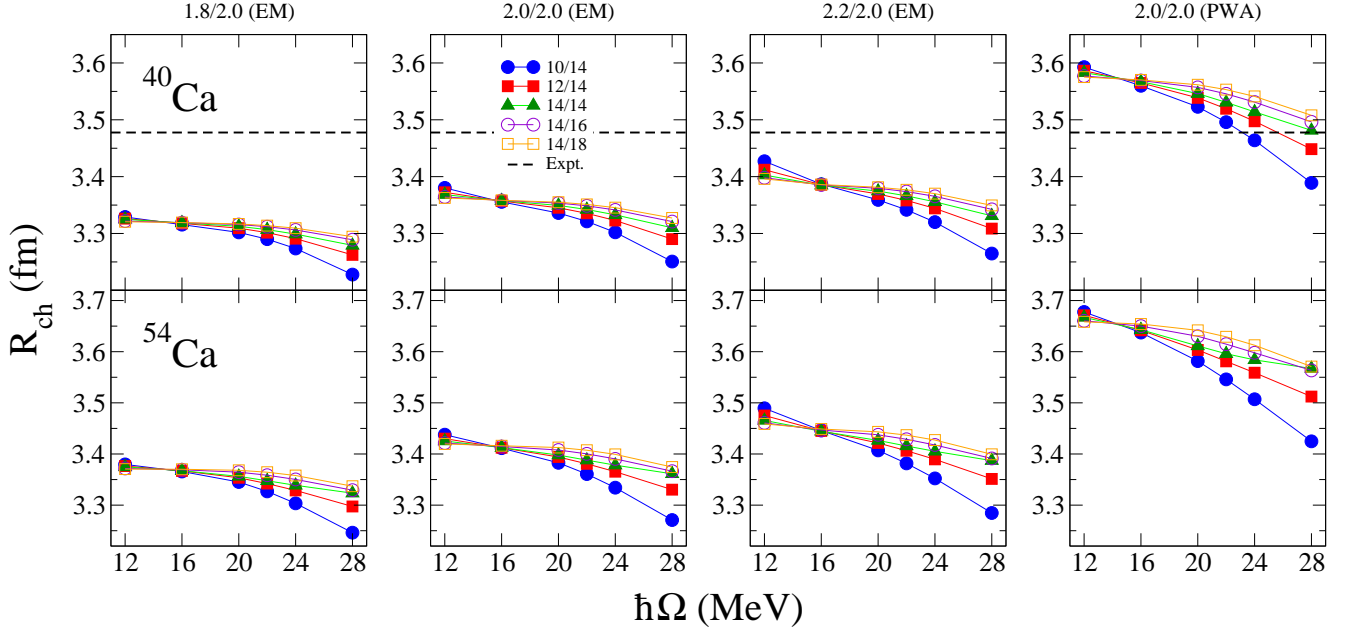


**Figure 9.2:** Convergence of charge radii for  $^{40}\text{Ca}$  (top panels) and  $^{54}\text{Ca}$  (bottom panels) calculated with the closed-shell IM-SRG. The legend is as in Fig. 9.1. The experimental charge radius for  $^{40}\text{Ca}$  [206] is given by the dashed line.

interaction agree with experiment to  $\approx 1\%$ , the other three Hamiltonians predict energies that are significantly underbound.

In Fig. 9.2, we show the model-space convergence of the charge radii for  $^{40}\text{Ca}$  and  $^{54}\text{Ca}$ . Although the ground-state energy of  $^{40}\text{Ca}$  calculated from the 1.8/2.0 (EM) interaction is in remarkable agreement with experiment, the corresponding charge radius, shown in the left column of Fig. 9.2, is significantly smaller than experiment. With increasing SRG resolution scale  $\lambda_{\text{NN}}$ , the charge radii increase but are still too small compared to experiment, while for the 2.0/2.0 (PWA) Hamiltonian, the calculated charge radius is instead somewhat too large. It will be very interesting to compare the charge-radii calculations for  $^{54}\text{Ca}$ , shown in the lower panels of Fig. 9.2 with future experimental results. Even the recent measurement of the charge radius of  $^{52}\text{Ca}$  [37], manifesting a strong increase from  $^{48}\text{Ca}$  onward, could not be explained fully by ab initio coupled-cluster calculations, see Sec. 8.3.

In Fig. 9.3, we show the model-space convergence for ground-state energies of  $^{56}\text{Ni}$  and  $^{78}\text{Ni}$ . Similar to the calcium isotopes (see Fig. 9.1) the minima in the ground-state energies are near  $\hbar\Omega = 16\text{MeV}$ . The energies obtained from the 1.8/2.0 (EM) Hamiltonian are again in very good agreement with experiment, while the other three Hamiltonians give results that are underbound to different degrees. The increase in particle number from calcium to nickel clearly results in slower model-space convergence. As seen in Table 9.1, enlarging the single-particle basis from  $e_{\text{Max}} = 12 \rightarrow 14$  changes the ground-state energy of  $^{78}\text{Ni}$  by 0.9MeV for the 1.8/2.0 (EM) interaction at  $\hbar\Omega = 16\text{MeV}$ , compared to 5.0MeV for the 2.2/2.0 (EM) interaction. The change in energy when increasing the cut in the 3N matrix elements from  $E_{3\text{Max}} = 16 \rightarrow 18$  is 2.0MeV for 1.8/2.0 (EM), already not completely converged. This effect is even larger for 2.0/2.0 (EM) and 2.2/2.0 (EM) and maximal for 2.0/2.0 (PWA), where the change is 5.0MeV. Again, for the 1.8/2.0 (EM) interaction, the agreement with experiment is good in both cases, but it is clear that the model space must be increased beyond  $e_{\text{Max}}/E_{3\text{Max}} = 14/18$  to claim fully converged results in this region, and likely for any nucleus with  $N, Z \gtrsim 50$ . We also note the unusual behavior of the  $^{78}\text{Ni}$  results for  $e_{\text{Max}}/E_{3\text{Max}} = 14/14$  at  $\hbar\Omega = 28\text{MeV}$  in Fig. 9.3 is probably caused by truncation artifacts due to the  $E_{3\text{Max}}$  cut.

In Fig. 9.4, we show the model-space convergence of the charge radii for  $^{56}\text{Ni}$  and  $^{78}\text{Ni}$ . Similar to the calcium isotopes discussed above, we see a gradual increase with increasing SRG resolution scale and a larger value for the 2.0/2.0 (PWA) interaction. While the results for  $^{56}\text{Ni}$  appear well converged for all starting Hamiltonians, this is less the case for  $^{78}\text{Ni}$  either with respect to  $e_{\text{Max}}$  or  $E_{3\text{Max}}$ , and especially for the larger cutoffs and the 2.0/2.0 (PWA) interaction.

Before studying the systematics of the ground-state energies and charge radii of closed shell nuclei, we compare our results to the coupled-cluster calculations of Hagen *et al.* [243] for the 1.8/2.0 (EM) interaction. Considering

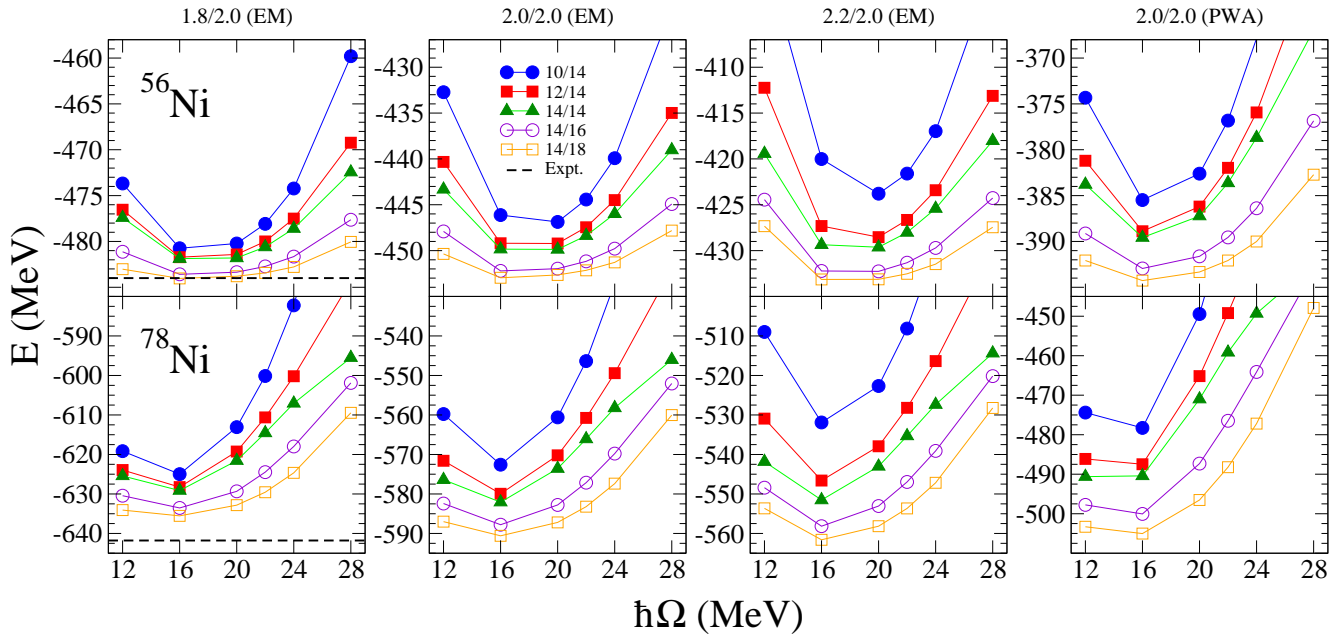


**Figure 9.3:** Convergence of ground-state energies for  $^{56}\text{Ni}$  (top panels) and  $^{78}\text{Ni}$  (bottom panels) calculated with the closed-shell IM-SRG. The legend is as in Fig. 9.1. Note that the experimental ground-state energy for  $^{78}\text{Ni}$  is extrapolated within the atomic mass evaluation.

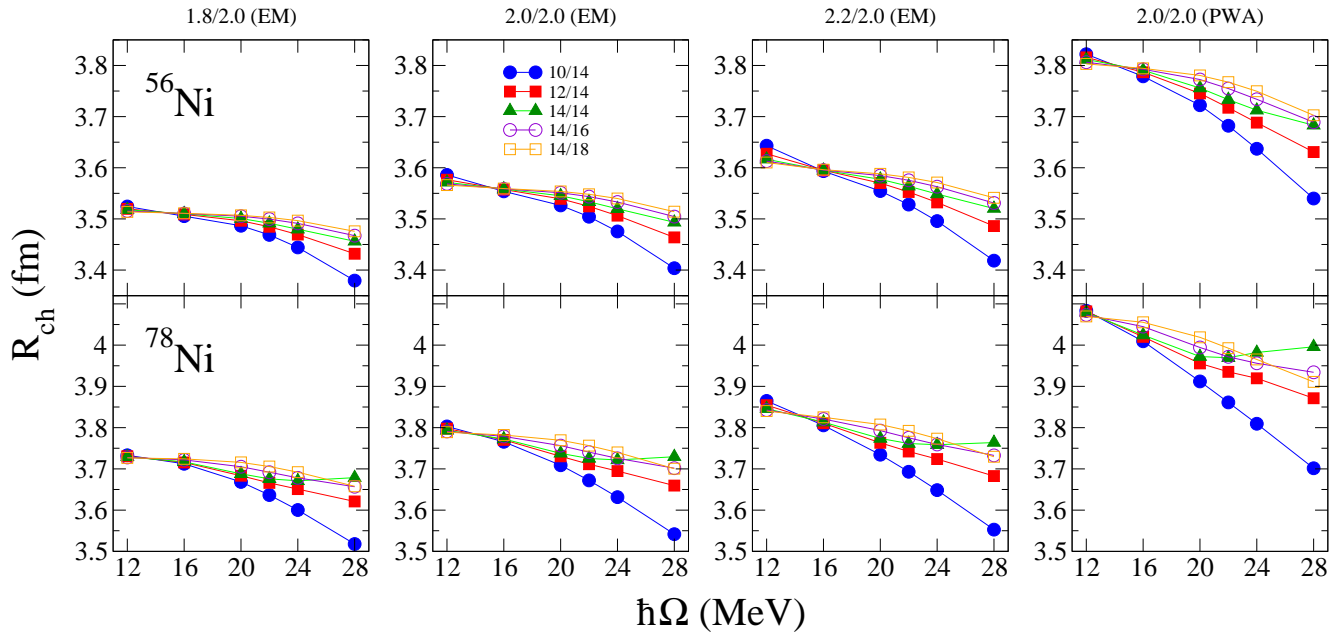


**Figure 9.4:** Convergence of charge radii for  $^{56}\text{Ni}$  (top panels) and  $^{78}\text{Ni}$  (bottom panels) calculated with the closed-shell IM-SRG. The legend is as in Fig. 9.1.

the same model-space truncation  $e_{\text{Max}}/E_{3\text{Max}} = 14/16$  and harmonic-oscillator frequency  $\hbar\Omega = 16$  MeV, we find good agreement within  $\approx 1\%$  for  $^{16}\text{O}$ :  $-127.2$  MeV (IM-SRG(2)) vs.  $-128$  MeV ( $\Lambda$ -CCSD(T)); for  $^{40}\text{Ca}$ :  $-344.5$  MeV vs.  $-348$  MeV; for  $^{48}\text{Ca}$ :  $-416.1$  MeV vs.  $-419$  MeV; and for  $^{78}\text{Ni}$ :  $-633.6$  MeV vs.  $-637$  MeV, while there is a difference of more than 3% for  $^4\text{He}$  ( $-29.2$  MeV vs.  $-28.2$  MeV).

Finally, in Figs. 9.5 and 9.6 we show ground-state energies and charge radii, respectively, for selected closed-shell nuclei from  $^4\text{He}$  to  $^{78}\text{Ni}$ . Except for the neutron-rich oxygen isotopes  $^{22,24}\text{O}$  all calculated ground-state energies from the 1.8/2.0 (EM) interaction are in very good agreement with experiment. Interestingly the other three interactions follow the same pattern but are shifted by as much as 1.5 MeV/A in the case of the 2.0/2.0 (PWA) interaction. The experimental charge radii are enclosed by the 2.2/2.0 (EM) and 2.0/2.0 (PWA) results, but the trend observed

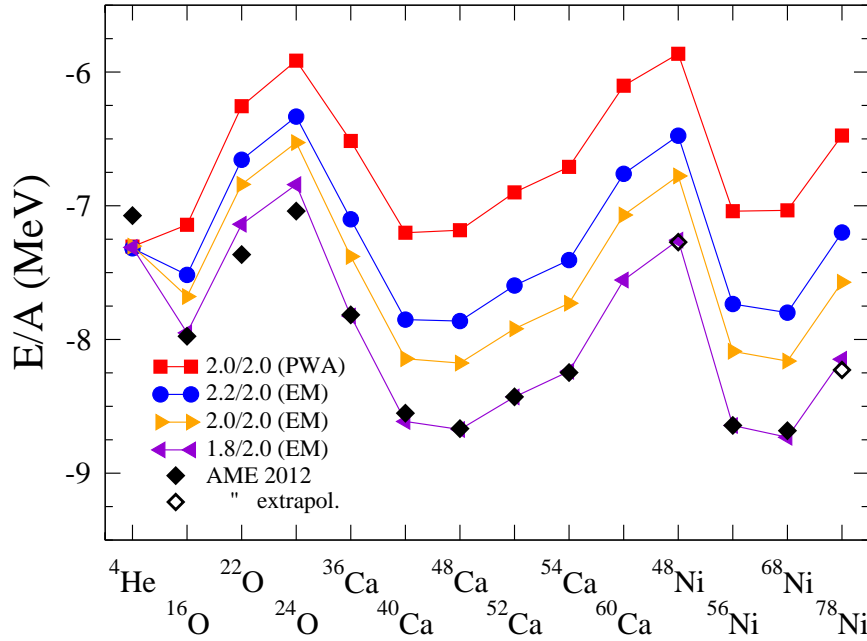


**Figure 9.5:** Systematics of the energy per nucleon  $E/A$  of closed-shell nuclei from  ${}^4\text{He}$  to  ${}^{78}\text{Ni}$  calculated with the IM-SRG for the four Hamiltonians considered. The results are compared against experimental ground-state energies from the AME 2012 [190] (extrapolated for  ${}^{48,78}\text{Ni}$ ).

for the closed-shell nuclei studied in detail already above appears to hold at least up to  ${}^{78}\text{Ni}$ . That is, radii with 1.8-2.2/2.0 are too small, but 2.0/2.0 (PWA) gives slightly too large radii. As in the case of ground-state energies, the radii systematics is similar for all Hamiltonians, with mainly only a constant shift for the different interactions. This behavior for the ground-state energy and charge radii is reminiscent of the Coester-like line for the saturation points of the four Hamiltonians considered [29].

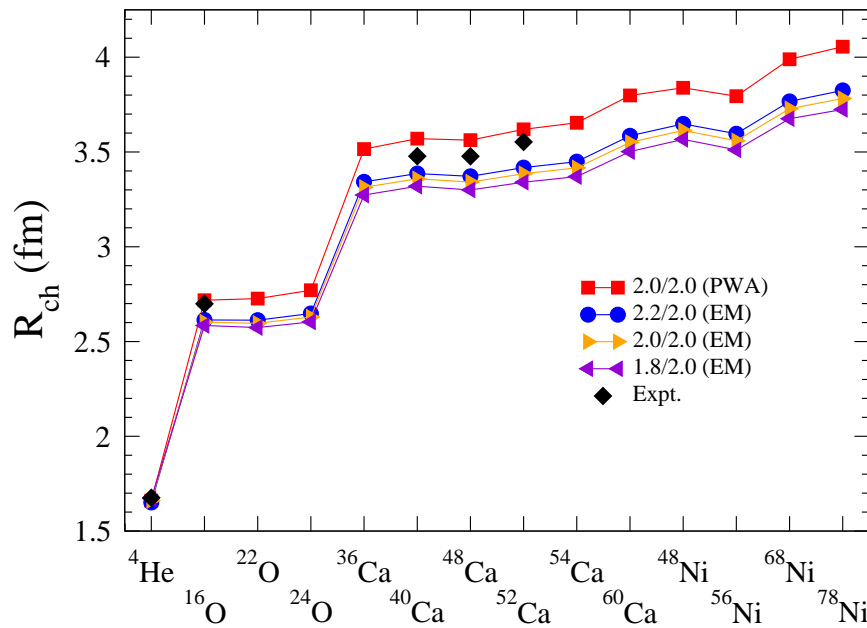


**Figure 9.6:** Systematics of charge radii of closed-shell nuclei from  ${}^4\text{He}$  to  ${}^{78}\text{Ni}$  calculated with the IM-SRG for the four Hamiltonians considered. The results are compared against experimental charge radii [206] where available.

## 9.2 Closed-shell nuclei in the vicinity of $A \sim 100$

The analysis of the model-space convergence of  $^{78}\text{Ni}$  in the last section already revealed that the model space must be increased beyond  $e_{\text{Max}}/E_{3\text{Max}} = 14/18$  to claim fully converged results. Nevertheless, we briefly want to investigate the model-space convergence of  $^{100,120}\text{Sn}$ , shown in Fig. 9.7. We limit the discussion to harmonic-oscillator frequencies  $\hbar\Omega = (12 - 20)$  MeV close to the minimum. For the 1.8/2.0 (EM) interaction, the agreement with experiment is good in both  $N, Z \gtrsim 50$  isotopes, but it is obvious that the model space must be increased well beyond  $e_{\text{Max}}/E_{3\text{Max}} = 14/18$  to check for convergence in  $E_{3\text{Max}}$ . The results based on Hamiltonians with larger resolution scales are clearly not converged in  $e_{\text{Max}}$  or  $E_{3\text{Max}}$ . The truncation artifacts due to the  $E_{3\text{Max}}$  cut are visible in the  $e_{\text{Max}}/E_{3\text{Max}} = 14/14$  results for  $^{120}\text{Sn}$ . At  $e_{\text{Max}} = 14$  the additional cut in 3N matrix elements  $E_{3\text{Max}} = 14$  removes important contributions from the calculation. By increasing it to 16 or 18 the convergence pattern recurs to a more regular behavior. This highlights the inevitability of careful convergence checks.

The range of HO frequencies used here is in the regime of ultraviolet extrapolations. However, recent studies have focused on the two-body system [247], necessitating an extension to the many-body sector. Infrared extrapolations, using larger values for the HO frequency, have been recently performed for coupled-cluster calculations [248]. It would be interesting to extend this formalism to the  $E_{3\text{Max}}$  cut to study possible extrapolations to quasi-exact results.

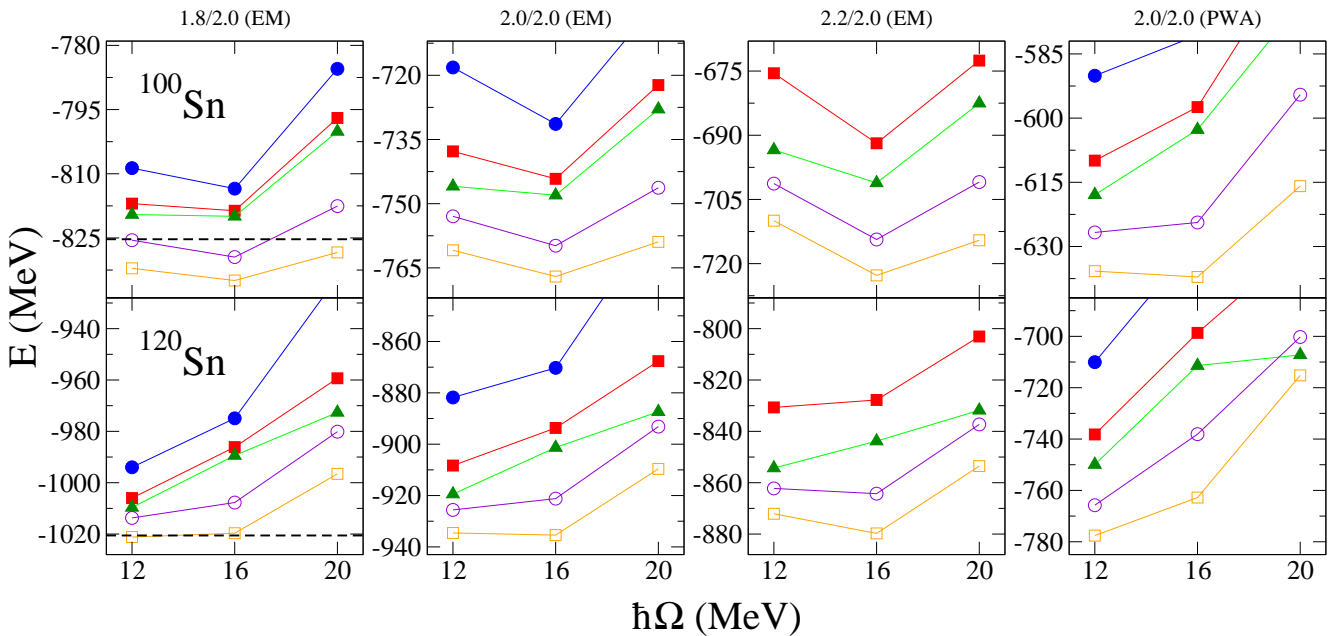


**Figure 9.7:** Convergence of ground-state energies for  $^{100}\text{Sn}$  (top panels) and  $^{120}\text{Sn}$  (bottom panels) calculated with the closed-shell IM-SRG. The legend is as in Fig. 9.1.

## 9.3 Open-shell isotopic chains

In this section, we move beyond closed-shell systems to explore ground- and excited-state systematics throughout a selection of isotopic chains in the  $sd$  and  $pf$  shells, namely sodium, sulfur, calcium, manganese, and nickel. The valence-space (VS) IM-SRG method used here was shown to agree with large-space methods to better than 1% for ground-state energies [145].

We also calculate charge radii, less studied within the context of ab initio approaches [12, 37, 103, 136, 249], with the VS-IM-SRG for the first time, where the proton mean-square radius operator of Eq. (8.2) is transformed via the same unitary transformation as the Hamiltonian. This gives a valence-space radius operator to be used with valence-space wave functions, after which the core point-proton radius and corrections of Eq. (8.3) are applied to obtain the absolute charge radius. We note that induced two-body corrections to the radius operator are included naturally in the VS-IM-SRG formalism.

### 9.3.1 Ground-state energies and radii

Given the remarkable agreement with experimental ground-state energies for closed-shell systems from the 1.8/2.0 (EM) interaction discussed in Sec. 9.1, we compare the systematics of ground-state energies calculated with this interaction to experimental data where they exist in the isotopic chains mentioned above. For sodium, sulfur, and calcium we take  $e_{\text{Max}}/E_{3\text{Max}} = 12/16$ , while for manganese and nickel we use  $e_{\text{Max}}/E_{3\text{Max}} = 14/16$ . In all cases  $\hbar\Omega = 16 \text{ MeV}$  is taken for the harmonic-oscillator frequency. In addition, we directly compare single-reference IM-SRG and valence-space results in calcium and nickel for the closed-shell cases. The valence space is defined to be one major harmonic-oscillator shell for protons and neutrons. For example, for the sulfur chain we take a proton and neutron  $sd$  valence space above an  $^{16}\text{O}$  core for  $N < 20$ , a proton  $sd$  valence space above a  $^{28}\text{O}$  core for  $N = 20$ , and a proton  $sd$  neutron  $pf$  valence space above a  $^{28}\text{O}$  core for  $N > 20$ . It should be noted that at oscillator shell closures for neutrons, no explicit neutron excitations are allowed in the valence space. In particular for systems near the transition from one valence space to another, contributions from cross-shell excitations will be important. These excitations are incorporated approximately by the IM-SRG decoupling, and our truncation to two-body operators is insufficient for these isotopes. We mark these oscillator closures as a vertical dotted line in all figures. Preliminary efforts indicate that the VS-IM-SRG approach is capable of decoupling the relevant mixed valence spaces [250], and thus treating these excitations explicitly.

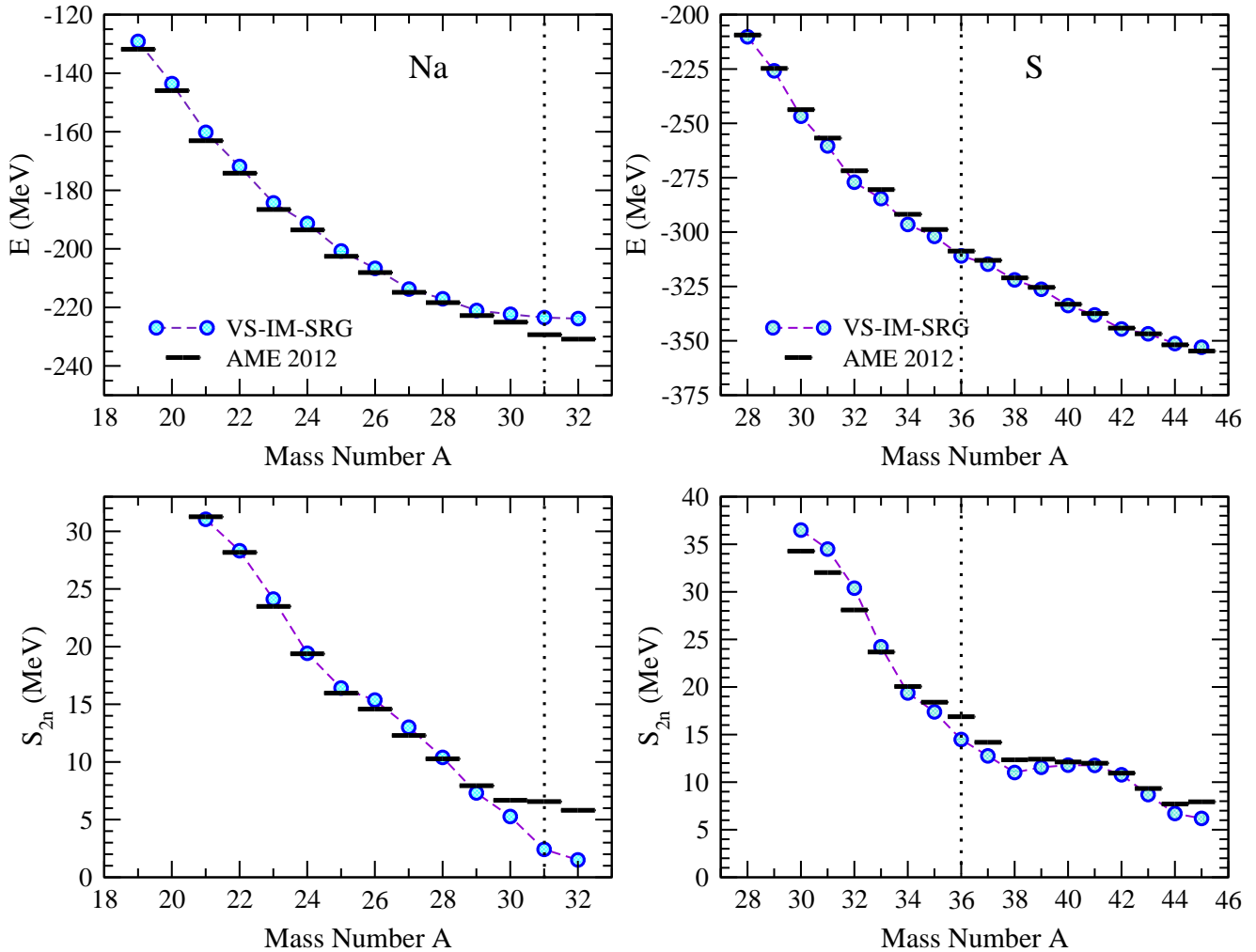


**Figure 9.8:** Ground-state energies (top) and two-neutron separation energies (bottom) of sodium (left) and sulfur (right) isotopes for the 1.8/2.0 (EM) Hamiltonian (circles) compared to experiment (AME 2012, bars) [190]. See text for details on the valence spaces used. The vertical dotted line marks the end of the  $sd$  shell at  $N = 20$ .

Beginning in the  $sd$  region, we show in Fig. 9.8, ground-state energies and two-neutron separation energies  $S_{2n}$  for sodium and sulfur isotopes, respectively. In both cases we find good agreement with absolute experimental

ground-state energies, outside of  $^{31,32}\text{Na}$ , which are somewhat underbound. The ground states of  $^{30-32}\text{Na}$  are dominated by deformed configurations [193, 194], not captured in neutron  $sd$  or  $pf$  valence-space calculations. These island-of-inversion isotopes will be investigated further in the context of decoupling neutron  $sd - pf$  cross-shell valence spaces. Likewise, the  $S_{2n}$  results are in remarkable agreement with data, except in the region near  $N = 20$ . In Ref. [145], sodium isotopes were also investigated with the VS-IM-SRG approach, but instead using the EM 500 MeV potential with local  $N^2\text{LO 3N}$  forces [251] consistently SRG evolved to  $\lambda = 1.88 \text{ fm}^{-1}$ . For this choice of Hamiltonian the isotopes  $^{22}\text{Na}$  up to  $^{32}\text{Na}$  are overbound, while the rest of the chain is in good agreement with experiment. With three protons above the closed  $Z = 8$  proton shell, no other ab initio method is currently able to calculate sodium isotopes. Except for the single-reference and VS-IM-SRG calculations of  $^{32,36}\text{S}$  with the SRG-evolved NN+3N forces mentioned above [145], which display significant overbinding not seen with the 1.8/2.0 (EM) interaction used here, there are no other ab initio calculations available for these open-shell sulfur isotopes.

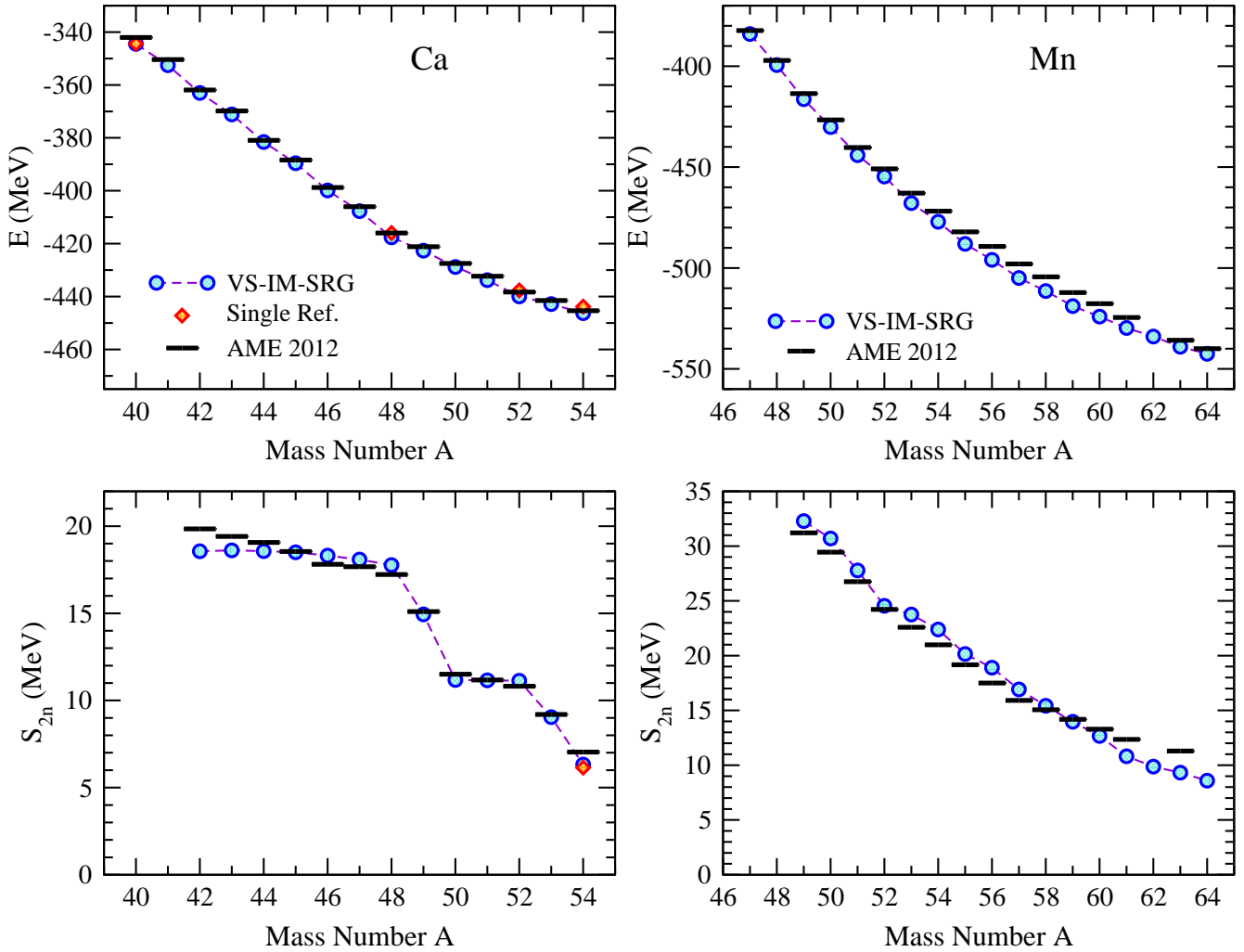


**Figure 9.9:** Ground-state energies (top) and two-neutron separation energies (bottom) of calcium (left) and manganese (right) isotopes for the 1.8/2.0 (EM) Hamiltonian (circles) compared to experiment (AME 2012, bars) [190]. See text for details on the valence spaces used. For closed-subshell calcium isotopes we also show the results of the single-reference IM-SRG (diamonds) for comparison.

In the  $pf$  shell, the agreement with experimental data remains good as well, as shown in Figs. 9.9 and 9.10 for calcium, manganese, and nickel isotopic chains, respectively. In calcium, we also compare with the corresponding single-reference results for  $^{40,48,52,54}\text{Ca}$ , where, as noted in Ref. [145], the VS-IM-SRG results agree with the single-reference calculations to better than 1%. We also reproduce well the sharp decreases in  $S_{2n}$  values after  $N = 28$  and  $N = 32$ , in good agreement with recent precision experiments [35, 166], indicating that the shell closures at  $N = 28$  and  $N = 32$  are well reproduced with the 1.8/2.0 (EM) interaction. We therefore also expect predictions of  $S_{2n}$  values past  $N = 34$  to be reliable, at least qualitatively, when the data become available. Similar good agreement is seen for all trends in the manganese isotopes, which, with five protons above the  $Z = 20$



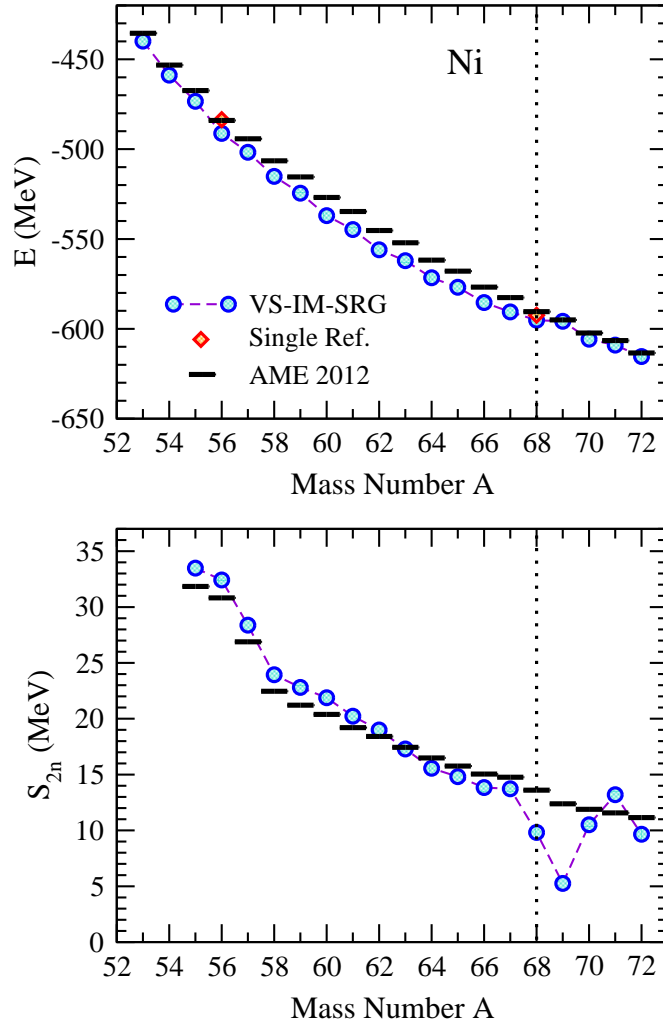


**Figure 9.10:** Ground-state energies (top) and two-neutron separation energies (bottom) of nickel isotopes compared to experiment, with the same legend and details as in Fig. 9.9. The vertical dotted line marks the end of the  $pf$  shell at  $N = 40$ .

proton shell closure, are currently inaccessible to all other ab initio methods. Finally, we see that throughout the nickel chain, absolute ground-state energies become modestly overbound in the mid-shell region on the order of up to 10 MeV. All other experimental trends (aside from the artificial kink in the vicinity of  $N = 40$ ) are well reproduced, including the sharp drop past  $N = 28$ . We also note that the somewhat larger discrepancy between single-reference and VS-IM-SRG results for  $^{56}\text{Ni}$  is likely due to the ground-state configuration obtained in the valence-space diagonalization being only 30% pure filled proton and neutron  $f_{7/2}$ . While experimental energies are known past  $A = 72$ , this represents our current limitation of diagonalizing the valence-space Hamiltonian exactly with modest computational resources. Using standard extensions and/or controlled truncations, isotopes as heavy as  $^{80}\text{Ni}$  may be reached, though as seen in Sec. 9.1, such results may not be completely converged in terms of  $E_{3\text{Max}}$ . The results for the calcium and nickel isotopes using the consistently SRG-evolved EM 500 MeV potential with local  $N^2\text{LO}$  3N forces [251] are significantly overbound up to 100 MeV [145], highlighting the importance of considering saturation for whether chiral interactions can describe bulk properties of nuclei across the nuclear chart.

We illustrate the versatility of the VS-IM-SRG approach in Fig. 9.11 by comparing our calculations of charge radii for the complete  $pf$ -shell manganese chain to experimental data obtained by collinear-laser spectroscopy at ISOLDE, CERN [252]. From Fig. 9.6, we expect charge radii predicted with the 1.8/2.0 (EM) and 2.0/2.0 (PWA) interactions to be systematically too small and too large, respectively. While this is indeed seen, an interesting trend in charge radii is predicted in both cases, with a roughly parabolic shape to  $N = 28$ , followed by a sharp increase for  $N > 28$ . Experimental data show this trend, albeit with more pronounced structures, as also seen in recent experimental measurements of charge radii in calcium isotopes [37]. While neither interaction perfectly reproduces experiment, 2.0/2.0 (PWA) only moderately overpredicts charge radii and should provide a reasonably

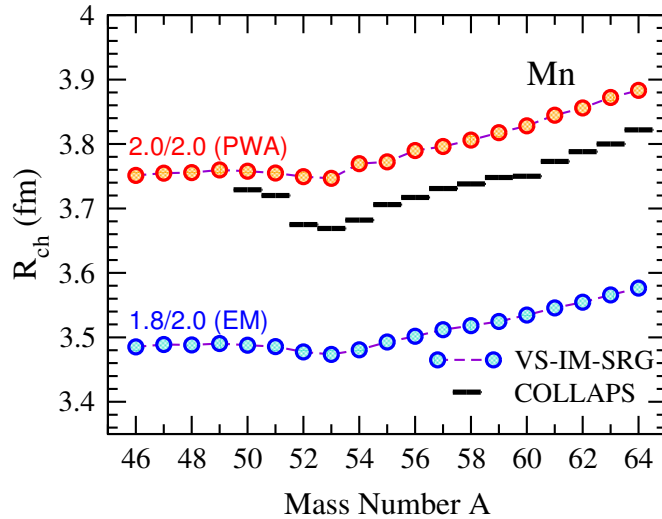


**Figure 9.11:** Charge radii of manganese isotopes for the 1.8/2.0 (EM) (blue circles) and 2.0/2.0 (PWA) (red circles) Hamiltonian compared to recent experimental measurements by the COLLAPS collaboration [252]. See text for details on the valence spaces used.

reliable guide to trends across isotopic chains. The general absence of systematic data highlights the importance of continued systematic experimental investigations of charge radii.

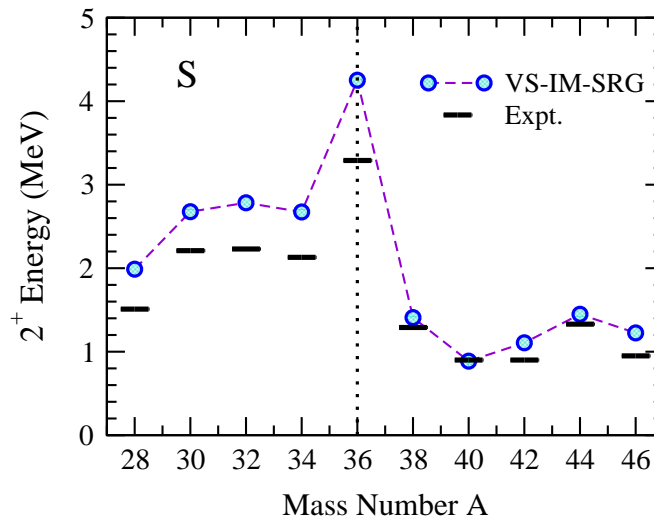


**Figure 9.12:** First excited  $2^+$  energies of even sulfur isotopes for the 1.8/2.0 (EM) Hamiltonian (circles) compared to experiment [197]. See text for details on the valence spaces used. The vertical dotted line marks the end of the  $sd$  shell at  $N = 20$ .

### 9.3.2 Excited states

Given the remarkable description of experimental ground-state properties from the 1.8/2.0 (EM) interaction, it is also of interest to investigate to what extent the structure of excited states is captured. In the VS-IM-SRG approach, all excited states allowed within a given valence space are obtained directly via diagonalization. Here we focus on first excited  $2^+$  states and associated shell closures in the subset of even-even sulfur, calcium, and nickel isotopes.

Beginning with sulfur, shown in Fig. 9.12, we see an overall good reproduction of the experimental trends in  $2^+$  energies. When neutrons occupy the  $sd$  valence space, however, these energies are systematically several hundred keV too high. Beyond  $N = 20$ , when the neutron valence space changes to the  $pf$  shell, agreement with data improves, including the modest peak at  $N = 28$  in  $^{44}\text{S}$ . Given the absence of allowed neutron excitations at  $N = 20$ , the  $2^+$  energy here is artificially too high and is expected to decrease when such degrees of freedom are included in the valence space.

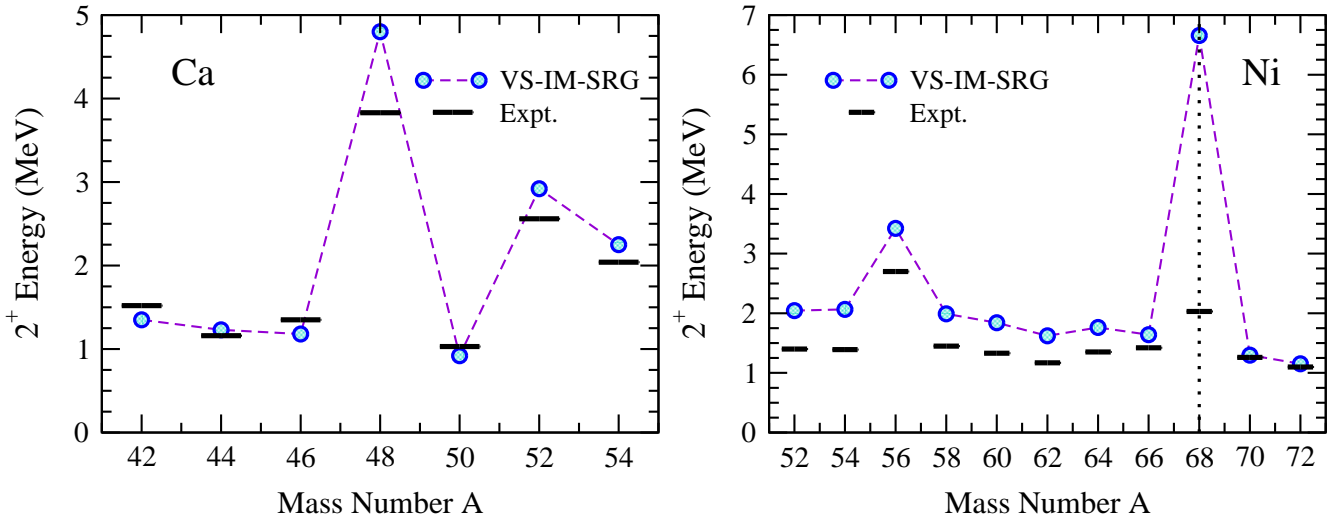


**Figure 9.13:** First excited  $2^+$  energies of even calcium (left) and nickel (right) isotopes for the 1.8/2.0 (EM) Hamiltonian (circles) compared to experiment [197]. See text for details on the valence spaces used. The vertical dotted line marks the end of the  $pf$  shell at  $N = 40$ .

For the calcium isotopes, shown on the left Fig. 9.13, the calculated results agree well with data for open-shell cases. While relative peaks are seen at the  $N = 28, 32$  shell closures as well as the recently measured  $N = 34$  closure in  $^{54}\text{Ca}$  [36], they are systematically too high, particularly in  $^{48}\text{Ca}$ . While we might initially attribute this to neglected proton excitations due to the choice of valence space, similar features are also seen in the nickel isotopes, which allow both proton and neutron excitations except at  $N = 40$ . For the nickel isotopes, a similar picture to sulfur is seen on the right of Fig. 9.13. Where when neutrons fill the  $pf$  shell, the  $2^+$  energies reproduce the experimental trend, but are systematically several hundred keV too high. When neutrons begin filling the  $sdg$  orbits past  $^{68}\text{Ni}$ , the results agree very well with data, making predictions out to  $^{80}\text{Ni}$  possible to investigate the closed-shell nature of  $^{78}\text{Ni}$ . The very high  $2^+$  state in  $^{68}\text{Ni}$  is clearly due to a lack of allowed neutron excitations, and should again be regarded as an artifact of the many-body approximation.

The pattern of too-high  $2^+$  energies in closed-shell systems is a common feature of our calculations. The origin of this behavior is unclear, but some direction might be provided by coupled-cluster calculations of  $^{48}\text{Ca}$  and  $^{78}\text{Ni}$  [243]. In this work, it was found that using the same 1.8/2.0 (EM) interaction, when particle-hole excitations were limited to the coupled-cluster singles and doubles (CCSD) approximation, the first excited  $2^+$  state in  $^{48}\text{Ca}$  was approximately 1 MeV too high, very close to our result. When perturbative triples excitations were then included, this energy was lowered to close to the experimental value, and a similar decrease was seen in the first  $2^+$  energy in  $^{78}\text{Ni}$ . Because the IM-SRG(2) approximation in this work is analogous to the CCSD truncation [14], we might expect a similar improvement in extensions of IM-SRG(2) analogous to the perturbative triples of coupled cluster. Due to the final step of diagonalizing in the valence space, however, the expectation would be that much of this physics should already be captured, as long as excitations near the Fermi surface were of dominant importance. As the development of a controlled approximation to IM-SRG(3) is currently in progress, we so far have no means to check whether such an improvement will remedy the too-high  $2^+$  states at closed shells. Nevertheless, this appears to be a deficiency in the many-body method, not the interaction.



---

## 10 Summary and outlook

---

In this thesis we have presented calculations of ground- and excited-state properties of closed- and open-shell nuclei based on a set of chiral NN+3N interactions. These interactions are based on the EM 500 MeV  $N^3\text{LO}$  NN potential [27] evolved to low-resolution scales and non-local  $N^2\text{LO}$  3N interactions with 3N low-energy couplings (LEC) adjusted at each resolution scale to the  $^3\text{H}$  binding energy and  $^4\text{He}$  charge radius. Employing these NN+3N interactions in perturbative calculations of symmetric nuclear matter leads to results consistent with the empirical saturation point within theoretical uncertainties. This agreement for symmetric nuclear matter, representing an idealized system that probes densities also found in medium-mass or heavy nuclei, motivated the investigation of finite nuclei using these Hamiltonians. The low-momentum scale of the Hamiltonians also makes them more amenable to a perturbative calculation for nuclei.

Until a few years ago many-body perturbation theory (MBPT) for deriving valence-space interactions from NN+3N Hamiltonians was the only many-body method to access doubly-open shell nuclei in the medium-mass regime, e.g., along  $sd$ -shell isotopic chains between oxygen and calcium. Our study of  $sd$ -shell isotopes pointed out that the change from second to third order in MBPT is indeed smaller than the uncertainty in the input Hamiltonian, stemming from the resolution-scale dependence and different sets of LECs. Most experimental two-neutron and two-proton separation energies and  $2^+$  excitation energies are consistent with our theoretical results and lie within our uncertainty estimates.

Following the extensive interest in the masses of neutron-rich calcium isotopes, both experimentally [35, 166] and theoretically [141, 147, 253, 254], we investigated the stable, neutron-rich isotope  $^{48}\text{Ca}$  in detail within a larger theory collaboration. We calculated energies, radii, and charge densities from coupled-cluster theory. Our result for the neutron skin, the difference between the root mean square point-neutron and point-proton radius, is significantly smaller than results from energy density functionals (EDF). Moreover, we made predictions for the dipole polarizability and the weak form factor. Recently, the dipole polarizability of  $^{48}\text{Ca}$  was determined experimentally and agrees with our prediction [198]. A special opportunity to further benchmark our calculations with experimental results was a recent collinear laser spectroscopy measurement by the COLLAPS collaboration, determining the charge radii up to  $^{52}\text{Ca}$  for the first time. Coupled-cluster calculations predict charge radii of the same size for  $^{40}\text{Ca}$  and  $^{48}\text{Ca}$  for all NN+3N Hamiltonians, while EDFs that do not include these charge radii in their parameter optimization lead to charge radii of different size. However, the very steep increase in the charge radii towards  $^{52}\text{Ca}$  can currently not be explained by our coupled-cluster calculations. This is also a very interesting open puzzle regarding the neutron shell closure at  $N = 32$ , which is seen in the two-neutron separation energies [35].

Another many-body method increasing the reach of ab initio calculations to the medium-mass regime is the in-medium similarity renormalization group (IM-SRG), developed in the last decade [14]. We used the formulation of the IM-SRG to calculate ground-state properties of closed-shell nuclei and its extension for the decoupling of valence-space interactions to access open-shell nuclei. In a systematic study of closed-shell nuclei we investigated the convergence properties of the different NN+3N Hamiltonians. For the lower NN resolution scales  $1.8\text{--}2.0\text{ fm}^{-1}$  we have observed a fast convergence of ground-state energies in the number of major oscillator shells  $e_{\text{Max}}$  up to mass number  $A \sim 80$ . The additional  $E_{3\text{Max}}$  cut on the 3N matrix elements prevents, however, complete convergence of absolute ground-state energies in this mass regime. Nevertheless, both truncations allow a relative convergence of the ground-state energy of  $^{78}\text{Ni}$  to about  $\leq 1\%$  at the optimal harmonic-oscillator (HO) frequency. The binding-energy systematics of closed-shell nuclei from  $^4\text{He}$  to  $^{78}\text{Ni}$  is reproduced with the  $1.8/2.0$  NN+3N interaction, while the other Hamiltonians show a similar pattern but give results that are successively underbound. While all Hamiltonians predict also similar charge radii systematics, experimental radii are enclosed by results for the  $2.2/2.0$  and  $2.0/2.0$  (PWA) NN+3N Hamiltonians. The decoupling of valence-space interactions starting from the  $1.8/2.0$  NN+3N Hamiltonian leads to ground- and excited-state results with a similar level of agreement with experiment found for the ground-state energies of closed-shell nuclei. These results allow intriguing predictions for future experiments and point out the importance of realistic saturation properties for the correct description of finite nuclei.

Having summarized the main points of this thesis, we want to give an outlook on future research projects. Since there has been a lot of development on chiral interactions in recent years, e.g., the new set of non-local NN interactions introduced in Ref. [90], it will be important to perform more comprehensive studies, since the chiral NN+3N Hamiltonians introduced in Sec. 4 all started from the EM 500 MeV  $N^3\text{LO}$  NN potential [27]. The new set of NN interactions is provided for all orders in the chiral expansion from LO to  $N^4\text{LO}$ , enabling studies of the order-by-order convergence. However, consistent NN+3N calculations at  $N^2\text{LO}$  and  $N^3\text{LO}$  require the determination of the  $N^2\text{LO}$  3N couplings. For this one may use the properties of few-nucleon systems, similar to the

---

NN+3N Hamiltonians employed in this work, or, alternatively one could require the reproduction of the empirical saturation point in calculations of symmetric nuclear matter.

For an improved convergence the initial NN+3N Hamiltonian can be evolved consistently, e.g., in momentum-space [119], taking into account induced 3N interactions arising from the evolution of the initial NN interaction. Nevertheless, since this transformation is only unitary at the 3N level, induced 4N contributions may arise as seen in the SRG evolution of local  $N^2LO$  3N forces [255] in the HO basis. The consistent NN+3N evolution in momentum space provides an ideal framework for developing new generators, which may result in a smaller amount of induced 4N contributions.

While we have used both perturbative and non-perturbative methods to obtain valence-space interactions a comprehensive comparison of both approaches is still lacking due to the different starting points. While the MBPT calculation of valence-space interactions is utilizing a HO basis, the valence space IM-SRG decoupling is employing a Hartree-Fock basis. The comparison of both methods in the HF basis using the new framework of Ref. [186] with a possible improvement of the order-by-order convergence in MBPT calculations is an interesting topic for a future work.

## A Isobaric multiplet mass equation applied in the $sd$ -shell

In this section we study the Isobaric Multiplet Mass Equation (IMME) for the  $A = 20$  and  $A = 21$  multiplets. We document this in the Appendix, because it was a spin-off project of the interactions developed and the methods used in this thesis. Before going into this we briefly recap the concept of isospin and derive the IMME in perturbation theory. Exploring the impact of isospin-symmetry breaking on nuclear structure is a challenge for nuclear theory, as it relates to the symmetries of QCD and their breaking. The valence-space calculations for the  $A = 20$  and  $A = 21$  multiplets use either the phenomenological isospin-symmetric USD Hamiltonians [162] supplemented with an isospin-non-conserving (INC) part [256] or isospin-non-conserving interactions derived from chiral NN and 3N forces at third order in MBPT, as outlined in Sec. 6.2. The first direct mass measurements of the most proton-rich members of these isospin multiplets,  $^{20,21}\text{Mg}$ , using the Penning trap mass spectrometer TITAN at TRIUMF, Vancouver (Canada), reduced the uncertainties in their masses by 15 and 22 times, respectively. This results in a significant departure from the expected behavior of the IMME in both the  $A = 20$  and  $A = 21$  multiplets. The results have been published jointly with experimentalists in Ref. [53]. In addition, we discuss the recent measurement of the excitation energy of the  $T = 2$  state in  $^{20}\text{Na}$  [257], which represented the most uncertain member of the  $A = 20$  quintet. The inclusion of this measurement resulted in a revalidation of the quadratic form of the IMME in the  $A = 20$  multiplet.

The discovery of the neutron in 1932 by Chadwick [1] clarified that the strong force acts similarly on protons and neutrons. This motivated the concept of isospin, introduced by Heisenberg [258], characterizing them as the projections of a two-state system, i.e., the nucleon, in isospin space. This is in analogy to the spin quantum number, however, while the spin of a particle is determined by its projection on the quantization axis in spin space the isospin state of the nucleon is determined by its projection in the abstract isospin space.

The total isospin  $T$  of a nucleus, composed of  $N$  neutrons and  $Z$  protons, is determined by the vector sum of single-nucleon isospins. Thus, the total isospin projection is  $T_z = (N - Z)/2$  and therefore  $|N - Z|/2 \leq T \leq (N + Z)/2$ . Omitting the Coulomb interaction among protons, charge-symmetry and charge-independence of strong interactions can lead to identical properties of nuclei with the same mass number, but with different neutron and proton numbers. An interaction is charge symmetric when the interaction between two protons is identical to that between neutrons ( $V_{pp} = V_{nn}$ ), while it is charge independent if  $V_{nn} = V_{pp} = V_{pn}$  for the  $T = 1$  channels. In addition, the Pauli principle constrains the number of possible configurations and thereby the range for which symmetries can be observed. In summary, the total isospin quantum number  $T$  connects charge symmetry/independence and the Pauli principle and, hence, is a good quantum number to characterize analogue states in isobaric multiplets [259]. These states are called isobaric analogue states (IAS).

However, isospin is not an exact symmetry in nature, broken by electromagnetic interactions and the up and down quark mass difference in QCD. Isospin-symmetry breaking operators lift the  $(2T + 1)$ -fold degeneracy, resulting in isospin multiplets labeled by  $T_z$ . It was first demonstrated by Wigner [260] and later derived by Weinberg and Treiman [261] that the mass excess  $ME$  of an IAS can be parametrized as a function of the isospin projection  $T_z$  by

$$ME(\alpha, T, T_z) = a(\alpha, T) + b(\alpha, T)T_z + c(\alpha, T)T_z^2, \quad (\text{A.1})$$

where  $\alpha$  represents all other relevant quantum numbers of the state including the mass number  $A$ , while  $a$ ,  $b$  and  $c$  are the expansion coefficients of the isobaric multiplet mass equation. The mass excess  $ME$  for a state of a given isotope is defined as the difference between its actual mass and its mass number. For the derivation of the IMME we follow Ref. [262], starting with the eigenstates  $|\alpha, T, T_z\rangle$  of the charge-independent Hamiltonian  $H_{CI}$ . Since  $H_{CI}$ , by definition, conserves the isospin  $T$ , the eigenvalues are independent of  $T_z$ , i.e., the isobaric analogue states are degenerate. A charge-violating Hamiltonian  $H_{CV}$  will lift this degeneracy and can be treated as a perturbation in case the induced energy splitting is small compared to the contribution from the charge-independent interaction. The total binding energy is determined by

$$BE(\alpha, T, T_z) = \langle \alpha, T, T_z | H_{CI} + H_{CV} | \alpha, T, T_z \rangle. \quad (\text{A.2})$$

If only two-body forces are contributing to the charge-violating Hamiltonian, it can be decomposed

$$H_{CV} = \sum_{k=0}^2 H_{CV}^{(k)}, \quad (\text{A.3})$$

where  $k = 0, 1, 2$  correspond to isoscalar, isovector, and isotensor components of this interaction, respectively. The total energy splitting for the members of the isobaric multiplet in lowest order of perturbation theory is then given by

$$\Delta E(\alpha, T, T_z) = \langle \alpha, T, T_z | \sum_{k=0}^2 H_{CV}^{(k)} | \alpha, T, T_z \rangle. \quad (\text{A.4})$$

By applying the Wigner-Eckart theorem the  $T_z$  dependence can be explicitly extracted to

$$\Delta E(\alpha, T, T_z) = \sum_{k=0}^2 (-1)^{T-T_z} \begin{pmatrix} T & k & T \\ -T_z & 0 & T_z \end{pmatrix} \langle \alpha, T || H_{CV}^{(k)} || \alpha, T \rangle, \quad (\text{A.5})$$

where the last factor is the reduced matrix element of the set of tensor operators  $H_{CV}^{(k)}$ . Inserting the analytical expressions for the Wigner  $3j$  symbols leads to

$$\begin{aligned} \Delta E(\alpha, T, T_z) = \frac{1}{\sqrt{2T+1}} & \left[ \langle \alpha, T || H_{CV}^{(0)} || \alpha, T \rangle \right. \\ & + \frac{T_z}{\sqrt{T(T+1)}} \langle \alpha, T || H_{CV}^{(1)} || \alpha, T \rangle \\ & \left. + \frac{3T_z^2 - T(T+1)}{\sqrt{T(T+1)(2T+3)(2T-1)}} \langle \alpha, T || H_{CV}^{(2)} || \alpha, T \rangle \right]. \quad (\text{A.6}) \end{aligned}$$

By reordering the terms in Eq. (A.6) according to their power in the isospin projection  $T_z$  we obtain the following contributions to the coefficients  $a$ ,  $b$  and  $c$  in Eq. (A.1)

$$\begin{aligned} a &= \frac{1}{\sqrt{2T+1}} \langle \alpha, T || H_{CV}^{(0)} || \alpha, T \rangle - \frac{T(T+1)}{\sqrt{(2T+1)T(T+1)(2T+3)(2T-1)}} \langle \alpha, T || H_{CV}^{(2)} || \alpha, T \rangle \\ &+ \langle \alpha, T, T_z | H_{CI} | \alpha, T, T_z \rangle + \frac{1}{2} (ME_n + ME_H) A, \\ b &= \frac{1}{\sqrt{(2T+1)T(T+1)}} \langle \alpha, T || H_{CV}^{(1)} || \alpha, T \rangle + (ME_n - ME_H), \\ c &= \frac{3}{\sqrt{(2T+1)T(T+1)(2T+3)(2T-1)}} \langle \alpha, T || H_{CV}^{(2)} || \alpha, T \rangle, \quad (\text{A.7}) \end{aligned}$$

with the neutron  $ME_n$  and the hydrogen mass excesses  $ME_H$ . Thus, the  $a$  coefficient contains contributions from the isoscalar and isotensor parts, while the  $b$  and  $c$  coefficients are purely isovector and isotensor, respectively. Since Eq. (A.1) describes the mass excess the coefficient  $a$  in Eq. (A.7) contains the contribution from the charge-independent Hamiltonian and  $A$  times the averaged neutron-hydrogen mass excess, while the coefficient  $b$  contains the neutron-hydrogen mass excess difference  $ME_n - ME_H = 782.3$  keV [263].

While the Coulomb interaction is expected to be dominant, the quadratic form of the IMME is even valid in the presence of any charge-asymmetric and charge-dependent NN component. Those additional terms just lead to a change in the coefficients. Deviations from the quadratic form, e.g., a non-vanishing cubic  $d(\alpha, T)T_z^3$  or quartic  $e(\alpha, T)T_z^4$  term, can arise from higher-order perturbations, 3N forces and isospin mixing of energetically close lying states with different isospin. Such deviations have been found in the  $A = 9$   $J^\pi = 3/2^-$  [264] and  $A = 31$  [265, 266], 33 [263] and 35 [267]  $J^\pi = 3/2^+$ ,  $T = 3/2$  quartets. Moreover, the  $A = 8$  [268] and 32 [269, 270]  $T = 2$  quintets also require an extension of the quadratic IMME.

Many experimental tests of the IMME on proton-rich systems were hindered by excessive in-beam contamination. Substantial isobaric background often prevented ground-state measurements of exotic nuclei, especially for nuclei produced at low rates. The development of a novel technology for on-line laser ion sources that suppresses any background contamination, allowed the first direct mass measurements of the most proton-rich members of the  $A = 20$  and 21 isospin multiplets, i.e.,  $^{20,21}\text{Mg}$ , using the Penning trap mass spectrometer TITAN at TRIUMF, Vancouver (Canada) [53]. Being the lightest isospin multiplets where all members are stable against particle emission, and the lightest isospin multiplets which can be described within the  $d_{5/2}$ ,  $s_{1/2}$ , and  $d_{3/2}$  orbitals ( $sd$  shell), the  $A = 20$  and 21 multiplets provide an excellent test of the IMME.



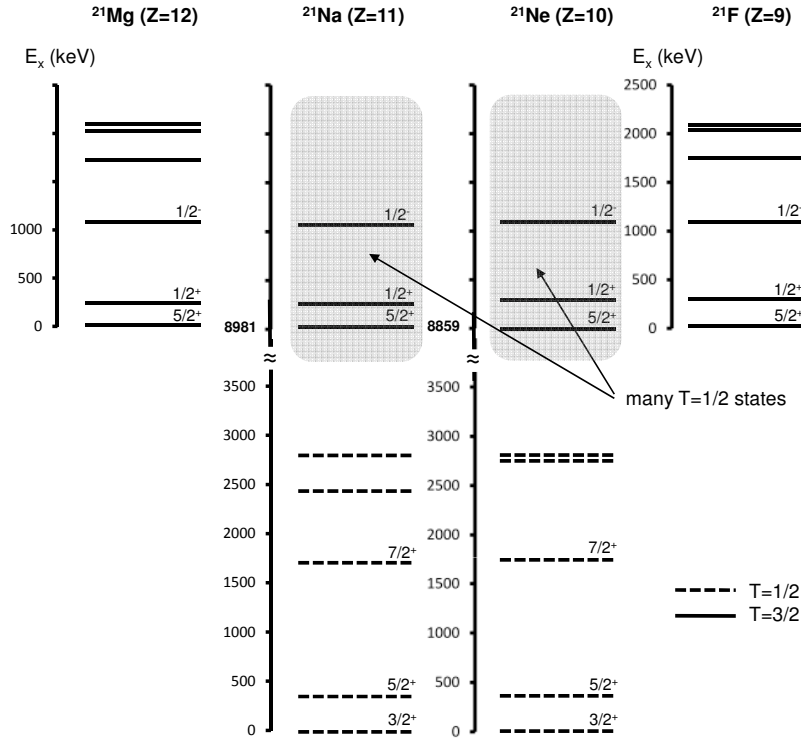


**Figure A.1:** Level scheme of the members of the  $A = 21$  multiplet. Taken from [262].

The high-precision Penning-trap measurement determined a mass excess of 10903.85(74) keV for  $^{21}\text{Mg}$ , which agrees well with the tabulated value 10914(16) keV from AME2012 [190]. The mass excess of 17477.7(18) keV for  $^{20}\text{Mg}$  deviates by 81 keV as compared to 17559(27) keV from the AME2012, which is a shift of  $3\sigma$ . In both cases the precision was increased by more than one order of magnitude, reducing the uncertainties in the masses of  $^{20,21}\text{Mg}$  by 15 and 22 times, respectively

Determining the energy level of an isospin multiplet member relies on knowing both the ground-state and excited-state energies accurately. For different experimental techniques, the measured excitation energy depends on separation energies, which can change with improved mass measurements. New mass measurements of the ground states of  $^{20}\text{Na}$  [271] and  $^{19}\text{Ne}$  [272] led to an improved proton separation energy value for  $^{20}\text{Na}$  of 2190.1(11) keV. This value is required to derive the excitation energy of the  $J^\pi = 0^+$ ,  $T = 2$  state in  $^{20}\text{Na}$ . Combining a new measurement of the excitation energy [273] with the value compiled in [271], an averaged value of 6524.0(98) keV is obtained, a result that is shifted by 10 keV relative to the tabulated value [197]. In  $^{21}\text{Mg}$ , with the level scheme shown in the left column of Fig. A.1, a new measurement of the  $J^\pi = 1/2^+$  state was completed [274], which, when averaged with the National Nuclear Data Center (NNDC) [275] value, yields 200.5(28) keV. Both of these new values are included in the following analysis.

Table A.1 summarizes the fit results of the quadratic, and higher order forms of the IMME for the  $A = 20$  and 21 multiplets. For each multiplet the  $\chi^2$  of the fit greatly increased, as compared to the tabulated values [263]. The most uncertain member of the  $A = 20$  multiplet is now  $^{20}\text{Na}$ , with nearly all of the uncertainty originating from the excitation energy of the  $T = 2$  state. The best fit is obtained when a cubic term is included, resulting in  $d = 2.8(1.1)$  keV, and  $\chi^2 = 3.7$ , a result that is an order of magnitude larger than the literature  $\chi^2$  value of 0.2 [263]. For the  $T = 3/2$ ,  $A = 21$  multiplets, the  $\chi^2$  for a quadratic fit have increased to 28 and 9.7 for the  $J^\pi = 5/2^+$  and  $1/2^+$ , respectively, as compared to the literature  $\chi^2$  values of 3.0 and 3.5 [263]. The IMME clearly fails in both of the  $A = 21$  multiplets. Large cubic terms are required for both multiplets, with  $d = 6.7(13)$  keV for the  $J^\pi = 5/2^+$  multiplet and  $d = -4.4(14)$  keV for the  $J^\pi = 1/2^+$  multiplet.

The  $sd$  shell is particularly interesting because it can be accessed by phenomenological and ab initio methods. The phenomenological isospin-symmetric USD Hamiltonians [162] generally reproduce data very well throughout the  $sd$  shell, but ultimately need to be supplemented with an isospin-non-conserving (INC) part [256]. In addition, there are valence-space calculations based on chiral NN and 3N forces, without phenomenological adjustments. The resulting  $sd$  shell Hamiltonians are inherently isospin asymmetric and have successfully described proton- and neutron-rich systems [164, 188], but it was still an open question how well they work in systems with both proton

**Table A.1:** Extracted IMME parameters for the  $A = 20$  and  $21$  multiplets. Mass excesses are taken from [190] and excitation energies  $E_x$  from [197] and [275], except where noted. Also shown are the  $d$  and  $e$  coefficients for cubic and quartic fits and the  $\chi^2$  values of the fit. Shell model calculation results using the USDA and USDB plus INC interactions are presented.

Nuclide	$T_z$	$ME(\text{g.s.})$ (keV)		$E_x$ (keV)
$A = 20, J^\pi = 0^+, T = 2$				
$^{20}\text{O}$	+2	3796.17 (89)		0.0
$^{20}\text{F}$	+1	-17.45 (3)		6519.0 (30)
$^{20}\text{Ne}$	0	-7041.9306 (16)		16732.9 (27)
$^{20}\text{Na}$	-1	6850.6 (11)		6524.0 (97) <sup>a</sup>
$^{20}\text{Mg}$	-2	17477.7 (18) <sup>b</sup>		0.0
Ref.	$a$ (keV)	$b$ (keV)	$c$ (keV)	$\chi^2$
This Work	9689.79 (22)	-3420.57 (50)	236.83 (61)	10.2
Ref. [263]	9693 (2)	-3438 (4)	245 (2)	1.1
	Fit	$d$ (keV)	$e$ (keV)	$\chi^2$
	Cubic	2.8 (11)	-	3.7
	Quartic Only	-	0.89 (12)	9.9
	Quartic	5.4 (17)	-3.5 (18)	-
	USDA	-0.1	-	
	USDA	-	-1.7	
	USDB	-0.1	-	
$A = 21, J^\pi = 5/2^+, T = 3/2$				
$^{21}\text{F}$	+3/2	-47.6 (18)		0.0
$^{21}\text{Ne}$	+1/2	-5731.78 (4)		8859.2 (14)
$^{21}\text{Na}$	-1/2	-2184.6 (3)		8976.0 (20)
$^{21}\text{Mg}$	-3/2	10903.85 (74) <sup>b</sup>		0.0
Ref.	$a$ (keV)	$b$ (keV)	$c$ (keV)	$\chi^2$
This Work	4898.4 (13)	-3651.36 (63)	235.00 (77)	28.0
Ref. [263]	4894 (1)	-3662 (2)	243 (2)	3.0
	Fit	$d$ (keV)	$\chi^2$	
	Cubic	6.7 (13)	-	
	USDA	-0.3		
	USDB	0.3		
$A = 21, J^\pi = 1/2^+, T = 3/2$				
$^{21}\text{F}$	+3/2	-47.6 (18)		279.93 (6)
$^{21}\text{Ne}$	+1/2	-5731.78 (4)		9148.9 (16)
$^{21}\text{Na}$	-1/2	-2184.6 (3)		9217.0 (20)
$^{21}\text{Mg}$	-3/2	10903.85 (74) <sup>b</sup>		200.5 (28) <sup>c</sup>
Ref.	$a$ (keV)	$b$ (keV)	$c$ (keV)	$\chi^2$
This Work	5170.4 (14)	-3633.6 (10)	220.9 (10)	9.7
Ref. [263]	5171 (10)	-3617 (2)	217 (2)	3.5
	Fit	$d$ (keV)	$\chi^2$	
	Cubic	-4.4 (14)	-	
	USDA	-1.2		
	USDB	1.9		

<sup>a</sup> Average of Refs. [271, 273]

<sup>b</sup> Present work

<sup>c</sup> Average of Refs. [274, 275]

and neutron valence degrees of freedom. Therefore the current measurements provided valuable new tests of these methods.

We first calculated the IMME in the  $sd$  shell with the USDA and USDB isospin-conserving Hamiltonians [162], supplemented with the INC Hamiltonian of Ref. [256]. The results for the  $A = 20$  and  $21$   $d$  and  $e$  coefficients are presented in Table A.1. For  $A = 20$ , the USDA value for  $e$ , which comes from mixing of states with similar energy but different isospin in  $^{20}\text{F}$ ,  $^{20}\text{Ne}$ , and  $^{20}\text{Na}$ , agrees with experiment only when  $e$  is also included in the IMME fit. Here, the largest mixing comes from a pair of close-lying  $J^\pi = 0^+$ ,  $T = 0, 2$  states in  $^{20}\text{Ne}$ . With the USDB Hamiltonian, these two states are nearly degenerate resulting in an uncertainty of the energy of the good isospin states that is too large to give a meaningful result. The calculated  $d$  term, on the other hand, comes from mixing in  $^{20}\text{F}$  and  $^{20}\text{Na}$ . With the USDB, the  $J^\pi = 0^+$ ,  $T = 1$  levels in these nuclei are well separated from the  $T = 2$  isobaric analog state (IAS), leading to a small energy-mixing shift and hence a too small  $d$  value.

For the  $A = 21$  systems, the USD values of  $d$  also do not agree with experiment. The non-zero values come from mixing of the  $T = 3/2$  states with close-lying  $T = 1/2$  states in  $^{21}\text{Ne}$  and  $^{21}\text{Na}$ . For instance, the largest shift in the  $J^\pi = 5/2^+$  multiplet is due to a  $T = 1/2$  state in  $^{21}\text{Ne}$ , which for the USDA lies 372 keV below the IAS, instead of the 50 keV necessary to reproduce  $d = 6.7$  keV. Experimentally, several  $T = 1/2$  states with unidentified spin lie around the IAS [197] as indicated by the shaded area in the middle columns of Fig. A.1. This illustrates the challenge in obtaining accurate calculations capable of describing the new experimental findings.

In addition we calculated the properties of the  $A = 20$  and  $21$  multiplets from valence-space Hamiltonians constructed within the framework of many-body perturbation theory [161], based on low-momentum [115] NN and 3N forces derived from chiral effective field theory [5], without empirical adjustments.

All contributions to chiral NN forces, discussed in Sec. 2.2.2, were isospin-symmetric. Since isospin symmetry is violated by strong and electromagnetic interactions those effects also need to be included in chiral EFT. The  $\text{N}^3\text{LO}$  NN potential EM 500 MeV, used in this study of the  $A = 20$  and  $A = 21$  multiplets, follows the counting scheme for isospin-symmetry breaking contributions of Ref. [276] and includes the pion-mass difference ( $m_{\pi^\pm} \neq m_{\pi^0}$ ) in the one-pion exchange and the Coulomb potential (static  $1\gamma$  exchange) in pp scattering. Those leading order isospin-symmetry breaking terms are denoted  $\text{L}\phi$ . Entem and Machleidt also include  $\text{NL}\phi$  isospin-symmetry breaking effects, which arise from the pion-mass difference in the NLO two-pion exchange,  $\pi\gamma$  exchange and two charge-dependent contact interactions of order  $q^0$ . The charge-dependent LECs allow an accurate fit of the  $^1S_0$  scattering lengths  $a_{pp}$ ,  $a_{np}$  and  $a_{nn}$ . In Ref. [6] Machleidt and Entem rendered more precisely their procedure for the pion-mass splitting in the NLO two-pion exchange, used in the EM 500 MeV potential. Since the effect of the pion-mass splitting in the NLO two-pion exchange is only non-negligible in the  $^1S_0$  state, it was absorbed in the  $^1S_0$  charge-dependent contact. Note that a slightly different counting of the isospin-breaking effects as compared to Ref. [276] was introduced in [87]. See also [6].

The construction of the chiral NN+3N Hamiltonian, employed in this study of the IMME, followed the same strategy as described in Sec. 4. Actually, it was constructed even before those specified in Sec. 4. Nevertheless we briefly recap the basic idea. The charge dependent EM 500 MeV potential was evolved to a low-momentum interaction  $V_{\text{low}k}$  with  $\Lambda_{\text{low}k} = 2.0 \text{ fm}^{-1}$ . This low-momentum interaction was supplemented with the  $\text{N}^2\text{LO}$  3N interaction, using the non-local regulator specified in Eq. (2.26) with  $n_{3N} = 2$  and  $\Lambda_{3N} = 2.0 \text{ fm}^{-1}$ . The low-energy couplings  $c_D$ ,  $c_E$  have been fit to the  $^3\text{H}$  binding energy and  $^4\text{He}$  charge radius using Faddeev- and Faddeev-Yakubovsky calculations.

Since we want to derive interactions for the  $sd$  and the extended  $sdf7p3$  valence space, 3N interactions are normal ordered with respect to a  $^{16}\text{O}$  harmonic-oscillator Slater determinant. The normal-ordered one- and two-body contributions of the 3N interactions are added to the low-momentum NN interactions before performing the third-order MBPT calculation.

These isospin-asymmetric Hamiltonians describe ground- and excited-state properties in neutron-rich oxygen isotopes [153, 188, 189] and proton-rich  $N = 8$  isotones [164]. Here we use the valence-space Hamiltonians of Refs. [188] and Ref. [164] for the neutron-neutron and proton-proton parts, respectively, and include for the first time valence-space proton-neutron interactions. The ground-state energies of  $^{20,21}\text{Mg}$  are shown in Table A.2. The calculated ground-state energy of  $^{20}\text{Mg}$  is in very good agreement with experiment, while  $^{21}\text{Mg}$ , with one neutron above the closed  $N = 8$  shell, is overbound by 1.6 MeV. For the  $A = 20$  multiplet, the  $d$  coefficient is found to be  $-18$  keV, i.e., giving isospin-symmetry breaking larger than in experiment. As  $T_z$  increases, other members of the  $A = 21$ ,  $T = 3/2$  multiplet become less overbound than  $^{21}\text{Mg}$  ( $^{21}\text{F}$  is only 0.8 MeV overbound). This, however, also results in larger cubic terms for the  $A = 21$  multiplets ( $d = -38$  keV for  $A = 21$ ,  $J^\pi = 5/2^+$ ). Therefore, the new experimental findings cannot be described with these Hamiltonians, but they nonetheless provide a promising first step towards understanding isospin-symmetry breaking based on electromagnetic and strong interactions.

As already mentioned the  $T = 2$  excited state in  $^{20}\text{Na}$  is the most uncertain member of the  $A = 20$  quintet. A recent measurement used the super-allowed  $0^+ \rightarrow 0^+$  beta decay of  $^{20}\text{Mg}$  to access it and measured the state's

**Table A.2:** Experimental and calculated ground-state energies (in MeV) of  $^{20,21}\text{Mg}$  with respect to  $^{16}\text{O}$ . USDA and USDB results include the INC Hamiltonian discussed in the text.

Nuclide	Exp.	USDA	USDB	NN + 3N
$^{20}\text{Mg}$	-6.94	-6.71	-6.83	-6.89
$^{21}\text{Mg}$	-21.59	-21.79	-21.81	-23.18

subsequent  $\gamma$  decay to deduce the excitation energy to  $6498.4 \pm 0.5$  keV [257]. The difference from the recommended value of  $6525 \pm 14$  keV [277] is 27 keV (1.9 standard deviations), while the precision has been increased by a factor of 28. A summary of experimental results for the  $A = 20$  quintet is given in Table A.3. Glassman *et al.* also applied a standard quadratic IMME as well as a cubic, a quartic, and a quartic fit with the cubic coefficient set to zero to check the necessity of extra terms in the IMME. The results for the coefficients and the  $\chi^2$  values of the fits are reported in Table A.4. The quadratic IMME fit to the data yields  $\chi^2 = 4.8$ , while the inclusion of a cubic term leads to a  $d$  coefficient of  $0.8 \pm 0.5$  keV. This value is consistent with zero, and consistent with the USDA and USDB results of  $-0.1$  keV (cf. Table A.1) within two standard deviations. In addition, the quartic only fit results in an  $e$  coefficient consistent with zero within one standard deviation, while the  $d, e$  coefficients for the quartic fit are also consistent with zero in two and one standard deviations, respectively. Thus, the quadratic IMME for the  $A = 20$ ,  $T = 2$  quintet is revalidated when including the new measurement of the excitation energy for the  $T = 2$  state in  $^{20}\text{Na}$ .

**Table A.3:** IMME input mass excesses,  $ME(T = 2)$ , for the lowest  $A = 20$ ,  $T = 2$  quintet, including the constituent ground-state mass excesses  $ME(\text{g.s.})$  and excitation energies  $E_x$ . The values for the  $T_z = +2, +1, 0$  states and the value of  $ME(\text{g.s.})$  for the  $T_z = -1$  state are from Ref. [277]. The value for the  $T_z = -2$  state is from Ref. [53]. The value of  $E_x$  for the  $T_z = -1$  state is from Ref. [257].

Nuclide	$T_z$	$ME(\text{g.s.})$ (keV)	$E_x$ (keV)	$ME(T = 2)$ (keV)
$^{20}\text{O}$	+2	3796.2(9)		3796.2(9)
$^{20}\text{F}$	+1	-17.463(30)	6521(3)	6503(3)
$^{20}\text{Ne}$	0	-7041.9306(16)	16732.8(28)	9690.9(28)
$^{20}\text{Na}$	-1	6850.6(11)	6498.4(5)	13349.0(12)
$^{20}\text{Mg}$	-2	17477.7(18)		17477.7(18)

**Table A.4:** IMME coefficients (keV) and  $\chi^2$  values of the fits for the lowest  $A = 20$ ,  $T = 2$  quintet from Ref. [257].

coefficient	quadratic	cubic	quartic only	quartic
$a$	9691.1(14)	9689.7(17)	9690.9(28)	9690.9(28)
$b$	-3420.6(5)	-3423.4(20)	-3420.6(5)	-3423.7(21)
$c$	236.5(5)	236.8(5)	236.9(38)	234.4(41)
$d$	-	0.8(5)	-	0.8(6)
$e$	-	-	-0.1(8)	0.5(9)
$\chi^2$	4.8	0.28	2.4	-

---

## Bibliography

---

- [1] J. Chadwick, “Possible Existence of a Neutron,” *Nature* **129**, 312 (1932).
- [2] C. F. von Weizsäcker, “Zur Theorie der Kernmassen,” *Z. Phys.* **96**, 431 (1935).
- [3] H. Yukawa, “On the Interaction of Elementary Particles I,” *Proc. Phys. Math. Soc. Jap.* **17**, 48 (1935), [*Prog. Theor. Phys. Suppl.*1,1(1935)].
- [4] S. Weinberg, “Nuclear forces from chiral Lagrangians,” *Phys. Lett. B* **251**, 288 (1990).
- [5] E. Epelbaum, H.-W. Hammer, and U.-G. Meißner, “Modern Theory of Nuclear Forces,” *Rev. Mod. Phys.* **81**, 1773 (2009).
- [6] R. Machleidt and D. R. Entem, “Chiral effective field theory and nuclear forces,” *Phys. Rep.* **503**, 1 (2011).
- [7] J. Carlson, “Green’s function Monte Carlo study of light nuclei,” *Phys. Rev. C* **36**, 2026 (1987).
- [8] S. C. Pieper and R. B. Wiringa, “Quantum Monte Carlo calculations of light nuclei,” *Ann. Rev. Nucl. Part. Sci.* **51**, 53 (2001).
- [9] J. Carlson, S. Gandolfi, F. Pederiva, S. C. Pieper, R. Schiavilla, K. E. Schmidt, and R. B. Wiringa, “Quantum Monte Carlo methods for nuclear physics,” *Rev. Mod. Phys.* **87**, 1067 (2015).
- [10] B. R. Barrett, P. Navrátil, and J. P. Vary, “Ab initio no core shell model,” *Prog. Part. Nucl. Phys.* **69**, 131 (2013).
- [11] R. Roth, “Importance Truncation for Large-Scale Configuration Interaction Approaches,” *Phys. Rev. C* **79**, 064324 (2009).
- [12] G. Hagen *et al.*, “Neutron and weak-charge distributions of the  $^{48}\text{Ca}$  nucleus,” *Nature Phys.* **12**, 186 (2016).
- [13] G. Hagen, T. Papenbrock, M. Hjorth-Jensen, and D. J. Dean, “Coupled-cluster computations of atomic nuclei,” *Rep. Prog. Phys.* **77**, 096302 (2014).
- [14] H. Hergert, S. K. Bogner, T. D. Morris, A. Schwenk, and K. Tsukiyama, “The In-Medium Similarity Renormalization Group: A Novel Ab Initio Method for Nuclei,” *Phys. Rep.* **621**, 165 (2016).
- [15] V. Somà, T. Duguet, and C. Barbieri, “Ab initio self-consistent Gorkov-Green’s function calculations of semi-magic nuclei: Formalism at second order with a two-nucleon interaction,” *Phys. Rev. C* **84**, 064317 (2011).
- [16] D. Lee, “Lattice simulations for few- and many-body systems,” *Prog. Part. Nucl. Phys.* **63**, 117 (2009).
- [17] S. K. Bogner, R. J. Furnstahl, and R. J. Perry, “Similarity Renormalization Group for Nucleon-Nucleon Interactions,” *Phys. Rev. C* **75**, 061001(R) (2007).
- [18] E. D. Jurgenson, P. Navrátil, and R. J. Furnstahl, “Evolution of Nuclear Many-Body Forces with the Similarity Renormalization Group,” *Phys. Rev. Lett.* **103**, 082501 (2009).
- [19] R. Roth, J. Langhammer, A. Calci, S. Binder, and P. Navrátil, “Similarity-Transformed Chiral NN+3N Interactions for the Ab Initio Description of  $^{12}\text{C}$  and  $^{16}\text{O}$ ,” *Phys. Rev. Lett.* **107**, 072501 (2011).
- [20] G. Hagen, T. Papenbrock, D. J. Dean, A. Schwenk, A. Nogga, *et al.*, “Coupled-cluster theory for three-body Hamiltonians,” *Phys. Rev. C* **76**, 034302 (2007).
- [21] S. Binder, J. Langhammer, A. Calci, P. Navrátil, and R. Roth, “Ab Initio calculations of medium-mass nuclei with explicit chiral 3N interactions,” *Phys. Rev. C* **87**, 021303(R) (2013).
- [22] S. Binder, P. Piecuch, A. Calci, J. Langhammer, P. Navrátil, and R. Roth, “Extension of coupled-cluster theory with a noniterative treatment of connected triply excited clusters to three-body Hamiltonians,” *Phys. Rev. C* **88**, 054319 (2013).
- [23] J. A. Wheeler, “Molecular Viewpoints in Nuclear Structure,” *Phys. Rev.* **52**, 1083 (1937).

- [24] S. D. Drell and K. Huang, “Many-Body Forces and Nuclear Saturation,” *Phys. Rev.* **91**, 1527 (1953).
- [25] A. Akmal, V. R. Pandharipande, and D. G. Ravenhall, “The Equation of state of nucleon matter and neutron star structure,” *Phys. Rev. C* **58**, 1804 (1998).
- [26] A. Lejeune, U. Lombardo, and W. Zuo, “Nuclear matter EOS with a three-body force,” *Phys. Lett. B* **477**, 45 (2000).
- [27] D. R. Entem and R. Machleidt, “Accurate charge-dependent nucleon-nucleon potential at fourth order of chiral perturbation theory,” *Phys. Rev. C* **68**, 041001(R) (2003).
- [28] K. Hebeler, S. K. Bogner, R. J. Furnstahl, A. Nogga, and A. Schwenk, “Improved nuclear matter calculations from chiral low-momentum interactions,” *Phys. Rev. C* **83**, 031301(R) (2011).
- [29] C. Drischler, K. Hebeler, and A. Schwenk, “Asymmetric nuclear matter based on chiral two- and three-nucleon interactions,” *Phys. Rev. C* **93**, 054314 (2016).
- [30] M. Thoennessen, “Current status and future potential of nuclide discoveries,” *Rep. Prog. Phys.* **76**, 056301 (2013).
- [31] J. Erler, N. Birge, M. Kortelainen, W. Nazarewicz, E. Olsen, A. M. Perhac, and M. Stoitsov, “The limits of the nuclear landscape,” *Nature* **486**, 509 (2012).
- [32] J. D. Cockroft and E. T. S. Walton, “Artificial production of fast protons,” *Nature* **129**, 242 (1932).
- [33] D. J. Morrissey and B. M. Sherrill, “In-Flight Separation of Projectile Fragments,” in *The Euroschool Lectures on Physics with Exotic Beams, Vol. I*, Lecture Notes in Physics, Vol. 651, edited by J. Al-Khalili and E. Roeckl (Springer, Berlin, Heidelberg, 2004) p. 113.
- [34] M. Huyse, “The Why and How of Radioactive-Beam Research,” in *The Euroschool Lectures on Physics with Exotic Beams, Vol. I*, Lecture Notes in Physics, Vol. 651, edited by J. Al-Khalili and E. Roeckl (Springer, Berlin, Heidelberg, 2004) p. 1.
- [35] F. Wienholtz *et al.*, “Masses of exotic calcium isotopes pin down nuclear forces,” *Nature* **498**, 346 (2013).
- [36] D. Steppenbeck *et al.*, “Evidence for a new nuclear ‘magic number’ from the level structure of  $^{54}\text{Ca}$ ,” *Nature* **502**, 207 (2013).
- [37] R. F. Garcia Ruiz *et al.*, “Unexpectedly large charge radii of neutron-rich calcium isotopes,” *Nature Phys.* **12**, 594 (2016).
- [38] O. Kamigaito, T. Dantsuka, M. Fujimaki, N. Fukunishi, H. Hasebe, Y. Higurashi, E. Ikezawa, H. Imao, M. Kase, M. Kidera, M. Komiyama, K. Kumagai, T. Maie, T. Nagatomo, T. Nakagawa, M. Nakamura, J. Ohnishi, H. Okuno, K. Ozeki, N. Sakamoto, K. Suda, S. Watanabe, T. Watanabe, Y. Watanabe, K. Yamada, and H. Yamasawa, “Present Status and Future Plan of RIKEN RI Beam Factory,” in *Proceedings, 7th International Particle Accelerator Conference (IPAC 2016), Busan, Korea, May 8-13, 2016* (2016) p. 1281.
- [39] O. Kester, P. Spiller, and H. Stöcker, “FAIR project at GSI,” in *Challenges and Goals for Accelerators in the XXI Century* (World Scientific, Singapore, 2016) Chap. 32, p. 611.
- [40] J. Wei *et al.*, “FRIB Accelerator: Design and Construction Status,” in *Proceedings, 13th Heavy Ion Accelerator Technology Conference (HIAT2015), Yokohama, Japan, September 7-11, 2015* (2016) p. MOM1102.
- [41] M. Arnould, S. Goriely, and K. Takahashi, “The r-process of stellar nucleosynthesis: Astrophysics and nuclear physics achievements and mysteries,” *Phys. Rep.* **450**, 97 (2007).
- [42] X. Roca-Maza, G. Colò, and H. Sagawa, “New Skyrme interaction with improved spin-isospin properties,” *Phys. Rev. C* **86**, 031306(R) (2012).
- [43] F. Chappert, M. Girod, and S. Hilaire, “Towards a new Gogny force parameterization: Impact of the neutron matter equation of state,” *Phys. Lett. B* **668**, 420 (2008).

- 
- [44] P. Haensel, A. Y. Potekhin, and D. G. Yakovlev, *Neutron Stars 1*, Astrophysics and Space Science Library, Vol. 326 (Springer, New York, 2007).
- [45] P. Demorest, T. Pennucci, S. Ransom, M. Roberts, and J. Hessels, “Shapiro Delay Measurement of A Two Solar Mass Neutron Star,” *Nature* **467**, 1081 (2010).
- [46] J. Antoniadis *et al.*, “A Massive Pulsar in a Compact Relativistic Binary,” *Science* **340**, 1233232 (2013).
- [47] S. Guillot, R. E. Rutledge, and E. F. Brown, “Neutron Star Radius Measurement with the Quiescent Low-Mass X-ray Binary U24 in NGC 6397,” *Astrophys. J.* **732**, 88 (2011).
- [48] J. M. Lattimer, “The nuclear equation of state and neutron star masses,” *Ann. Rev. Nucl. Part. Sci.* **62**, 485 (2012).
- [49] K. Hebeler, J. M. Lattimer, C. J. Pethick, and A. Schwenk, “Constraints on Neutron Star Radii Based on Chiral Effective Field Theory Interactions,” *Phys. Rev. Lett.* **105**, 161102 (2010).
- [50] K. Hebeler, J. M. Lattimer, C. J. Pethick, and A. Schwenk, “Equation of state and neutron star properties constrained by nuclear physics and observation,” *Astrophys. J.* **773**, 11 (2013).
- [51] J. Simonis, K. Hebeler, J. D. Holt, J. Menéndez, and A. Schwenk, “Exploring *sd*-shell nuclei from two- and three-nucleon interactions with realistic saturation properties,” *Phys. Rev. C* **93**, 011302(R) (2016).
- [52] J. Simonis, S. R. Stroberg, K. Hebeler, J. D. Holt, and A. Schwenk, “Saturation with chiral interactions and consequences for finite nuclei,” *Phys. Rev. C* **96**, 014303 (2017).
- [53] A. Gallant *et al.*, “Breakdown of the Isobaric Multiplet Mass Equation for the  $A = 20$  and  $21$  Multiplets,” *Phys. Rev. Lett.* **113**, 082501 (2014).
- [54] A. Esposito, A. L. Guerrieri, F. Piccinini, A. Pilloni, and A. D. Polosa, “Four-quark hadrons: An updated review,” *Int. J. Mod. Phys. A* **30**, 1530002 (2015).
- [55] R. Aaij *et al.* (LHCb Collaboration), “Observation of  $J/\psi p$  Resonances Consistent with Pentaquark States in  $\Lambda_b^0 \rightarrow J/\psi K^- p$  Decays,” *Phys. Rev. Lett.* **115**, 072001 (2015).
- [56] D. B. Kaplan, “Five lectures on effective field theory,” in *Lectures delivered at the 17th National Nuclear Physics Summer School 2015, Berkeley, June 6-17, 2005* (2005) nucl-th/0510023 .
- [57] K. A. Olive *et al.* (Particle Data Group), “Review of Particle Physics,” *Chin. Phys. C* **38**, 090001 (2014), and 2015 update.
- [58] J. Goldstone, A. Salam, and S. Weinberg, “Broken Symmetries,” *Phys. Rev.* **127**, 965 (1962).
- [59] D. J. Gross and F. Wilczek, “Ultraviolet Behavior of Non-Abelian Gauge Theories,” *Phys. Rev. Lett.* **30**, 1343 (1973).
- [60] H. D. Politzer, “Reliable Perturbative Results for Strong Interactions?” *Phys. Rev. Lett.* **30**, 1346 (1973).
- [61] S. R. Beane, W. Detmold, K. Orginos, and M. J. Savage, “Nuclear Physics from Lattice QCD,” *Prog. Part. Nucl. Phys.* **66**, 1 (2011).
- [62] S. R. Beane, E. Chang, S. D. Cohen, W. Detmold, P. Junnarkar, H. W. Lin, T. C. Luu, K. Orginos, A. Parreño, M. J. Savage, and A. Walker-Loud (NPLQCD Collaboration), “Nucleon-nucleon scattering parameters in the limit of SU(3) flavor symmetry,” *Phys. Rev. C* **88**, 024003 (2013).
- [63] S. R. Beane, E. Chang, S. D. Cohen, W. Detmold, H. W. Lin, T. C. Luu, K. Orginos, A. Parreno, M. J. Savage, and A. Walker-Loud (NPLQCD Collaboration), “Light Nuclei and Hypernuclei from Quantum Chromodynamics in the Limit of SU(3) Flavor Symmetry,” *Phys. Rev. D* **87**, 034506 (2013).
- [64] S. R. Beane, E. Chang, S. Cohen, W. Detmold, H. W. Lin, K. Orginos, A. Parreño, M. J. Savage, and B. C. Tiburzi (NPLQCD Collaboration), “Magnetic Moments of Light Nuclei from Lattice Quantum Chromodynamics,” *Phys. Rev. Lett.* **113**, 252001 (2014).
-

- 
- [65] S. Dürr, Z. Fodor, J. Frison, C. Hoelbling, R. Hoffmann, S. D. Katz, S. Krieg, T. Kurth, L. Lellouch, T. Lippert, K. K. Szabo, and G. Vulvert, “Ab Initio Determination of Light Hadron Masses,” *Science* **322**, 1224 (2008).
- [66] R. Machleidt, “High precision, charge dependent Bonn nucleon-nucleon potential,” *Phys. Rev. C* **63**, 024001 (2001).
- [67] R. B. Wiringa, V. G. J. Stoks, and R. Schiavilla, “Accurate nucleon-nucleon potential with charge independence breaking,” *Phys. Rev. C* **51**, 38 (1995).
- [68] D. B. Kaplan, M. J. Savage, and M. B. Wise, “A New expansion for nucleon-nucleon interactions,” *Phys. Lett. B* **424**, 390 (1998).
- [69] P. F. Bedaque and U. van Kolck, “Nucleon-deuteron scattering from an effective field theory,” *Phys. Lett. B* **428**, 221 (1998).
- [70] H. Krebs, E. Epelbaum, and U.-G. Meißner, “Nuclear forces with  $\Delta$ -excitations up to next-to-next-to-leading order. I. Peripheral nucleon-nucleon waves,” *Eur. Phys. J. A* **32**, 127 (2007).
- [71] S. Weinberg, “Phenomenological Lagrangians,” *Physica A* **96**, 327 (1979).
- [72] S. Weinberg, “Effective chiral Lagrangians for nucleon - pion interactions and nuclear forces,” *Nucl. Phys. B* **363**, 3 (1991).
- [73] S. Weinberg, “Three-body interactions among nucleons and pions,” *Phys. Lett. B* **295**, 114 (1992).
- [74] E. Epelbaum, “Few-nucleon forces and systems in chiral effective field theory,” *Prog. Part. Nucl. Phys.* **57**, 654 (2006).
- [75] R. J. N. Phillips, “The two-nucleon interaction,” *Rep. Prog. Phys.* **22**, 562 (1959).
- [76] E. Epelbaum and U.-G. Meißner, “Isospin-violating nucleon-nucleon forces using the method of unitary transformation,” *Phys. Rev. C* **72**, 044001 (2005).
- [77] E. Epelbaum, H. Krebs, and U.-G. Meißner, “Precision Nucleon-Nucleon Potential at Fifth Order in the Chiral Expansion,” *Phys. Rev. Lett.* **115**, 122301 (2015).
- [78] U. van Kolck, “Few-nucleon forces from chiral Lagrangians,” *Phys. Rev. C* **49**, 2932 (1994).
- [79] S. Ishikawa and M. R. Robilotta, “Two-pion exchange three-nucleon potential:  $\mathcal{O}(q^4)$  chiral expansion,” *Phys. Rev. C* **76**, 014006 (2007).
- [80] V. Bernard, E. Epelbaum, H. Krebs, and U.-G. Meißner, “Subleading contributions to the chiral three-nucleon force. I. Long-range terms,” *Phys. Rev. C* **77**, 064004 (2008).
- [81] V. Bernard, E. Epelbaum, H. Krebs, and U.-G. Meißner, “Subleading contributions to the chiral three-nucleon force II: Short-range terms and relativistic corrections,” *Phys. Rev. C* **84**, 054001 (2011).
- [82] K. Hebeler, H. Krebs, E. Epelbaum, J. Golak, and R. Skibinski, “Efficient calculation of chiral three-nucleon forces up to  $N^3\text{LO}$  for ab initio studies,” *Phys. Rev. C* **91**, 044001 (2015).
- [83] E. Epelbaum, “Four-nucleon force in chiral effective field theory,” *Phys. Lett. B* **639**, 456 (2006).
- [84] E. Epelbaum, “Four-nucleon force using the method of unitary transformation,” *Eur. Phys. J. A* **34**, 197 (2007).
- [85] T. Krüger, I. Tews, K. Hebeler, and A. Schwenk, “Neutron matter from chiral effective field theory interactions,” *Phys. Rev. C* **88**, 025802 (2013).
- [86] E. Epelbaum, H. Krebs, and U.-G. Meißner, “Improved chiral nucleon-nucleon potential up to next-to-next-to-next-to-leading order,” *Eur. Phys. J. A* **51**, 53 (2015).
- [87] E. Epelbaum, W. Glöckle, and U.-G. Meißner, “The Two-nucleon system at next-to-next-to-next-to-leading order,” *Nucl. Phys. A* **747**, 362 (2005).



- 
- [88] P. Büttiker and U.-G. Meißner, “Pion-nucleon scattering inside the Mandelstam triangle,” *Nucl. Phys. A* **668**, 97 (2000).
- [89] N. Fettes, U.-G. Meißner, and S. Steininger, “Pion-nucleon scattering in chiral perturbation theory. 1. Isospin symmetric case,” *Nucl. Phys. A* **640**, 199 (1998).
- [90] D. R. Entem, R. Machleidt, and Y. Nosyk, “High-quality two-nucleon potentials up to fifth order of the chiral expansion,” *Phys. Rev. C* **96**, 024004 (2017).
- [91] E. Epelbaum, W. Glöckle, and U.-G. Meißner, “Improving the convergence of the chiral expansion for nuclear forces II: Low phases and the deuteron,” *Eur. Phys. J. A* **19**, 401 (2004).
- [92] E. Epelbaum, W. Glöckle, and U.-G. Meißner, “Improving the convergence of the chiral expansion for nuclear forces – I: Peripheral phases,” *Eur. Phys. J. A* **19**, 125 (2004).
- [93] A. Gezerlis, I. Tews, E. Epelbaum, S. Gandolfi, K. Hebeler, A. Nogga, and A. Schwenk, “Quantum Monte Carlo Calculations with Chiral Effective Field Theory Interactions,” *Phys. Rev. Lett.* **111**, 032501 (2013).
- [94] A. Gezerlis, I. Tews, E. Epelbaum, M. Freunek, S. Gandolfi, K. Hebeler, A. Nogga, and A. Schwenk, “Local chiral effective field theory interactions and quantum Monte Carlo applications,” *Phys. Rev. C* **90**, 054323 (2014).
- [95] V. Baru, E. Epelbaum, C. Hanhart, M. Hoferichter, A. E. Kudryavtsev, and D. R. Phillips, “The Multiple-scattering series in pion-deuteron scattering and the nucleon-nucleon potential: perspectives from effective field theory,” *Eur. Phys. J. A* **48**, 69 (2012).
- [96] H. Krebs, A. Gasparyan, and E. Epelbaum, “Chiral three-nucleon force at  $N^4$ LO: Longest-range contributions,” *Phys. Rev. C* **85**, 054006 (2012).
- [97] H. Krebs, A. Gasparyan, and E. Epelbaum, “Chiral three-nucleon force at  $N^4$ LO: II. Intermediate-range contributions,” *Phys. Rev. C* **87**, 054007 (2013).
- [98] D. R. Entem, N. Kaiser, R. Machleidt, and Y. Nosyk, “Peripheral nucleon-nucleon scattering at fifth order of chiral perturbation theory,” *Phys. Rev. C* **91**, 014002 (2015).
- [99] D. R. Entem, N. Kaiser, R. Machleidt, and Y. Nosyk, “Dominant contributions to the nucleon-nucleon interaction at sixth order of chiral perturbation theory,” *Phys. Rev. C* **92**, 064001 (2015).
- [100] A. Ekström, G. Baardsen, C. Forssén, G. Hagen, M. Hjorth-Jensen, G. R. Jansen, R. Machleidt, W. Nazarewicz, T. Papenbrock, J. Sarich, and S. M. Wild, “Optimized Chiral Nucleon-Nucleon Interaction at Next-to-Next-to-Leading Order,” *Phys. Rev. Lett.* **110**, 192502 (2013).
- [101] A. Ekström, B. D. Carlsson, K. A. Wendt, C. Forssén, M. Hjorth-Jensen, R. Machleidt, and S. M. Wild, “Statistical uncertainties of a chiral interaction at next-to-next-to leading order,” *J. Phys. G: Nucl. Part. Phys.* **42**, 034003 (2015).
- [102] B. D. Carlsson, A. Ekström, C. Forssén, D. F. Strömberg, G. R. Jansen, O. Lilja, M. Lindby, B. A. Mattsson, and K. A. Wendt, “Uncertainty analysis and order-by-order optimization of chiral nuclear interactions,” *Phys. Rev. X* **6**, 011019 (2016).
- [103] A. Ekström, G. R. Jansen, K. A. Wendt, G. Hagen, T. Papenbrock, B. D. Carlsson, C. Forssén, M. Hjorth-Jensen, P. Navrátil, and W. Nazarewicz, “Accurate nuclear radii and binding energies from a chiral interaction,” *Phys. Rev. C* **91**, 051301(R) (2015).
- [104] R. Navarro Pérez, J. E. Amaro, and E. Ruiz Arriola, “Phenomenological High Precision Neutron-Proton Delta-Shell Potential,” *Phys. Lett. B* **724**, 138 (2013).
- [105] R. Navarro Pérez, J. E. Amaro, and E. Ruiz Arriola, “Error analysis of nuclear forces and effective interactions,” *J. Phys. G: Nucl. Part. Phys.* **42**, 034013 (2015).
- [106] H. Feldmeier, T. Neff, R. Roth, and J. Schnack, “A Unitary correlation operator method,” *Nucl. Phys. A* **632**, 61 (1998).

- 
- [107] S. K. Bogner, T. T. S. Kuo, and A. Schwenk, “Model-independent low momentum nucleon interaction from phase shift equivalence,” *Phys. Rep.* **386**, 1 (2003).
- [108] S. D. Glazek and K. G. Wilson, “Renormalization of Hamiltonians,” *Phys. Rev. D* **48**, 5863 (1993).
- [109] S. D. Glazek and K. G. Wilson, “Perturbative renormalization group for Hamiltonians,” *Phys. Rev. D* **49**, 4214 (1994).
- [110] F. Wegner, “Flow-equations for Hamiltonians,” *Annalen der Physik* **506**, 77 (1994).
- [111] R. Roth, S. Reinhardt, and H. Hergert, “Unitary Correlation Operator Method and Similarity Renormalization Group: Connections and Differences,” *Phys. Rev. C* **77**, 064003 (2008).
- [112] R. J. Furnstahl and K. Hebeler, “New applications of renormalization group methods in nuclear physics,” *Rep. Prog. Phys.* **76**, 126301 (2013).
- [113] A. C. Hindmarsh, P. N. Brown, K. E. Grant, S. L. Lee, R. Serban, D. E. Shumaker, and C. S. Woodward, “Sundials: Suite of nonlinear and differential/algebraic equation solvers,” *ACM Trans. Math. Softw.* **31**, 363 (2005).
- [114] R. J. Furnstahl, “The Renormalization Group in Nuclear Physics,” *Nucl. Phys. Proc. Suppl.* **228**, 139 (2012).
- [115] S. K. Bogner, R. J. Furnstahl, and A. Schwenk, “From low-momentum interactions to nuclear structure,” *Prog. Part. Nucl. Phys.* **65**, 94 (2010).
- [116] E. Anderson, S. K. Bogner, R. J. Furnstahl, E. D. Jurgenson, R. J. Perry, and A. Schwenk, “Block Diagonalization using SRG Flow Equations,” *Phys. Rev. C* **77**, 037001 (2008).
- [117] N. M. Dicaire, C. Omand, and P. Navrátil, “Alternative similarity renormalization group generators in nuclear structure calculations,” *Phys. Rev. C* **90**, 034302 (2014).
- [118] W. Li, E. R. Anderson, and R. J. Furnstahl, “Similarity Renormalization Group with Novel Generators,” *Phys. Rev. C* **84**, 054002 (2011).
- [119] K. Hebeler, “Momentum-space evolution of chiral three-nucleon forces,” *Phys. Rev. C* **85**, 021002(R) (2012).
- [120] K. A. Wendt, “Similarity Renormalization Group Evolution of Three-Nucleon Forces in a Hyperspherical Momentum Representation,” *Phys. Rev. C* **87**, 061001(R) (2013).
- [121] H. Hergert, “In-Medium Similarity Renormalization Group for Closed and Open-Shell Nuclei,” *Phys. Scripta* **92**, 023002 (2017).
- [122] E. R. Anderson, S. K. Bogner, R. J. Furnstahl, and R. J. Perry, “Operator Evolution via the Similarity Renormalization Group I: The Deuteron,” *Phys. Rev. C* **82**, 054001 (2010).
- [123] M. D. Schuster, S. Quaglioni, C. W. Johnson, E. D. Jurgenson, and P. Navrátil, “Operator evolution for ab initio theory of light nuclei,” *Phys. Rev. C* **90**, 011301(R) (2014).
- [124] E. Epelbaum, A. Nogga, W. Glöckle, H. Kamada, U.-G. Meißner, and H. Witała, “Three-nucleon forces from chiral effective field theory,” *Phys. Rev. C* **66**, 064001 (2002).
- [125] M. C. M. Rentmeester, R. G. E. Timmermans, and J. J. de Swart, “Determination of the chiral coupling constants  $c_3$  and  $c_4$  in new pp and np partial-wave analyses,” *Phys. Rev. C* **67**, 044001 (2003).
- [126] I. Sick, “Precise root-mean-square radius of  $^4\text{He}$ ,” *Phys. Rev. C* **77**, 041302(R) (2008).
- [127] G. P. Kamuntavičius, R. K. Kalinauskas, B. R. Barrett, S. Mickevičius, and D. Germanas, “The general harmonic-oscillator brackets: compact expression, symmetries, sums and Fortran code,” *Nucl. Phys. A* **695**, 191 (2001).
- [128] W. Glöckle, *The Quantum Mechanical Few-Body Problem* (Springer, Berlin, Heidelberg, 1983).

- 
- [129] R. Skibinski, J. Golak, K. Topolnicki, H. Witała, H. Kamada, W. Glöckle, and A. Nogga, “The Tucson-Melbourne Three-Nucleon Force in the automatized Partial-Wave Decomposition,” *Eur. Phys. J. A* **47**, 48 (2011).
- [130] P. Navrátil, B. R. Barrett, and W. Glöckle, “Spurious states in the Faddeev formalism for few-body systems,” *Phys. Rev. C* **59**, 611 (1999).
- [131] P. Navrátil and W. E. Ormand, “Ab initio shell model with a genuine three-nucleon force for the  $p$ -shell nuclei,” *Phys. Rev. C* **68**, 034305 (2003).
- [132] A. Nogga, P. Navrátil, B. R. Barrett, and J. P. Vary, “Spectra and binding energy predictions of chiral interactions for  ${}^7\text{Li}$ ,” *Phys. Rev. C* **73**, 064002 (2006).
- [133] J. E. Lynn, J. Carlson, E. Epelbaum, S. Gandolfi, A. Gezerlis, and A. Schwenk, “Quantum Monte Carlo Calculations of Light Nuclei Using Chiral Potentials,” *Phys. Rev. Lett.* **113**, 192501 (2014).
- [134] J. E. Lynn, I. Tews, J. Carlson, S. Gandolfi, A. Gezerlis, K. E. Schmidt, and A. Schwenk, “Chiral Three-Nucleon Interactions in Light Nuclei, Neutron- $\alpha$  Scattering, and Neutron Matter,” *Phys. Rev. Lett.* **116**, 062501 (2016).
- [135] H. Hergert, S. Binder, A. Calci, J. Langhammer, and R. Roth, “Ab Initio Calculations of Even Oxygen Isotopes with Chiral Two-Plus-Three-Nucleon Interactions,” *Phys. Rev. Lett.* **110**, 242501 (2013).
- [136] A. Cipollone, C. Barbieri, and P. Navrátil, “Isotopic chains around oxygen from evolved chiral two- and three-nucleon interactions,” *Phys. Rev. Lett.* **111**, 062501 (2013).
- [137] G. R. Jansen, J. Engel, G. Hagen, P. Navrátil, and A. Signoracci, “Ab initio coupled-cluster effective interactions for the shell model: Application to neutron-rich oxygen and carbon isotopes,” *Phys. Rev. Lett.* **113**, 142502 (2014).
- [138] E. Epelbaum, H. Krebs, T. A. Lähde, D. Lee, U.-G. Meißner, *et al.*, “Ab initio calculation of the spectrum and structure of  ${}^{16}\text{O}$ ,” *Phys. Rev. Lett.* **112**, 102501 (2014).
- [139] K. Hebeler, J. D. Holt, J. Menéndez, and A. Schwenk, “Nuclear forces and their impact on neutron-rich nuclei and neutron-rich matter,” *Ann. Rev. Nucl. Part. Sci.* **65**, 457 (2015).
- [140] K. Tsukiyama, S. K. Bogner, and A. Schwenk, “In-medium Similarity Renormalization Group for Nuclei,” *Phys. Rev. Lett.* **106**, 222502 (2011).
- [141] S. Binder, J. Langhammer, A. Calci, and R. Roth, “Ab initio path to heavy nuclei,” *Phys. Lett. B* **736**, 119 (2014).
- [142] G. R. Jansen, “Spherical Coupled-Cluster Theory for Open-Shell Nuclei,” *Phys. Rev. C* **88**, 024305 (2013).
- [143] T. D. Morris, N. Parzuchowski, and S. K. Bogner, “Magnus expansion and in-medium similarity renormalization group,” *Phys. Rev. C* **92**, 034331 (2015).
- [144] N. M. Parzuchowski, T. D. Morris, and S. K. Bogner, “Ab Initio Excited States from the In-Medium Similarity Renormalization Group,” *Phys. Rev. C* **95**, 044304 (2017).
- [145] S. R. Stroberg, A. Calci, H. Hergert, J. D. Holt, S. K. Bogner, R. Roth, and A. Schwenk, “Nucleus-dependent valence-space approach to nuclear structure,” *Phys. Rev. Lett.* **118**, 032502 (2017).
- [146] E. Gebrerufael, K. Vobig, H. Hergert, and R. Roth, “Ab Initio Description of Open-Shell Nuclei: Merging No-Core Shell Model and In-Medium Similarity Renormalization Group,” *Phys. Rev. Lett.* **118**, 152503 (2017).
- [147] V. Somà, A. Cipollone, C. Barbieri, P. Navrátil, and T. Duguet, “Chiral two- and three-nucleon forces along medium-mass isotope chains,” *Phys. Rev. C* **89**, 061301(R) (2014).
- [148] A. Tichai, J. Langhammer, S. Binder, and R. Roth, “Hartree-Fock many-body perturbation theory for nuclear ground-states,” *Phys. Lett. B* **756**, 283 (2016).

- [149] A. Tichai, E. Gebrerufael, and R. Roth, “Open-Shell Nuclei from No-Core Shell Model with Perturbative Improvement,” arXiv:1703.05664 .
- [150] T. A. Lähde, E. Epelbaum, H. Krebs, D. Lee, U.-G. Meißner, and G. Rupak, “Lattice Effective Field Theory for Medium-Mass Nuclei,” *Phys. Lett. B* **732**, 110 (2014).
- [151] S. Elhatisari, E. Epelbaum, H. Krebs, T. A. Lähde, D. Lee, N. Li, B.-n. Lu, U.-G. Meißner, and G. Rupak, “Ab initio Calculations of the Isotopic Dependence of Nuclear Clustering,” *Phys. Rev. Lett.* **119**, 222505 (2017).
- [152] R. Roth, S. Binder, K. Vobig, A. Calci, J. Langhammer, and P. Navrátil, “Medium-Mass Nuclei with Normal-Ordered Chiral NN+3N Interactions,” *Phys. Rev. Lett.* **109**, 052501 (2012).
- [153] T. Otsuka, T. Suzuki, J. D. Holt, A. Schwenk, and Y. Akaishi, “Three-Body Forces and the Limit of Oxygen Isotopes,” *Phys. Rev. Lett.* **105**, 032501 (2010).
- [154] H. Hergert, S. K. Bogner, S. Binder, A. Calci, J. Langhammer, *et al.*, “In-Medium Similarity Renormalization Group with Chiral Two- Plus Three-Nucleon Interactions,” *Phys. Rev. C* **87**, 034307 (2013).
- [155] E. Gebrerufael, A. Calci, and R. Roth, “Open-shell nuclei and excited states from multireference normal-ordered Hamiltonians,” *Phys. Rev. C* **93**, 031301(R) (2016).
- [156] G. C. Wick, “The Evaluation of the Collision Matrix,” *Phys. Rev.* **80**, 268 (1950).
- [157] G. F. Bertsch, “Role of core polarization in two-body interaction,” *Nucl. Phys.* **74**, 234 (1965).
- [158] T. T. S. Kuo and G. E. Brown, “Structure of finite nuclei and the free nucleon-nucleon interaction: An application to  $^{18}\text{O}$  and  $^{18}\text{F}$ ,” *Nucl. Phys.* **85**, 40 (1966).
- [159] B. R. Barrett and M. W. Kirson, “Higher-order terms and the apparent non-convergence of the perturbation expansion for the effective interaction in finite nuclei,” *Nucl. Phys. A* **148**, 145 (1970).
- [160] T. T. S. Kuo, “Folded-diagram theory of the effective interaction in nuclei, atoms and molecules,” in *Lecture Notes in Physics*, Vol. 364, edited by T. T. S. Kuo and E. Osnes (Springer, Berlin, Heidelberg, 1990) p. 1.
- [161] M. Hjorth-Jensen, T. T. S. Kuo, and E. Osnes, “Realistic effective interactions for nuclear systems,” *Phys. Rep.* **261**, 125 (1995).
- [162] B. A. Brown and W. A. Richter, “New ‘USD’ Hamiltonians for the *sd* shell,” *Phys. Rev. C* **74**, 034315 (2006).
- [163] P. J. Ellis, T. Engeland, M. Hjorth-Jensen, M. P. Kartamyshev, and E. Osnes, “Model calculation of effective three-body forces,” *Phys. Rev. C* **71**, 034301 (2005).
- [164] J. D. Holt, J. Menéndez, and A. Schwenk, “Three-body forces and proton-rich nuclei,” *Phys. Rev. Lett.* **110**, 022502 (2013).
- [165] J. D. Holt, T. Otsuka, A. Schwenk, and T. Suzuki, “Three-body forces and shell structure in calcium isotopes,” *J. Phys. G: Nucl. Part. Phys.* **39**, 085111 (2012).
- [166] A. T. Gallant *et al.*, “New Precision Mass Measurements of Neutron-Rich Calcium and Potassium Isotopes and Three-Nucleon Forces,” *Phys. Rev. Lett.* **109**, 032506 (2012).
- [167] J. D. Holt, J. Menéndez, and A. Schwenk, “The role of three-nucleon forces and many-body processes in nuclear pairing,” *J. Phys. G: Nucl. Part. Phys.* **40**, 075105 (2013).
- [168] K. Tsukiyama, S. K. Bogner, and A. Schwenk, “In-medium similarity renormalization group for open-shell nuclei,” *Phys. Rev. C* **85**, 061304(R) (2012).
- [169] S. K. Bogner, H. Hergert, J. D. Holt, A. Schwenk, S. Binder, A. Calci, J. Langhammer, and R. Roth, “Nonperturbative shell-model interactions from the in-medium similarity renormalization group,” *Phys. Rev. Lett.* **113**, 142501 (2014).

- 
- [170] S. R. White, “Numerical canonical transformation approach to quantum many-body problems,” *The Journal of Chemical Physics* **117**, 7472 (2002).
- [171] W. Magnus, “On the exponential solution of differential equations for a linear operator,” *Commun. Pure Appl. Math.* **7**, 649 (1954).
- [172] S. Blanes, F. Casas, J. Oteo, and J. Ros, “The magnus expansion and some of its applications,” *Phys. Rep.* **470**, 151 (2009).
- [173] F. Coester, “Bound states of a many-particle system,” *Nuclear Physics* **7**, 421 (1958).
- [174] F. Coester and H. Kümmel, “Short-range correlations in nuclear wave functions,” *Nuclear Physics* **17**, 477 (1960).
- [175] H. Kümmel, K. H. Lührmann, and J. G. Zabolitzky, “Many-Fermion theory in exp(S)- (or coupled cluster) form,” *Phys. Rep.* **36**, 1 (1978).
- [176] D. J. Dean and M. Hjorth-Jensen, “Coupled-cluster approach to nuclear physics,” *Phys. Rev. C* **69**, 054320 (2004).
- [177] I. Shavitt and R. J. Bartlett, *Many-Body Methods in Chemistry and Physics: MBPT and Coupled-Cluster Theory*, Cambridge Molecular Science (Cambridge University Press, 2009).
- [178] D. Thouless, “Stability conditions and nuclear rotations in the Hartree-Fock theory,” *Nuclear Physics* **21**, 225 (1960).
- [179] A. G. Taube and R. J. Bartlett, “Improving upon CCSD(T): ACCSD(T). I. Potential energy surfaces,” *The Journal of Chemical Physics* **128**, 044110 (2008).
- [180] G. Hagen, D. J. Dean, M. Hjorth-Jensen, T. Papenbrock, and A. Schwenk, “Benchmark calculations for  $^3\text{H}$ ,  $^4\text{He}$ ,  $^{16}\text{O}$  and  $^{40}\text{Ca}$  with ab initio coupled-cluster theory,” *Phys. Rev. C* **76**, 044305 (2007).
- [181] G. Hagen, T. Papenbrock, D. J. Dean, and M. Hjorth-Jensen, “Medium-mass nuclei from chiral nucleon-nucleon interactions,” *Phys. Rev. Lett.* **101**, 092502 (2008).
- [182] J. F. Stanton and R. J. Bartlett, “The equation of motion coupled-cluster method. A systematic biorthogonal approach to molecular excitation energies, transition probabilities, and excited state properties,” *The Journal of Chemical Physics* **98**, 7029 (1993).
- [183] J. Čížek, “On the Use of the Cluster Expansion and the Technique of Diagrams in Calculations of Correlation Effects in Atoms and Molecules,” in *Advances in Chemical Physics: Correlation Effects in Atoms and Molecules, Volume 14* (John Wiley & Sons, Inc., 1969) p. 35.
- [184] B. A. Brown, “The nuclear shell model towards the drip lines,” *Prog. Part. Nucl. Phys.* **47**, 517 (2001).
- [185] E. Caurier, G. Martinez-Pinedo, F. Nowacki, A. Poves, and A. P. Zuker, “The Shell model as unified view of nuclear structure,” *Rev. Mod. Phys.* **77**, 427 (2005).
- [186] N. Tsunoda, K. Takayanagi, M. Hjorth-Jensen, and T. Otsuka, “Multi-shell effective interactions,” *Phys. Rev. C* **89**, 024313 (2014).
- [187] J. D. Holt, J. Menéndez, J. Simonis, and A. Schwenk, “Three-nucleon forces and spectroscopy of neutron-rich calcium isotopes,” *Phys. Rev. C* **90**, 024312 (2014).
- [188] J. D. Holt, J. Menéndez, and A. Schwenk, “Chiral three-nucleon forces and bound excited states in neutron-rich oxygen isotopes,” *Eur. Phys. J. A* **49**, 39 (2013).
- [189] C. Caesar *et al.* (R3B collaboration), “Beyond the Neutron Drip-Line: The Unbound Oxygen Isotopes  $^{25}\text{O}$  and  $^{26}\text{O}$ ,” *Phys. Rev. C* **88**, 034313 (2013).
- [190] M. Wang, G. Audi, A. H. Wapstra, F. G. Kondev, M. MacCormick, X. Xu, and B. Pfeiffer, “The AME2012 atomic mass evaluation,” *Chin. Phys. C* **36**, 1603 (2012).

- [191] M. Bellegric *et al.*, “Search for neutron excitations across the  $N = 20$  shell gap in  $^{25-29}\text{Ne}$ ,” *Phys. Rev. C* **72**, 054316 (2005).
- [192] Y. Yanagisawa *et al.*, “The first excited state of  $^{30}\text{Ne}$  studied by proton inelastic scattering in reversed kinematics,” *Phys. Lett. B* **566**, 84 (2003).
- [193] V. Tripathi *et al.*, “Competition between normal and intruder states inside the ‘island of inversion’,” *Phys. Rev. C* **76**, 021301(R) (2007).
- [194] P. Doornenbal *et al.*, “Exploring the ‘Island of Inversion’ by in-beam  $\gamma$ -ray spectroscopy of the neutron-rich sodium isotopes  $^{31,32,33}\text{Na}$ ,” *Phys. Rev. C* **81**, 041305(R) (2010).
- [195] M. Seidlitz *et al.*, “Coulomb excitation of  $^{31}\text{Mg}$ ,” *Phys. Lett. B* **700**, 181 (2011).
- [196] T. Motobayashi *et al.*, “Large deformation of the very neutron-rich nucleus  $^{32}\text{Mg}$  from intermediate-energy Coulomb excitation,” *Phys. Lett. B* **346**, 9 (1995).
- [197] <http://www.nndc.bnl.gov/ensdf/>, .
- [198] J. Birkhan *et al.*, “Electric dipole polarizability of  $^{48}\text{Ca}$  and implications for the neutron skin,” *Phys. Rev. Lett.* **118**, 252501 (2017).
- [199] C. J. Horowitz, K. S. Kumar, and R. Michaels, “Electroweak Measurements of Neutron Densities in CREX and PREX at JLab, USA,” *Eur. Phys. J. A* **50**, 48 (2014).
- [200] G. P. Kamuntavicius, “Root-mean-square radii of light atomic nuclei: Neutron skin,” *Phys. Rev. C* **56**, 191 (1997).
- [201] G. Hagen, T. Papenbrock, and D. J. Dean, “Solution of the center-of-mass problem in nuclear structure calculations,” *Phys. Rev. Lett.* **103**, 062503 (2009).
- [202] R. Kanungo *et al.*, “Exploring the anomaly in the interaction cross section and matter radius of  $^{23}\text{O}$ ,” *Phys. Rev. C* **84**, 061304(R) (2011).
- [203] P.-G. Reinhard, J. Piekarewicz, W. Nazarewicz, B. K. Agrawal, N. Paar, and X. Roca-Maza, “Information content of the weak-charge form factor,” *Phys. Rev. C* **88**, 034325 (2013).
- [204] A. Ong, J. C. Berengut, and V. V. Flambaum, “The Effect of spin-orbit nuclear charge density corrections due to the anomalous magnetic moment on halonuclei,” *Phys. Rev. C* **82**, 014320 (2010).
- [205] C. J. Horowitz and J. Piekarewicz, “Impact of spin-orbit currents on the electroweak skin of neutron-rich nuclei,” *Phys. Rev. C* **86**, 045503 (2012).
- [206] I. Angeli and K. Marinova, “Table of experimental nuclear ground state charge radii: An update,” *Atomic Data and Nuclear Data Tables* **99**, 69 (2013).
- [207] I. Tanihata, H. Hamagaki, O. Hashimoto, Y. Shida, N. Yoshikawa, K. Sugimoto, O. Yamakawa, T. Kobayashi, and N. Takahashi, “Measurements of Interaction Cross-Sections and Nuclear Radii in the Light  $p$ -Shell Region,” *Phys. Rev. Lett.* **55**, 2676 (1985).
- [208] J. Zenihiro *et al.*, “Neutron density distributions of  $^{204,206,208}\text{Pb}$  deduced via proton elastic scattering at  $E_p = 295$  MeV,” *Phys. Rev. C* **82**, 044611 (2010).
- [209] C. M. Tarbert *et al.*, “Neutron skin of  $^{208}\text{Pb}$  from Coherent Pion Photoproduction,” *Phys. Rev. Lett.* **112**, 242502 (2014).
- [210] S. Abrahamyan, Z. Ahmed, H. Albatineh, K. Aniol, D. S. Armstrong, *et al.*, “Measurement of the Neutron Radius of  $^{208}\text{Pb}$  Through Parity-Violation in Electron Scattering,” *Phys. Rev. Lett.* **108**, 112502 (2012).
- [211] T. W. Donnelly, J. Dubach, and I. Sick, “Isospin Dependences in Parity Violating Electron Scattering,” *Nucl. Phys. A* **503**, 589 (1989).

- [212] A. Tamii, I. Poltoratska, P. von Neumann-Cosel, Y. Fujita, T. Adachi, *et al.*, “Complete electric dipole response and the neutron skin in  $^{208}\text{Pb}$ ,” *Phys. Rev. Lett.* **107**, 062502 (2011).
- [213] T. Hashimoto *et al.*, “Dipole polarizability of  $^{120}\text{Sn}$  and nuclear energy density functionals,” *Phys. Rev. C* **92**, 031305(R) (2015).
- [214] D. M. Rossi *et al.*, “Measurement of the Dipole Polarizability of the Unstable Neutron-Rich Nucleus  $^{68}\text{Ni}$ ,” *Phys. Rev. Lett.* **111**, 242503 (2013).
- [215] M. Bender, P.-H. Heenen, and P.-G. Reinhard, “Self-consistent mean-field models for nuclear structure,” *Rev. Mod. Phys.* **75**, 121 (2003).
- [216] P.-G. Reinhard and W. Nazarewicz, “Information content of a new observable: The case of the nuclear neutron skin,” *Phys. Rev. C* **81**, 051303(R) (2010).
- [217] J. Piekarewicz, B. K. Agrawal, G. Colo, W. Nazarewicz, N. Paar, P. G. Reinhard, X. Roca-Maza, and D. Vretenar, “Electric dipole polarizability and the neutron skin,” *Phys. Rev. C* **85**, 041302(R) (2012).
- [218] H. J. Emrich, G. Fricke, G. Mallot, H. Miska, H. G. Sieberling, J. M. Cavedon, B. Frois, and D. Goutte, “Radial distribution of nucleons in isotopes  $^{40,48}\text{Ca}$ ,” *Nucl. Phys. A* **396**, 401 (1983).
- [219] S. Bacca, N. Barnea, G. Hagen, G. Orlandini, and T. Papenbrock, “First Principles Description of the Giant Dipole Resonance in  $^{16}\text{O}$ ,” *Phys. Rev. Lett.* **111**, 122502 (2013).
- [220] S. Bacca, N. Barnea, G. Hagen, M. Miorelli, G. Orlandini, and T. Papenbrock, “Giant and pigmy dipole resonances in  $^4\text{He}$ ,  $^{16,22}\text{O}$ , and  $^{40}\text{Ca}$  from chiral nucleon-nucleon interactions,” *Phys. Rev. C* **90**, 064619 (2014).
- [221] J. Ahrens *et al.*, “Total Nuclear Photon Absorption Cross-Sections for Some Light Elements,” *Nucl. Phys. A* **251**, 479 (1975).
- [222] M. Kortelainen, J. McDonnell, W. Nazarewicz, E. Olsen, P.-G. Reinhard, J. Sarich, N. Schunck, S. M. Wild, D. Davesne, J. Erler, and A. Pastore, “Nuclear energy density optimization: Shell structure,” *Phys. Rev. C* **89**, 054314 (2014).
- [223] I. Angeli, Y. P. Gangrsky, K. P. Marinova, I. N. Boboshin, S. Y. Komarov, B. S. Ishkhanov, and V. V. Varlamov, “N and Z dependence of nuclear charge radii,” *J. Phys. G: Nucl. Part. Phys.* **36**, 085102 (2009).
- [224] C. W. P. Palmer, P. E. G. Baird, S. A. Blundell, J. R. Brandenberger, C. J. Foot, D. N. Stacey, and G. K. Woodgate, “Laser spectroscopy of calcium isotopes,” *J. Phys. B: At. Mol. Phys.* **17**, 2197 (1984).
- [225] A. Andl, K. Bekk, S. Goring, A. Hanser, G. Nowicki, H. Rebel, G. Schatz, and R. C. Thompson, “Isotope shifts and hyperfine structure of the  $4s^2\ ^1S_0 - 4s4p\ ^1P_1$  transition in calcium isotopes,” *Phys. Rev. C* **26**, 2194 (1982).
- [226] L. Vermeeren, R. E. Silverans, P. Lievens, A. Klein, R. Neugart, C. Schulz, and F. Buchinger, “Ultrasensitive radioactive detection of collinear-laser optical pumping: Measurement of the nuclear charge radius of  $^{50}\text{Ca}$ ,” *Phys. Rev. Lett.* **68**, 1679 (1992).
- [227] G. Fricke and K. Heilig, *Nuclear Charge Radii*, edited by H. Schopper (Springer, Berlin, Heidelberg, 2004).
- [228] L. Vermeeren, P. Lievens, R. E. Silverans, U. Georg, M. Kiem, A. Klein, R. Neugart, M. Neuroth, and F. Buchinger, “The Mean square nuclear charge radius of  $^{39}\text{Ca}$ ,” *J. Phys. G: Nucl. Part. Phys.* **22**, 1517 (1996).
- [229] A.-M. Mårtensson-Pendrill, A. Ynnerman, H. Warston, L. Vermeeren, R. E. Silverans, A. Klein, R. Neugart, C. Schulz, and P. Lievens (ISOLDE Collaboration), “Isotope shifts and nuclear-charge radii in singly ionized  $^{40-48}\text{Ca}$ ,” *Phys. Rev. A* **45**, 4675 (1992).
- [230] T. Kortelainen, M. Lesinski, J. Moré, W. Nazarewicz, J. Sarich, N. Schunck, M. V. Stoitsov, and S. Wild, “Nuclear energy density optimization,” *Phys. Rev. C* **82**, 024313 (2010).

- 
- [231] E. E. Saperstein and S. V. Tolokonnikov, “Self-consistent theory of finite Fermi systems and radii of nuclei,” *Phys. Atom. Nucl.* **74**, 1277 (2011).
- [232] J.-P. Delaroche, M. Girod, J. Libert, H. Goutte, S. Hilaire, S. Peru, N. Pillet, and G. F. Bertsch, “Structure of even-even nuclei using a mapped collective Hamiltonian and the D1S Gogny interaction,” *Phys. Rev. C* **81**, 014303 (2010).
- [233] G. A. Lalazissis, T. Niksic, D. Vretenar, and P. Ring, “New relativistic mean-field interaction with density-dependent meson-nucleon couplings,” *Phys. Rev. C* **71**, 024312 (2005).
- [234] S. Goriely, N. Chamel, and J. M. Pearson, “Further explorations of Skyrme-Hartree-Fock-Bogoliubov mass formulas. XIII. The 2012 atomic mass evaluation and the symmetry coefficient,” *Phys. Rev. C* **88**, 024308 (2013).
- [235] D. M. Rossi *et al.*, “Charge radii of neutron-deficient  $^{36}\text{K}$  and  $^{37}\text{K}$ ,” *Phys. Rev. C* **92**, 014305 (2015).
- [236] E. Caurier, K. Langanke, G. Martinez-Pinedo, F. Nowacki, and P. Vogel, “Shell model description of isotope shifts in calcium,” *Phys. Lett. B* **522**, 240 (2001).
- [237] M. L. Bissell *et al.*, “Proton-Neutron Pairing Correlations in the Self-Conjugate Nucleus  $^{38}\text{K}$  Probed via a Direct Measurement of the Isomer Shift,” *Phys. Rev. Lett.* **113**, 052502 (2014).
- [238] S. A. Fayans, “Towards a universal nuclear density functional,” *JETP Lett.* **68**, 169 (1998).
- [239] K. Minamisono *et al.*, “Charge Radii of Neutron Deficient  $^{52,53}\text{Fe}$  Produced by Projectile Fragmentation,” *Phys. Rev. Lett.* **117**, 252501 (2016).
- [240] S. A. Fayans, S. V. Tolokonnikov, E. L. Trykov, and D. Zawischa, “Nuclear isotope shifts within the local energy density functional approach,” *Nucl. Phys. A* **676**, 49 (2000).
- [241] R. F. Garcia Ruiz, M. Bissell, K. Blaum, N. Frömmgen, M. Hammen, *et al.*, “Ground-State Electromagnetic Moments of Calcium Isotopes,” *Phys. Rev. C* **91**, 041304(R) (2015).
- [242] C. Drischler, V. Somà, and A. Schwenk, “Microscopic calculations and energy expansions for neutron-rich matter,” *Phys. Rev. C* **89**, 025806 (2014).
- [243] G. Hagen, G. R. Jansen, and T. Papenbrock, “Structure of  $^{78}\text{Ni}$  from first-principles computations,” *Phys. Rev. Lett.* **117**, 172501 (2016).
- [244] S. R. Stroberg, H. Hergert, J. D. Holt, S. K. Bogner, and A. Schwenk, “Ground and excited states of doubly open-shell nuclei from ab initio valence-space Hamiltonians,” *Phys. Rev. C* **93**, 051301(R) (2016).
- [245] B. A. Brown and W. D. M. Rae, “The Shell-Model Code NuShellX@MSU,” *Nuclear Data Sheets* **120**, 115 (2014).
- [246] C. Patrignani *et al.* (Particle Data Group), “Review of Particle Physics,” *Chin. Phys. C* **40**, 100001 (2016).
- [247] S. König, S. K. Bogner, R. J. Furnstahl, S. N. More, and T. Papenbrock, “Ultraviolet extrapolations in finite oscillator bases,” *Phys. Rev. C* **90**, 064007 (2014).
- [248] R. J. Furnstahl, G. Hagen, T. Papenbrock, and K. A. Wendt, “Infrared extrapolations for atomic nuclei,” *J. Phys. G: Nucl. Part. Phys.* **42**, 034032 (2015).
- [249] V. Lapoux, V. Somà, C. Barbieri, H. Hergert, J. D. Holt, and S. Stroberg, “Radii and Binding Energies in Oxygen Isotopes: A Challenge for Nuclear Forces,” *Phys. Rev. Lett.* **117**, 052501 (2016).
- [250] S. R. Stroberg and J. D. Holt, “private communication,” (2017).
- [251] P. Navrátil, “Local three-nucleon interaction from chiral effective field theory,” *Few Body Syst.* **41**, 117 (2007).



- [252] H. Heylen *et al.*, “Changes in nuclear structure along the Mn isotopic chain studied via charge radii,” *Phys. Rev. C* **94**, 054321 (2016).
- [253] G. Hagen, M. Hjorth-Jensen, G. R. Jansen, R. Machleidt, and T. Papenbrock, “Evolution of shell structure in neutron-rich calcium isotopes,” *Phys. Rev. Lett.* **109**, 032502 (2012).
- [254] H. Hergert, S. K. Bogner, T. D. Morris, S. Binder, A. Calci, J. Langhammer, and R. Roth, “Ab initio multireference in-medium similarity renormalization group calculations of even calcium and nickel isotopes,” *Phys. Rev. C* **90**, 041302(R) (2014).
- [255] R. Roth, A. Calci, J. Langhammer, and S. Binder, “Evolved Chiral NN+3N Hamiltonians for Ab Initio Nuclear Structure Calculations,” *Phys. Rev. C* **90**, 024325 (2014).
- [256] W. E. Ormand and B. A. Brown, “Empirical isospin-nonconserving Hamiltonians for shell-model calculations,” *Nucl. Phys. A* **491**, 1 (1989).
- [257] B. E. Glassman *et al.*, “Revalidation of the isobaric multiplet mass equation for the  $A = 20$  quintet,” *Phys. Rev. C* **92**, 042501(R) (2015).
- [258] W. Heisenberg, “On the structure of atomic nuclei,” *Z. Phys.* **77**, 1 (1932).
- [259] E. Wigner, “On the Consequences of the Symmetry of the Nuclear Hamiltonian on the Spectroscopy of Nuclei,” *Phys. Rev.* **51**, 106 (1937).
- [260] E. P. Wigner, Proceedings of the Robert A. Welch Conference on Chemical Research (Robert A. Welch Foundation, Houston, Texas) **1**, 67 (1957).
- [261] S. Weinberg and S. B. Treiman, “Electromagnetic Corrections to Isotopic Spin Conservation,” *Phys. Rev.* **116**, 465 (1959).
- [262] S. M. Lenzi and M. A. Bentley, “Isospin symmetry breaking in mirror nuclei,” in *Lectures given at Ecole Internationale Joliot Curie 2010* (2010).
- [263] Y. H. Lam, B. Blank, N. A. Smirnova, J. B. Bueb, and M. S. Antony, “The isobaric multiplet mass equation for  $A \leq 71$  revisited,” *Atomic Data and Nuclear Data Tables* **99**, 680 (2013).
- [264] M. Brodeur, T. Brunner, S. Ettenauer, A. Lapierre, R. Ringle, B. A. Brown, D. Lunney, and J. Dilling, “Elucidation of the anomalous  $A = 9$  isospin quartet behaviour,” *Phys. Rev. Lett.* **108**, 212501 (2012).
- [265] A. Kankainen *et al.*, “Mass of astrophysically relevant  $^{31}\text{Cl}$  and the breakdown of the isobaric multiplet mass equation,” *Phys. Rev. C* **93**, 041304(R) (2016).
- [266] M. B. Bennett *et al.*, “Isobaric multiplet mass equation in the  $A = 31$ ,  $T = 3/2$  quartets,” *Phys. Rev. C* **93**, 064310 (2016).
- [267] C. Yazidjian *et al.*, “Evidence for a breakdown of the Isobaric Multiplet Mass Equation: A study of the  $A = 35$ ,  $T = 3/2$  isospin quartet,” *Phys. Rev. C* **76**, 024308 (2007).
- [268] R. J. Charity *et al.*, “Isobaric multiplet mass equation for  $A = 7$  and 8,” *Phys. Rev. C* **84**, 051308(R) (2011).
- [269] A. A. Kwiatkowski *et al.*, “Precision test of the isobaric multiplet mass equation for the  $A = 32$ ,  $T = 2$  quintet,” *Phys. Rev. C* **80**, 051302(R) (2009).
- [270] A. Kankainen *et al.*, “High-precision mass measurement of  $^{31}\text{S}$  with the double Penning trap JYFLTRAP improves the mass value for  $^{32}\text{Cl}$ ,” *Phys. Rev. C* **82**, 052501(R) (2010).
- [271] C. Wrede *et al.*, “Toward precise  $Q_{EC}$  values for the superallowed  $0^+ \rightarrow 0^+$   $\beta$  decays of  $T = 2$  nuclides: The masses of  $^{20}\text{Na}$ ,  $^{24}\text{Al}$ ,  $^{28}\text{P}$ , and  $^{32}\text{Cl}$ ,” *Phys. Rev. C* **81**, 055503 (2010).
- [272] W. Geithner *et al.*, “Masses and Charge Radii of  $^{17-22}\text{Ne}$  and the Two-Proton-Halo Candidate  $^{17}\text{Ne}$ ,” *Phys. Rev. Lett.* **101**, 252502 (2008).

- 
- [273] J. P. Wallace *et al.*, “ $\beta$ -delayed proton-decay study of  $^{20}\text{Mg}$  and its implications for the  $^{19}\text{Ne}(p,\gamma)^{20}\text{Na}$  break-out reaction in X-ray bursts,” *Phys. Lett. B* **712**, 59 (2012).
- [274] C. A. Diget *et al.*, “Structure of excited states in  $^{21}\text{Mg}$  studied in one-neutron knockout,” *Phys. Rev. C* **77**, 064309 (2008).
- [275] R. B. Firestone, “Nuclear Data Sheets for  $A = 21$ ,” *Nuclear Data Sheets* **103**, 269 (2004).
- [276] M. Walz, U.-G. Meißner, and E. Epelbaum, “Charge-dependent nucleon-nucleon potential from chiral effective field theory,” *Nucl. Phys. A* **693**, 663 (2001).
- [277] M. MacCormick and G. Audi, “Evaluated Experimental Isobaric Analogue States from  $T = 1/2$  to  $T = 3$  and associated IMME coefficients,” *Nucl. Phys. A* **925**, 61 (2014), [Erratum: *Nucl. Phys. A* 925, 296 (2014)].

---

## Acknowledgement

---

I would like to thank Prof. Achim Schwenk for his excellent supervision, for his outstanding encouragement and numerous helpful discussions during the past years. I am deeply grateful to him for enabling the opportunity to participate in workshops and conferences. I am also indebted to him for proofreading this thesis and for providing helpful comments.

I would also like to thank Prof. Hans-Werner Hammer for agreeing to be the second reviewer of my thesis.

Special thanks should be given to my collaborators, first of all thanks to Jason D. Holt and Javier Menéndez for the collaboration on the valence-space interactions derived from many-body perturbation theory. I am indebted as well to Kai Hebeler for his work on the partial-wave decomposition of 3N forces and numerous useful discussions. Benchmarks and helpful discussions with Heiko Hergert are also greatly appreciated. I would also like to thank Jason D. Holt and Ragnar Stroberg for the collaboration on IM-SRG calculations of closed- and open-shell nuclei. In addition, many thanks to all current and former members of the strongint group.

This work was supported by the ERC Grant No. 307986 STRONGINT, and the BMBF under Contract No. 05P15RDFN1. Computations were performed with an allocation of computing resources at the Computing Center of the TU Darmstadt (Lichtenberg), at the Max-Planck-Institute for Nuclear Physics, and at the Jülich Supercomputing Center (JURECA).

Ein großer Dank gebührt meinen Eltern, die mich bei all meinen Vorhaben unterstützt haben.



### Zur Person

Name Johannes Simonis  
Geburtsdatum 25. Juni 1988  
Geburtsort Dernbach/Westerwaldkreis  
Nationalität deutsch

### Akademische Ausbildung

seit 2013 Doktorand am Institut für Kernphysik - Theoriezentrum, Technische Universität Darmstadt  
Betreuer: Professor Achim Schwenk, Ph. D.

2011-2013 Master of Science in Physik, Technische Universität Darmstadt  
Thesis: Three-nucleon forces at neutron-rich extremes,  
Betreuer: Professor Achim Schwenk, Ph. D.

2007-2011 Bachelor of Science in Physik, Technische Universität Darmstadt  
Thesis: Polarization transfer coefficients from high-resolution polarized proton scattering at  $0^\circ$ ,  
Betreuer: Professor Dr. Peter von Neumann-Cosel

2007 Abitur, Konrad-Adenauer-Gymnasium, Westerburg



---

# Erklärung zur Dissertation

Hiermit versichere ich, die vorliegende Dissertation ohne Hilfe Dritter nur mit den angegebenen Quellen und Hilfsmitteln angefertigt zu haben. Alle Stellen, die aus Quellen entnommen wurden, sind als solche kenntlich gemacht. Diese Arbeit hat in gleicher oder ähnlicher Form noch keiner Prüfungsbehörde vorgelegen.

Darmstadt, den 4. Juli 2017

---

(Johannes Simonis)

---